BIO-INSPIRED HAIR FLOW SENSOR ARRAYS: FROM NATURE TO MEMS

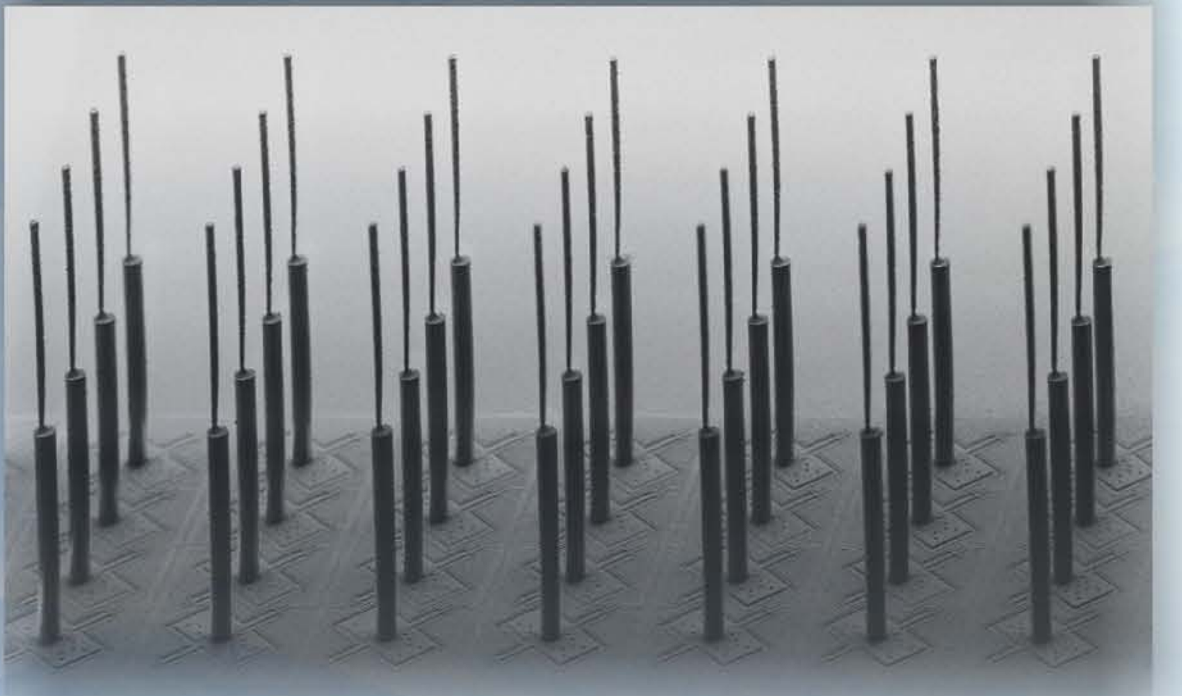

AHMAD MOHAMMAD KHALAF DAGAMSEH

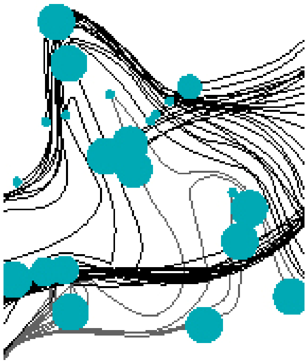

Bio-inspired Hair Flow-Sensor Arrays: From Nature to MEMS

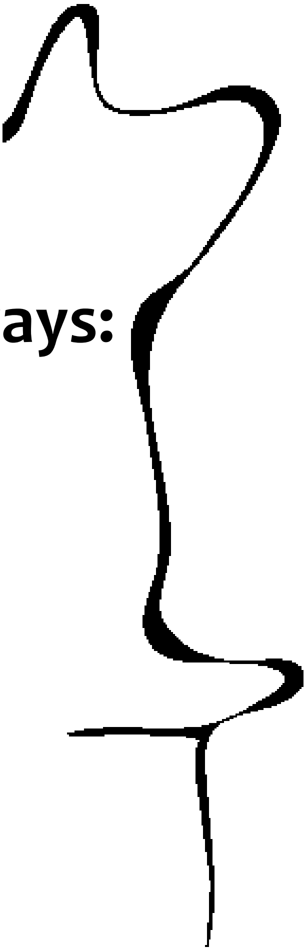

Ahmad Dagamseh

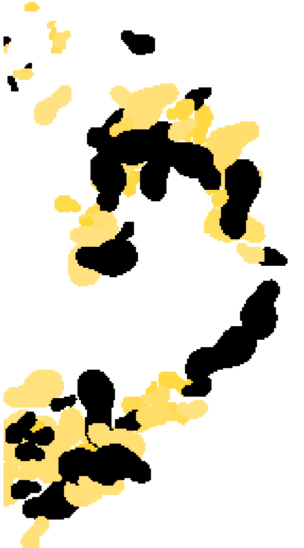

Graduation committee:

Chairman and secretary:	
Prof. dr. ir. A.J. Mouthaan	University of Twente, NL
Promotor:	
Prof. dr. ir. G.J.M. Krijnen	University of Twente, NL
Assistant-Promotor	
Dr. ir. R.J. Wiegerink	University of Twente, NL
Members:	
Prof. dr. ir. S. Stramigioli	University of Twente, NL
Prof. dr. J. Schmitz	University of Twente, NL
Prof. dr. ir. H. Peremans	University of Antwerp, BE
Prof. J. Miller	Montana State University, USA
Prof. dr. P.J. French	Delft University of Technology, NL

The research described in this thesis was carried out at the Transducers Science and Technology (TST) Group of the MESA$^+$ research Institute for Nanotechnology, University of Twente, The Netherlands. It has been financially supported by the Future and Emergent Technologies arm of the IST Programme under the Customized Intelligent Life-Inspired Arrays (CILIA) project and by the BioEARS VICI grant project of the Dutch Technology Foundation (STW/NWO).

UNIVERSITY OF TWENTE.
MESA+
INSTITUTE FOR NANOTECHNOLOGY
stw

Cover design by Ahmad Dagamseh.

Title: Bio-inspired Hair Flow-Sensor Arrays: From Nature to MEMS
Author: Ahmad Dagamseh
Printing: Wöhrmann Print Service, Zutphen, The Netherlands.
ISBN: 978-90-365-3308-9
DOI : 10.3990/1.9789036533089
Official URL: http://dx.doi.org/10.3990/1.9789036533089

BIO-INSPIRED HAIR FLOW-SENSOR ARRAYS: FROM NATURE TO MEMS

DISSERTATION

to obtain
the degree of doctor at the University of Twente,
on the authority of the rector magnificus,
prof. dr. H. Brinksma,
on account of the decision of the graduation committee,
to be publicly defended
on Wednesday 21 December 2011 at 12:45 hrs.

by

Ahmad Mohammad Khalaf Dagamseh

born on 5 December 1981
in Irbid, Jordan

This dissertation has been approved by:

The promoter: Prof. dr. ir. G.J.M. Krijnen
The assistant Promoter: Dr. ir. R.J. Wiegerink

*To **my parents**, my wife ' **Sarah** ' and our beloved coming son ' **Taym** '...*

Table of Contents

Chapter

1

FLOW SENSORS ‘make sense’

Sensing is a fundamental property of virtually all living creatures. Since behaviour and action require guidance (which is attained by sensors and sensory systems), it is hardly possible to live without sensing and life would ‘make little sense’. Throughout the animal kingdom, one finds a fascinating richness and diversity of sensors and sensory systems. In this chapter we present an example of these sensory systems (i.e. crickets hair sensors). It forms the source of inspiration underlying the development of an artificial hair-sensor based system for flow pattern measurements.

1.1. Biological background

Animals live in complex environments. However, they have developed many ways for survival through communication, defence against predators and capture of prey. Running of rabbits at high speeds, camouflage of chameleons, appalling smells of skunks, protective shields of turtles, swimming of fish and jumping of crickets are some examples of these surviving and defence mechanisms. For these mechanisms to function properly, these animals are equipped with dedicated sensory systems to collect information from the environment allowing it to judiciously be employed at minimal (energy, food) cost. Quite often this information is derived from (large) arrays of sensors (e.g. from eyes, ears, nose, lateral-line, hair-sensor canopies, etc.). So, in general, they will have to be evolved or need to have learned, to deal with large amounts of information.

The cricket, as an example of an insect that has such a sensory system, is described in this chapter from an engineering point of view and as a source of inspiration. The information presented here (and its underlying bulk of literature) forms the basis of our research and is our source of inspiration in developing highly-sensitive flow sensory array-systems, dedicated to the acquisition of spatio-temporal flow patterns. From this point of view the following questions are interesting: What are the main sensing mechanisms that cause crickets to respond to flow stimuli? What kinds of receptors are used to detect flows from approaching objects? What are the mechanical/neural properties of these sensors? How do the properties and spatial arrangements of these sensors help crickets?

1.1.1. Mechanoreceptor hairs in crickets: a case study

The spider-cricket escape behaviour has been well studied by biologists and neurophysiologists [Miller et al., 1991 & Casas et al., 2010]. As any moving object within a fluidic medium causes flow, an approaching predator is preceded by air-motion. Crickets exploit this air-motion using 10s – 100s of filiform hairs, spaced with small separation distances, to detect movement of their predators, even with stimulus energy of the order of k_BT (4×10^{-21} Joule at 300 °K) [Shimozawa et al., 2003 & Shimozawa 2005]. This allows crickets to run in directions away from their predators. Yet, the complete mechanism is not fully understood. Scientists need to consider the flow phenomena, the hair-sensor design, the arrangement of many hairs in array structures and the relative contribution of each of the hair-sensors in the cercal system, as well as the neuronal integration of all the available signals to the overall response of the sensory system of the cricket.

Two large mechano-sensory hair arrays, called cerci, residing at the crickets' rear of their body, form the sensing part of a cricket's escape mechanism [Shimozawa et al., 1998]. Each cercus is covered with up to a few hundred mechanoreceptive hair-sensors with varying geometric and mechanical properties such as length, diameter and rotational stiffness. Each filiform hair has an elongated paraboloid shape which varies between 30 and 1500 µm in length and 1 to 10 µm in base diameter [Shimozawa et al., 1984a]. The filiform hair is seated at its base in a visco-elastic socket which allows for rotation in a preferential plane of movement (directionality of the hair) and also provides a mechanical stopper for large rotations. Each hair is connected via a dendrite to a neuron [Gnatzy et al., 1989]. Due to the airflow generated by an approaching predator, viscous drag-torque induced rotations of the filiform hair are transmitted to the sensory neuron which, on exceeding a certain threshold, triggers an action potential. The spikes, or spike rates, encode the flow information. The cumulative flow-information gathered by the cerci, processed in large part in the terminal abdominal ganglion (TAG), allows the crickets to assess the flow-source and to act appropriately (e.g. by turning away rapidly from the stimulus). The high sensitivity of the hair-sensors enables perceiving tiny fluid movements (as low as 30 µm/s [Shimozawa et al., 2003]) while their small shape limits interference with the flow. Figure 1.1 illustrates the basic structure of the cercal sensory system as found in crickets.

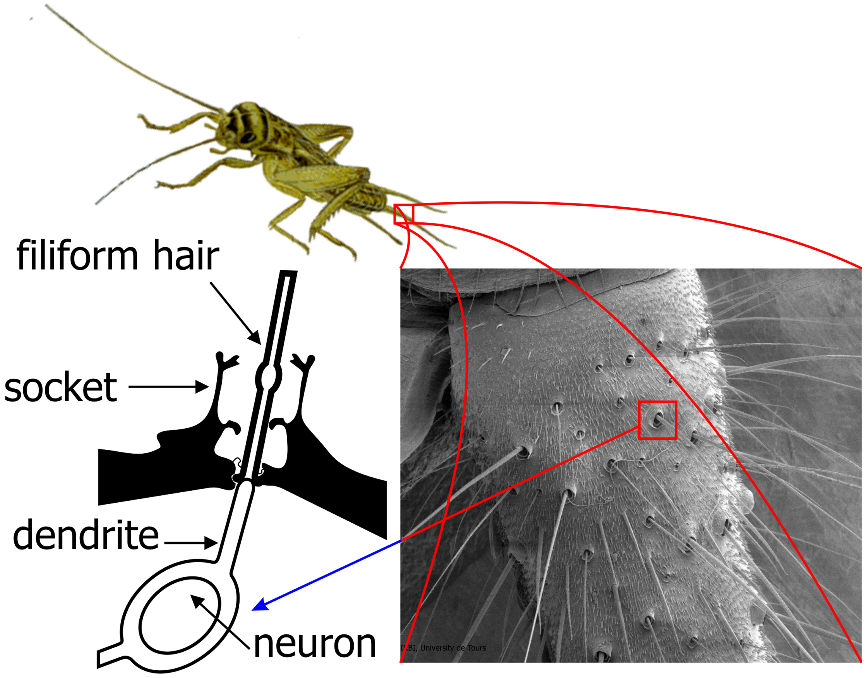

Figure 1.1: Basic structure of the mechanosensory system of crickets; the hair, the cercus and neuronal innervation [Dangles et al., 2005].

1.1.2. Why particle velocity?

Flows and pressure gradients, e.g. generated by source movements, go hand-in-hand. Organs which sense fluid motion can be sensitive either to pressure changes or particle displacement. Sensing pressure changes is commonly performed using membrane based structures (e.g. ears) while sensing particle displacement is often accomplished using hair-like receptors. Both, pressure variation and particle displacement depend on the distance from the source (*r*), the size of the source, the frequency and the properties of the medium (i.e. water or air). Within the near-field range (i.e. where $k.r \ll 1$ with k the wavenumber $2\pi/\lambda$ and λ the wavelength), air effectively can be considered incompressible and moves in phase with the vibrating surface. In this range, the particle velocity over pressure ratio is relatively large and hence the first is relatively easily perceived. For small sized animals (e.g. insects and spiders) the near-field range is large compared with their body length (few centimetres). Therefore, unsurprisingly, small animals are often equipped with particle velocity sensors (hair-like sensors) not pressure sensors (ears) to detect movements in the range of DC to a few hundreds of Hertz [Tautz et al., 1978]. For biological flow sources, dipole radiation may resemble natural flow sources such as wing-beats of flying insects or tail movement of fish accurately [Tautz et al., 1978 & Krijnen et al., 2010].

The hair-sensors are considered flow velocity sensors since at the frequencies of interest and at the size of the hair, or the spacing of the hairs or even the interaction distance between predator and prey, pressure gradients are extremely small and the hairs can be assumed to move solely due to viscous drag. Additionally, particle velocity sensors enable to determine the direction of the flow, a benefit compared to pressure sensing which to large degree can be considered omnidirectional (unless additional sensors are used to determine the flow-direction from pressure gradients but these are unimportant on the size of insects and the frequencies of concern).

1.2. Sensory systems in nature

In nature, animals can collect and process enormous amounts of information from the surroundings using arrays of sensors linked to peripheral and or central nerve system(s). These sensor arrays are highly sensitive, powerful and have built in redundancy. This is advantageous in such that malfunction of one of its elements will not impair the performance of the entire organ. The sensitivity of these systems, incredibly, has reached a point where flow levels which are only just distinguishable from noise, or even less when benefiting from noise itself, can be detected [Levin et al., 1996]. To achieve this, creatures have evolved with various tricks such as mechanical amplification and filtering using arrays of sensors which ‘lock’ to the signal and ‘zoom in’ to the source [McHenry et al., 2008]. Additionally, arrays with identical elements can be used to suppress the undesired signals and hence, improvement in the signal-to-noise ratio (SNR).

However, in these biological systems signal perception and interpretation is only partly understood. Further understanding potentially can help to attain the level of complexity, functionality and sensitivity of the natural systems in man-made sensory systems. This has driven humans to develop bio-inspired man-made systems; be it with respect to the sensing principle, shape and information processing strategies or any combination of these. The main challenge is to, efficiently, exploit the lessons learned from nature into engineered technologies.

1.3. Challenges in sensory systems

Although sensor-array systems hold promise for a range of sensory problems, in general they pose considerable technical challenges, particularly when the array task is concerned with pattern recognition. They are mainly related to sensor design, array design, array interfacing and data processing.

Proper sensor - measurand interaction and sensor readout are determining factors in system feasibility and complexity. E.g. the number of array connections can be significantly limited by clever array interfacing mechanisms rather than using direct sensor interfacing. Time division multiplexing (TDM) as well as Frequency division Multiplexing (FDM) are examples of arrays interfacing techniques. Performing on-chip digital signal processing is another possibility to transmit sensors' data with considerable simplification of the wiring. Moreover, the resulting decrease in required processing power and hardware benefits larger arrays and sensor densities.

1.4. MEMS & biology; hand-in-hand

1.4.1. Bio-mimetics and bio-inspiration

Recently, taking advantage of concepts found in nature has become an attractive route to produce sensors and systems with either better performance or increased capabilities compared to more traditional sensors. This bio-inspired approach, also called biomimicry, is a much wider and burgeoning field that examines principles and solutions for challenging environmental interaction problems as derived from biological examples. Added values of bio-inspired sensor designs are mainly sought in innovative options to surpass limited performance and robustness of traditionally engineered sensory systems at one hand but also help scientists to understand nature on the other hand. This new paradigm has attained impressive levels by taking advantage from concepts from nature, which has a large variety of sensory systems that are already optimized for survival [Vincent 2001].

Mimicking biological systems is performed in many ways such as 'stealing' sensor principles, morphological designs, materials properties, behaviour, computational algorithms or any combination of these from nature. However, in a biomimetic approach, directly copying nature's designs not necessarily has any benefits since the sensors purpose and context may be quite different from those of their natural counterparts. Fully understanding the biological systems assist engineers to extract meaning and principles and to manipulate their own systems within the design space to attain the best performance. By looking at nature, Micro-Electro Mechanical Systems (MEMS) techniques can be exploited to fabricate high-density sensory arrays, possibly matching the performance of the biological systems. This requires multi-disciplinary cooperation from e.g. (neuro-)biologists, physicists, chemists, material scientists and engineers to understand, investigate and implement such bio-inspired systems.

1.4.2. Why MEMS?

Modern sensor array systems and their applications require high spatial and temporal resolution measurements to capture the features of the respective physical fields. Using conventional sensors to build a large number of high-density sensory arrays is not a practical proposition. This would require assembly of a large number (up to hundreds or thousands) of sensor elements, ending up being highly impractical. MEMS technology enables fabrication of sensing devices with microscale features and arrayed structures [Hasegawa et al., 2004]. The size and weight problem may be overcome because MEMS offers tremendous possibilities to fabricate light and small sensors in high-density structures benefiting from advanced silicon technology. The high surface-area to volume ratio at the microscale (or even nanoscale) means that microsensors tend to have more sensitivity for surface related phenomena than for body-forces and, therefore, can help to attain high SNR for physical fields that interact through surface forces. Additionally, the small size of microsensors makes it possible to obtain rather localized measurements (e.g. of interest for sensors in biomedical applications [Grayson et al., 2004]). Interfacing circuitry enables a MEMS sensing element to become a fully functional transducer (possibly actuating as well as sensing). Array interconnects can be significantly simplified by integrating digital processing tasks on chip, which is more robust to transmission than low-level analogues. Building on these strengths the market for MEMS devices is expected to grow [Device Basics 2003] and array costs may be reduced when sensor-arrays are made in mass production (like e.g. ink-jet print-heads have shown).

1.5. Flow sensors 'make sense'

Since in natural environments flow is virtually everywhere, it is not surprising that flow sensory systems are found in many creatures helping them to locate prey, detect threats and predators [Coombs 2001 & Dangles et al., 2006]. Although flow is a very common phenomenon, the understanding of flow and flow signatures are far from trivial. Scientifics (in various disciplines) try to understand and model the dynamic representation of fluid flow around objects by devising measurement setups and sensory systems along with their developing theories [Shimozawa et al., 1984b & Casas et al., 2008]. Determining the flow rate of fluids is a common example for flow measurement in industrial and (bio-)medical applications [Ho et al., 1998 & Viarani et al., 2006]. Another example is the detection of flow patterns which can be used for detecting specific events as generated by the relative flow to object movement [Barth et al., 1995, Casas et al., 2008 & Kant et al., 2009]. The characteristics of the measured flow patterns can be exploited to determine size, position and number of flow sources [Franosch et al., 2005 & Casas et al., 2008]. This can be beneficial for biological, biomedical and control applications.

Historically, many flow sensors have been developed with different sensing principles such as thermal anemometry (e.g., hot-wire or hot-film anemometers [Perry 1982], Laser Doppler Velocimetry (LDV), Particle Image Velocimetry (PIV), indirect inference from pressure differences [Richter et al., 1999], through the Coriolis effect [Haneveld et al., 2010] and by utilising wall shear-forces [Brücker 2010]. However, the common flow measurement techniques such as hot-wire anemometry pose difficulties in measuring low flow velocities and directions are not unambiguously measured. Although LDV provides accurate flow velocity and directionality measurements, the complexity of the setup, its bulkiness and the costs make it difficult to implement for anything else than scientific or engineering purposes. Additionally, it only provides single point measurements excluding spatio-temporal flow measurements on or near moving surfaces. PIV delivers two-dimensional flow-patterns but also at the cost of a bulky and costly set-up that is primarily suitable for scientific and engineering purposes.

Recently, MEMS techniques have shown ample potential for fabrication of miniaturized flow sensors, utilizing various detection principles [Neda et al., 1996, Lai et al., 1997 & Dijkstra et al., 2008]. MEMS based flow sensors offer advantages in obtaining high-spatial resolution sensory systems and have shown a high sensitivity, a lower cost, a faster response and a lower power consumption compared to traditional flow sensors. The first flow sensor based on silicon micromachining technology was shown in 1974 [Van Putten 1974 & Nguyen 1997]. Several principles of these micromachined sensors based on heat transfer [de Bree et al., 1999, Chen et al., 2003 & Kim et al., 2004], momentum transfer [Svedin et al., 1998, Su et al., 2002 & Haneveld et al., 2009] and pressure measurements [Cho et al., 1993] have been demonstrated afterwards.

1.6. Scope of this thesis

Biological hair-sensors are among the most sensitive systems that appear in nature. The aim here is to take inspiration by this biological system (cricket hairs) in order to develop high-performance array systems made of artificial hair flow-sensors and to be applied in flow pattern measurements. This can be beneficial for engineers, e.g. in robotics applications, as well for biologists in helping them to understand the biological systems (using the artificial counterparts) and verifying their hypothesis.

The limitations imposed by practical difficulties in measuring flow patterns motivated us to develop highly sensitive hair-like flow sensors and additionally to make high-density hair sensor arrays. These arrays should be able to simultaneously measure low-amplitude, high-resolution flow patterns with sufficient temporal resolution (bandwidth up to 1 kHz). This thesis describes our route to sensitive artificial hair flow-sensor arrays by improved hair design and clever interfacing strategies and the application of these arrays in flow pattern measurements. The impact of interfacing on the performance of the hair sensor is analysed and a single hair-sensor able to measure a minute airflow down to about 1 mm/s is realized from the acquired knowledge under certain acquisition conditions. Targeting 'live' (i.e. real-time) flow-pattern measurements, different array interfacing schemes are investigated in which FDM has shown to be the appropriate candidate for interfacing the hair-sensor arrays under the conditions they are currently operated. Spatio-temporal flow pattern measurements are demonstrated with arrays of hairs using harmonically or transient flows (i.e. due to a moving sphere acting as dipole source) and the results are used to localize the sources. With such system, different representations and post processing techniques of these signals can be used to acquire, with increased flexibility, more information about flow and afterwards to perform an action. This formulates the basics of a sensory array system that can be implemented (for example) in:

- Monitoring flow fields at critical surfaces or positions (i.e. flow-based camera);

- Supporting biologists to study and understand nature by means of making artificial systems equivalent to their counterparts in nature;
- Assisting in performing spatio-temporal flow pattern measurements, which can be used in tracking moving objects and avoid collisions for robotic control and industrial applications.

In this thesis, chapter two briefly describes the principles underlying our artificial hair flow-sensors (biological source of inspiration, fluid-hair interaction model, design basics, fabrication and characterization).

Chapter three discusses the interfacing circuitry of the hair sensor and possibilities to improve its design. Adapting the electrode design of the hair sensor has resulted in a considerable improvement in its detection-limit and sensitivity direction.

Chapter four introduces different possibilities for addressing hair sensor arrays targeting performing live measurements for applications of flow pattern recognition. Detailed analysis is done to compare the application of each scheme to hair-sensor arrays and their possible impact on the performance of individual array elements. This is followed by the design and fabrication of a single-chip hair sensor array using Silicon-On-Insulator (SOI) technology with the possibility of interrogating array elements individually using FDM.

Next, chapter five presents the application of hair sensor arrays in flow field measurements, at the position of array sensors. This is performed by measuring (as an example) the dipole field in a (virtual) lateral-line system (LLS). Using artificial hair sensors, a virtual lateral-line system is used for dipole source localization and then a lateral-line with discrete sensors is studied. Additionally, array signal processing (ASP) techniques (beamforming) are used with hair-sensor arrays to determine position of the dipole source.

In chapter six the ability of the hair sensor to perform spatio-temporal flow field measurements i.e. transient airflow, is investigated. Single-chip arrays are used to measure the transient response due to a moving source (i.e. inspired by the cricket-spider escape mechanism) while, simultaneously, implementing FDM. The hair-sensor array shows its ability to measure the flow field with sufficient temporal and spatial resolution.

The thesis ends with chapter seven which summarizes our achievements in realizing the basics of a ‘flow-camera’ and in which possible directions for further research in this respect are proposed.

1.7. References

[Barth et al., 1995] Barth, F.G., Humphrey, J.A., Wastl, U., Halbritter, J. & Brittinger, W. (1995) "Dynamics of arthropod filiform hairs. III. Flow patterns related to air movement detection in a spider (Cupiennius salei KEYS.)", Philosophical Transactions of the Royal Society B: Biological Sciences, 347, pp. 397–412.

[Brücker 2010] Brücker, Ch. (2010) "Time-resolved wall-shear stress imaging on surfaces coated with arrays of flexible micro-pillars", In the 48th AIAA Aerospace Sciences Meeting Including the New Horizons Forum and Aerospace Exposition, Art. no. 20100494.

[Casas et al., 2008] Casas, J., Steinmann, T. & Dangles, O. (2008) "The aerodynamic signature of running spiders", PLoS ONE, 3, Art. no. e2116.

[Casas et al., 2010] Casas, J., Steinmann, T. & Krijnen, G. (2010) "Why do insects have such a high density of flow-sensing hairs? Insights from the hydromechanics of biomimetic MEMS sensors", Journal of the Royal Society Interface, 7, pp. 1487–1495.

[Chen et al., 2003] Chen, J., Fan, Z., Zou, J., Engel, J. & Liu, C. (2003) "Two-dimensional micromachined flow sensor array for fluid mechanics studies", Journal of aerospace Engineering, 16, pp. 85–97.

[Cho et al., 1993] Cho, S.T. & Wise, K.D. (1993) "A high-performance microflowmeter with built-in self test", Sensors and Actuators A: Physical, 36, pp. 47–56.

[Coombs 2001] Coombs, S. (2001) "Smart skins: information processing by lateral line flow sensor", Autonomous Robots, 11, pp. 255–261.

[Dangles et al., 2005] Dangles, O., Magal, C., Pierre, D., Olivier, A. & Casas, J. (2005) "Variation in morphology and performance of predator-sensing system in wild cricket populations", J. Exp. Bio., 208, pp. 461–468.

[Dangles et al., 2006] Dangles, O., Ory,N., Steinmann, T., Christides, J.P.& Casa, J. (2006) "Spider's attack versus cricket's escape: velocity modes determine success", Anim. Behav., 72, pp. 603–610.

[de Bree et al., 1999] de Bree, H-E., Jansen, H., Lammerink, T.S.J., Krijnen, G.J.M., & Elwenspoek, M. (1999) "Bi-Directional Fast Flow Sensor with a Large Dynamic Range", Journal of Micromechanics and Microengineering, 9, pp. 186–189.

[Device Basics 2003] Device Basics (2003) Semiconductor International, pp. 128, www.semiconductor.net.

[Dijkstra et al., 2008] Dijkstra, M., Boer M.J.D., Berenschot, J.W., Lammerink, T.S.J., Wiegerink, R.J. & Elwenspoek, M. (2008) "Miniaturized thermal flow sensors with planar-integrated sensor structures on semicircular surface channels", Sensors and actuators A: Physical, 143, pp. 1–6.

[Franosch et al., 2005] Franosch, J-M.P., Sichert, A.B., Suttner, M.D. & Van Hemmen, J.L. (2005) "Estimating position and velocity of a submerged moving object by the clawed frog Xenopus and by fish", Biological Cybernetics, 93, pp. 231–238.

[Gnatzy et al., 1989] Gnatzy, W. & Hustert, R. (1989) "Cricket behaviour and neurobiology", London: Cornell.

[Grayson et al., 2004] Grayson, R., Shawgo, S., Johnson, M., Flynn, T., Li, Y., Cima, J. & Langer, R. (2004) "A BioMEMS review: MEMS technology for physiologically integrated devices", In: proceedings of the IEEE, 92, pp. 6–21.

[Haneveld et al., 2009] Haneveld, J., Lammerink, T.S.J., de Boer, M.J. & Wiegerink, R.J. (2009) “Micro coriolis mass flow sensor with integrated capacitive readout”, In: IEEE 22nd International Conference on MEMS, Sorrento, Italy, pp. 463–466.

[Haneveld et al. 2010] Haneveld, J., Lammerink, T.S.J., De Boer, M.J., Sanders, R.G.P., Mehendale, A., Lötters, J.C., Dijkstra, M. & Wiegerink, R.J. (2010) "Modeling, design, fabrication and characterization of a micro Coriolis mass flow sensor", Journal of Micromechanics and Microengineering, 20, Art. no. 125001.

[Hasegawa et al., 2004] Hasegawa, Y., Shikida, M., Shimizu, T., Miyaji, T., Sasaki, H., Sato, K. & Itoigawa, K. (2004) “Micromachined active tactile sensor for hardness detection”, Sensors and Actuators A: Physical, 114, pp. 141–146.

[Ho et al., 1998] Ho, C.M. & Tai, Y.C. (1998) "Micro-Electro_mechanical_systems (MEMS) and fluid flows", Annu. Rev. Fluid Mech., 30, pp.579–612.

[Kant et al., 2009] Kant, R. & Humphrey, J. (2009) "Response of cricket and spider motion-sensing hairs to airflow pulsations", Journal of the Royal Society Interface, 6, pp. 1047–1064.

[Kim et al., 2004] Kim, S., Nam, T. & Park, S. (2004) “Measurement of flow direction and velocity using a micromachined flow sensor”, Sensors and Actuators A: Physical, 114, pp. 312–318.

[Krijnen et al., 2010] Krijnen, G.J.M., Lammerink, T.S.J. & Wiegerink, R.J. (2010) “Learning from crickets: artificial hair-sensor array developments”, In: IEEE sensors conference, Hawaii, USA. pp. 2218–2223.

[Lai et al., 1997] Lai, P.T., Liu, B., Zheng, X., Li, B., Zhang, S. & Wu, Z. (1997) “Monolithic integrated spreading-resistance silicon flow sensor”, Sensors and Actuators A: Physical, 58, pp. 85–88.

[Levin et al., 1996] Levin, J.E. & Miller, J.P. (1996) "Broadband neural encoding in the cricket cercal sensory system enhanced by stochastic resonance", Nature, 380, pp. 165–168.

[McHenry et al., 2008] McHenry, M.J., Strother, J.A. & Van Netten, S.M. (2008) "Mechanical filtering by the boundary layer and fluid-structure interaction in the superficial neuromast of the fish lateral line system", Journal of Comparative Physiology A: Neuroethology, Sensory, Neural, and Behavioral Physiology, 194, pp. 795–810.

[Miller et al., 1991] Miller, J.P., Jacobs, G.A. & Theunissen, F.E. (1991) "Representation of sensory information in the cricket cercal sensory system. I. Response properties of the primary interneurons", Journal of Neurophysiology, 66, pp. 1680–1689.

[Neda et al., 1996] Neda, T., Nakamura, K. & Takumi, T. (1996) “A polysilicon flow sensor for gas flow meters”, Sensors and Actuators A: Physical, 54, pp. 626–631.

[Nguyen 1997] Nguyen N.T. (1997) “Micromachined flow sensors - A review", Flow Measurement and Instrumentation, 8, pp. 7–16.

[Perry 1982] Perry, A.E. (1982) “Hot wire anemometry”, Clarendon, Oxford, England.

[Richter et al., 1999] Richter, M., Wackerle, M. Woias, P. & Hillerich, B. (1999) "A novel flow sensor with high time resolution based on differential pressure principle", In proc., 12th International Conference on Micro Electro Mechanical Systems, Orlando, Fla., pp. 118–123.

[Shimozawa et al., 1984a] Shimozawa, T., & Kanou, M. (1984) "Varieties of filiform hairs: range fractionation by sensory afferents and cercal interneurons of a crickets", Journal of Comparative Physiology, A155, pp. 485–493.

[Shimozawa et al., 1984b] Shimozawa, T., & Kanou. M. (1984) "The aerodynamics and sensory physiology of range fractionation in the cercal filiform sensilla of the cricket Gryllus bimaculatus", J. Comp Physiol, A 155, pp. 495–505.

[Shimozawa et al., 1998] Shimozawa, T., Kumagai, T., & Baba, Y. (1998) "Structural scaling and functional design of the cercal wind-receptor hairs of cricket", Journal of Comparative Physiology, A183, pp. 171–186.

[Shimozawa et al., 2003] Shimozawa, T., Murakami, J. & Kumagai, T. (2003) "Cricket wind receptors: thermal noise for the highest sensitivity known", In Sensors and sensing in biology and engineering (eds F. G. Barth, F.G., Humphrey, J.A.C. & Secomb, T.W.) pp. 147–157. New York, NY: Springer-Wein.

[Shimozawa 2005] Shimozawa, T. (2005) "Biological insight into future technology - What living cells tell us", In the 3rd IEEE/EMBS Special Topic Conference on Microtechnology in Medicine and Biology, Art. no. 1548417.

[Su et al., 2002] Su, Y., Evans, A.G.R., Brunnschweiler, A. & Ensell, G. (2002) "Characterization of a highly sensitive ultrathin piezoresistive silicon cantilever probe and its application in gas flow velocity sensing", Journal Micromech. Microeng., 12, pp. 780–785.

[Svedin et al., 1998] Svedin, N., Kälvesten, E., Stemme, E., & Stemme, G. (1998) "A Lift-Force Flow Sensor Designed for Acceleration Insensitivity", Sensors and Actuators A: Physical, 68, pp. 263–268.

[Tautz et al., 1978] Tautz, J. & Markl, H. (1978) "Caterpillars detect flying wasps by hairs sensitive to airborne vibration", Behavioral Ecology and Sociobiology, 4, pp.101–110.

[Van Putten et al., 1974] Van Putten, A.F.P. & Middelhoek, S. (1974) "Integrated silicon anemometer", Electronics Letters, 10, pp. 425–426.

[Viarani et al., 2006] Viarani, N., Massari, N., Gottardi, M., Simoni, A., Margesin, B., Faes, A., Decarli, M. & Guarnieri, V. (2006) "A low-cost microsystem for noninvasive uroflowmetry", IEEE Transactions on Instrumentation and Measurement, 55, pp. 964–971.

[Vincent 2001] Vincent, J. (2001) "Stealing ideas from nature", Chapter 3 in Deployable structures, Springer-verlag, Vienna, Pellegrino E. (Ed.), pp. 51–58.

Chapter

2

BACK TO INSECTS

Virtual all creatures are immersed in fluidic environments (e.g. water or air) which may be disturbed by animal motion, relative to the surroundings, causing specific fluidic signatures. Depending on frequency, fluid properties and source – observer distance these fluidic motions may manifest themselves more as bulk flow (incompressible and near to the source) or more as a travelling wave (compressible flow, particle velocity) and in far field conditions they may be more apparent through either pressure variations or through flow phenomena. The animal kingdom shows ample examples of species that have evolved with either extremely pressure-sensing or flow-sensing capabilities. This chapter presents the state of the art in artificial hair flow-sensors. This is followed with an introduction to the basics (i.e. theoretical models, design basics, fabrication process and characterization) of our hair sensor approach. A description for the research performed with our hairs concludes this chapter driven with the motivation of measuring airflow patterns.

2.1. Bio-inspired hair flow-sensors

Since a few years, the mechano-sensory hairs of crickets have been a common research topic for both biologists and engineers [Casas et al., 2010 & Krijnen et al., 2007]. Biologists try to understand nature by testing their hypotheses using bio-inspired systems while engineers try to design high-performance sensory systems based on the knowledge of their counterparts in nature. Several groups have reported different sensor designs for measuring particle velocity flow either in air or water [de Bree 1997, Fan et al., 2002, Dijkstra et al., 2005, Krijnen et al., 2007 & Wang et al., 2007]. These designs can be categorized according to their sensing mechanism (heat transfer, force transfer), sensitivity direction (either normal or parallel to the substrate), transduction principle (piezoelectric, piezoresistive or capacitive), sensing environment (air or water) and used materials (various silicon-nitride compositions and polymers such as SU-8). In this section we will discuss briefly some of the hair-based flow sensors only.

In MEMS, free standing cantilevers are often used as transducer for mechanical forces. When the obstacle is immersed in a flow, a drag force will result in a deflection and/or a rotation. Zou et al. [Zou et al. 2001] have developed a three dimensional assembly process called Plastic Deformation Magnetic Assembly (PDMA) which is used in the fabrication of piezoresistive flow sensor arrays to work in water with the intend to imitate the lateral-line system in fish [Fan et al., 2002 & Yang et al., 2011]. Each array element consists of a fixed-free cantilever with piezoresistive elements at its base. In the PDMA process, a magnetic field is used to bend the cantilever, which remains bent after the magnetic field is removed. Results show that they were able to measure water flow down to 0.2 m/s. N. Chen et al. adapted the process in [Zou et al. 2001] by replacing the obstacle fabricated using the PDMA process with 700 µm SU-8 hairs at tips of cantilevers and strain gauges at their base [Chen et al., 2007]. The sensor was designed to operate in water but also shown to work in air. In water, the sensor response to ac flows has shown a linear response with a detection limit of about 0.7 mm/s at 50 Hz oscillating flow measured at 2 Hz bandwidth. Figure 2.1 shows an example of flow hair sensors fabricated out-of-plane for applications in water.

In literature, there are many examples of airflow sensors. Kim et al. [Kim et al., 2000] developed a cantilever-based gasflow sensor with piezoresistive elements at its base using $n/n^+/n$ doped silicon layers. The cantilevers were curled up (to be exposed to the airflow stream parallel to the substrate) by annealing them at 450 C^o, where the height was controlled by varying the annealing time and temperature. Su et al. [Su et al., 2002] have realized a silicon cantilever based airflow sensor with integrated strain gauge at its base. The measurement range was shown to be in range of 0.07 to 20 m/s. Xu et al. [Xu et al., 2004] developed a micro-cantilevers array (with varying lengths) functioning as optical waveguides and used for acoustic applications. Light is generated by a light emitting diode (LED) and collected by a photo diode. The micro-cantilevers were used to pick up the drag force and, as a waveguide, to guide and modulate the light to produce a signal by light detectors. Wang et al. [Wang et al., 2007] fabricated an airflow sensor with a free-standing micro-cantilever structure where the airflow is determined by measuring the change in resistance using an external LCR meter. The results show that the sensor has 0.0284 Ω/m/s sensitivity with a detection range of up to 45 m/s and response time of 0.53 seconds. Lee et al. [Lee et al., 2009] proposed a flow sensor by arranging eight cantilevers on an octagonal shape based on the piezoresistive effect. The tips of the bimorph cantilevers bend upwards due to the difference in the thermal expansion of silicon nitride and silicon films. The flow rate and its direction were determined by measuring the resistor signal from each cantilever. Figure 2.2 shows an example of cantilever-based flow sensors.

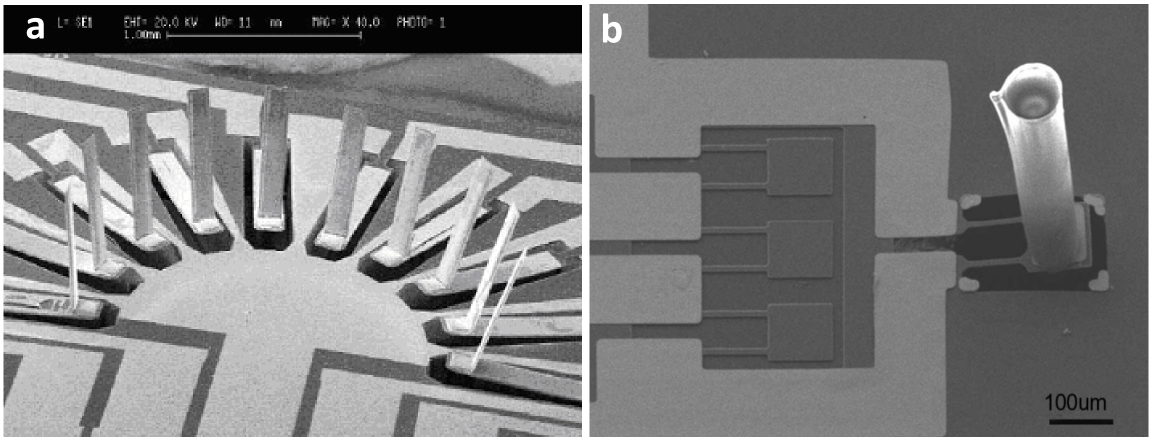

Figure 2.1: Out-of-plane artificial hair flow sensor where the obstacles were (a) fabricated using the PDMA process [Fan et al., 2002] and (b) made of polymer materials [Chen et al., 2007].

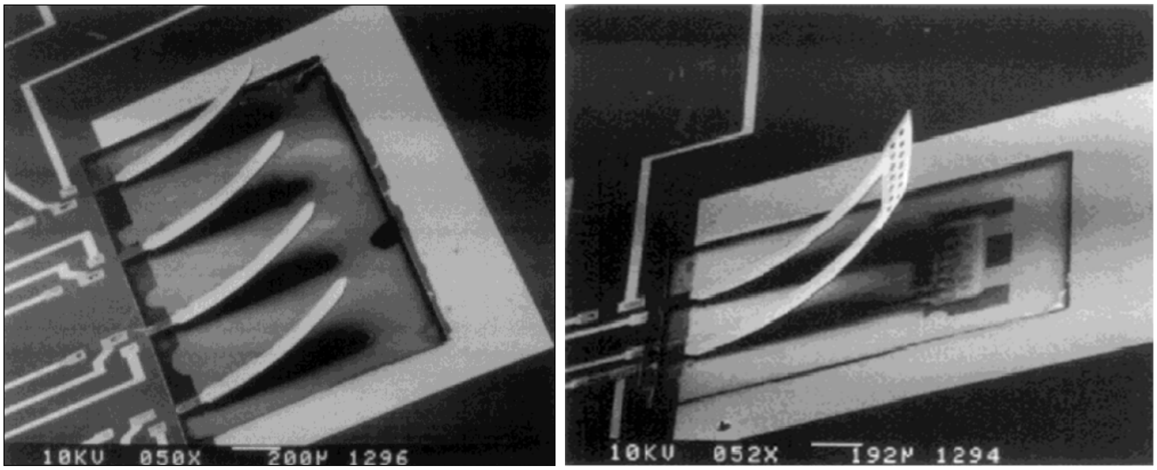

Figure 2.2: Cantilever-based gasflow sensor [Kim et al., 2000].

However, cantilever-based flow sensors are also sensitive to fluid flow acting normal to the substrate. In best cases, the cantilever bends upwards several tens of micrometers using induced stress. This is a limitation for this type of sensors, since the amount of drag torque picked up by the obstacle determines the amount of deflection and thereby its sensitivity. Additionally, the surface area needed to fabricate the cantilevers scales with their lengths or widths. This poses limitations for high-density arrays with cantilevers as basic element. To overcome this, several groups have developed flow sensors with out-of-plane obstacles (i.e. no cantilever as an obstacle inspired) by biological examples such as the lateral-line system in fish [Chen et al., 2007] and cerci in crickets [Dijkstra et al., 2005]. The artificial hairs were made in different lengths and widths (100 to 900 um length and 25 to 80 um width) using different materials such as silicon, silicon nitride composition and SU-8. The advantage is that these devices are sensitive to flow acting parallel to the substrate and can be fabricated in high-density arrays, with different sensor-orientations, easily.

Ozaki et al. [Ozaki et al., 2000] has demonstrated the fabrication of 1-DOF and 2-DOF sensory hairs. The 1-DOF design consists of cantilevers with different lengths with piezoresistive elements at the base (similar to the cantilever designs discussed above). The 2-DOF design consists of a long wire (5 mm) attached manually to the centre of cross-shaped beam with integrated strain gauges. Both designs showed an ability to measure airflows in the range from a few cm/s to 2 m/s. However, the fabrication scheme of the hair structure poses restrictions with respect to high-density arrays. Dijkstra et al. [Dijkstra et al., 2005 & Krijnen et al., 2006] fabricated flow-sensor arrays imitating the filiform hairs of crickets. Surface micromachining technology has been used to fabricate suspended silicon nitride membranes and hairs were made by a repeated lithography process to form double layers of SU-8 (negative photoresist). Chen et al. [Chen et al., 2007] have used polymer material (SU-8) at the tip of the cantilever to make hairs of 700 µm length. The biomimetic flow sensor presented in [Dijkstra et al., 2005 & Krijnen et al., 2006], as inspired by crickets, forms the core of our study. The basic principle, various design improvements and applications using single sensors and array structures have been demonstrated and will be discussed in this thesis.

2.2. Our approach

Recently we have developed in our group (Transducers Science & Technology group, University of Twente) an artificial hair flow-sensor array, inspired by the mechano-sensory system of crickets [Dijkstra et al., 2005]. The achieved bio-inspired design, though based on viscous drag captured by hairs, differs from the biological one in the materials used (primarily inorganic vs organic), occupied area and transduction mechanism (electro-mechanical vs mechano-chemical). This section presents an overview of the developments of our artificial hair flow-sensor. Design basics, fabrication and characterization will be shown briefly. The development line of this approach has been enabled by various projects started by the EU sponsored Cricket Inspired perCeption And Decision Automata (CICADA) project followed by the EU sponsored Customized Intelligent Life-Inspired Arrays (CILIA) and currently continued in the NWO sponsored Bio-inspired Engineering of ARray Sensors (Bio-EARS). The line of research can be summarized:

1. Modelling flow-hair interactions;
2. Developing appropriate sensing mechanisms;
3. Devising fabrication processes with limited complexity and overcoming technical challenges in the fabrication of single and arrays of hair-sensors;

4. Improving sensor performance (detection limit, sensitivity, bandwidth and directionality) by:
    a) Adapting the mechanical design of the sensor based on understanding the fluid mechanics of airflow surrounding the hair-shaft;
    b) The proper choice of materials used in the sensor;
    c) Implementing additional principles exploiting nonlinearity such as parametric amplification and stochastic resonance.
5. Investigating the most efficient ways to interface single sensors and arrays of hair- sensors;
6. Developing and implementing appropriate electronics for interfacing single and arrays of hair-sensors;
7. Designing hair-sensor array systems and exploiting the diversity of multi-hair sensors for measuring flow patterns;
8. Applying mechanical filtering to arrays of hair-sensors;
9. Improving the robustness of the sensors;
10. Applying hair-sensor arrays for flow pattern measurements.

2.2.1. Mathematical model

In natural hair flow-sensors, the transduction of the flow-velocity into an action potential is executed by three structures: the hair shaft (which picks up the drag-torque), the socket (which provides the pivot point and determines much of the dynamics of the sensor) and the neural system (where the actual coding of the hair-rotation into action potentials takes place). In the modelling we restrict ourselves to the first two structures. The idea is to simultaneously calculate viscous drag-torque and hair mechanical response from given flow velocity distributions as function of space and time. We will not add any new contributions to the existing literature on this subject but rather will apply the prevailing models specifically to our artificial hair-sensor system in order to gain insight and find rational design-choices optimizing them.

Several studies have been reported in literature considering the functioning of hair-like flow-sensors [Barth et al., 1993, Humphrey et al., 2003 & Bathellier et al., 2005]. Generally, in these studies the hair has been modelled as an inverted pendulum which can be described by a damped second order mechanical system. Hair- length (L_h), hair-width (D_h), hair-mass and material properties of the hair-socket determine the mechanical response of the system through the hair's moment of inertia, spring stiffness, damping and the extent of the hair into fluid-flow around the cercus. These hairs are sensitive to fluid flow velocities in lower frequency ranges with resonance frequencies between 85-500 Hz [Shimozawa et al., 1998]. Figure 2.3 shows a schematic representation for the hair sensor and an example as found in crickets.

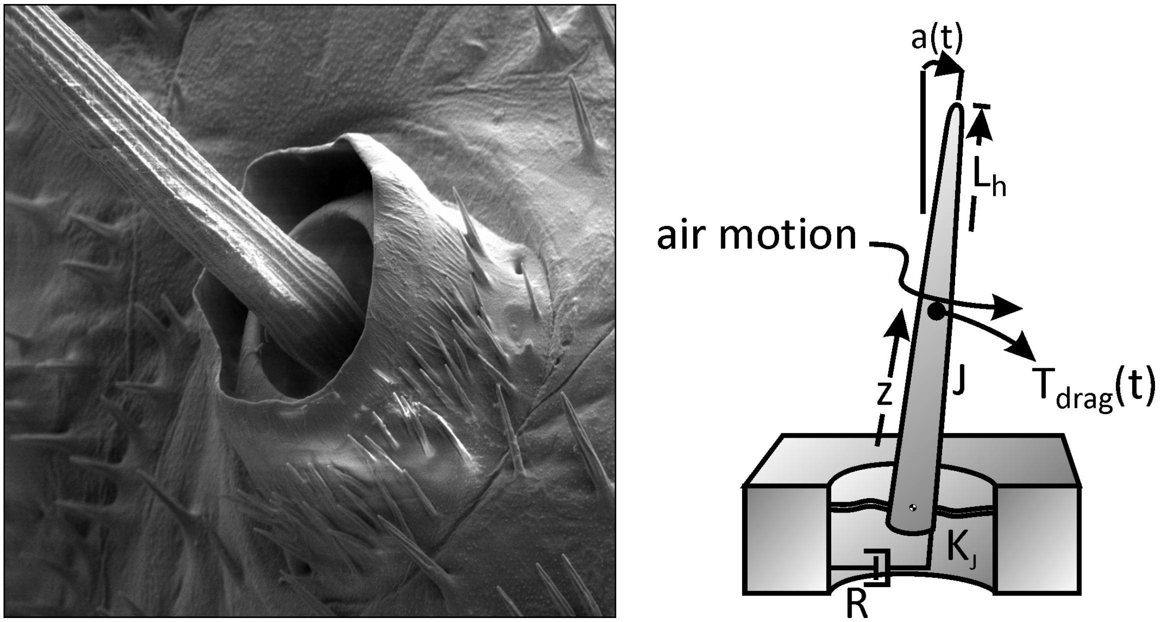

Figure 2.3: (a) An SEM image for the filiform hair sensor of crickets (courtesy of J. Casas, IRBI, University of Tours) and (b) schematic drawing for the mechanical model of the filiform hair sensor represented as inverted pendulum [Shimozawa et al. 1998].

Fluid-hair interaction

The interaction between hair-shaft and air can be described as an immersed object in surrounding fluid. The hair is modelled as a cylindrical object on top of a substrate. The overall system performance is largely affected by the fluid-hair interaction. The air oscillates with flow velocity V_f parallel to the substrate and normal to the hair shaft. It is a function of the distance (z) from the substrate. By modelling the substrate as a flat plane, assuming incompressibility, low Reynolds numbers and while applying the no-slip boundary condition, the fluid-velocity on top of the substrate is given by eq. 2.1 [Stokes 1851 & Shimozawa et al., 1984]. Figure 2.4 shows the velocity profile along the hair shaft at different time instants.

$$V_f(z) = U_o \sin(2\pi f.t) - U_o e^{-\beta.z}.\sin(2\pi f.t - \beta.z) \tag{2.1}$$

where U_o is the peak amplitude of the far-field velocity, $U_o \sin(2\pi f.t)$ is the velocity of the fluid at far distance from the substrate and $\beta = \sqrt{\pi f / \nu}$ is proportional to the reciprocal of the boundary layer thickness with f as the oscillating airflow frequency (Hz) and ν as the kinematic viscosity of the fluid (e.g. for air $\nu_{air} = 1.5 \times 10^{-5}$ [m^2/s] at 20 °C).

The natural hair, when subjected to airflow, rotates with angular displacement (α) due to the viscous drag forces acting on the shaft and transmits its rotation to the neural system [Shimozawa et al., 1998 & Humphrey et al., 2008]. The absolute relative velocity (V_r) between fluid flow (V_f) and hair motion (V_h) as:

$$V_r = V_f - V_h \tag{2.2a}$$

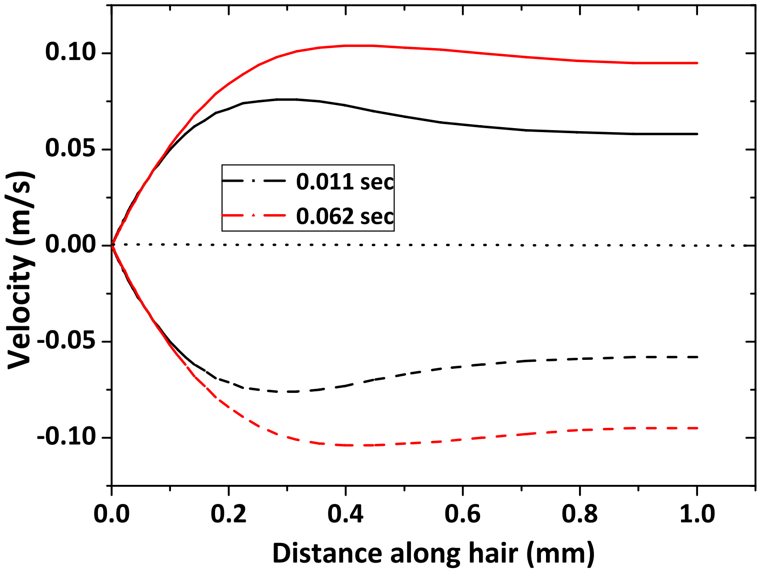

Figure 2.4: Simulated fluid (air) velocity profile (at *f*=100 Hz) as function of distance from substrate surface at different time instants.

with

$$V_h = z \cdot \frac{d\alpha}{dt} \tag{2.2b}$$

To accommodate Stokes theory [Stokes 1851] the following approximations are applied [Humphrey et al., 2008]:

- the pendulum is approximated as a cylinder;
- small rotations are assumed which implies that the fluid is normal to the hair-shaft;
- the dimensionless parameter (*s*<<1, eq. 2.3) which implies that Reynolds number (*Re*<<1, eq. 2.4).

$$s = \left(\frac{D_h}{4}\right)\left(\frac{2\pi f}{\nu}\right)^{1/2} \ll 1 \tag{2.3}$$

Given the assumption of displacements that are comparable to the hair-diameter Reynolds number becomes:

$$Re = \frac{VD_h}{\nu} \propto s^2 = \frac{D_h^2 f}{\nu} \ll 1 \tag{2.4}$$

The drag forces are composed of forces due to fluid viscosity and fluid density acting on hair shaft per unit length in which [Humphrey et al., 2008]:

$$F_{tot}(t) = F(\mu, V_r) + F(\mu, \dot{V}_r) + F(\rho, \dot{V}_r) \tag{2.5}$$

where μ is the viscosity of the fluid (ex. for air $\mu_{air} = 1.82 \times 10^{-5}$ [N.s.m^{-2}] at 20 ^{o}C) and

$$F(\mu, V_{\mathrm{r}}) = 4\pi\mu G V_{\mathrm{r}} \tag{2.6}$$

$$F(\mu, \dot{V}_{\mathrm{r}}) = \frac{-\pi\mu G}{2gf}\dot{V}_{\mathrm{r}} \tag{2.7}$$

$$F(\rho, \dot{V}_{\mathrm{r}}) = \rho\pi(D_{\mathrm{h}}/2)^2\dot{V}_{\mathrm{r}} \tag{2.8}$$

Here, $\dot{V}_{\mathrm{r}}$ represents the time rate of change of V_{r} along the hair-shaft with

$$G = \frac{-g}{g^2 + (\pi/4)^2} \tag{2.9}$$

and

$$g = \ln(s) + 0.577 \tag{2.10}$$

The total drag torque (T_{drag}) is determined by calculating the total drag forces acting along the hair shaft times the distance to the rotational point:

$$T_{\mathrm{drag}} = \int_0^{L_{\mathrm{h}}} F_{\mathrm{tot}}(z,t).z.dz \tag{2.11}$$

where F_{tot} is the force per unit length (including the effect of the virtual mass of the fluid) acting normal to the hair at positio*n* (*z*) along its length. J. Humphrey has shown that for most of the air motion oscillation cycle the ratio between the torque associated with added mass and the total torque in the hair system is >10% [Humphrey et al. 1993]. Therefore, for obtaining an accurate representation of the hair motion the contribution of the virtual mass should not be neglected.

Fluid forces acting on hair shaft and its mechanical properties determine the overall hair response. The mechanics of the hair sensor motion, as governed through the conservation of angular momentum and approximated as a forced damped harmonic system, require that [Humphrey et al., 1993]:

$$J_{\mathrm{eff}}\frac{d^2\alpha(t)}{dt^2} + R_{\mathrm{eff}}\frac{d\alpha(t)}{dt} + S\alpha(t) = T_{\mathrm{drag}}(t) \tag{2.12}$$

where R_{eff} is the total damping in the system which includes friction at hair base (R) as well as friction between the added mass of fluid and the surrounding air (R_{μ}) (see eq. 2.13), S is the rotational spring constant and J is the total moment of inertia of the hair system (eq. 2.14). It is worthwhile mentioning that Stokes [Stokes 1851] considered in his drag force analysis the added mass to the hair shaft due to the fluid flow which is moving in phase with the cylinder. This contribution results in the force expressed by eq. 2.8.

$$R_{\mu} = 4\pi\mu G(L_{\mathrm{h}}^3/3) \tag{2.13}$$

$$J_{\mathrm{eff}} = J_{\mathrm{h}} + J_{\mathrm{VM}} \tag{2.14}$$

where J_h is hair moment of inertia which is determined by its geometry according to eq. 2.15.

$$J_h = \frac{\pi\rho_h D_h^2}{48}\left(4L_h^3 + \frac{3}{4}D_h^2 L_h\right) \tag{2.15}$$

where ρ_h is the density of the hair material, J_{VM} represents the moment of inertia of the added mass of the fluid moving with the hair as given by [Humphrey et al., 1993] as:

$$J_{VM} = \frac{-\pi\mu G L_h^3}{6gf} + \frac{\pi\rho D_h^2 L_h^3}{12} \tag{2.16}$$

where ρ is the density of the fluid (ex. for air ρ_{air} = 1.2 [kg.m^{-3}]at 20 ^{o}C).

Further analysis [Shimozawa et al., 1998 & Humphrey et al., 2008] leads, by solving eq. 2.12 with eq. 2.11, to an expression for the angular displacement of the hair as function of the oscillation frequency (ω) according to eq. 2.17.

$$\alpha_o(\omega) = \frac{T_{do}}{J_{eff}} \frac{1}{\omega_o^2 - \omega^2 + j\omega(R_{eff}/J_{eff})} \tag{2.17}$$

where T_{do} is the amplitude of the drag-torque, ω is frequency of the oscillating flow and ω_o is the resonance frequency of the system. Figure 2.5 shows the frequency response of a hair sensor to oscillating airflows.

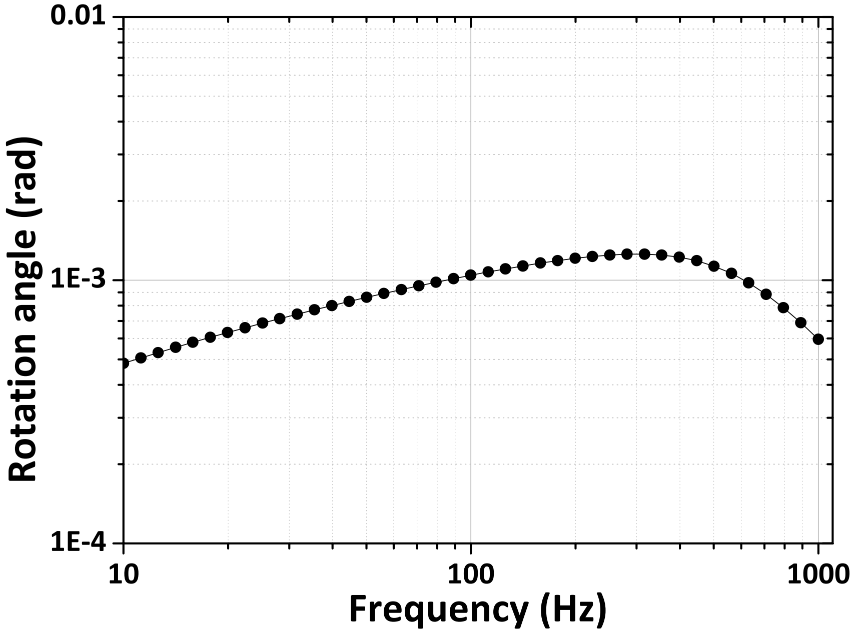

Figure 2.5: Simulated frequency response of a hair sensor. The simulations were performed with 1 mm hair length, $J = 2.7 \times 10^{-16}$ [kg.m^2], $R = 1.7 \times 10^{-13}$ [kg.m^2.s^{-1}] and $S = 3.75 \times 10^{-9}$ [N.m.rad^{-1}].

2.2.2. Mechanical hair design

Design & sensing principle

Figure 2.6 represents the structure of the mechano-receptive sensory-hairs with their source of inspiration. The artificial hair flow-sensor, as inspired by crickets' filiform hairs, is fabricated using MEMS surface micro-machining technology resulting in suspended silicon nitride membranes with about 1 mm long SU-8 hairs on top. The electrodes deposited on top of the membrane form capacitors with a common underlying electrode, namely the silicon substrate. Due to the viscous drag torque acting on the hair, the membrane tilts and, consequently, the capacitors, on both halves of the sensor, change equally but oppositely. These capacitive changes are detected differentially as a measurement representing the airflow surrounding the hair shaft.

Based on the hair sensor geometry and flow dynamics, each design parameter of the hair sensor (S, L_h and D_h) influences its response (e.g. low-frequency sensitivity and sensing bandwidth) accordingly. If either sensitivity or bandwidth is small, the hair sensor performance is strongly limited. For instance, small rotational stiffness enables picking up low amplitude drag torques (i.e. sensitivity is proportional to T_{drag}/S). On the other hand, at a given moment of inertia a smaller stiffness also results in a lower resonance frequency. Additionally, the drag torque depends monotonically on increasing length and diameter of the hair. Accordingly, long and wide hairs are required for high sensitivities. However, this increases the total moment of inertia and lowers the resonance frequency that determines the bandwidth.

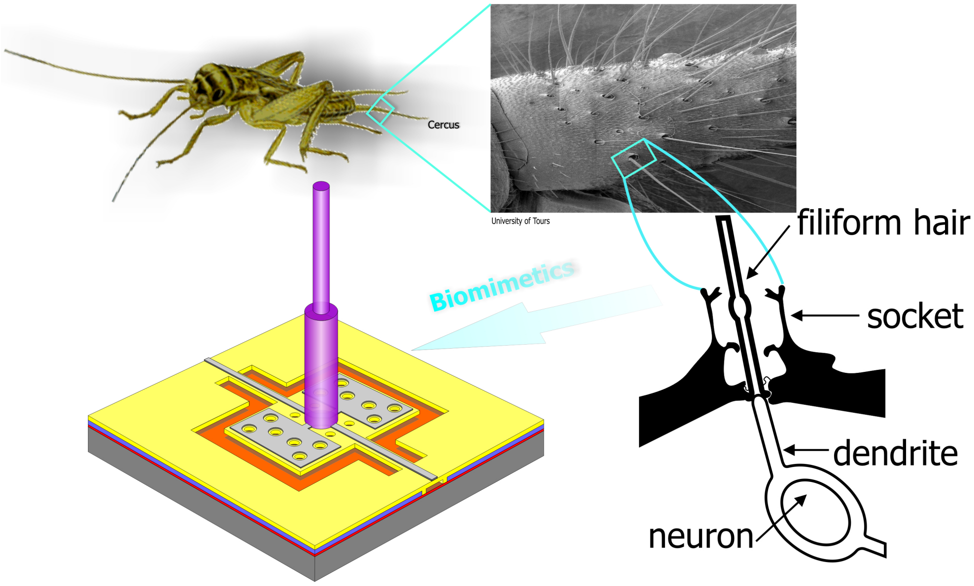

Figure 2.6: Artificial hair sensor geometry and its biological source of inspiration (SEM image courtesy of Jérome Casas, IRBI, Université de Tours).

Optimizing sensor parameters becomes essential to achieve high sensitivity while maintaining a sufficiently wide bandwidth. To address this design-question a Figure of

Merit (FoM) was defined as the product of hair sensitivity and usable bandwidth [Krijnen et al., 2007]:

$$\text{FoM} = \text{Bandwidth} \times \text{Sensitivity}$$

Hence, FoM can be represented in terms of hair mechanical properties as:

$$\text{FoM} = \omega_o \cdot \frac{T_{\text{drag}}}{S} = \sqrt{\frac{S}{J}} \cdot \frac{T_{\text{drag}}}{S} \propto \sqrt{\frac{S}{\rho_h L_h^3 D^2}} \cdot \frac{L_h^2 D_h^{1/3}}{S} \tag{2.18}$$

where the dependence of the drag-torqoue on a hair was derived from parametric studies of the stokes drag-force. The expression can be simplified as:

$$\text{FoM} \propto \sqrt{\frac{L_h}{\rho_h S D_h^{4/3}}} \tag{2.19}$$

The above definition for the FoM provides directions to enhance the performance of the artificial hair flow-sensor. Judging from eq. 2.19 one should make thin hairs, use long hair-shafts, use torsional beams with small torsional stiffness and use low density materials (e.g. SU-8 polymer material). These results are consistent with what is available in natural hairs of crickets. Figure 2.7 shows a frequency response comparison between crickets' hairs (model predictions and measurements) and the model predictions for artificial hair sensors.

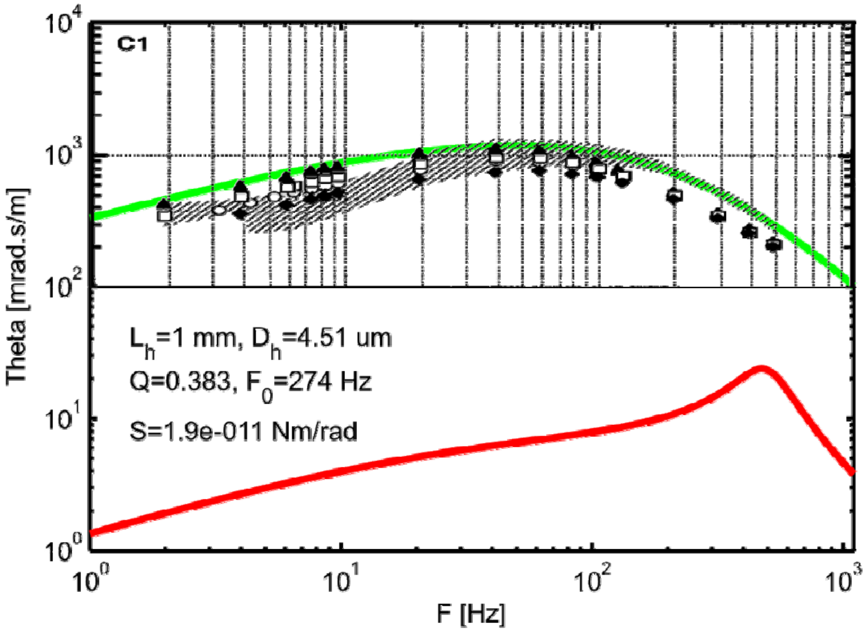

Figure 2.7: Comparison of cricket hair sensor measured response (markers) [Shimozawa et al., 1998] with model predictions (green line) and predicted artificial hair sensor response (red line) [Krijnen et al., 2007].

Incorporating the above design modifications (rules) has resulted in sensitive hair flow-sensors with large bandwidth. However, compared to the artificial hair-sensor, the natural hair-sensors of crickets still show 100 times higher mechanical sensitivity. This is related to the smaller diameter and low torsional stiffness of natural hairs (natural hair with 1 mm length has $S \approx 2 \times 10^{-11}$ N.m/rad, $J = 5 \times 10^{-18}$ kg.m^2 and $R = 5 \times 10^{-14}$ N.m.s/rad [Shimozawa et al., 1998] compared with our hair sensor (artificial hair with 1 mm length has $S \approx 4.5 \times 10^{-9}$ N.m/rad, $J = 2 \times 10^{-16}$ kg.m^2 and $R = 1.6 \times 10^{-12}$ N.m.s/rad)). Table 2.1 shows sensor sensitivity improvement factors due to various modifications of design parameters [Bruinink et al., 2009].

Apart from the hair-mechanics, the dimensions of the capacitor electrodes were analysed: small inter-electrode gaps, rectangular shaped electrodes and long electrodes (rather than wide) are beneficial for good sensitivity [Bruinink et al., 2009]. Further analysis in this part showed the importance of membrane curvature (which degrades hair capacitors' sensitivity by decreasing the relative capacitance changes). This was addressed using low stress material (silicon rich nitride) to fabricate the membrane from and sputtering aluminium (instead of chromium) at room temperature on top.

Table 2.1: Improvements in the sensitivity of artificial hair flow-sensor (Bruinink et al., 2009).

Design parameter	**Improvements factor**
Hair length (450 µm to 900 µm)	4
Hair diameter (50 µm to 25 µm)	0.8
Membrane shape (circular to rectangular)	1.5
Torsion beams : length(75 µm to 100 µm) Width (10 µm to 5 µm)	1.8
Electrodes gap (1 µm to 0.6 µm)	2.7
Membrane curvature (2.5 µm to no bending)	4.3

Fabrication

Figure 2.8 shows a 3D schematic of the artificial hair flow-sensor geometry. The fabrication process starts with the deposition of a 200 nm thin silicon nitride protective layer using Low Pressure Chemical Vapour Deposition (LPCVD) on a highly conductive silicon wafer (Figure 2.8-I). This is followed by LPCVD of a 600 nm poly-silicon sacrificial layer, which determines the capacitors' gap, and patterning by Reactive-Ion Etching (RIE) (Figure 2.8-II). The bottom silicon layer forms the common electrode of the integrated capacitors.

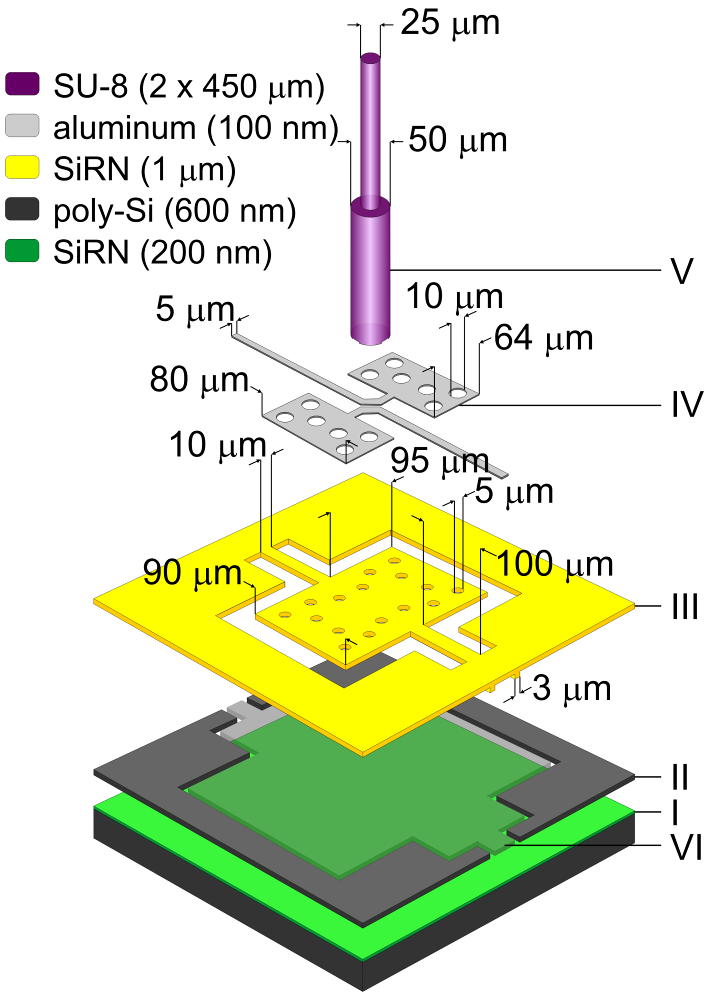

Figure 2.8: A 3D schematic representing structure of the artificial hair flow-sensor fabricated using MEMS technology [Bruinink et al., 2009].

A 1 µm thick silicon rich nitride layer is deposited by LPCVD and afterwards patterned by RIE (Figure 2.8-III) forming the membrane and spring structures. The top capacitor electrodes are formed by sputtering and etching a 100 nm-thick aluminium layer onto the membrane (Figure 2.8-IV). Subsequently, the SU-8 hairs are fabricated with two different diameters (50 µm for the bottom part and 25 µm for the top part) using a two-step photolithography process (Figure 2.8-V). Finally, the hair-sensors are released from the substrate by etching the sacrificial poly-silicon layer (Figure 2.8-VI). In this design, each hair flow-sensor contains a group of 124 hairs with the same orientation, connected in parallel to increase the capacitance changes. The maximum sensitivity axis of each individual hair is aligned with a 45^{o} tilting angle relative to the long axis of the sensor die to achieve high-density hairs array. Figure 2.9 shows an SEM image for part of the hair flow-sensor illustrating grouping of hairs and the 45^{o} tilting angle of the maximum sensitivity axis.

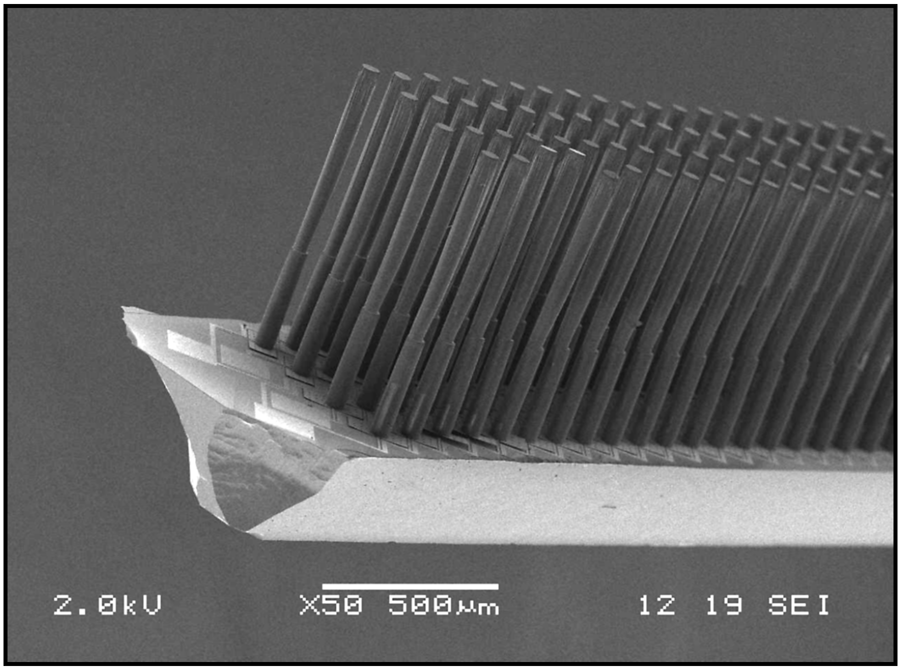

Figure 2.9: An SEM image for the artificial hair flow-sensor showing the grouping principle [Krijnen et al., 2007].

Characterization

The fabricated hair sensors have shown ample sensitivity to airflow. Different measurements such as laser vibrometry [Krijnen et al., 2007], white light interferometry and capacitive measurements [Dijkstra et al., 2005 & Van Baar et al., 2005] have been used to investigate performance and mechanical behaviour.

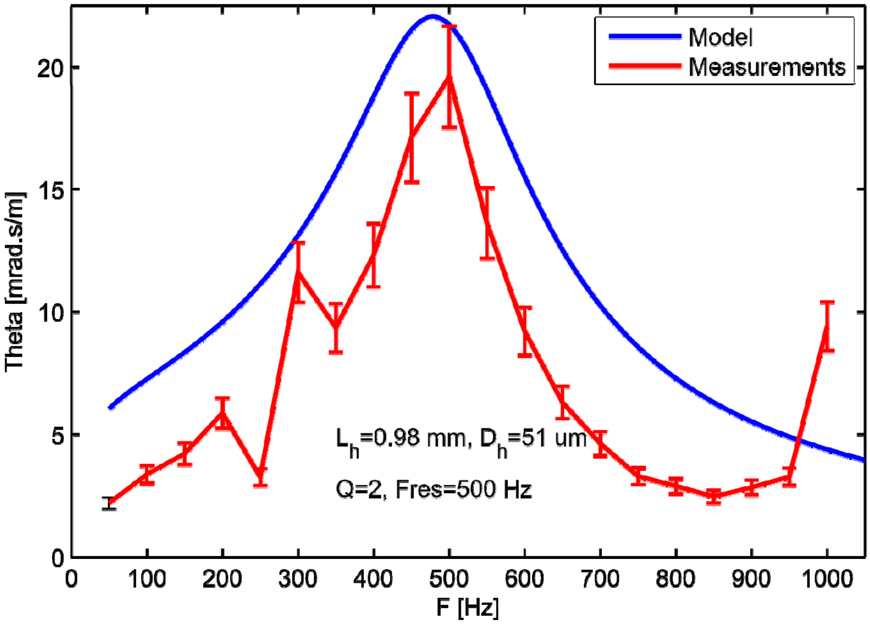

Figure 2.10: Normalized frequency response of the realized artificial hair flow-sensor (measured optically) compared with the theoretical model [Jaganatharaja et al., 2007].

Figure 2.10 shows an optically measured frequency response for a specific hair sensor compared to theoretical model-predictions. The results with respect to the normalized rotation angle show very satisfying similarity (despite the scatter seen in the measurements) considering that the only fitted parameter was the damping. This indicates that the theoretical models [Humphrey et al., 1993 & Shimozawa et al., 1998] are well applicable to our artificial hair sensors.

Using a capacitive measurement set-up, hair sensors have shown a level of preferred directionality similar to a figure of eight. Due to a limited stiffness in the directions perpendicular to the rotational axis the hairs may show small movements in a direction perpendicular to this axis but this results in a common change in capacitance on both sides of the rotation axis which is suppressed by the differential capacitive read-out. Figure 2.11 shows directionality measurements of the hair sensor.

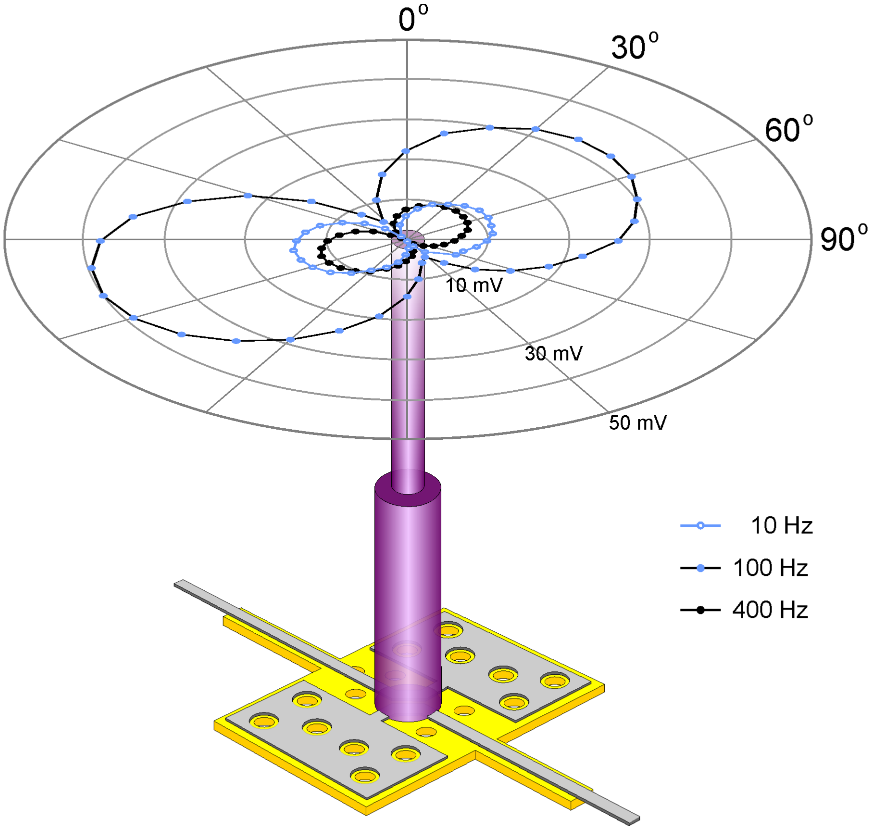

Figure 2.11: Directionality measurements for the hair sensor using a capacitive measurement setup [Bruinink et al., 2009].

The detection limit of the hair sensor was investigated at different conditions. The results show that the hair sensor is sensitive to airflows down to a few mm/s. Figure 2.12 shows the detection limit measurements of the hair sensor at different acquisition conditions [Bruinink et al., 2009].

The possibility to improve the sensitivity of the hair sensor was identified; exploiting electrostatic transduction for sensing also allows for electro-mechancial improvements using electrostatic actuation. This includes using DC-bias voltages to adapt the effective

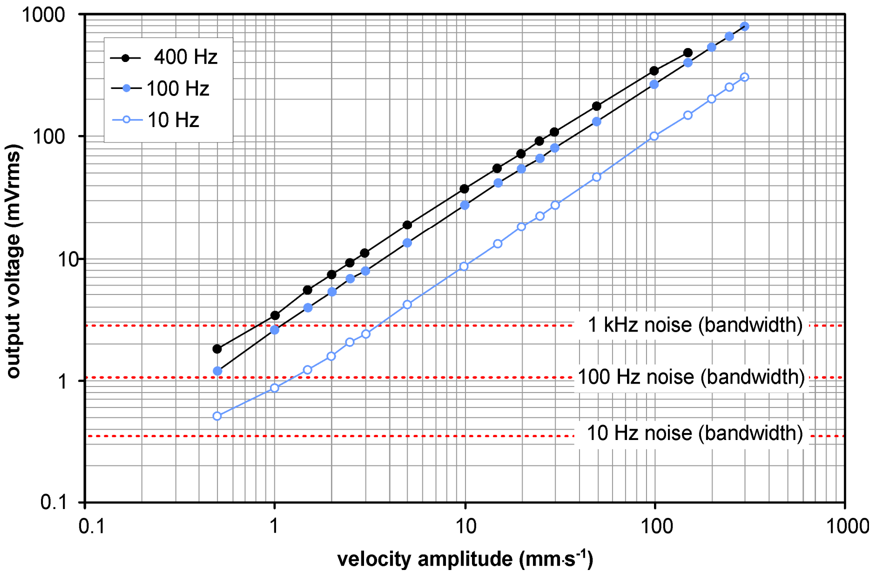

Figure 2.12: Detection limit measurements of the hair sensor using different flow frequencies acquired at different bandwidth [Bruinink et al., 2009].

spring stiffness resulting in higher sensitivity and frequency focusing [Krijnen et al., 2006], but also parametric amplification [Carr et al., 2000, Droogendijk et al., 2010a & Droogendijk et al., 2011] and stochastic resonance [Levin et al., 1996, Droogendijk et al., 2010b].

2.3. Conclusions

Being permanently exposed to fluid motions, many creatures (e.g. spiders, crickets and fish) are equipped with flow sensors helping them to survive. The cercal flow sensor system of crickets is an example sensory system motivating engineers to design hair-like flow sensors and learn from e.g. the cricket-spider escape mechanism. In this chapter we briefly presented the rationale of using hair-like sensors to detect fluid flows. The theoretical basics of the natural flow sensors, and the artificial hair-sensors as well, were described. Targeting flow pattern measurements and driven by the impressive performance of biological filiform hairs, artificial hair flow-sensors have been previously realized and a theoretical model, design basics, a fabrication process and characterization (methods) were presented. The artificial hair-sensors show sensitivity to airflow with detection limit in the range of a few mm/s and have good directionality nicely matching a figure of eight. However, crickets hair-sensors still perform 100 times better than our hair sensors. By adapting the design and improving the electronic interfacing (while at the same time interfacing sensor-arrays), we believe that artificial hair sensory systems nearly matching the ones available in crickets can be achieved. How to increase the flow sensitivity and to interface arrays will be described in the next two chapters.

2.4. References

[Barth et al., 1993] Barth, F.G., Wastl, U., Humphrey, J.A.C. & Devarakonda, R. (1993) “Dynamics of arthropod filiform hairs. II. Mechanical properties of spider trichobothria (Cupiennius salei KEYS)”, Phil. Trans. R. Soc. Lond. B340, pp. 445–461.

[Bathellier et al., 2005] Bathellier, B., Barth, F.G., Albert, J.T. & Humphrey, J.A.C. (2005) “Viscosity-mediated motion coupling between pairs of trichobothria on the leg of the spider Cupiennius salei”, Journal of Comparative Physiology A: Neuroethology, Sensory, Neural, and Behavioral Physiology, 191, pp. 733–746.

[Bruinink et al., 2009] Bruinink, C.M., Jaganatharaja, R.K., de Boer, M.J., Berenschot, E., Kolster, M.L., Lammerink, T.S.J., Wiegerink, R.J. & Krijnen, G.J.M. (2009) “Advancement in technology and design of biomimetic flow-sensor arrays”, In Proceedings of the IEEE MEMS, Italy, pp. 152–155.

[Carr et al., 2000] Carr, D.W., Evoy, S., Sekaric, L., Craighead, H.G., & Parpia J.M. (2000) “Parametric amplification in a torsional microresonator”, Appl. Phys. Lett., 77, pp. 1545–1547.

[Casas et al., 2010] Casas, J., Steinmann, T. & Krijnen, G. (2010) “Why do insects have such a high density of flow-sensing hairs? Insights from the hydromechanics of biomimetic MEMS sensors”, Journal of the Royal Society Interface, 7, pp. 1487–1495.

[Chen et al., 2007] Chen, N., Tucker, C., Engel, J., Yang, Y., Pandya, S., & Liu, C. (2007) “Design and characterization of artificial haircell sensor for flow sensing with ultrahigh velocity and angular sensitivity”, Journal of microelectromechanical systems, 16, pp. 999–1014.

[de Bree 1997] de Bree, H-E. (1997) “The microflown”, Ph.D. thesis, University of Twente, Enschede, The Netherlands.

[Dijkstra et al., 2005] Dijkstra, M., Van Baar, J.J., Wiegerink, R.J., Lammerink, T.S.J., De Boer, J.H., & Krijnen, G.J.M. (2005) “Artificial sensory hairs based on the flow sensitive receptor hairs of crickets”, Journal of Micromechanics and Micro-engineering, 15, pp. S132–S138.

[Droogendijk et al., 2010a] Droogendijk, H. & Krijnen, G.J.M. (2010) "Simulation Studies of Parametric Amplification in Bio-inspired Flow Sensors" In: 21st Micromechanics and Micro systems Europe workshop, Enschede, The Netherlands, pp. 149–152.

[Droogendijk et al., 2010b] Droogendijk, H. & Krijnen, G.J.M. (2010) "Parametric Amplification and Stochastic Resonance in Bio-Inspired Hair Flow Sensors" In: The Sense of Contact 12, Zeist, The Netherlands. FHI Federatie Van Technologie branches.

[Droogendijk et al., 2011] Droogendijk, H., Bruinink, C.M., Sanders, R.G.P., & Krijnen, G.J.M. (2011) “Non-degenerate parametric amplification and filtering in biomimetic hair flow sensors”, In proceeding of Transducers 2011 conference, Beijing, pp. 2038–2041.

[Fan et al., 2002] Fan, Z., Chen, J., Zou, J., Bullen, D., Liu, C. & Delcomyn, F. (2002) “Design and fabrication of artificial lateral line flow sensors”, Journal of Micromechanics and Microengineering, 12, pp. 655–661.

[Humphrey et al. 1993] Humphrey, J.A.C., Devarakonda, R., Iglesias, I. & Barth, F. (1993) "Dynamics of arthropod filiform hairs. I. Mathematical modeling of the hair and air-motions", Phil. Trans.: Bio. Sc., 340, pp. 423–444.

[Humphrey et al., 2003] Humphrey, J.A.C., Barth,F.G., & Voss, K. (2003) "The motion-sensing hairs of arthropods: using physics to understand sensory ecology and adaptive evolution", In Ecology of Sensing (ed. F. G. Barth and A. Schmid), pp.105–115. Berlin, Heidelberg, New York: Springer-Verlag.

[Humphrey et al., 2008] Humphrey, J.A.C. & Barth, F.G. (2008) "Medium flow-sensing hairs: biomechanics and models", In Advances in insect physiology, 34 (eds J. Casas, J. & Simpson, S.J.), pp. 1–80, Amsterdam, The Netherlands, Elsevier.

[Jaganatharaja et al., 2007] Jaganatharaja, R.K., Izadi, N., Floris, J., Lammerink, T.S.J., Wiegerink, R.J., & Krijnen, G.J.M. (2007) "Model-based optimization and adaptivity of cricket-inspired biomimetic artificial hair sensor arrays", In: MicroMechanics Europe Workshop (MME), Guimarães, Portugal, pp. 203–206.

[Kim et al., 2000] Kim, D., Kang, S., Sim, J., & Shin, J. (2000) "Characteristics of piezoresistive mass flow sensors fabricated by porous silicon micromachining", Jpn. J. Appl. Phys., 39, pp. 7134–7137.

[Krijnen et al., 2006] Krijnen, G.J.M., Dijkstra, M.A., van Baar, J.J.J., Shankar, S.S., Kuipers, W., de Boer, J.H., Altpeter, D., Lammerink, T.S.J., & Wiegerink, R.J. (2006) "MEMS based hair flow-sensors as model systems for acoustic perception studies", Nanotechnology, 17, pp. S84–S89.

[Krijnen et al., 2007] Krijnen, G.J.M., Lammerink, T.S.J., Wiegerink, R.J. & Casas, J. (2007) "Cricket inspired flow-sensor arrays", In proceedings of the 6th IEEE Conference on sensors, Atlanta, USA, pp. 539–546.

[Lee et al., 2009] Lee, C.Y., Wen, C.Y., Hou, H.H., Yang, R.J., Tsai, C.H. & Fu, L.M. (2009) "Design and characterization of MEMS-based flow-rate and flow–direction microsensor", Microfluid. Nanofluid., 6, pp. 363–371.

[Levin et al., 1996] Levin, J. & Miller, J. (1996) "Broadband neural encoding in the cricket cercal sensory system enhanced by stochastic resonance", Nature, 380, pp. 165–168.

[Ozaki et al., 2000] Ozaki, Y., Ohyama, T., Yasuda, T. & Shimoyama, I. (2000) "An air flow sensor modeled on wind receptor hairs of insects", In Proceedings of the IEEE Micro Electro Mechanical Systems, pp. 531–536.

[Shimozawa et al., 1984] Shimozawa, T., & Kanou. M. (1984) "The aerodynamics and sensory physiology of range fractionation in the cercal filiform sensilla of the cricket Gryllus bimaculatus", J. Comp Physiol, A 155, pp. 495–505.

[Shimozawa et al., 1998] Shimozawa, T., Kumagai, T., & Baba, Y. (1998) "Structural scaling and functional design of the cercal wind-receptor hairs of cricket", Journal of Comparative Physiology, A183, pp. 171–186.

[Shimozawa et al., 2003] Shimozawa, T., Murakami, J. & Kumagai, T. (2003) "Cricket wind receptors: thermal noise for the highest sensitivity known", In Sensors and sensing in biology and engineering (eds F. G. Barth, J. A. C. Humphrey & T. W. Secomb) pp. 147–157. New York, NY: Springer-Wein.

[Stokes 1851] Stokes, G.G. (1851) “On the effect of the internal friction of fluid on the motion of pendulums”, Trans Cambridge Philos Soc 9: 8ff. (Reprinted in Mathematical and physical papers, vol III, pp 1–141. Cambridge University Press, 1901).

[Su et al., 2002] Su, Y., Evans, A.G.R., Brunnschweiler, A. & Ensell, G. (2002) “Characterization of a highly sensitive ultrathin piezoresistive silicon cantilever probe and its application in gas flow velocity sensing”, Journal Micromech. Microeng., 12, pp. 780–785.

[Van Baar et al., 2005] Van Baar, J.J., Dijkstra, M., Wiegerink, R., Lammerink, T.S.J., De Boer, R. & Krijnen, G.J.M. (2005) “Arrays of cricket-inspired sensory hairs with capacitive motion detection”, In Proceedings of the 18th IEEE international conference on MEMS, Miami, USA, pp. 646–649.

[Wang et al., 2007] Wang, Y.H., Lee, C.Y. & Chiang, C.M. (2007) “A MEMS-based air flow sensor with a free-standing micro-cantilever structure”, Sensors, 7, pp. 2389–2401.

[Xu et al., 2004] Xu, T., Bachman, M., Zeng, F. & Li, G. (2004) “Polymeric microcantilever array for auditory front-end processing”, Sensors and Actuators A: Physical, 114, pp. 176–182.

[Yang et al., 2011] Yang, Y., Klein, A., Bleckmann, H., Liu, C. (2011) "Artificial lateral line canal for hydrodynamic detection", Applied Physics Letters, 99, art. no. 023701.

[Zou et al., 2001] Zou, J., Chen, J. & Liu, C. (2001) “Plastic deformation magnetic assembly (PDMA) of out-of-plane microstructures: technology and application”, Journal Microelectromech. Syst., 10, pp. 302–309.

Chapter

3

ARTIFICIAL HAIR-SENSOR

Biologically inspired sensor-designs are investigated as a possible path to surpass the performance of more traditionally engineered designs. Inspired by crickets, artificial hair sensors have shown the ability to detect minute flow signals. This chapter addresses developments in the fabrication, interfacing and characterization of biomimetic hair flow-sensors towards sensitive high-density arrays. Improvement of the electrode design of the hair sensors has resulted in a reduction of the smallest hair movements that can be measured. In comparison to the previous hair-sensor array design the detection limit was improved arguably at least by twelve-fold, down to 1 mm/s airflow amplitude at 250 Hz and as measured in a bandwidth of 3 kHz. The directivity pattern closely resembles a figure of eight. These sensitive hair-sensors open possibilities for high-resolution spatio-temporal flow pattern observations.

3.1. Introduction

The promise of bio-inspired sensor designs to have better performance, robustness and higher accuracy compared to traditionally engineered designs can only be realized when the sensor interfacing does not hamper to capitalize on these added values. In this chapter, we show the advancements in interfacing and fabrication of our artificial hair sensors. The renewed hair sensor design enables improved sensor directivity and reduced detection limit compared with the previous hair-sensor design.

In literature, various transduction mechanisms have been exploited in micromechanical sensors; mainly piezoresistive, thermal, optical and capacitive read-out techniques. However, some of these mechanisms do not meet our pre-requests in making sensitive hair flow-sensors in high-density arrays using MEMS technology with low power consumption and little complexity. To measure flow, most of the existing resistive flow-sensors exploit either the thermo-resistance or piezo-resistance effect. The main advantage of (piezo)resistive sensors is the simplicity of their read-out circuitry and fabrication process. However, piezoresistive materials have larger temperature sensitivity and smaller overall sensitivity compared with some other transduction principles, e.g. capacitive read-out [Tabib-Azar et al., 1995]. This makes it unpractical to implement in high-density arrays due to the large power dissipation which would cause drift and crosstalk between individual array elements. On the other hand, piezoelectric devices have the advantage in that they generate charge or voltage variations without any significant dissipation which is beneficial when implemented in large arrays. However, the high output impedance, low-frequency response [Ko 1986] and difficulties in integration of piezoelectric materials in (surface) micro-machining [Kuijpers 2004] are drawbacks for this technique.

Due to its simplicity, high accuracy, fast response, long-term stability, low temperature drift and low power consumption compared with other detection mechanisms, capacitive read-out is often the preferred option in micromechanical sensors [Tabib-Azar et al., 1995] e.g. to detect parameters such as acceleration [Bao et al., 2000], pressure [Ko 1986] and displacement [Neubauer et al., 1990]. Additionally, capacitive sensing facilitates integration of a large number of hair-sensors into arrays while maintaining small array dimensions, low power dissipation in combination with surmountable fabrication complexity and a limited number of interconnects. This, in combination with the ability to measure small changes in capacitance enables high-density arrays of sensitive hair-based sensors.

Based on the above comparison, the capacitive and piezoresistive schemes seem to be the most suitable for integration with MEMS technology for applications in flow sensing. Both techniques can be implemented in high-density arrays for flow pattern observations. Capacitive devices have higher sensitivities than piezoresistive devices at similar dimensions [Ko 1986 & Zwijze 2000] which increases as the gap size decreases. While on the other hand, thermal and piezoresistive principles do not suffer from parasitic capacitance as present with capacitive and piezoelectric sensing. The circuit complexity is low for piezo- and thermo-resistive sensors. Furthermore, power dissipation and response time are likely to be higher in resistive devices compared to capacitive devices

[Kuijpers 2004]. An illustrative comparison between different sensing mechanisms, applied for pressure sensors, can be found in literature [Ko 1986, Tabib-Azar et al., 1995 & Kuijpers 2004].
According to our sensor design requirements, high-density sensitive hairs arrays can be realized utilizing capacitance detection. Several capacitive detection methods have been described in literature. Most of these methods are based on capacitive bridges [Peters et al., 1993], relaxation oscillators [Tapson et al., 1994 & Mochizuki et al., 1998] and charge sensitive amplifiers [Wouters et al., 1994]. However, the interfacing circuitry has many challenges in detecting small capacitance changes and in eliminating the adverse influences of parasitic capacitance and electrostatic actuation. In the following sections we will discuss basic design principles for the interfacing of capacitive artificial hair-sensors. This is followed by a description of how the sensor design is adapted targeting improved sensor performance (detection limit, directionality) and aptness for fabrication and interfacing of high-density arrays.

3.2. Artificial hair-sensor

Sensing principle

The basic structure of the hair flow-sensor is shown in Figure 3.1. Two identical capacitors are symmetrically integrated in the sensor to measure the airflow. A variation in the gap between the integrated electrodes results in a capacitance variation.

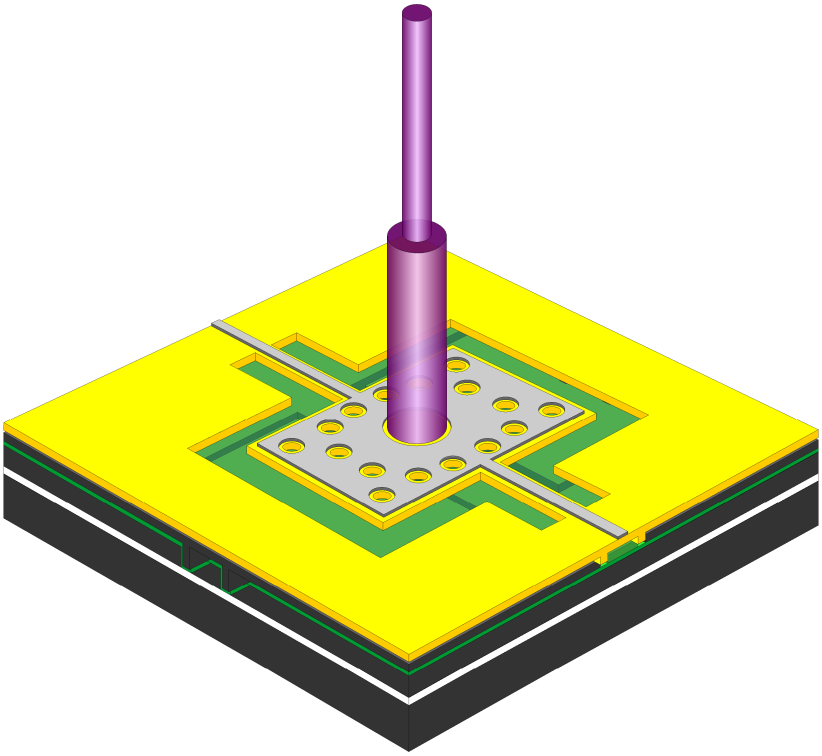

Figure 3.1: A 3D schematic representation of the mechanical design of the artificial hair flow-sensor as it is fabricated using MEMS technology.

Based on the differential capacitive design both sides of the differential capacitors ideally have equal capacitances when the membrane is in its equilibrium position. In our

AC differential read-out scheme, this results in a zero current flow into the common electrode. When the hair is exposed to an external airflow this results in a difference in capacitance. In combination with two mutually out-of-phase AC voltage sources (delivering the carrier signals) the differential changes in capacitance are converted into an amplitude modulated voltage signal (AM signal). A synchronous demodulation technique, which consists of a multiplier followed by a low-pass filter, is used to recover the original airflow signal from the AM signal. Since the capacitive changes are measured differentially, common noise is expected to be reduced significantly as long as the disturbances are equal on both sides of the sensor. The structural design of the sensor is shown in figure 3.1 while the fabrication process of the hair sensor has been described in chapter two.

Figure 3.2 shows a block diagram for the read-out of one artificial hair-sensor. The charge amplifier is used as the interfacing circuit to the hair sensor. A Direct Digital Synthesis (DDS) is used to generate two out-of-phase AC carrier signals for probing the hair sensor. The carrier amplitude is controlled digitally with a resolution of 256 steps. An analog multiplier is the heart of the demodulation stage which is driven by two signals (i.e. a reference signal and the AM signal). This is followed by a low-pass filter and a Sigma-Delta Analog-to-Digital Converter (ADC). All components of each sensor channel are controlled by an external 32-bit microcontroller (LPC2368) with clock-frequency of 72 MHz and various input/output peripherals such as USB, CAN and I^2C, etc. More information about the hair sensor electronics and controllers can be found in [Lammerink 2009].

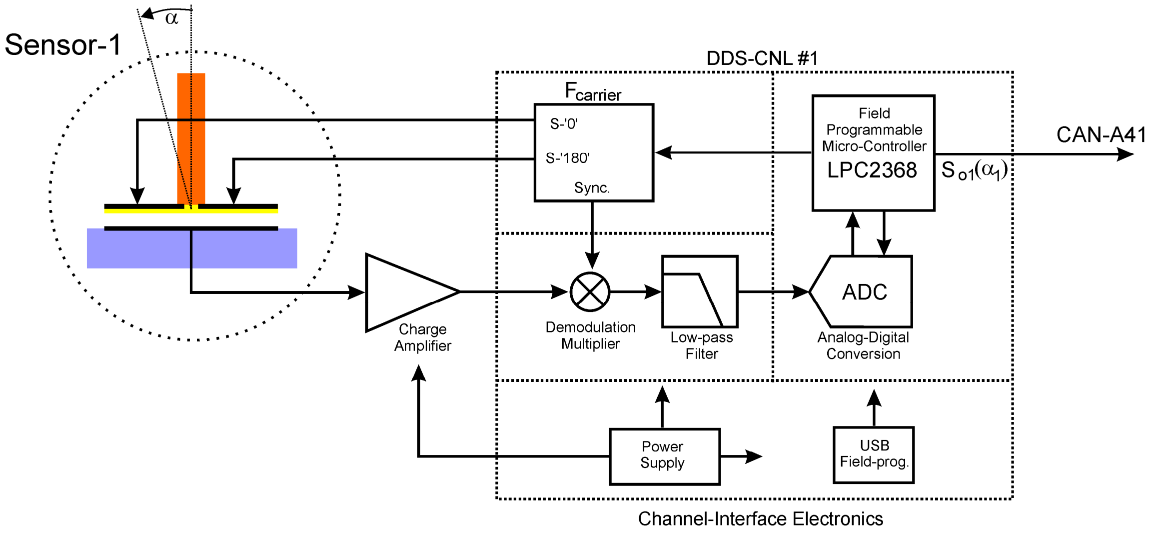

Figure 3.2: A block diagram representing the read-out electronics of one artificial hair-sensor channel [Lammerink 2009].

Figure 3.3 shows images for the realized (a) Printed Circuit Board (PCB) of the charge amplifier circuitry used to interface the hair sensor and (b) the PCB which includes the carrier signal generator (i.e. DDS) for probing the integrated hair capacitors, the synchronous demodulator and the low-pass filter for recovering the actual airflow signal.

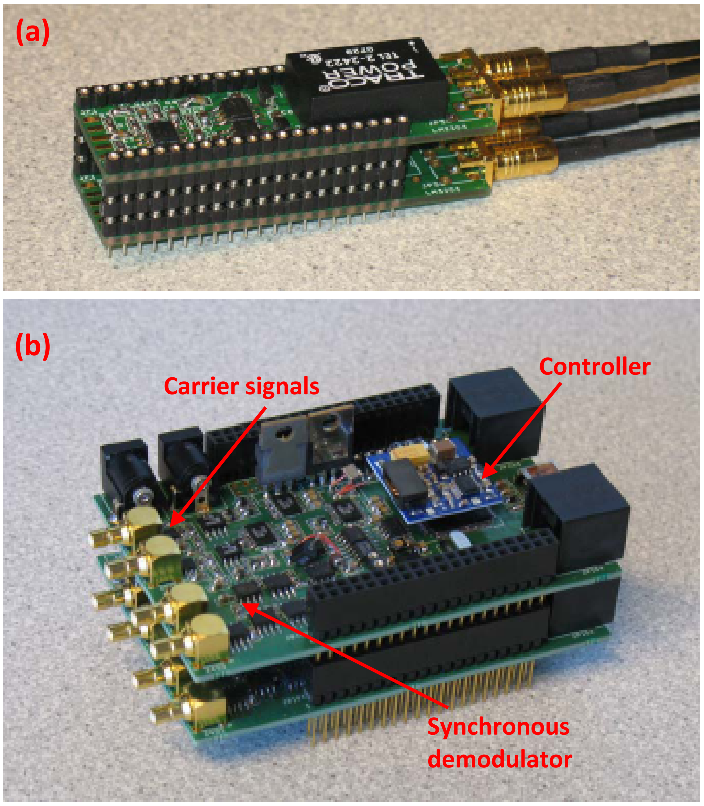

Figure 3.3: Photographs of the PCB's of (a) the charge amplifier and (b) the DDS system with synchronous demodulator. Note the stackability of the latter.

Potentially, digital demodulation can also be performed by digitizing the AM signal and transferring it to a computer (PC) for further digital signal processing. High speed ADC with sampling frequency of 65 MHz is used to transfer the AM signal to PC for demodulation. The demodulation stage consists of a digital band-pass filter (in our case the filter passes the carrier frequency i.e. 1 MHz with at least 1 kHz bandwidth), envelope detector followed by a low-pass filter to recover the original airflow signal. Figure 3.4 shows a cartoon of the entire acquisition setup of the artificial hair-sensor with airflow measurement conducted by one hair sensor and transferred to PC as an example.

Previously, we have reported the sensitivity of the hair flow-sensors to harmonic airflows using both laser vibrometry (mechanical responsivity) [Krijnen et al., 2007] and capacitive measurements (overall sensitivity) [Dijkstra et al., 2005 & Bruinink et al., 2009]. Several essential designs and fabrication parameters have been considered to improve the sensitivity of these artificial hair flow-sensors i.e. using longer SU-8 hairs, smaller inter-electrode gaps and optimal electrode design [Van Baar et al., 2005 & Izadi et al., 2007]. In the previous design, each hair flow-sensor consisted of a group of 124 hairs with identical orientation and connected in parallel to increase the capacitance changes. Under ideal circumstances, i.e. identical hair flow-sensors, no mutual mechanical (viscous) coupling and independent white noise, compared to a single-hair sensor the resulting electrical signal is expected to be increased by a factor of 124 while the noise amplitudes are increased only by a factor of $(124)^{1/2}$ resulting in a signal-to-noise ratio (SNR) increase of about 11 times. The maximum sensitivity axis of each individual hair is aligned at 45^{o} relative to the long axis of the sensor die (see chapter 2). An SEM image for part of the hair-flow-sensor illustrating grouping of hairs and the orientation angle of the maximum sensitivity axis is shown in Figure 3.5.

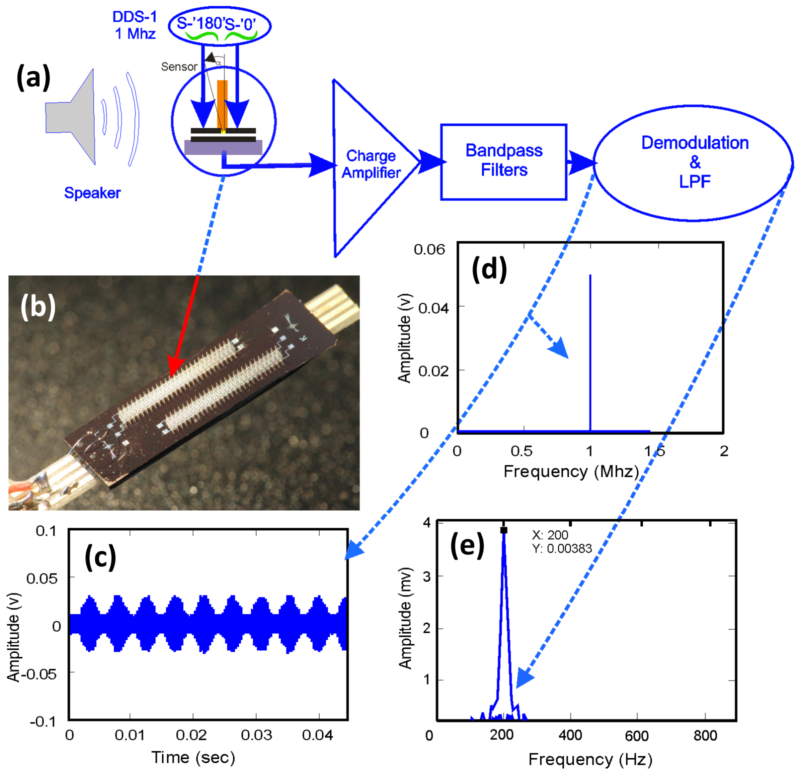

Figure 3.4: (a) Schematic representation of the sensing and demodulation process setup of the artificial hair flow-sensor (b) Image for artificial hair sensor as demonstration of the set-up using a 200 Hz oscillating airflow, where (c) shows the output voltage measured at the charge amplifier (AM signal at 1 MHz), the (d) Fast Fourier Transform (FFT) of the AM signal and (e) the FFT of the demodulated signal.

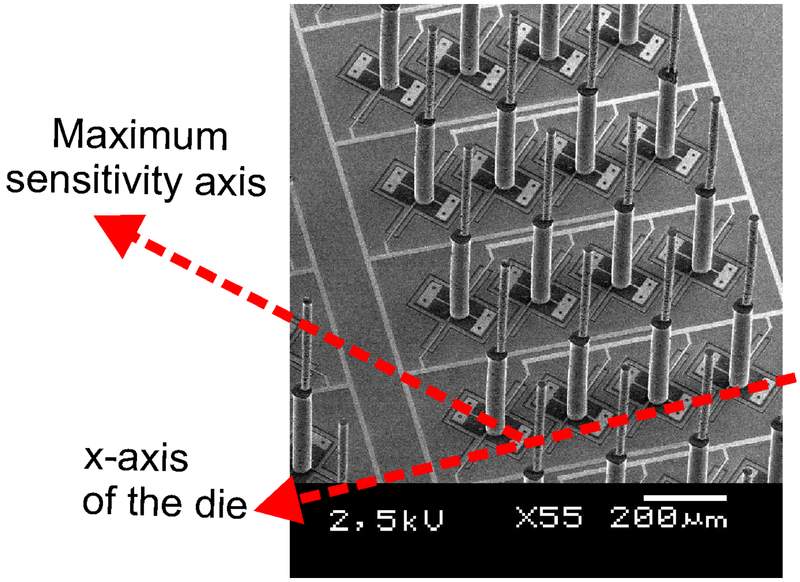

Figure 3.5: An SEM image of an artificial hair flow-sensor of the previous generation.

3.3. Hair sensor interfacing

To avoid clouding the improvements in the detection limit of the hair sensor, achieved by an optimal sensor design, special attention has been paid to the interfacing electronics and hair sensor interconnects. A differential capacitive read-out technique is the starting point for the hair sensor (re-) design. A harmonic AC voltage at a frequency of about one MHz is used as carrier signal. This relative high carrier frequency is advantageous since: 1) it allows for a relative large sensor current $I \propto j\omega C_s$ and hence the SNR is improved, 2) by offsetting the sensor output in the frequency domain the susceptibility to electronic $1/f$ noise is reduced and 3) additionally the meaningful detection of a change in sensor capacitance requires the frequency of the electric field to be substantially higher than the frequencies at which the hair-sensors need to operate (flow-signals up to about 1 kHz). Consequently, the high carrier frequency supports the operational bandwidth of the sensory system.

Figure 3.6 shows a typical interfacing circuit to measure differential capacitance changes. Two high-frequency AC carrier signals with equal amplitude (≈ 1 MHz, ≈ 1V) and in anti-phase (180^{o}) are connected to the hair sensor top electrodes. The carrier signal is produced by the DDS system with digitally controlled amplitude, frequency and phase. The output is an AM modulated signal with amplitudes proportional to the relative capacitance changes and hence, in first order, to the rotation of the hair.

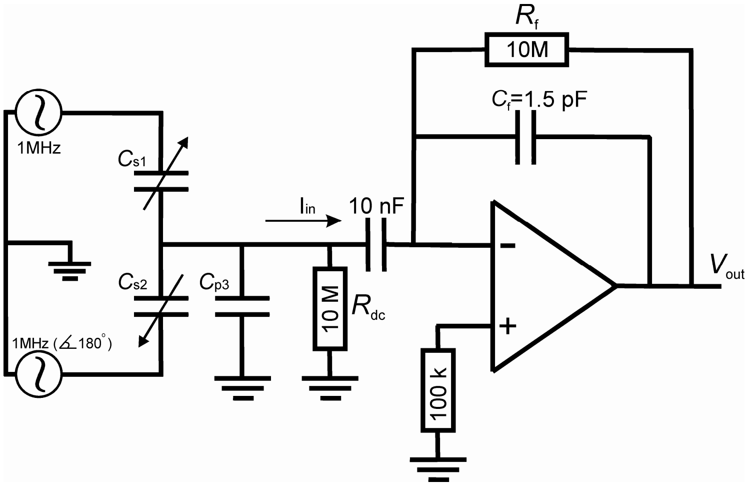

Figure 3.6: Schematic diagram of the interfacing circuit used to detect capacitance changes in the artificial hair flow-sensors.

Based on the design of our hair sensor, the change in the sensing capacitors ΔC results from the change in the capacitors gap between the moving membrane and the common electrode. This change of capacitance represents a measurement of airflow surrounding the hair. The sensor capacitors are modelled up to first order in the rotation angle α by:

$$C_{s1} = \frac{\varepsilon_0 wL}{g_{\mathrm{eff}}}\left(1+\frac{\alpha}{2}\frac{L}{g_{\mathrm{eff}}}\right) \quad , \quad C_{s2} = \frac{\varepsilon_0 wL}{g_{\mathrm{eff}}}\left(1-\frac{\alpha}{2}\frac{L}{g_{\mathrm{eff}}}\right) \qquad (3.1)$$

where C_{s1} and C_{s2} are the integrated capacitors of the hair sensors, ε_0 is the permittivity of vacuum, g_{eff} is the effective gap between the membrane and the common electrode in the equilibrium position including the silicon-nitride membrane (i.e. g+$t_{\mathrm{SiN}}/\varepsilon_{\mathrm{rSiN}}$ where

t_{SiN} is thickness of the silicon nitride layer, $\varepsilon_{\mathrm{rSiN}}$ is its permittivity and g is the air gap), w is the width and L the length of the capacitor electrodes and α is the drag-induced rotation angle. For small rotation angle, which is the case in the normal operational range of the sensors, the voltage output is a linear function of the rotation angle. Figure 3.7 shows the simulated capacitances of the hair sensor as function of rotation angle.

In the circuit design (shown in Figure 3.6), the generated signal at the common electrode is measured by a trans-impedance amplifier, which consists of an operational amplifier (op-amp) with capacitive (C_f) and resistive feedback (R_f).

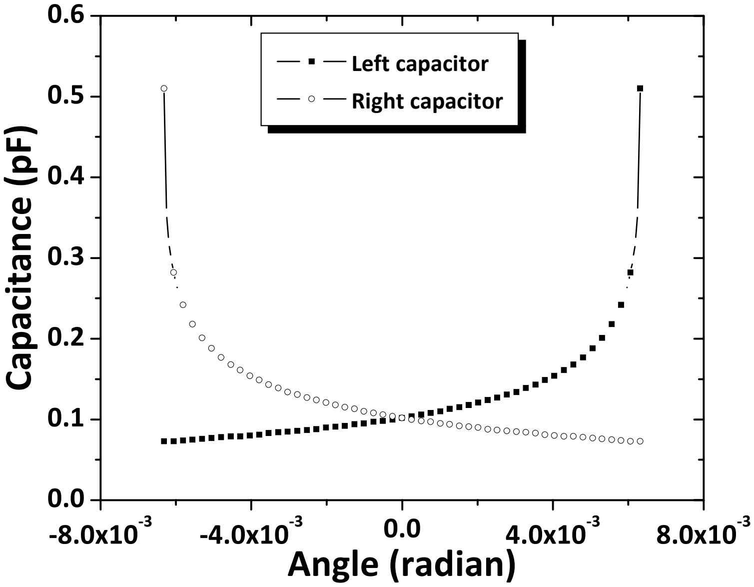

Figure 3.7: Simulated hair sensor capacitances as function of rotation angle. The maximum rotation angle is about 6 mrad for 0.6 mm capacitor gap.

The value of the feedback capacitor is chosen small with little tolerance since it is determining the system gain according to:

$$V_{\mathrm{out}} = V_{\mathrm{i}} \cdot \frac{2\Delta C}{C_{\mathrm{f}}} \approx V_{\mathrm{i}} \cdot \frac{\alpha w L^2}{C_{\mathrm{f}} g_{\mathrm{eff}}^2} \qquad (3.2)$$

where V_{out} is the output of the amplifier which is an amplitude modulated signal and V_{i} is the carrier amplitude.

The following sections show the main points of attention in designing the interfacing of the artificial hair flow-sensors. The effect of parasitic capacitances, inherent to the hair-sensor layout, in combination with the non-ideal characteristics of the interfacing circuitry have been investigated and analyzed.

3.3.1. Parasitic capacitances

Capacitance-based sensors are susceptible to parasitics between sensor elements and other circuit parts, notably cables and ground. A major challenge in fabricating high-sensitivity arrays is reducing these parasitics. In the design of our hair flow-sensors the parasitic capacitances are due to the electrodes connecting the sensors, the capacitances between circuit interconnects and the input capacitance of the interfacing circuit.

These parasitic capacitances increase the input noise gain of the amplifier. This implies a reduction in the SNR by a factor of $(1+(C_{p3}/(C_o+C_f)))$ when associated with the small sensor capacitance changes (see section 3.3.3), where C_{p3} is the total parasitic capacitance at the sensor-electronics interface and C_o is the sensor capacitance without airflow. Additionally, the variations in parasitic capacitances cause a drift in the linear response of the sensor resulting in capacitance changes partially representing non-airflow contributions. Furthermore, parasitics reduce the operational bandwidth of the amplifier, increase the effects of noise and, hence, lead to a reduced SNR.

3.3.2. Non-ideal op-amp

Practical op-amps have a finite open-loop-gain, internal noise sources, offset voltages and nonzero output impedances. Particularly, the open-loop-gain is frequency dependent and decreases at higher frequencies. Additionally, hair sensor geometry and bond pads add parasitic capacitance to the sensory system. For a real op-amp with feedback loop, the close loop gain (A_{cl}) becomes [Graeme et al., 1971 & Graeme 1993]:

$$A_{cl}(j\omega)=\frac{A_{cl\_ideal}(j\omega)}{1+(A_{ol}(j\omega)\beta(j\omega))^{-1}} \tag{3.3}$$

where A_{cl_ideal} is the closed-loop gain with an ideal op-amp, A_{ol} is the open-loop-gain of the real op-amp and $ß$ is a feedback factor. Based on circuit analysis of the interfacing circuitry shown in Figure 3.6, including a non-ideal op-amp in combination and the hair-sensor, and using superposition techniques the ideal closed-loop gain becomes:

$$A_{cl\_ideal}(j\omega)=-\frac{Z_f(j\omega)}{Z_s(j\omega)}=-\frac{j\omega R_f(C_{s1}+C_{s2})}{1+j\omega R_f C_f} \tag{3.4}$$

where Z_s and Z_f are the equivalent impedances of the input circuitry and feedback circuitry, respectively.

Assuming the op-amp has a very high input impedance the overall feedback factor can be expressed by the voltage divider formed by the equivalent input impedance and feedback impedances, with C_{s1} and C_{s2} parallel with C_{p3}, as:

$$\beta(j\omega)=\frac{Z_s}{Z_s+Z_f}=\frac{1+j\omega R_f C_f}{1+j\omega R_f(C_{s1}+C_{s2}+C_f+C_{p3})} \tag{3.5}$$

The mathematical model of the open-loop gain can be described as single-pole transfer function according to:

$$A_{ol}(j\omega)=\frac{A_o}{(1+j\omega/\omega_{cut})} \tag{3.6}$$

where A_o is the DC open-loop gain of the op-amp, ω_{cut} is the -3 dB cut-off angular frequency. With the unity-gain-bandwidth of the op-amp ($\omega_{unity}=A_o\omega_{cut}$), the open-loop gain becomes:

$$A_{ol}(j\omega)=\frac{\omega_{unity}}{(\omega_{cut}+j\omega)} \tag{3.7}$$

with $\omega \gg \omega_{\text{cut}}$

$$A_{\text{ol}}(j\omega) = \omega_{\text{unity}} / j\omega \tag{3.8}$$

Substituting eq. 3.4, 3.5 and 3.8 into 3.3, the closed-loop gain of the amplifier becomes:

$$A_{\text{cl}}(j\omega) = \frac{-j\omega R_{\text{f}}\left(C_{\text{s1}} + C_{\text{s2}}\right)}{1 + j\omega R_{\text{f}} C_{\text{f}} + \dfrac{j\omega}{\omega_{\text{unity}}}\left(1 + j\omega R_{\text{f}}\left(C_{\text{s1}} + C_{\text{s2}} + C_{\text{p3}} + C_{\text{f}}\right)\right)} \tag{3.9}$$

and hence A_{cl} can be simplified to

$$A_{\text{cl}}(j\omega) = \frac{-\left(C_{\text{s1}} + C_{\text{s2}}\right)}{C_{\text{f}}} \frac{j\omega R_{\text{f}} C_{\text{f}}}{\left(1 + (j\omega/\omega_1)\right)\left(1 + (j\omega/\omega_2)\right)} \tag{3.10}$$

and the operation bandwidth of the system can be expressed as (adapted from [Gamio et al., 2001]):

$$\omega_{1,2} = \frac{\left(R_{\text{f}} C_{\text{f}} + \dfrac{1}{\omega_{\text{unity}}}\right) \mp \sqrt{\left(R_{\text{f}} C_{\text{f}} + \dfrac{1}{\omega_{\text{unity}}}\right)^2 - \left(\dfrac{4R_{\text{f}}\left(C_{\text{s1}} + C_{\text{s2}} + C_{\text{f}} + C_{\text{p3}}\right)}{\omega_{\text{unity}}}\right)}}{\left(\dfrac{2R_{\text{f}}\left(C_{\text{s1}} + C_{\text{s2}} + C_{\text{f}} + C_{\text{p3}}\right)}{\omega_{\text{unity}}}\right)} \tag{3.11}$$

where $\omega_{1,2}$ are the angular frequencies representing the operation bandwidth of the system (resulting from the combination of hair sensor and interfacing electronics).

Based on the previous circuit analysis, the interfacing circuit is designed to operate at $\omega_1 \ll \omega \ll \omega_2$. With $\omega_{\text{unity}} \gg 1/(R_{\text{f}} C_{\text{f}})$, $\omega_1 \ll \omega_2$ and $C_{\text{s1}} + C_{\text{s2}} \ll C_{\text{p3}} + C_{\text{f}}$ op-amp imperfections and any variation in the stray capacitances have minor influence on the circuit gain. Thus, the system is robust, stray immune and the operation bandwidth becomes as shown in Figure 3.8 which can be simplified as:

$$\omega_1 = \frac{1}{R_{\text{f}} C_{\text{f}}} \quad , \quad \omega_2 = \frac{\omega_{\text{unity}} C_{\text{f}}}{C_{\text{f}} + C_{\text{p3}}} \tag{3.12}$$

Improvement of the detection limit of the hair sensors is mainly limited by the external electromagnetic interference (*EMI*) and the presence of parasitic capacitances. Using the charge amplifier, virtual grounding is provided and hence the sensed signal is no longer sensitive to the wiring parasitics or amplifier input capacitance (the circuit is stray immune). Additionally, due to the presence of the coupling capacitor (10 nF) at the input of the amplifier, grounding the amplifier inputs through a fixed resistor ($R_{\text{dc}} \gg 1/2\pi f(C_{\text{s1}}+C_{\text{s2}})$) stabilizes the dc potential at the sensor-electronics interface and avoids undefined electrostatic forces due to voltage variation and prevents inputs from floating [Boser 1997].

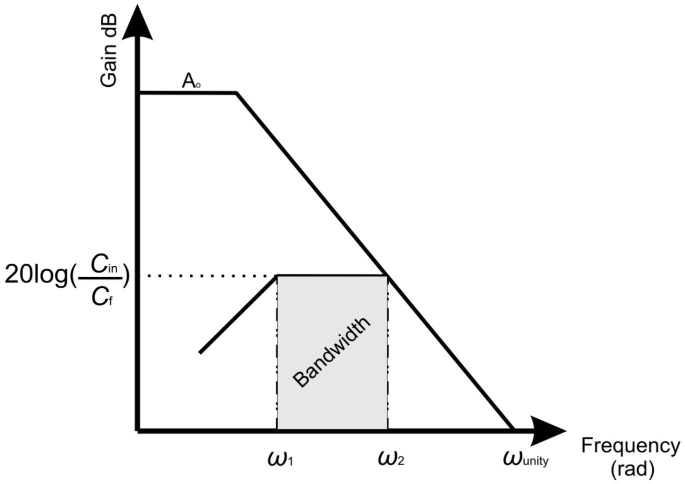

Figure 3.8: Bode plot representation of the charge amplifier interfacing circuit showing the working bandwidth. C_{in} is the total input capacitance at the sensor-electronics interface (see table 3.1).

3.3.3. Electrical noise

The interfacing circuitry utilizes several noise reduction techniques to minimize the effects of the op-amp's internal noise sources. A high open-loop gain, low input capacitance and high gain-bandwidth product in combination with low bias currents, low voltage- and current input noise sources are the main characteristics of the op-amp to be chosen. These design guidelines minimize the effects of op-amp imperfections and the impact of stray capacitors. The synchronous detection mechanism following the charge amplifier circuit further reduces the amount of noise by filtering only the AM signal at the carrier frequency. A wideband, high-speed commercial amplifier (OPA 847) with ultra low-noise power spectral density (0.85 nV/Hz$^{1/2}$) voltage noise and (2.5 pA/Hz$^{1/2}$) current noise at f > 100 kHz [OPA 847 datasheet] is used for the design of the charge amplifier.

The hair sensor has various noise sources associated with it of which electrical noise and thermo-mechanical noise may be the main contributors. In the following section, we will analyse noise sources associated with the current interfacing circuit to determine the dominant electrical noise source.

Based on the interfacing circuitry with noise sources shown in Figure 3.9, the output-referred electrical-noise density includes contributions by the (i) equivalent internal voltage noise source (e_{ni}) of the op-amp (ii) equivalent internal current noise source (I_{ni}) of the op-amp and (iii) the thermal current noise source (I_{nRf}) of the feedback resistor. The total output-referred noise-voltage density (e_{no}) can be expressed as:

$$e_{no} = \sqrt{V_{neo}^{\;2} + V_{nio}^{\;2} + V_{nRfo}^{\;2}} \qquad (3.13)$$

where

$$\begin{aligned} V_{\mathrm{neo}} &= e_{\mathrm{ni}} \cdot \left| H_{\mathrm{s}} \right| \\ V_{\mathrm{nio}} &= I_{\mathrm{ni}} \cdot \left| H_{\mathrm{I}} \right| \\ V_{\mathrm{nRfo}} &= I_{\mathrm{nRf}} \cdot \left| H_{\mathrm{I}} \right| \end{aligned} \tag{3.14}$$

with

$$\begin{aligned} I_{\mathrm{nRf}} &= \sqrt{\frac{4k_{\mathrm{B}}T}{R_{\mathrm{f}}}} \\ \left| H_{\mathrm{s}} \right| &= 1 + \frac{Z_{\mathrm{f}}}{Z_{\mathrm{s}}} \\ \left| H_{\mathrm{I}} \right| &= Z_{\mathrm{f}} \end{aligned} \tag{3.15}$$

where k_B is the Boltzmann constant (k_B=1.38 × 10^{-23} Joul/Kelvin), T is the absolute temperature, H_s and H_I are the transfer functions of the voltage and current noise sources, respectively.

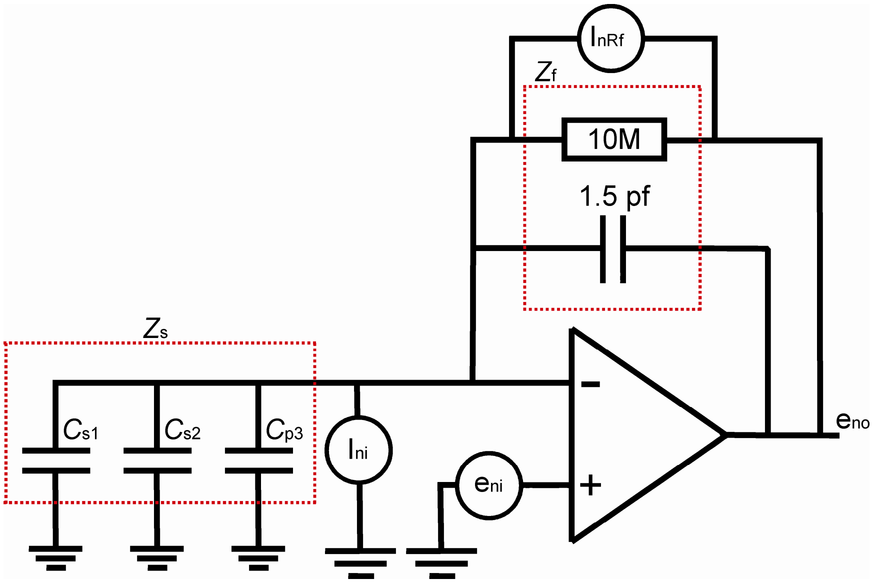

Figure 3.9: Interfacing circuitry for the artificial hair-sensor indicating equivalent noise sources.

The total output-referred noise density and its contributions are shown in Figure 3.10. With the current interfacing design and based on the op-amp noise specifications mentioned above, the dominant electrical noise source (at 1 MHz carrier frequency) is the current equivalent noise source of the op-amp. Figure 3.10 also shows a curve for the output referred thermo-mechanical noise due to the hair-sensor, which is expected to be 1 to 2 orders smaller than the electronics noise. Hence, the absolute detection-limit given by the thermo-mechanical noise of the sensor cannot be attained with the current electronics and transducer properties (see section 3.7).

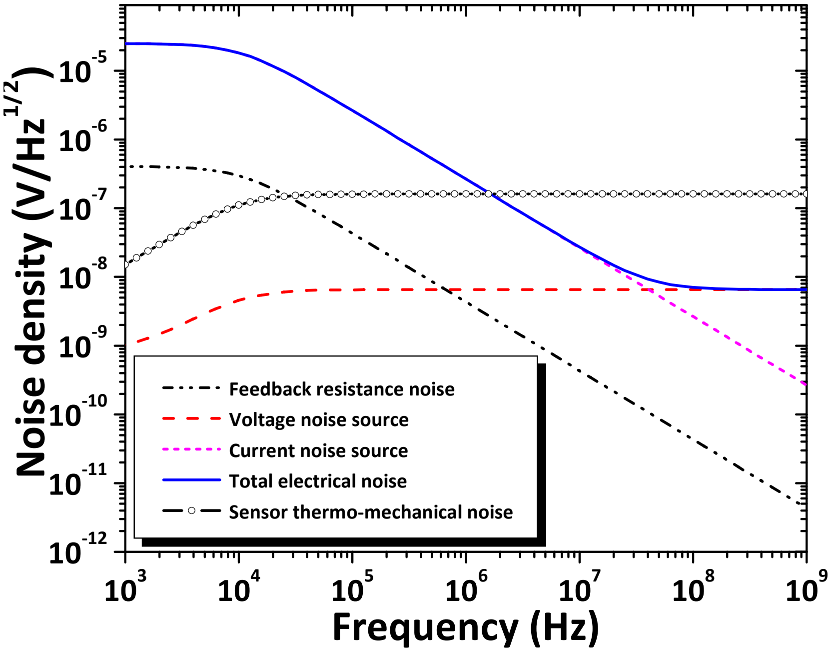

Figure 3.10: Output-referred noise density of the interfacing circuitry generated by different noise sources compared with the estimated thermo-mechanical noise of the hair sensory system.

3.3.4. Non-zero series resistance

At the input side of the hair sensor, the presence of non-zero series resistance interconnections combined with the sensor capacitance enlarges the effect of parasitic capacitance by forming low-pass filters. A high series resistance decreases the cut-off frequency of the generated filter and hence the carrier signal is attenuated. Taking into account the series resistances and stray capacitances, the interfacing circuit becomes as shown in Figure 3.11.

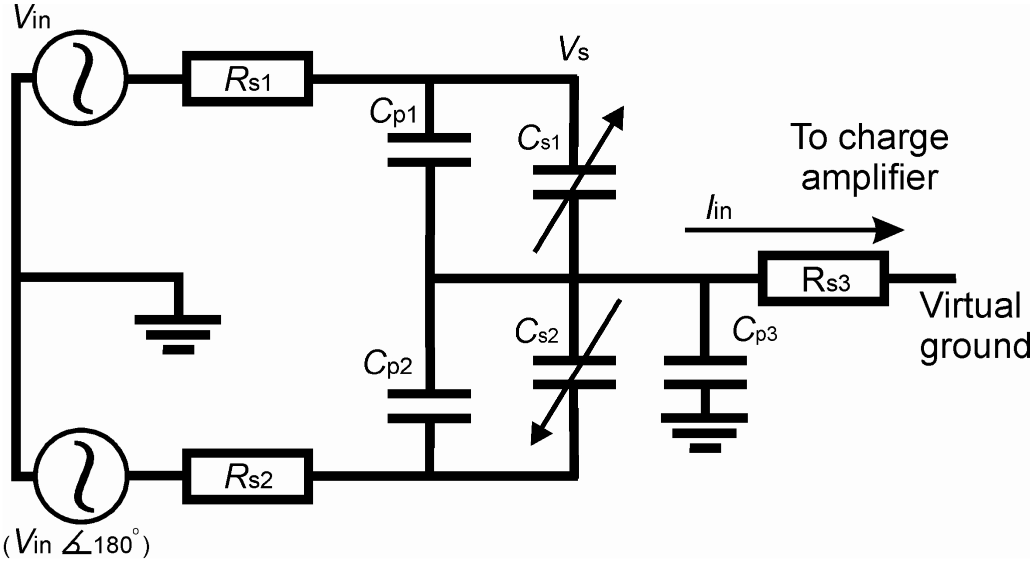

Figure 3.11: Equivalent electrical circuit of the artificial hair interfacing circuit including sensing, parasitic capacitors and series resistors.

Using superposition techniques, the current (I_{in}) flowing via R_{s3} is calculated by determining the equivalent impedance seen by R_{s1} and R_{s2}. With ideal op-amp and since the hair sensing capacitors are $C_{\mathrm{s1}}, C_{\mathrm{s2}} \ll C_{\mathrm{p1}}, C_{\mathrm{p2}}, C_{\mathrm{p3}}$ with carrier frequency of $(\omega \ll 1/(R_{\mathrm{s3}}C_{\mathrm{p3}}))$ the input current to the op-amp is:

$$I_{\mathrm{in}}(j\omega) = V_{\mathrm{in}} \frac{2j\omega\Delta C}{\left(1 + j\omega R_{\mathrm{s1}}C_{\mathrm{p1}}\right)\left(1 + j\omega R_{\mathrm{s3}}C_{\mathrm{p3}}\right)} \tag{3.16}$$

The feedback resistance can be neglected since it only affects the low frequency response. Hence, the output voltage ($V_o(j\omega)=I_{\mathrm{in}}.Z_{\mathrm{f}}$) becomes (adapted from [Gamio et al., 2001]):

$$V_{\mathrm{o}}(j\omega) = I_{\mathrm{in}}Z_{\mathrm{f}} = V_{\mathrm{in}} \frac{2\Delta C}{C_{\mathrm{f}}} \frac{1}{\left(1 + j\omega R_{\mathrm{s1}}C_{\mathrm{p1}}\right)\left(1 + j\omega R_{\mathrm{s3}}C_{\mathrm{p3}}\right)} \tag{3.17}$$

and the cut-off frequencies (according to eq. 3.10) become:

$$\omega_{\mathrm{c1}} = \frac{1}{R_{\mathrm{s1}}\,C_{\mathrm{p1}}}$$

$$\omega_{\mathrm{c2}} = \frac{1}{R_{\mathrm{s3}}\,C_{\mathrm{p3}}} \tag{3.18}$$

where R_{s1}, R_{s2} are the series resistances of the activation electrodes[1], R_{s3} is the series resistance of the sensing (common) electrode[2], $C_{\mathrm{p1,2}}$ are the parasitic capacitances from the activation electrodes to ground, ω_{c1} and ω_{c2} are the cut-off frequencies of the formed low-pass filters seen at the output of the carrier signal source and at the input of the charge amplifier, respectively. To minimize the effects of parasitic capacitances and series resistances, the corner frequencies ω_{c1} and ω_{c2} should be much higher than the carrier frequency ω (see table 3.1).

3.4. Single-hair sensor

In view of the characteristics of the bio-inspired artificial hair flow-sensor, the generated signal is small and prone to various sources of noise. The combined electronics input-referred noise and thermal-mechanical noise sources pose a fundamental limit on the detectable flow. This noise is amplified and imposed on the output signal due to the parasitic capacitance formed between the hair sensor parts and from the sensor parts to ground. In this chapter, the term “current hair-sensor” represents the new hair flow-sensor design fabricated using SOI technology while “previous hair-sensor” represents the hair sensor fabricated using the old technology shown in section 3.2.

---

[1] Activation electrodes are the electrodes that provide the input carrier signals to the sensor (input). Due to the design symmetry, R_{s1}, can be replaced with R_{s2} in the above equations.

[2] The sensing electrode is the electrode that provides the amplitude modulated carrier signal (output).

3.4.1. Previous hair-sensor design

Previously, we have shown advancements in the fabrication and design of flow-sensitive hair-sensor by improving their mechanical properties [Krijnen et al., 2006 & Bruinink et al., 2009]. The fabrication process of the hair-sensor is summarized in section (3.2) according to [Bruinink et al., 2009]. However, in that hair sensor design the underlying silicon substrate forms the common electrode of the integrated capacitors. This generates large parasitic capacitance in parallel with the sensing capacitors, as shown in Figure 3.12, which results in amplification of noise sources as explained in section 3.2. Additionally, the extra parasitics added to the sensing capacitors significantly decrease the fractional capacitance change due to the measurand. This makes the detection of small capacitance changes, which mainly determines the sensor sensitivity, a challenge. Therefore, to increase the change in capacitance and hence the SNR, 124 hairs were connected in parallel (i.e. adding the capacitance changes but averaging out noise from similar but independent hairs). Figure 3.12 shows an equivalent circuit of the hair flow-sensor illustrating parasitic capacitors (about 24 pF) as they are in parallel with the 124 hair sensing capacitors (7.9 pF).

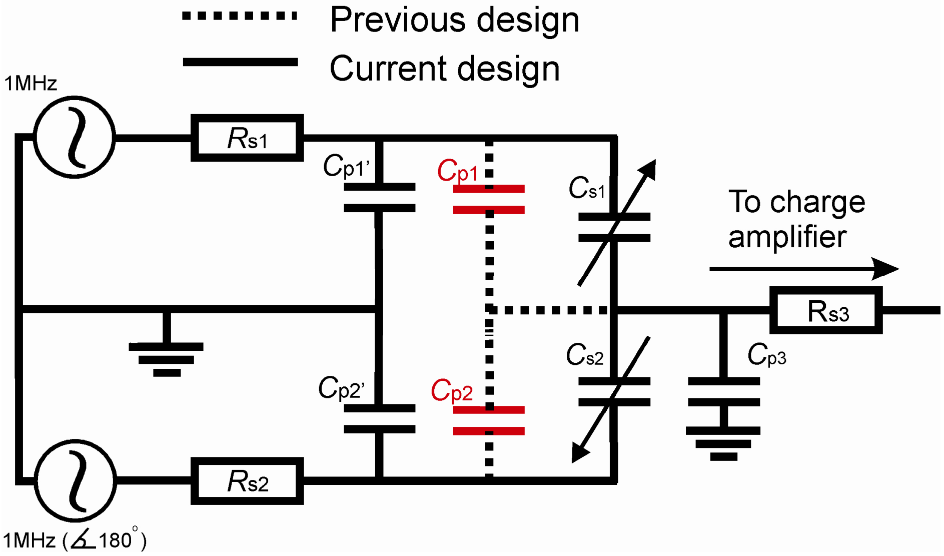

Figure 3.12: A schematic illustrating the equivalent circuit of the previous hair-sensor design (dashed lines and capacitors in red), current hair-sensor design (continuous lines), parasitic capacitors and series resistances as they are connected with the interfacing circuit.

3.4.2. Current hair-sensor design

Since it is expected that the electronics noise is the dominant noise source in our case (see section 3.7.3), any reduction will likely improve the detection limit of the flow-sensor as well. The next stage in enhancing the sensor performance is to reduce the parasitic capacitance inherent to the use of the silicon substrate as common electrode. In the current hair-sensor, all of the interfacing circuit design techniques (section 3.3) have been implemented to reduce the effect of the op-amp imperfections and the role of parasitic capacitances. Here we look at improvement of the detection limit by reducing the parasitic effects. The use of Silicon-on-Insulator (SOI) technology allows us to redesign the electrode system of the hair sensor and to significantly reduce parasitic capacitances, while still having overall compatibility with the previous fabrication process.

In the current hair-sensor design, the electrodes used for the carrier signal are separately defined in the silicon device layer (by deep isolation trenches) while the common electrode for the output signal is implemented by aluminium electrodes on top of the membrane. Consequently, the overlap between hair-sensor electrodes can be minimal assuring reduced parasitic capacitances between the carrier signal and output signal electrodes. To further improve hair-sensor performance, the sensor die is shielded by connecting the inactive areas in the device layer and the carrier wafer to ground. For complete die shielding, the carrier wafer is connected to the common ground of the interfacing circuitry assuring minimal interference. Additionally, maintaining the symmetry in the electrode design allows for maximum benefit of the differential capacitance detection-principle. This cancels out the effect of remaining parasitic capacitors (C_{p1} and C_{p2}) across the sensing capacitors. Taking into account the series resistance in the carrier frequency electrodes, the equivalent circuit becomes as shown in Figure 3.12.

In the previous hair-sensor design, the bottom electrode was formed by the highly conductive silicon substrate while the carrier signal electrodes were made of aluminum on top of the membrane. In the current design, the functions of the top and bottom electrodes were exchanged. Additionally, deposition of an aluminum layer, outside the sensor areas, onto the bottom electrode helps to further decrease the series resistance of the carrier signals (R_{s1} and R_{s2}) without using the highly conductive silicon substrate. This helps to maintain the cut-off frequency of the generated low-pass filter much higher than the carrier frequency (see eq. 3.17). Additionally, the new design clearly shows improvements in widening the operational bandwidth and in increasing the cut-off frequency inherent with the parasitic capacitance and the non-zero series resistance of the connections. Figure 3.13 shows impedance measurements of a previous hair-sensor compared with a current single-hair sensor as function of frequency. Input capacitances (at the hair sensor side) were estimated using these measurements and shown in Table 3.1, which summarizes design improvements in the current hair-sensor design compared with the previous hair-sensor.

Since single-hair sensing concerns very small changes in capacitance, the new electrode design is needed to allow for a reduction in the number of hairs per device to ultimately one, while still sensing minute airflows. The flow signal detected by the single-hair sensor virtually represents a ‘point measurement’ sensor while the previous design of the hair sensor represented an average of the airflows over all individual hairs. Figure 3.14 shows images of the current devices consisting of two single-hair sensors in perpendicular orientation with respect to the rotational axis of the membranes.

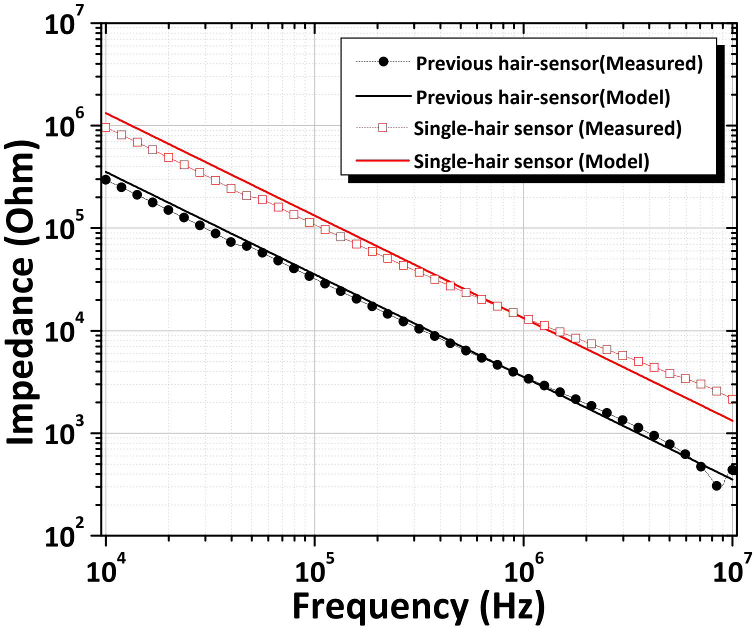

Figure 3.13: Impedance measurements (using a network analyzer) of a previous hair-sensor and a single-hair sensor as function of frequency. Values of the actual C_{in} were estimated from the fitting lines and shown in Table 3.1.

Table 3.1: Comparison between previous hair sensor and current hair-sensor designs considering the effects of the non-ideal op-amp characteristics and non-zero series resistance of the interconnects.

	Previous hair-sensor	Single-hair sensor
f_{c1} (Hz)	9.45 M	15.7 M
f_{c2} (Hz)	245 M	167 M
C_{p1}, C_{p2} (F)	24 p	25 f
C_{s1}, C_{s2} (F)(calculated)	7.5 p	0.06 p
C_{in} (F)(calculated)	40 p	10 p
C_{in} (F)(measured)	45 p	12 p
R_{s1} (Ω)	300	1 k
R_{s2} (Ω)	300	1 k
R_{s3}(Ω)	<100	300
f_1 (Hz)	10.6 k	10.6 k
f_2 (Hz)	354 M	1.3 G

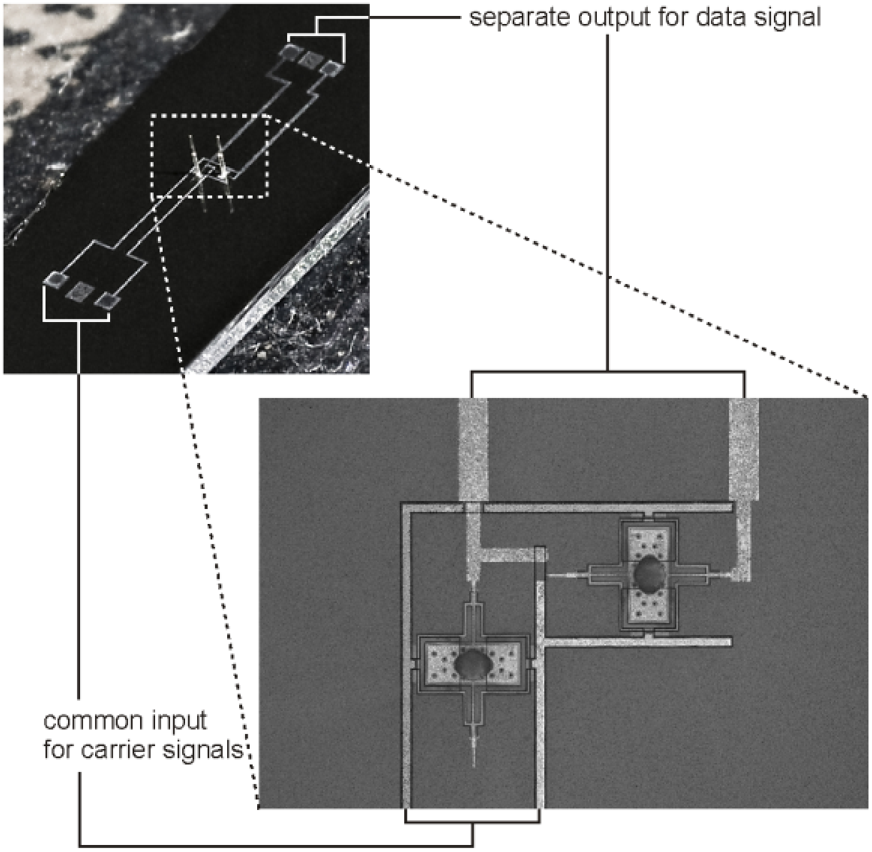

Figure 3.14: Images for the current device. Two single-hair sensors are oriented mutually perpendicular with respect to the rotational axis of the membranes. The activation electrodes are common to both sensors whereas the sensor electrodes are separate.

3.4.3. Fabrication

The adaptation of the fabrication scheme to the new design is enabled by the use of SOI wafers with rather manageable changes relative to the previous process (Figure 3.15). The fabrication of the current hair-sensor design starts by etching deep isolation trenches in the SOI device layer (25 µm, resistivity of 0.01 Ω·cm) down to the isolating SiO_2 layer by directional reactive ion etching (RIE) to form the bottom electrodes (Fig. 3.15-I).Afterwards, a thin nitride (Si_3N_4, 200 nm) layer and a thick poly-Si layer (1400 nm) are deposited by low-pressure chemical vapor deposition (LPCVD, Fig. 3.15-II/III) as etch-stop during later sacrificial layer etching (SLE) and to completely fill the isolation trenches separating the bottom electrodes, respectively. Two wet oxidation runs (1150 ^oC, 120 minutes) are necessary for smoothing the trench fillings and to reduce the poly-silicon layer thickness down to 600 nm, (Fig. 3.15-III). The patterning of the membranes (Fig. 3.15-IV), aluminum electrodes (Fig. 3.15-V) and processing of SU-8 hairs (Fig. 3.15-VI) have not undergone any changes with respect to the fabrication of previous hair-sensors. Finally, the hair structure is released by SLE of the poly-silicon (Fig. 3.15-VII) using XeF_2 gas.

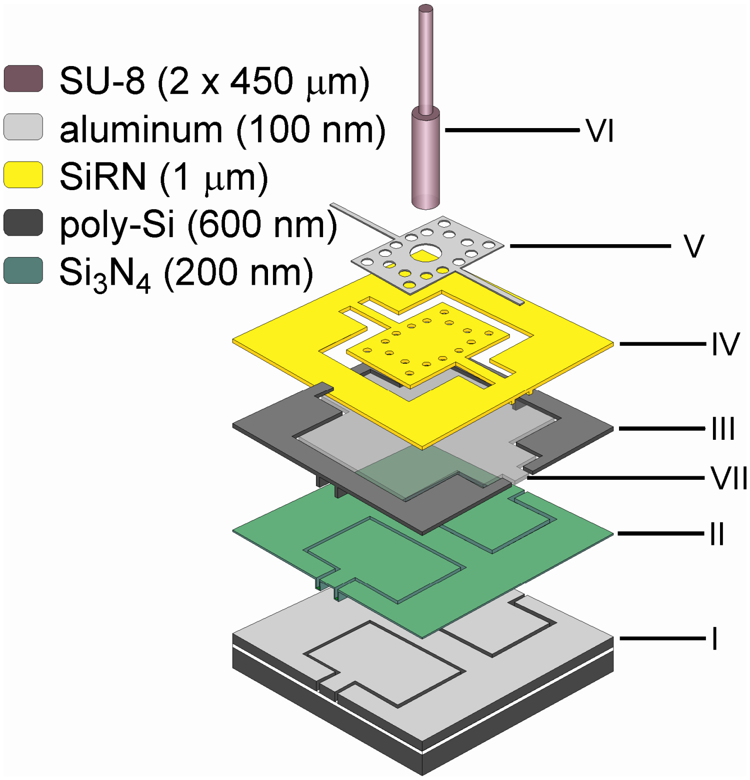

Figure 3.15: Schematic representation of the current hair-sensor fabrication process.

In the current fabrication process, trenches (2 μm wide and 25 μm deep) are used to define the sensor bottom electrodes. However, sharp transition edges can occur across the isolation trench (see Figure 3.16a) and can break the connection of the top electrode at crossing points with these edges. In order to completely fill the 2 μm wide trenches with a smooth transition we deposited (in addition to the 200 nm of Si_3N_4) a 1400 nm poly-silicon. Afterwards, two consecutive wet-oxidation runs are used to obtain a sacrificial poly-silicon layer of 600 nm in thickness. Figure 3.16 illustrates (a) sharp and (b) smooth transitions at the location of the trenches. Figure 3.17 illustrates the common electrode at the crossings with transition edges.

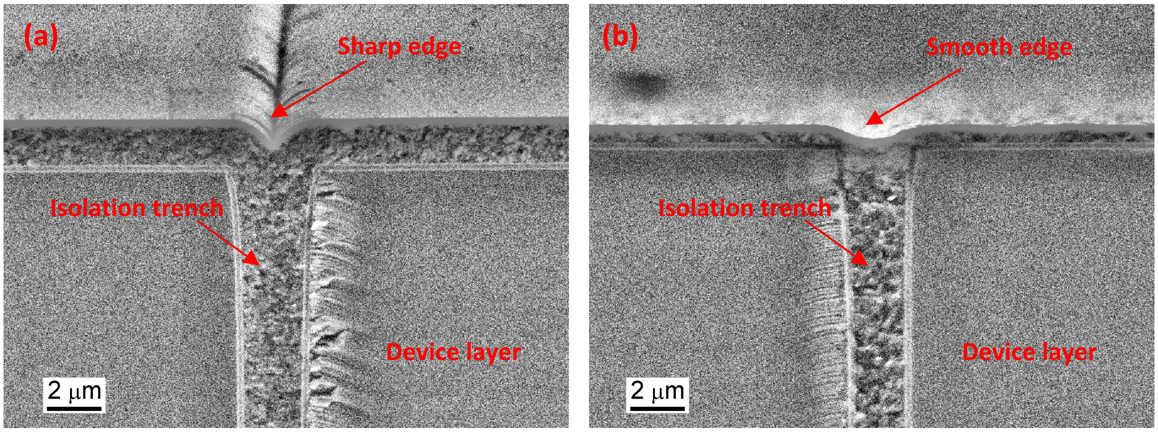

Figure 3.16: SEM images of trench filling: (a) trench after filling with 200 nm Si_3N_4 and 1400 nm poly-silicon; (b) trench after two consecutive stages of wet oxidation and wet-chemical etching in BHF.

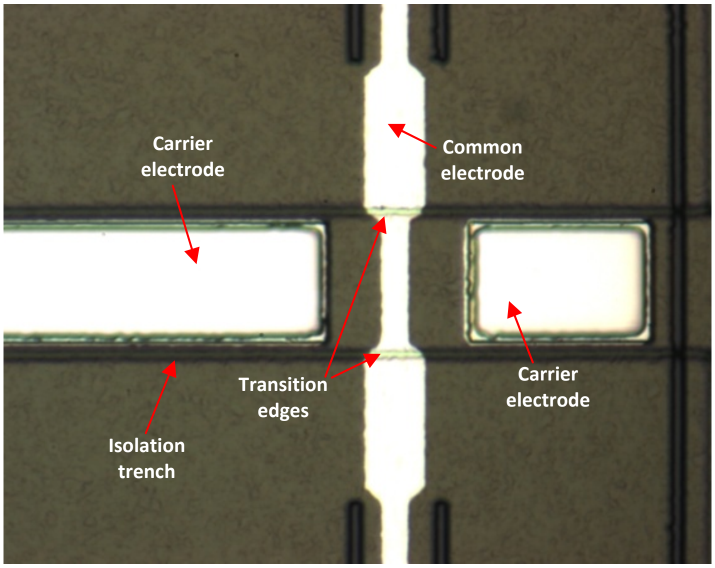

Figure 3.17: Optical microscope image of the device wafer after sputtering and patterning of aluminum.

3.5. Experimental setup

To assess the improvements of the current SOI based technology over the previous sensor implementation the detection limit and directivity of both the single-hair sensor and the previous hair-sensor were measured and compared. A loudspeaker was used to generate sinusoidal airflows. Two 1 MHz electrical signals 180° out of phase were used for the differential capacitive read-out method. The AM signals generated from the sensors were amplified and demodulated using the circuitry described in the previous sections and synchronous detection, respectively. The demodulated signal was filtered using a 3 kHz low-pass filter and recorded using a digital multimeter. The hair sensor was mounted on top of a rotating stage in very near field conditions [de Bree et al., 2004]. Figure 3.18 shows the setup dedicated to both the detection limit and directivity measurements.

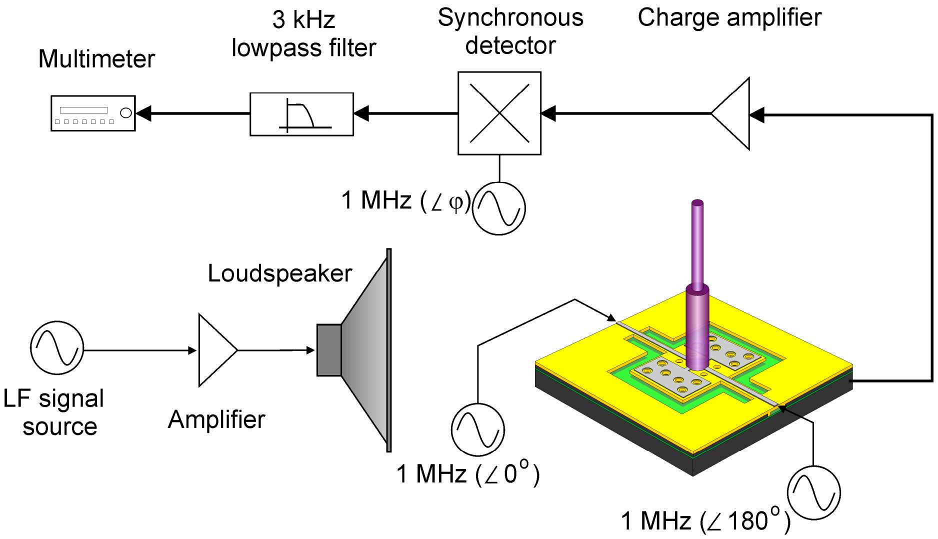

Figure 3.18: A schematic representing the measurement setup used for the detection limit and directivity measurements.

To assess the improvements due to the new design, both hair sensors have identical mechanical design and were measured using the same interfacing electronics. Figure 3.19 shows the frequency response of the previous hair-sensor compared with the current hair-sensor.

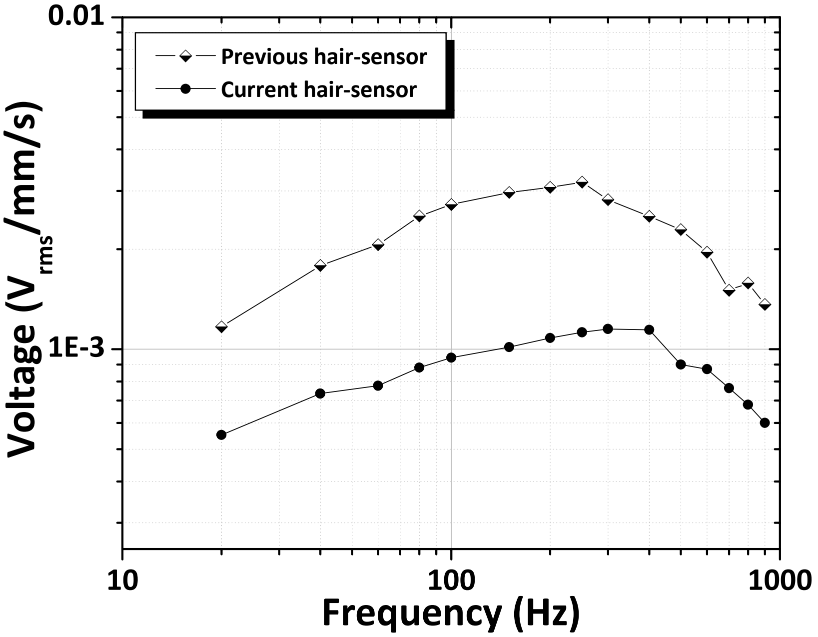

Figure 3.19: Frequency response measurements of the previous hair-sensor compared with the current hair-sensor normalized to airflow of 1 mm/s.

3.6. Results

3.6.1. Threshold flow determination

The detection limit measurements of both hair sensors were performed in the direction perpendicular to their rotational axis using airflow velocity amplitudes in the range of 0.1-50 mm/s oscillating at 100, 250 and 400 Hz. The detection limit is defined as the airflow amplitude at which the sensor response has a SNR equal to one. This is indicated by the intersection of the extrapolated sensor response with the line of constant noise. Figure 3.20 shows the asymptotic lines of the hair-sensor response and noise level as function of airflow velocity amplitude oscillating at 250 Hz for both the previous hair-sensor and the current hair-sensor. Clearly, the noise level of the current hair-sensor is reduced by a factor of 6.5, compared with the previous hair-sensor consisting of 124 hair-sensors in parallel, the single-hair sensor shows a relative improvement of 52 % in the threshold response down to 1.06 mm/s airflow amplitude as measured in a bandwidth of 3 kHz. The same procedure is performed to determine the detection limit at different oscillating frequency and the results are shown in Table 3.2.

3.6.2. Directivity measurements

Figure 3.21 shows the directivity measurements (for sensors rotated over 360^{o} with 10^{o} steps) of both the previous and single-hair sensors compared to an ideal figure of eight shaped directivity. The measurements show that the previous hair-sensor has a maximum sensitivity axis at an angle about 25° rotated relative to the long axis of the sensor die. The single-hair sensor does not show this pronounced deviation, but it does show a difference in sensitivity for perpendicularly oriented hair-sensors. This difference may be due to the differences in flow disturbances associated with the absence of a four-fold or circular symmetry of the die despite the identical sensor-design (see figure 3.14).

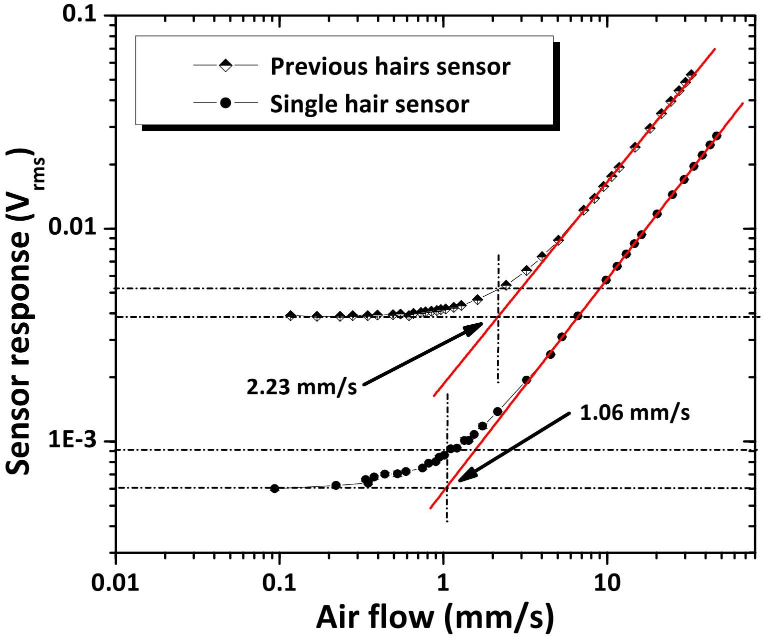

Figure 3.20: Voltage response of both the previous hair-sensor and the single-hair sensor as function of flow velocity amplitude at 250 Hz plotted together with the asymptotic lines (in red) to determine the threshold flow amplitude.

Table 3.2: Detection limit of the single-hair sensor and previous hair-sensor at different oscillating flow frequencies.

	Detection limit (mm/s)	
Frequency (Hz)	Previous hair-sensor*	Single-hair sensor
100	2.58 (14.4)	1.21
250	2.23 (12.4)	1.06
400	2.57 (14.3)	1.15
** Numbers within parentheses are inferred single-hair detection limits from arrays of 124 sensors. See discussion section.*		

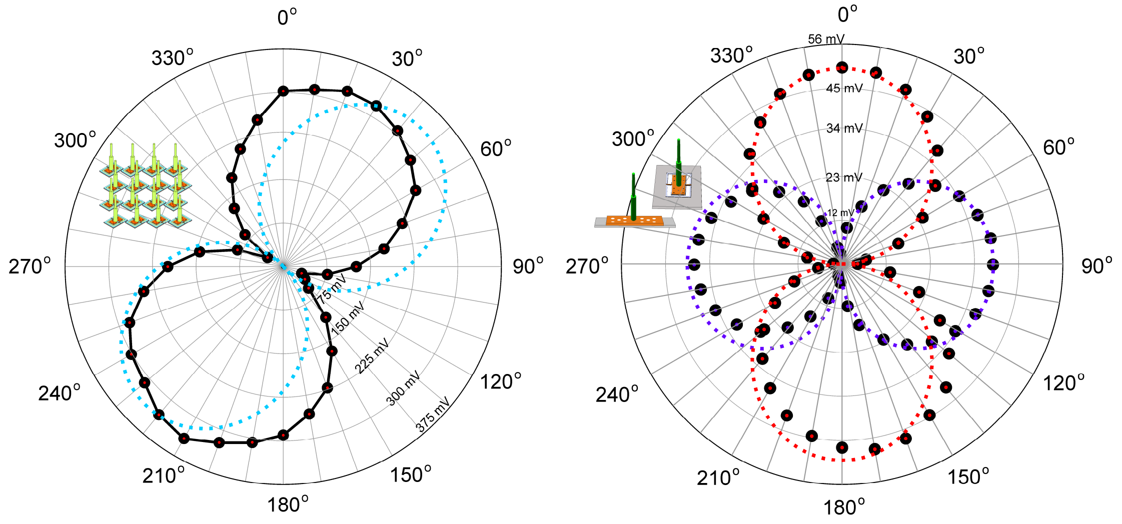

Previous hair-sensor

Current-hair sensor

Figure 3.21: Directivity measurements for the (a) previous hair-sensor and (b) single-hair sensor. The measured directivity shapes (bullets) are compared with perfect figures of eight (dashed lines) oriented in the same direction as the sensor orientation on the die. The maximum sensitivity axis of the previous hair-sensor was tilted 45 degrees relative to the long axis of the sensor die due to the sensor design while the single-hair sensor is mounted with a 0 degree angle.

3.7. Discussion

3.7.1. Directivity

The directivity measurements show a 25^{o} rotation angle of the maximum sensitivity axis of the previous hair-sensor compared with an almost ideal figure of eight for the single-hair sensor. This can be attributed to the:

(i) elimination of viscous coupling effects (i.e. effects of hair presence on a neighbouring hair by virtue of the finite viscosity of air [Bathellier et al., 2005 & Jaganatharaja 2011]) for the single-hair sensor, especially at low airflow frequencies;

(ii) asymmetric flow disturbances caused by array effects in the previous hair-sensor design as a result of grouping many hairs on one die. Consequently, the overall response will be the average response of all the individual hairs. However, connected hairs are not identical and hence hair-sensor signals are not completely correlated.

Thus, reducing the number of hairs to single elements makes it possible to fabricate point sensors sensitive to airflow in one direction while decreasing the size of the sensor die.

Additionally, due to grouping of hair-sensors in the previous design some practical issues appeared. In this design, hairs positioned on the same die are not perfectly identical (i.e. due to misalignment of hairs relative to the membranes) due to which the capacitance of one half of the hair membrane becomes larger. This causes a capacitance misbalance between both halves of the membrane leading to electrostatic forces induced by the carrier signals. Consequently, a net torque is generated even at rest position (i.e. a pre-tilt of the hair sensors, even without being exposed to airflow). This pre-tilt can be compensated for by adjusting the amplitudes of the carrier signals at both sides of the sensor membrane. However, this is a global optimization of the entire array but does not necessarily mean that each individual sensor is optimally interfaced. An indication for this effect may be inferred from the rather large response of the sensors at perpendicular flows (i.e. 'the circles of the figure of eight are not closed').

3.7.2. Detection limit

Improvement in the detection limit can be attributed to the present modifications in the single-hair sensor design, the fabrication technology and interfacing. However, the response of the previous hair-sensor and noise level do not scale with the number of array elements (i.e. the output voltage and noise level are not 124 times and $124^{1/2}$, respectively, as large as compared with a single-hair sensor). In the results obtained while using the same electronics, the single-hair sensor clearly shows a reduction in noise level by a factor of 6.5 compared with the previous hair-sensor (section 3.6).

(i) The dominant noise source (currently) is the electronics noise which is common for both sensors since the same electronics were used to perform the measurements. However, due to the non-identical equivalent sensor circuit at the sensor-electronics interface (see Figure 3.12) the noise gain of the previous hair-sensor is larger (i.e. gain of the output voltage is proportional to C_{in}/C_f, where C_{in} is the total input capacitance at the sensor-electronics interface). The input capacitance includes parasitics and equivalent hair sensor capacitances which are larger for the previous hair-sensor than for the single-hair sensor. Thus the gain factor for the previous hair-sensor is larger (see section 3.3.3);

(ii) The symmetry in the design of the single-hair sensor reduces effects of parasitics by using the differential read-out mechanism which cancels out effects of common parasitics at both halves of the membrane. The symmetry in the previous hair design was less well preserved and hence parasitics were not equally well cancelled by the differential read-out;

(iii) Viscous coupling effects have influence on the flow-induced drag-torque acting on hairs [Jaganatharaja 2011]. This reduces the contribution of each individual hair in the overall die response and hence it scales by a factor less than the number of hairs (especially at low frequency range where viscous coupling is more effective). Thus, due to the elimination of viscous coupling effects in the single-hair sensor, its output will be larger than the average contribution of the single-hair elements in the previous hair-sensor;

(iv) The sensor constitution (124 hairs over an area of 10 x 1 mm^2 connected in parallel) causes some spatial blurring. For example, this can be seen in Figure 3.21 where the response of the previous sensor at perpendicular direction is not nearly zero. Again, this can be due to viscous coupling effects but there is also a geometrically variation of flow impact-direction on the sensors especially in the very near field conditions used in these measurements. Additionally, since hairs are slightly sensitive to pressure variations, and due to the sensor constitution, there may be some position dependent pressure effects. Moreover, in the previous hair-sensor, the hairs are spread in high density over a flat substrate (not a conical shaped substrate as for the cerci of crickets). This causes variation in shapes of the boundary layers around the hairs and in exposure of the hairs to the airflow. Hence, the contribution of each hair is weighted differently in the overall die response (i.e. the hairs at the edge of the die will be stronger represented than the hairs at the centre);

(v) Operating the previous hair-sensor requires adjusting the carrier signals. This causes each individual hair-sensor to operate sub-optimally while for the single-hair sensor the optimal carrier-signal adjustment can easily be obtained;

(vi) The total thermo-mechanical noise in the previous hair-sensor is larger compared with single-hair sensor due to the individual contributions of each hair;

The noise model (see Figure 3.10) predicts a voltage noise density of 0.26 $\mu V_{rms}/Hz^{1/2}$ at the output of the charge amplifier using a 1 MHz carrier frequency. At the output of the demodulator (synchronous demodulation with 420 mV_{rms} and 31 as DC-gain of the low-pass filter) with 600 Hz bandwidth (i.e. double side band of 300 Hz each) the total charge amplifier self-noise level is about 41.5 μV_{rms}. However, noise measurements have shown about 210 μV_{rms} which is 5 times larger than the expected amount of noise. The source of extra noise can be related to the contribution of the DDS system (i.e. carrier signals and the mixer at the demodulator stage).

To exclude contributions of the DDS system to the noise level two external function generators (Agilent 33220A) and a lock-in amplifier (DSP Lock-In Amplifier SR830) were used for sensor probing and synchronous demodulation with a 50 kHz carrier frequency. This frequency was chosen since the maximum operation range of the lock-in amplifier is about 100 kHz (Stanford research systems). The measurements have shown a voltage noise density of 6.5 $\mu V_{rms}/Hz^{1/2}$ at the output of the charge amplifier. The difference from the model predictions can be related to the increase in the gain of the current and voltage noise sources as function of frequency by a factor of 16.67 and 7.5 respectively (i.e. the feedback impedance of the charge amplifier is frequency dependent and, hence, the gain increases as the carrier frequency decrease (eq. 3.15)). The model prediction for the voltage noise density of the charge amplifier at 50 kHz (see Figure 3.10) shows about 5.2 $\mu V_{rms}/Hz^{1/2}$, which is reasonably close to our measurements with lock-in amplifier.

Using the voltage noise density measurements at 50 kHz a 62 μV_{rms} noise level is predicted (using eq. 3.15) at 1 MHz carrier frequency. The difference in the noise measurements (i.e. using the DDS system setup for sensor probing and synchronous demodulation which results in a total noise of about 210 μV_{rms}) can be related to the added noise by the mixer and the low-pass filter, which are not included in the model. To exclude this, the self-noise of the demodulator stage is measured by grounding its inputs. This shows about 80 μV_{rms} noise level at the demodulator output. Therefore, using the measured self-noise of the charge amplifier and demodulator stage at the output of the demodulator the noise due to the carrier signal generated by the DDS system can be extracted which is in the range of 68 μV_{rms}. Additionally, the multiplication property of the mixer makes the noise is not only additive but also multiplicative and, hence, it becomes more complex to be estimated. This suggests that by improving the DDS system the detection limit of the artificial hair flow-sensor can be significantly improved. Table 3.3 summarizes model predictions and measurements of the voltage noise density and noise level at different stages of the hair sensor acquisition channel.

Table 3.3: Model predictions compared with measurements for the noise of the interfacing circuit used in artificial hair flow-sensor.

	Noise density ($\mu V_{rms}/Hz^{1/2}$)	Noise level (μV_{rms})
Charge amplifier (model at 1MHz)	0.26	41.5
Charge amplifier (measured at 50 kHz)	6.5	1036
Charge amplifier (estimated at 1 MHz)[3]	0.39	62
Demodulator (measured at 1 MHz)	-	80
Entire system[4] (prediction at 1 MHz)	0.56	89
Entire system (measured 1 MHz)	1.31	210

It is tempting to compare the single-sensor detection limit of the previous sensor with the current sensor. If we assume that the SNR of a single sensor, integrated in an array of the previous design, is about $(124)^{1/2}$ smaller than for the entire design, then its detection limit would be larger by the same number. It can be argued that viscous coupling may play a role in the previous sensors. However, in the previous design the distance between any two sensors was at least 200 µm, i.e. a normalised inter-hair distance of about 4. From [Jaganatharaja 2011] we know that for this normalized inter-hair distance the viscous coupling coefficient is at most 0.5, i.e. without viscous coupling the hair-sensors would have had at most a twice as large rotation as they had while being in the large array of 124 sensors. Therefore, we argue that in the previous design the detection limit would have been at least $(124)^{1/2}/2 \approx 5.6$ times the array detection limit. These numbers have been put in parenthesis in table 3.2. From these inferred detection limits we conclude that the modifications we have made to the sensors and the careful analysis and optimization we have applied to the interfacing electronics have resulted in at least a twelve-fold improvement (reduction) in detection limit from over 1 cm/s to about 1 mm/s flow amplitude.

When we compare our artificial hair-sensor with crickets' hairs the latter shows over one order of magnitude better performance down to flow amplitudes below 30 µm/s

---

[3] Due to the increase in the voltage and current gain of the amplifier as function of frequency.

[4] Entire system includes the charge amplifier followed by the demodulator stage (i.e. mixer and low-pass filter).

[Shimozawa et al., 2003]. This can be attributed to differences in sensor materials and mechanical properties (see Table 3.4). Moreover, crickets reduce boundary-layer effects by the conical shape of their cercus, which locally increases the circumferential flow and thereby improves sensitivity. This is not easily attained with artificial hairs where a flat substrate is used.

As shown in Figure 3.22, it seems that crickets are smartly controlling damping in the system by making it nearly critically damped. This helps to obtain the maximum energy transfer from the flow by means of 'mechanical impedance matching' [Shimozawa et al., 1998). In artificial hair-sensors, squeeze film damping can be reduced by the design of the etching holes in the membrane and increasing the gap size. However, this deteriorates sensitivity of the system since capacitance changes are inversely proportional to the gap size squared.

Additionally and since the boundary layer is frequency dependent, crickets have different hair lengths, spread along the cercus and covering a large frequency range. This makes crickets professionals in using hair-sensor arrays not only in detecting tiny amplitudes of airflow but also to recognize flow shapes and perceive their meanings. Such a sensory system in combination with a complex neural system helps crickets to distinguish between real and false alarms, by performing multi-hair measurements instead of single-hair measurement. Our efforts in making arrays of artificial hair-sensors and demonstrating the use of these arrays for flow pattern measurements will be presented in chapters 4, 5 and 6.

Table 3.4: Hair sensor parameters of crickets [Shimozawa et al., 2003] compared with our MEMS-based single-hair sensor for 1 mm hair length.

	Cricket hair-sensor	Artificial hair-sensor
Moment of inertia (J) (kg.m^2)	6.5×10^{-18}	2.7×10^{-16}
Spring stiffness (S) (N.m/rad)	2×10^{-11}	4.4×10^{-9}
Torsional resistance (R) (N.m/rad.s^{-1})	2×10^{-14}	1.6×10^{-12}
Quality factor (Q)	0.47	0.59
Threshold velocity (V_{th}) (µm/s)	30	[5]at Q= 0.59➔93 at Q= 1.18➔ 52

---

[5] This threshold is based on the thermo-mechanical noise only and does not include electronic noise contributions. The difference for both Q factors stem from the relation between thermo-mechanical noise and damping. The shift in resonance has been taken into account and the indicated threshold results are at resonance.

3.7.3. Thermo-mechanical noise

In small mechanical structures, the moving parts give rise to thermo-mechanical noise associated with dissipative effects. In crickets, damping is caused by the hair-sockets due to material properties of the socket and viscous damping of the moving hairs (relative velocity between hair and the surrounding airflow). The damping in artificial hair-sensors is caused by both hair-viscous damping and, mostly, squeeze film damping as a consequence of membrane geometry in combination with the small gap of the integrated capacitors.

The fluid-damping elements are associated with noise sources. Here, we investigate the thermal-mechanical noise in our artificial hair-flow sensor caused by damping. The realization of such sensors with high sensitivities requires designs with both low thermo-mechanical noise and high-resolution measurements of angular displacement. The noise equivalent drag torque ($\overline{T}_{\mathrm{n}}$) resulting from the damping (R) in the hair sensory system can be related to the quality factor (Q) by:

$$\overline{T}_{\mathrm{n}} = \sqrt{4 k_{\mathrm{B}} T R} \qquad (3.19)$$

with

$$R = \frac{J(2.\pi f_{\mathrm{res}})}{Q} \qquad (3.20)$$

where f_{res} is the resonance frequency of the mechanical system which defines the system bandwidth.

The average hair angular displacement due to the thermo-mechanical noise integrated over the entire hair sensor bandwidth becomes:

$$\overline{\alpha}_{\mathrm{avg}} = \sqrt{\int_0^{\infty} \left(T_{\mathrm{n}}^{2} . \left| H_{\mathrm{s}}(\omega) \right|^{2} \right) d\omega} \qquad (3.21)$$

where H_{s} is the mechanical transfer function of the hair sensor using the mechanical parameters of the hair sensor. The detection limit can be determined from eq. 3.22.

$$V_{\mathrm{th}} = \frac{\overline{\alpha}_{\mathrm{avg}}}{\left| H_{\mathrm{s}}(\omega) \right|} \qquad (3.22)$$

In our artificial hair-sensor, the threshold flow velocity resulting from the thermo-mechanical noise is in the range of 52 µm/s (see table 3.4). Figure 3.22 shows the detection limit of artificial single-hair sensors with different Q compared with a virtual cricket hair-sensor with parameters obtained by allometric scaling rules of crickets-hairs as derived by T. Shimozawa [Shimozawa et al., 2003].

In contrast, parasitics in MEMS-based hair flow-sensors, inherent with capacitive measurements and self-noise of the interfacing electronics pose limitations to detect flow-signals, even above the limit imposed by thermo-mechanical noise. Unlike crickets' hairs the dominant noise source which (currently) determines the sensor threshold in MEMS-based hairs is the electronics noise. Figure 3.10 shows the calculated voltage noise density, of the artificial hair flow-sensor, at the output of the charge amplifier resulting from the angular rotations of the hair-shaft by thermo-mechanical noise. We estimated that the hair sensor with *Q*=0.59 shows an averaged 0.97 µrad rotation angle due to thermo-mechanical noise. The model predictions show that the thermo-mechanical noise is less than the electronic noise of the interfacing circuit with about a factor of 2 (at 1 MHz carrier frequency even without taking into account the noise added at the demodulator stage). From an electrical design point of view and in case we are able to reduce the electronic noise of the entire system to below the thermo-mechanical-noise level, the detection limit of artificial hair-sensor could improve to about 52 µm/s airflow amplitude, bordering the threshold flow-amplitude of crickets. Figure 3.22 shows the calculated detection limit (airflow amplitude causing a rotational angle equivalent to the expectation value of the noise induced angular rotation) of natural hair flow-sensors of crickets compared with the artificial hair-sensor at two values of the quality factor.

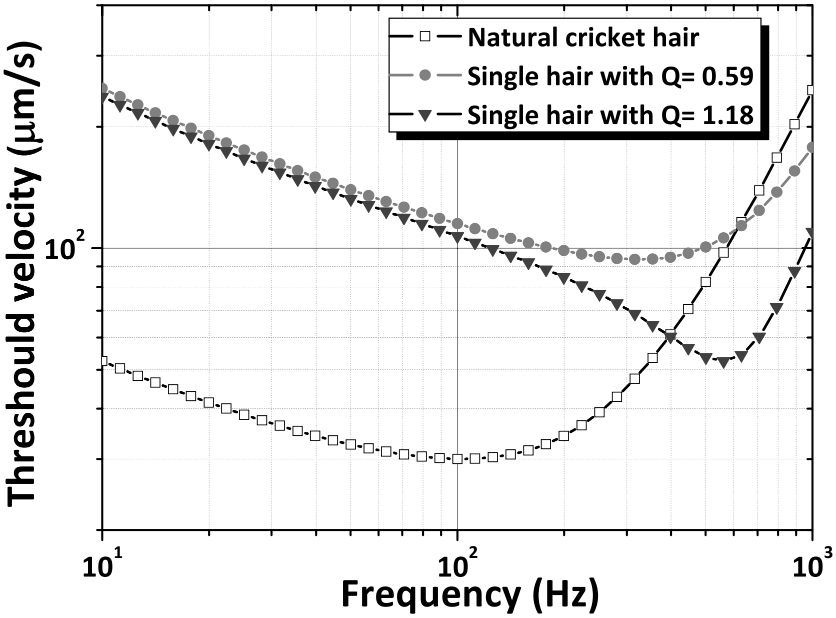

Figure 3.22: Simulated threshold velocity derived from thermal-mechanical noise for cricket hairs and artificial single-hair sensors. The damping in the single-hair sensor is estimated from quality factors of *Q*=0.59 and *Q*=1.18. The other simulation parameters are based on Table 3.4.

3.8. Conclusions

In this chapter, we have analysed effects of interfacing-circuit imperfections on the performance of capacitively interrogated biomimetic hair-sensors. The resulting interfacing design rules were used to improve hair sensor-design and interfacing electronics. The alterations in the fabrication technology, specifically the electrode implementation, has resulted in single-hair sensors that can act close to “point sensors” while simultaneously reducing the threshold flow twelve-fold down to about 1 mm/s at 3 kHz bandwidth. With this design, it is possible to determine flow phenomena at relative small scales, whereby it is unnecessary to integrate (average) over a large number of sensors, i.e. a large area of the die. We believe that further improvements on the interfacing electronics and sensor mechanics will eventually help to match the performance of our biomimetic flow-sensor to the sensory hairs of crickets with threshold flows down to 30 µm/s.

Additionally, taking advantage of deep isolation trenches to define the electrode areas, the SOI technology opens possibilities to fabricate wafer-scale arrays consisting of single-hair sensors as the basic array element. This allows making a broad range of sensory structures, vastly exceeding the possibilities of single-hair sensors. The combination of the ability to detect small capacitance changes as generated from a single-hair sensor and efficient array addressing techniques allows application of sensor arrays (with sensors densities of 50-100 elements per mm^2) for high-resolution spatio-temporal flow pattern observations. For example it will aid in the development of flow-cameras consisting of arrays of artificial hair-sensors, which are expected to be useful e.g. for surveillance and robotic applications.

3.9. References

[Bao et al., 2000] Bao, M., Yang, H., Yin, H. & Shen, S. (2000) "Effects of electrostatic forces generated by the driving signal on capacitive sensing devices", Sensors and Actuators, A: Physical, 84, pp. 213–219.

[Bathellier et al., 2005] Bathellier, B., Barth, F.G., Albert, J.T. & Humphrey, J.A.C. (2005) "Viscosity-mediated motion coupling between pairs of trichobothria on the leg of the spider Cupiennius salei", Journal of Comparative Physiology A: Neuroethology, Sensory, Neural, and Behavioral Physiology, 191, pp. 733–746.

[Boser 1997] Boser, B.E. (1997) “Electronics for micromachnied inertial sensors”, In proceedings of the 9th international conference on solid-state sensors and actuators (Transducers’97), Chicago, USA, pp. 1169–1172.

[Bruinink et al., 2009] Bruinink, C.M., Jaganatharaja, R.K., de Boer, M.J., Berenschot, J.W., Kolster, M.L., Lammerink, T.S.J., Wiegerink, R.J. & Krijnen, G.J.M. (2009) “Advancements in technology and design of biomimetic flow-sensor arrays”, In: 22nd IEEE International Conference on Micro Electro Mechanical Systems, Italy, pp. 152–155.

[de Bree et al., 2004] de Bree, H.E., Svetovoy, V.B., Raangs, R. & Visser, R. (2004) "The very near field - Theory, simulations, and measurements of sound pressure and particle velocity in the very near field", Proceedings of the ICSV11, St. Petersburg, Russia.

[Dijkstra et al., 2005] Dijkstra, M., Van Baar, J.J., Wiegerink, R.J., Lammerink, T.S.J., De Boer, J.H. & Krijnen, G.J.M. (2005) “Artificial sensory hairs based on the flow sensitive receptors hairs of crickets”, Journal of Microelectronics and Microengineering, 15, pp. S132–S138.

[Gamio et al., 2001] Gamio, J.C., Yang, W.Q. & Stott, A.L. (2001) “analysis of non-ideal characteristics of an ac-based capacitance transducer for tomography”, Measurement science and technology, 12, pp. 1076–1082.

[Graeme et al., 1971] Graeme, J.G., Tobey, G. & Huelsman, L.P. (1971) "Operational amplifiers, design and applications", New York: McGraw-Hill.

[Graeme 1993] Graeme, J. (1993) "Op amp performance analysis", Burr-Brown applicationBulletin, 602, AB045 http://www.nalanda.nitc.ac.in/industry/AppNotes/BurrBrown/Index.html.

[Izadi et al., 2007] Izadi, N., Kottumakulal Jaganatharaja, R., Floris, A. & Krijnen, G. (2007) “Optimization of cricket-inspired, biomimetic artificial hair sensors for flow sensing”, In: Proceedings of the 9th International Symposium on Design, Test, integration and packaging of MEMS / MOEMS, Stresa, Italy, pp. 112–115.

[Jaganatharaja 2011] Jaganatharaja, R. K. (2011) “Cricket Inspired Flow-Sensor Arrays”, Ph.D. thesis, University of Twente, Enschede - The Netherlands.

[Ko 1986] Ko, W.H. (1986) “Solid-state capacitive pressure transducers”, Sensors and Actuators, 10, pp. 303–320.

[Krijnen et al., 2006] Krijnen, G.J.M., Dijkstra, M., Van Baar, J.J., Shankar, S.S., Kuipers, W.J., De Boer, R.J.H., Altpeter, D., Lammerink, T.S.J. & Wiegerink, R. (2006) “MEMS based hair flow-sensors as model systems for acoustic perception studies”, Nanotechnology, 17, pp. S84–S89.

[Krijnen et al., 2007] Krijnen, G.J.M., Lammerink, T.S.J., Wiegerink, R.J. & Casas, J. (2007) “Cricket inspired flow-sensor arrays”, In proceedings of the 6th IEEE Conference on sensors, Atlanta, USA, pp. 539–546.

[Kuijpers 2004] Kuijpers, T. (2004) “Micromachined capacitive long-range displacement sensor for nano-positioning of microactuator systems”, Ph.D. thesis, University of Twente, Enschede - The Netherlands.

[Lammerink 2009] Lammerink, T.S.J. (2009) “LM2043 Daisy based, modular CILIA-Instrumentation”, User’s manual, V1.2.

[Mochizuki et al., 1998] Mochizuki, K., Watanabe, k., Masuda, T. & Katsura, M. (1998) “A relaxation-oscillator-based interface for high-accuracy ratiometric signal processing of differential-capacitance transducers”, IEEE Transactions on Instrumentation and Measurement, 47, pp. 11–15.

[Neubauer et al., 1990] Neubauer, G., Cohen, S.R., McClelland, G.M., Horne, D. & Mate, C.M. (1990) “Force microscopy with a bidirectional capacitance sensor”, Rev. Sci. Instrum., 61, pp. 2296–2307.

[OPA 847 datasheet] OPA847 datasheet, Texas Instruments, http://focus.ti.com/docs/prod/folders/print/opa847.html

[Peters et al., 1993] Peters, R.D. (1993) “Symmetric differential capacitive pressure sensor”, Rev. Sci. Instrum, 64, pp. 2256–2261.

[Shimozawa et al., 1998] Shimozawa, T., Kumagai, T. & Baba, Y. (1998) “Structural scaling and functional design of the cercal wind-receptor hair of cricket”, J. Comp. Physiology A, 183, pp. 171–186.

[Shimozawa et al., 2003] Shimozawa, T., Murakami, J. & Kumagai, T. (2003) “Cricket and wind receptors: thermal noise for the highest sensitivity known”, Sensors and Sensing in Biology and Engineering ed Barth, Humphry and Secomb (Vienna: Springer), chapter 10.

[Tabib-Azar et al., 1995] Tabib-Azar, M. & Garcia-Valenzuela, A. (1995) ”Sensing means and sensor shells: A new method of comparative study of piezoelectric, piezoresistive, electrostatic, magnetic and optical sensors”, Sensors and Actuator A: physical, 48, pp.87–100.

[Tapson et al., 1994] Tapson, J. & Greene, J.R. (1994) “Improved capacitance measurement by means of resonance locking”, Meas. Sci. Technol., 5, pp. 20–26.

[Van Baar et al., 2005] Van Baar, J.J., Dijkstra, M., Wiegerink, R.J., Lammerink, T.S.J., De Boer, R. & Krijnen, G.J.M. (2005) “Arrays of cricket-inspired sensory hairs with capacitive motion detection”, In Proceedings of the 18th IEEE international conference on MEMS, Miami, USA, pp. 646–649.

[Wouters et al., 1994] Wouters, P., de Cooman, M. & Puers, R. (1994) “A multi-purpose CMOS sensor interface for low-power applications”, IEEE J. Solid-State Circuits, 29, pp. 952–956.

[Zwijze 2000] Zwijze, A.F. (2000) “Micro-machined high capacity silicon load cells”, Ph.D. thesis, University of Twente, Enschede - The Netherlands.

Chapter

4

HAIR SENSOR ARRAYS

Flow sensor arrays uncover the potential to measure spatio-temporal flow patterns rather than flow measurements at just a single point. We present in this chapter the developments in design, fabrication and interfacing of biomimetic flow-sensor arrays, inspired by flow-sensitive organs (cerci) of crickets. For the purpose of high-resolution flow field visualization by our artificial hair flow-sensor arrays, various array-interfacing schemes are discussed and compared. Frequency Division Multiplexing (FDM) is shown to be an attractive method for efficient interrogation of capacitive array sensors. Using silicon-on-insulator (SOI) technology with deep trench isolation structures, hair-based flow sensors with differential capacitive read-out, arranged in single-chip arrays, have been successfully fabricated. FDM is implemented and used to interrogate individual hair sensors providing simultaneous real-time flow measurements from multiple hairs. This powerful approach is demonstrated by reconstruction of the field of a harmonic dipole field at the position of the hairs and by localizing this dipole source relative to the array elements.

4.1. Potential of sensor arrays

In the past decades and in various disciplines, sensor arrays have become important research topics for researchers developing smart systems. Sensor arrays contain a plurality of discrete sensor elements each of which provides information about single- or multi-modal stimuli. The array composition and structure can be extensive in quantity and dimension. By fusing the data from all sensors, the array-information can transcend to be more than just a set of measurements, revealing source-information by spatio-temporal flow variations. Likewise, inter- and extra-polation of data from various sensors allows for estimates of stimuli at points not coinciding with the discrete sensors.

In literature several examples of sensory array systems, in particular mechano-sensory arrays, have been reported. Applications in which such sensor arrays are used include finger-print sensors [Nigel 1999], image sensors [Aw et al., 1996], memory chips [Simoni et al., 1995], etc. Many of these arrays have been equipped with e.g. capacitive sensors [Nigel 1999] and photo sensors [Bruijn et al., 2004]. The CCD photodiode array system present in video cameras is an example of such an array in which each sensor measures the light at its position and the combination of all measurements reveals the image [Sartori et al., 1995]. In biomedical applications, several medical diagnostic techniques take advantage of sensor arrays. The brain neurons' activities are recorded (ElectroEncephaloGraphy (EEG)) using arrays of electrodes and the number, locations and strengths of the neural sources are estimated [Yaldiz et al., 2007]. Artificial electronic tongues and noses have generally employed arrays of sensors. In such systems, arrays of micro-cantilevers are used to detect the presence of specific substances based on (electro-) chemical reactions which can be used later for automatic classification and recognition [Gardner et al., 1992 & Hauptmann et al., 2000].

Biomimetic arrays

In animals ample examples of arrays of (highly sensitive) sensors can be found for which the fusion of the data retrieved by these sensors defines the function of the organ. Many mammalian senses are found in multisensory arrays; light receptors in the eye, smell and taste receptors in nose and tongue are some examples of such array systems. These sensor arrays are sensitive, versatile and intrinsically redundant. The large amount of data from all array elements is processed and the retrieved information is propagated through the various levels of the nervous system to instigate further action as needed.

Recently, the biomimetics approach in sensor array developments has become interesting for researchers [steinmann et al., 2006 & Casas et al., 2010]. Imitating the principles from eyes to the camera [Ko et al., 2008], whiskers of rodents to sensors for collision avoidance [Kima et al., 2007], sonar system in bats to acoustic detectors [Reijniers et al., 2007] and cricket or fish hairs to artificial hair flow-sensors [Krijnen et al., 2007 & Dagamseh et al., 2010] are examples of biomimetic sensors and sensory systems. The latter example of cricket hairs forms the core of the work presented here.

4.2. Array challenges

Sensor arrays pose considerable technical challenges in the design, interfacing and subsequent signal processing. These challenges, specifically array interfacing, can limit the overall performance of the array system (especially) when the array task is to perform real-time spatio-temporal pattern measurements. Such measurements can only be realized when each array element is interrogated individually and, preferably, continuously.

Generally our capacitive hair flow-sensor arrays are constructed from rows and columns of conductive electrodes separated by dielectrics and arranged in a grid where the capacitances are located at the row-column intersections. The number of sensors depends on the area of interest and the resolution required. To achieve spatio-temporal flow measurements each hair sensor needs to be individually connected to its own acquisition channel. One method to form real-time pictures of airflow (using our hair sensors) is attained by acquiring multiple signals simultaneously by means of physically separated signal-carrying channels for each array element i.e. Space Division Multiplexing (SDM). The advantage of this scheme is that all array elements are interrogated simultaneously and the performance (Signal-to-Noise Ratio (SNR), bandwidth, detection limit) of each interfaced hair sensor in the array show no deterioration compared its single hair-sensor equivalent. However, in large arrays technical challenges arise in making fast, parallel, accurate measurements while still maintaining a manageable number of read-out channels. The associated wiring complexity and required bond-pad real estate pose a large impetus for reduction of the number of connections. In our hair sensor, SDM would require a number of $3 \cdot n \cdot m$ connections, where n and m represent the number of columns and rows in the array respectively, and the factor of 3 stems from the fact that each sensor needs two inputs and one output due to the differential capacitive measurement method. Hence, the main drawback of SDM is the over-all system cost, limitations in available fabrication technology (for on-chip crossing of wires) and system complexity (number of signal-carrying channels which scales proportionally with the number of array elements). This makes it unattractive to use this scheme for large hair-sensor arrays. Thus, sharing transmission channels between multiple sensors is a much-needed approach to reduce the number of interconnects.

As a pre-requirement for addressing large numbers of sensors, the prospective mechanisms should not lead to any deterioration in the performance of the individual hair sensors. The suitability of any addressing scheme is determined by its impact on the acquisition mechanism and trade-offs between sensor sensitivity, crosstalk, SNR, and bandwidth. Additionally, the system cost, complexity of the architecture and the transmission speed of the signals must be considered. Here we will discuss the most promising addressing schemes for our hair flow-sensor arrays.

More specifically the main objectives of our work are:

1. Realize a strong reduction of the number of connections calling for interconnects that are shared between the individual hair flow-sensor;

2. Solutions need to have all interfacing complexity off-chip since our hair sensors have no on-chip electronic functionality;
3. The SNR of the addressed hair sensors in the array should not appreciably differ from that of single hair-sensors;
4. Maintaining minimum crosstalk between addressed sensors;
5. The addressing complexity should be kept to a minimum;
6. The addressing scheme should preserve the sensors bandwidth, which covers roughly DC to 1 kHz.

Bearing in mind our target for achieving live airflow measurements, this study answers several questions relevant to the bio-inspired hair flow-sensor arrays. What are the main interfacing mechanisms that can be implemented and how can they suit our hair sensor and array designs? What are the advantages and drawbacks of the various interfacing schemes? What are the main parameters, which significantly influence the performance of each interfacing scheme?

Additionally, we present, for the first time, single-chip flow-sensor arrays with simultaneous and separate read-out of individual hair-sensors. The combination of these arrays with the proposed array interfacing technique enables high-resolution digital flow-cameras, which form the basis for e.g. flow pattern observation, categorization and recognition. Up to date the research performed on these hair sensors has been confined mostly to the hair mechanical design, fabrication and characterization. In this chapter the key requirements for sensory array interfacing and addressing techniques with external circuits, to be applied on our hair flow-sensor arrays, are discussed and an implementation is demonstrated.

4.3. Array addressing

Event detection by sensing and observation of practical stimuli requires the measurement of multiple data, and sensor arrays are employed to meet these needs in a parallel and distributed fashion. However, performing assays on a large number of spatially distributed elements requires methods for multiplexing while rapid read-out of the sensors' signals is required to retain sufficient temporal information. Usually, interfacing large numbers of sensors is achieved by spatially wiring array elements or using multiplexing schemes, e.g. in the time or frequency domains, in order to reduce the number of connections. Frequency Division Multiplexing (FDM) [Chervenak et al., 1999 & Xu et al., 2006] and, more often, Time Division Multiplexing (TDM) techniques [Nelson et al., 1980 & Wright et al., 1992] are described in literature to extract signals individually from an array of sensors.

TDM is used for example to multiplex an array of intensity-based optical sensors i.e. in an optical time-domain reflectometer (OTDR) [Nelson et al., 1980]. In this system, the sensors are spatially distributed with different distances between the source and detector. A single pulse of appropriate duration at the input to the network produces series of distinct pulses at the output. These pulses represent time samples of the sensor outputs interleaved in a time sequence. The required duration of the input pulse is determined by the effective optical delay of the fiber connecting the sensor elements. Repetitive pulsing of the system allows each sensor to be addressed by simple time-selective gating of the detector. Rogers [Rogers 1980] suggested a method for measuring the spatial distribution of magnetic and electric fields, pressure, temperature and mechanical stress, as an application of arrays exploiting the OTDR concept.

The TDM and FDM schemes have also been used for the acquisition of magnetic resonance images (MRI). TDM is used to acquire multiple images by multiplexing the signals from each coil to a single channel [Wright et al., 1992]. Using FDM, two signals from different RF coils encoded with different frequencies were combined to be transmitted to a high-speed analog-to-digital converter (ADC) [Xu et al., 2006]. SQUID[1] time-division multiplexing is a well-developed method for reading out multiple transition-edge sensors in a single amplifier channel. In this system the number of SQUIDs is equal to the number of detectors but only one SQUID is turned on at a time i.e. TDM [Korte et al., 2003 & Doriese et al., 2007].

The TDM scheme has also been demonstrated for reading capacitive sensor arrays. This system consists of circuits for selecting specific column and row lines to activate a single array element. The selected element is connected to an inverting amplifier while the deselected elements are connected to a reference voltage [Sergio et al., 2002]. Such a method can be applied to any capacitive sensor array such as load cells sensory array systems [Zwijze 2000], capacitive finger-print sensors [Nigel 1999], and image sensors [Sartori et al., 1995, Aw et al., 1996 & Theuwissen 2003]. Figure 4.1 illustrates the basic principle of TDM as applied to a capacitive sensor array.

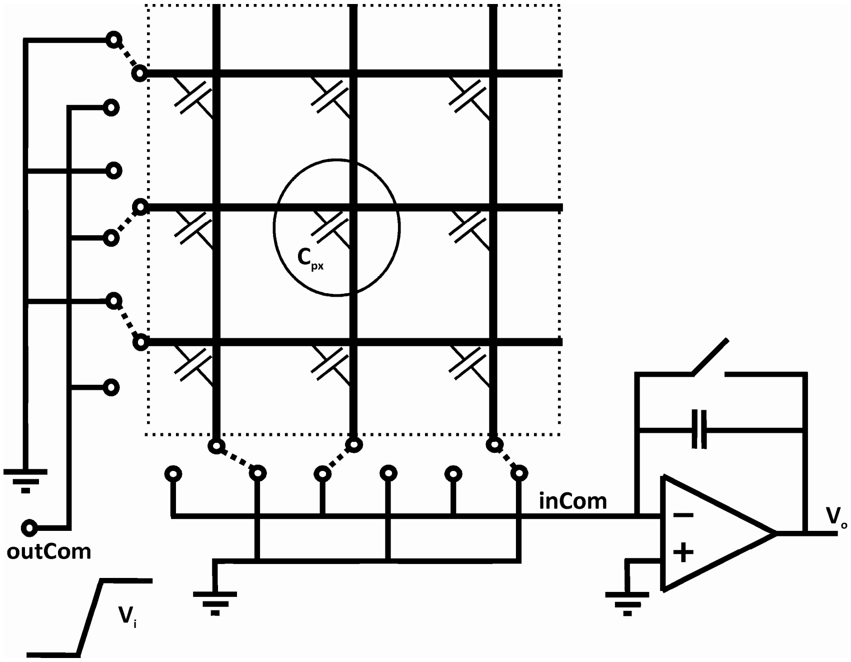

Figure 4.1: Principle of TDM scheme as it is applied to capacitive sensor array (adapted from [Sergio et al., 2002]).

---

[1] SQUID: Superconducting QUantum Interference Device

Image sensors typically contain Charge Coupled Devices (CCD) or Complementary Metal-Oxide-Semiconductor (CMOS) devices in which each pixel element is at the crossing of a specific row and column. In this system, the measurement operation begins by resetting all of the pixels. Next, the absorbed light energy generates charges in each individual pixel within the array, which represents the electrical replica of the optical image. Further, the sequential read-out unloads charges from each pixel element. The read-out circuit, which uses internal decoders and addressing control signals, scans the whole pixel array sequentially. One pixel is read at a time while the other pixels charges are stored in capacitors associated with and parallel to the photodiode of each pixel, waiting for signal acquisition. After completing the read-out cycle the sensor is again reset. Various technological and design techniques have been considered to achieve fast, compact and high charge-transfer efficiency while reducing crosstalk and noise at different levels of chip integration. Figure 4.2 shows a CCD image sensor which contains an array of pixels and control circuits. Various integrating levels for the electronics have been implemented to reduce noise, costs, complexity and scanning time [Sartori et al., 1995 & Theuwissen 2003].

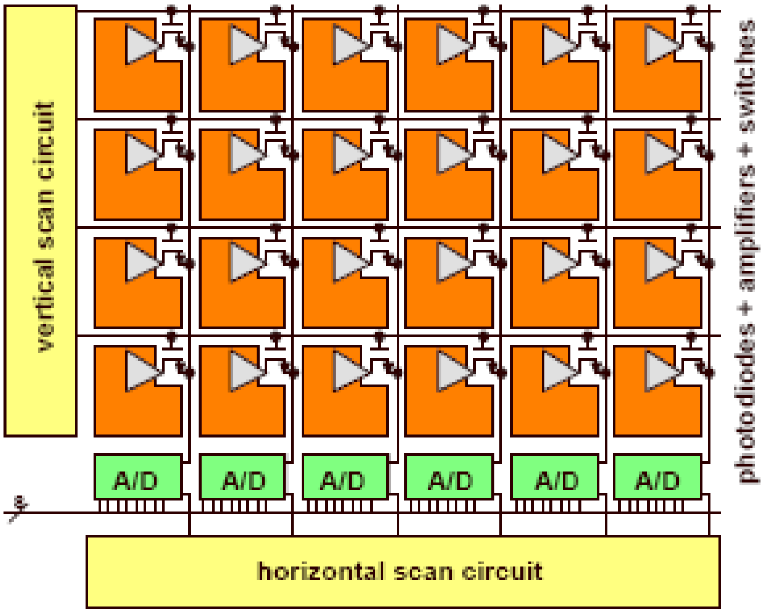

Figure 4.2: Schematic representation of image sensor showing pixels arrays and electronic control circuit [Theuwissen 2003].

The basic idea of multicarrier modulation was introduced and patented in the mid 60's by Chang [Chang 1970]. This technique has been widely used in communication systems and data transmission. Array addressing using FDM techniques has been demonstrated in fibre optic array systems and imaging arrays of micro-calorimeters using a transition edge sensor (TES) and SQUID devices [Dandridge 1994, Yoon et al., 2001 & Kiviranta et al., 2002]. In this system, array elements are probed with alternating currents at distinct frequencies. When the TES sensor absorbs signal power, its resistance changes cause modulation of the amplitude of the alternating probing current. The output signals are summed and connected to a single SQUID amplifier. At the electronics side the individual sensor signals are retrieved by a bank of frequency-selective demodulators.

The FDM scheme has also been used in radar-based frequency-modulated continuous wave (FMCW) techniques [Inaudi 2003]. The processing produces a beat frequency associated with each sensor element, allowing frequency de-multiplexing of the outputs, with the magnitude of the beat signal as a measure of the reflectance of the sensors. The FMCW technique enables the sensors to be located at different spatial locations to be discriminated.

A hybrid scheme is another possibility to multiplex sensor arrays. In this scheme, FDM and TDM are used to combine the beneficial attributes of both [McGarrity et al., 1995, Liu et al., 2008 & Reintsema et al., 2008]. The hybrid scheme has been used to multiplex arrays of reflective interferometric sensors [McGarrity et al., 1995], TES [Reintsema et al., 2008] and MRI sensors [Liu et al., 2008]. In a TES system, a first-stage of SQUID amplifiers, whose signals are time-division multiplexed into the second-stage SQUID, employ FDM to more efficiently utilize the available bandwidth. In this method, combination of time and frequency multiplexing is used for parallel acquisition of MRI images (see Figure 4.3). As a result of that only a single ADC and a commercial multi-carrier receiver are needed, which results in a less complex system.

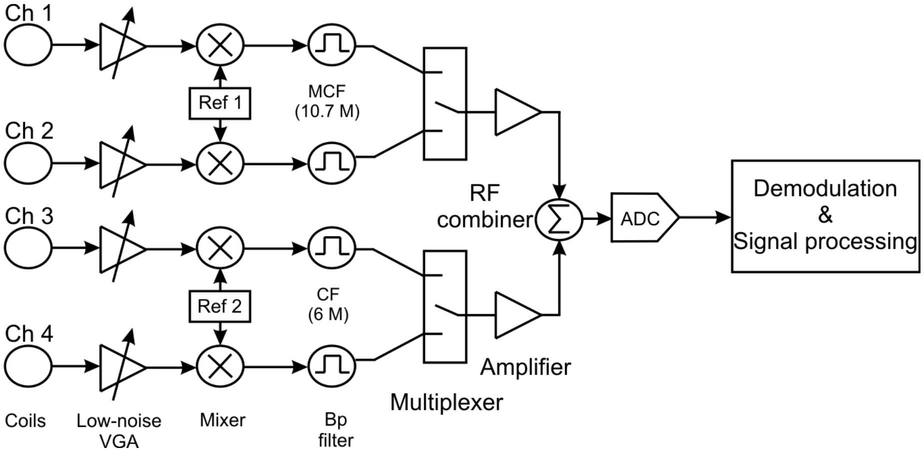

Figure 4.3: Block diagram representing four-channel parallel acquisition of MRI system using the hybrid scheme (adapted from [Reintsema et al., 2008]).

4.3.1 TDM

TDM is one of the possible schemes to reduce the number of input and output connections [Nelson et al., 1980 & Xu et al., 2006]. A possible TDM scheme applied to our hair-sensor arrays, shown in Figure 4.4, is achieved by scanning array elements with one multiplexer connected off-chip to the column side and one multiplexer on the row side. The two multiplexers determine the element to be measured. All acquired signals originating from multiple array elements share a single output-channel over time.

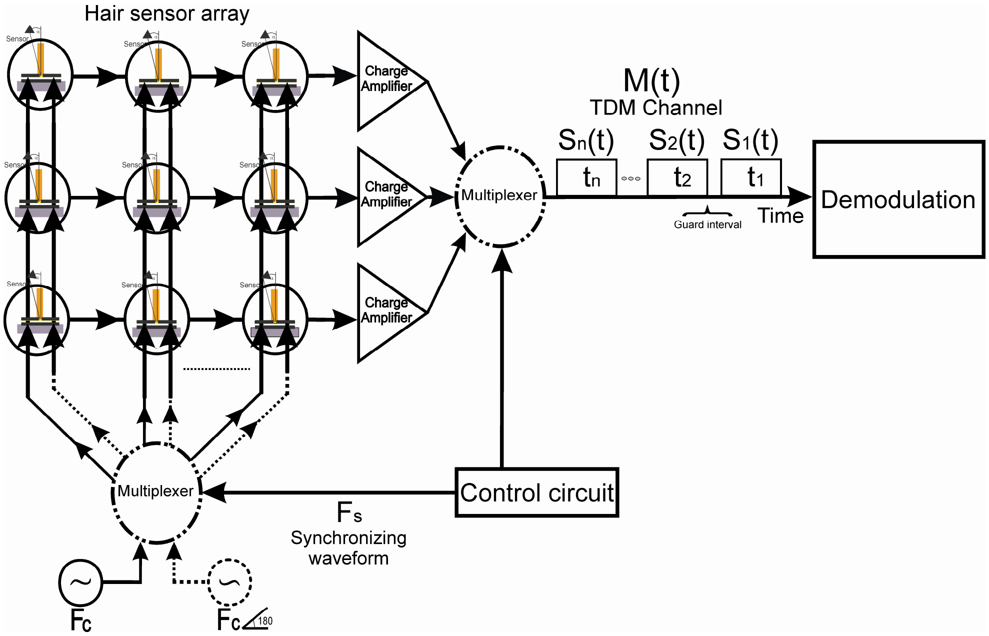

Figure 4.4: Block diagram of a possible TDM implementation for addressing hair-sensor arrays.

With TDM, the number of signal-carrying channels[2] and their interface connections can be greatly reduced when compared with SDM. However, there are some limitations especially for large sensor arrays:

- Perfect synchronism of the multiplexers control waveforms at the column and row sides is essential to prevent crosstalk. This requires the implementation of control circuits which add more complexity to the system;
- Loss of parallelism[3] inherent to the sequential scan of TDM due to the increase of sensor dead-time[4] as the number of array elements increases. This hampers the essential requirement in performing live measurements;
- The array bandwidth (i.e. the product of the number of multiplexed sensors times the bandwidth of each sensor) increases linearly with the number of sensors. On the other hand, to maintain a given array bandwidth the bandwidth available to each hair sensor in an array of N sensors can only be $1/N$ of the array bandwidth at maximum. Also, maintaining a given sensor-bandwidth imposes limitations on the TDM scheme for an increasing number of sensors. The acquisition time for each element reduces inversely proportional to the number of array elements. For instance, a sensor with a bandwidth Δf Hz requires $1/2\Delta f$ s maximum acquisition time intervals (i.e. a $2\Delta f$ Hz sampling rate). So an array of N sensors can only allow for $1/2N.\Delta f$ s acquisition time per sample thereby

---

[2] Signal-carrying channels represent the outputs of the array. In case of SDM each sensor has its own signal-carrying channel while in TDM the entire array has a single carrying channel.

[3] Parallelism denotes the ability to acquire signals from various sensors at the same time instance (i.e. performing live measurements).

[4] Dead-time of a sensor is the time when the sensor is not activated (not connected to the interfacing electronics channel).

degrading the individual SNR. In other words, increasing the array size N times requires reduction of the acquisition time of each single element by a factor of N to preserve the same sensor bandwidth according to:

$$T_{\text{element}} = \frac{T_{\text{array}}}{N} \tag{4.1}$$

where T_{element} is the acquisition time per array element and T_{array} is the acquisition time for the entire array system. Consequently, the individual SNR deteriorates by $N^{1/2}$;

- The switching circuits are an extra source of noise for the array system, specifically if they are integrated at the early stages of the acquisition system. The TDM scheme employs switches for scanning the array, generating considerable noise. Thus, the scope for integrating both the scanning and acquisition systems is reduced;
- In our hair sensor, the generated AM signals are in the MHz range, which requires both high frequency multiplexing and high sampling rate. Hence, the multiplexer has to scan over all array elements in cycling times that are smaller than one over two times the bandwidth of each hair element (Nyquist criterion). Using the TDM scheme imposes severe bandwidth requirements for the interfacing circuits and system bandwidth;
- The crosstalk between sensors is exacerbated due to the electrical coupling through small capacitances between the switch channels;
- There is a time lag between the detected signals from successively interrogated sensors, since each signal is measured at a slightly different time. This will result in timing errors up to the sampling interval in the spatio-temporal measurements.

4.3.2 FDM

Based on the above discussions, obviously, using TDM is not ideal for acquiring instantaneous array measurements. A different array-multiplexing scheme has to be used to overcome the disadvantages and limitations of TDM and SDM, especially when dealing with large numbers of sensors. We present alternative schemes based on FDM in which array signals are multiplexed in the frequency domain.

FDM is a well-known scheme in communication and data transmission. It refers to a type of modulation in which several carrier signals with different frequencies are modulated by several band-limited data signals to form one wide-band, multi-carrier signal. Thus, the available bandwidth is divided into a number of “frequency-channels”. If the multi-carrier signal has to be converted into a digital form, the maximum number of FDM channels that can be combined is limited by the Nyquist bandwidth of the ADCs i.e. the ratio of the Nyquist bandwidth of the ADC to the maximum frequency in the multicarrier signal. Therefore, higher speed ADCs are required to achieve more FDM channels. Figure 4.5 shows the principle of FDM.

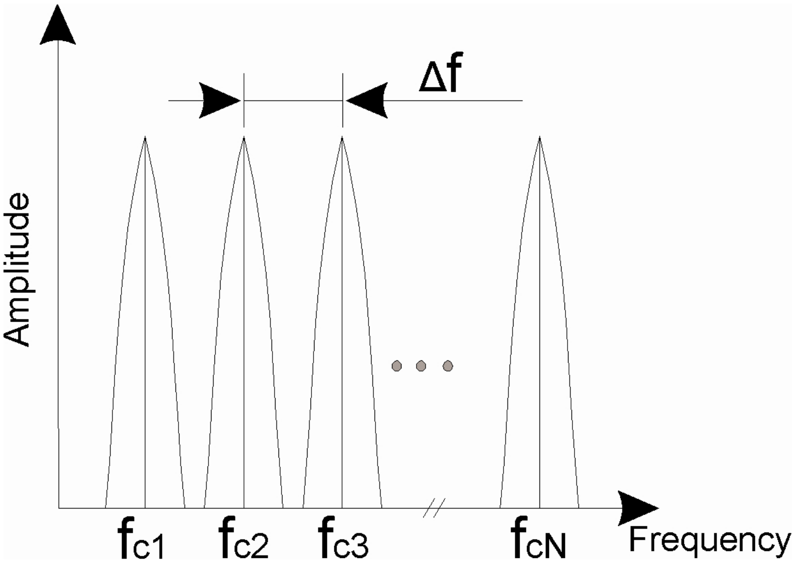

Figure 4.5: Schematic representing the spectrum of the multicarrier signal as attained using FDM.

A major advantage of FDM is sharing of the available bandwidth for signal transmission off-chip. This makes FDM inherently a parallel process without affecting the acquisition time of individual sensors i.e. the SNR is maintained irrespective of array size. Additionally, in the time domain no guard intervals are required for signal separation; therefore, neither switches nor multiplexing waveforms (as in TDM) are needed. As a result there is no switching noise and less hardware and fewer connections to perform the same task are needed. In effect, FDM can be executed as a pure analog scheme without any switching logic involved in the signal channel.

Figure 4.6 shows a schematic representation of a possible FDM scheme as applied to our hair-sensor array. Using FDM, a bank of oscillators is used to generate bi-phasic (180^{o} out of phase) sinusoidal signals i.e. carriers. These carriers are used to probe the array columns, which form the bottom electrodes of the capacitive-hair sensors (see the fabrication process of hairs arrays dedicated for FDM presented in chapter 3). Capacitance changes due to the imposing airflow modulate the amplitude of the carrier signals according to:

$$S(t) = A\cos(\omega_c t)H(t) \tag{4.2}$$

where $S(t)$ represents the transmitted AM signal from each hair sensor, A the amplitude of the carrier signal, ω_c the carrier frequency and $H(t)$ the flow signal from each hair sensor.

At the row side and due to the use of different carrier frequencies, the resulting signals appear as mutually frequency shifted signals allowing them to be combined (eq. 4.3) and transmitted through a single wire while staying distinguishable. The summation point not only consists of the common electrode of all hair-sensors in one row but also a connection to the input of a charge amplifier.

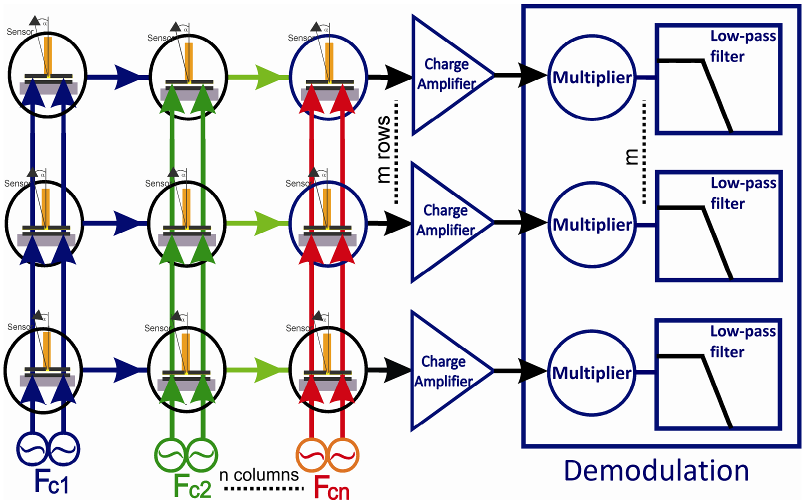

Figure 4.6: Multiplexing hair flow-sensors array using FDM technique.

$$q_k(t) = \sum_{j=1}^{n} S_{k,j}(t) \tag{4.3}$$

where k represents the row number, $q_k(t)$ the row signal stream of row k, $S_{k,j}(t)$ the signal of the sensor located at column j and row k and n is the total number of columns in the array.

Multiplying the composite output with a specific carrier frequency, used at the columns' side, the information from each individual hair sensor can be retrieved again in the baseband (i.e. demodulation process). Alternatively, the output signals can be converted to a digital form for more advanced processing operations.

Considering our requirement of achieving real-time measurements, the FDM scheme is favourable as a method of interfacing artificial hair-sensor arrays. In our hair sensor array the FDM, addressing scheme has advantages for:

- Performing spatio-temporal measurements, which requires a parallel measurement process. Such a system opens opportunities to measure, characterise and eventually recognise specific spatio-temporal flow signatures by the simultaneous extraction of individual sensor signals;
- Reducing hardware complexity and integration costs (i.e. reducing the number of interconnects by factor of $3 \cdot n \cdot m/(2 \cdot n+m)$ and charge amplifier count by factor of n, where n and m represent the number of array columns and rows, respectively. The reduction in complexity scales linearly and can be realized for large numbers of array elements. The optimal size, for the least number of connections, is when the number of rows is twice the number of columns;
- Maintaining the SNR, since the acquisition time for individual elements is constant, independent on array size;
- Array scalability i.e. the array size can be extended without deteriorating the SNR;

- Minimizing possible crosstalk, since neither synchronizing waveforms nor switches are required.

To further reduce the number of outputs while using the FDM approach, the frequencies in each row can also be shifted again to a different frequency range (up or down modulation). Figure 4.7 illustrates a possible application of the double FDM (DFDM) scheme to our hair-sensor arrays. DFDM can be realized using normal FDM and one charge amplifier (interfacing circuit of a hair sensor) per row as first stage. The output of each charge amplifier (i.e. each row composite signal) is input to a mixer which provides a distinct frequency shift along the available bandwidth. The mixer shifts the composite signal of each row to a new frequency band and hence, allows combining all carriers in one channel according to:

$$\begin{aligned} Q(t) &= \sum_{k=1}^{m} q_k(t) \cdot Y(\omega_{k,\text{shift}} t) \\ &= \sum_{k=1}^{m} \left[\left(\sum_{j=1}^{n} S_{k,j}(t) \right) \cdot Y(\omega_{k,\text{shift}} t) \right] \end{aligned} \tag{4.4}$$

where $Q(t)$ represents the entire array signal-stream, and $Y(\omega_{k,\text{shift}}\, t)$ the signal which provides the frequency shift for the signal stream of the k^{th} row.

However, the mixer may contribute extra noise to the sensor’s signal especially at the sensor-electronics interface. Thus, the second FDM should be implemented at the output stage of the interfacing circuit. The total array output stream can be digitized, filtered and demodulated to retrieve the original flow signals as measured by each hair sensor. The complexity of digital filters can be eased by sufficient frequency separation between sub-carriers (see Figure 4.7).

The demodulation process can also be performed in the digital domain and hence computer interfacing is required. The advantage of DFDM can be implemented to spread the signals over the spectrum with possible down-mixing of the stream signal to reduce requirements on the ADC. This makes it possible to invest in implementing high-performance digital band-pass filters to (i) reduce crosstalk between adjacent carrier signals and hence reduction in SNR and (ii) to increase the number of channels using a given bandwidth. This is different from TDM where crosstalk is prevented using time-based guard intervals and hence the SNR deteriorates.

Based on DFDM it would, for instance, be possible to combine signals from an array of 10 columns by 10 rows. The first FDM can be implemented using column-carrier frequencies ranging from 1 MHz to 1.9 MHz in 100 kHz steps. The second FDM can be realized by shifting the composite row signals to different frequency ranges thus occupying the frequency bands centred in between the carrier frequencies. Starting from 5 kHz with 5 kHz steps, this requires only one multiplier per row, possibly omitting frequency shifting of the signal of the first row. As a result, each individual sensor signal is shifted to a distinct frequency band and hence the output contains a composite signal representing AM signals from all array elements. The number of rows which can be addressed (m) using this architecture is:

$$m = \frac{\Delta f_{\text{columns}}}{2\,\Delta f_{\text{rows}}} - 1 \qquad (4.5)$$

where $\Delta f_{\text{columns}}$ is the column frequency separation, Δf_{rows} the row frequency separation.

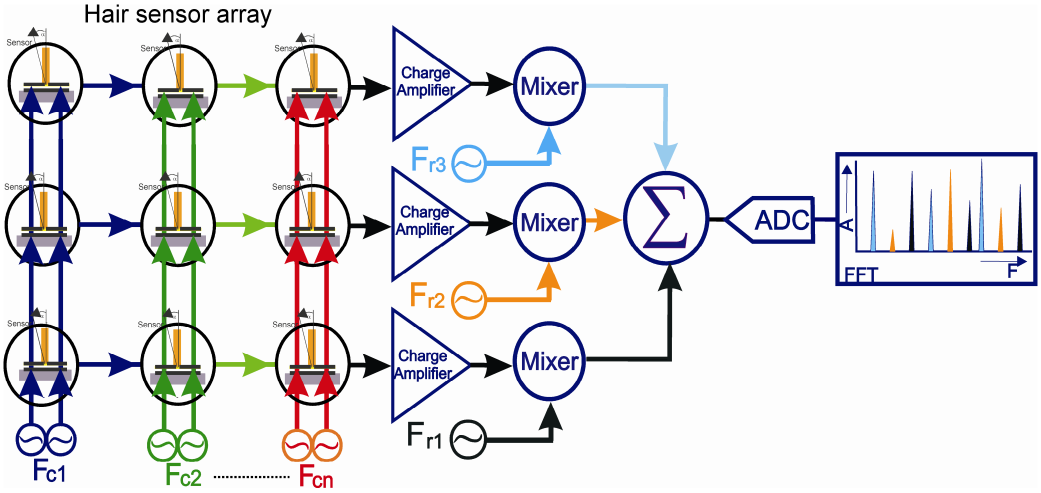

Figure 4.7: Schematic representation of a possible DFDM architecture for addressing capactive hair-sensor arrays.

The DFDM arrangement has the same advantages as single FDM for addressing hair sensor arrays and in addition delivers:

- An efficient mechanism to utilize the entire system bandwidth;
- The possibility to expand the size of the array on the basis of the number of frequency shifts at both, column and row sides. However, guard intervals are needed to prevent crosstalk;
- Frequency shifts to a unique band in the spectrum for each array element. This can be considered as additional coding for position of the hair sensor in the array;
- The possibility to down-convert AM signals using the second FDM stage to lower and intermediate frequencies. This reduces the Nyquist bandwidth requirements of the high-speed ADCs and opens up possibilities to reduce the hardware by using a single high-performance ADC with single processing unit.

4.4. Optimal addressing scheme

The hybrid scheme, which involves implementing FDM and TDM together to take advantage of both schemes, can be used in array addressing. E.g. columns are activated using FDM while signals at the row side are multiplexed using TDM. Combining FDM and TDM improves, to some extent, the multiplexing gain of the sensor array i.e. use of the available bandwidth and hardware efficiently. However, optimization for the number of hardware-channels and bandwidth is required to determine the optimal contribution of each scheme for each case separately. With the assistance of our previous knowledge of array design, sensor design and carrier frequency range it is clear that TDM is not the optimal solution since it uses only a fraction of time to connect a sensor to the read-out channel thereby limiting the sensor bandwidth, parallelism and reducing the SNR.

In line with our conditions and requirements and based on the above discussions (taking into account the impossibility of electronics integration on-chip), the FDM mechanism represents the most favourable addressing scheme to be implemented with our artificial hair flow-sensor arrays. FDM allows addressing and reconstruction of the original signal from individual sensors separately, which makes it feasible to measure spatio-temporal flow patterns across arrays of hair flow-sensors. DFDM can also be an option to transfer array signals using only a single channel and to convert it into the digital form using a single ADC. However, at this stage investing in mixers is not our preferable approach.

Summing up, the FDM approach maintains the sensor and array bandwidth as it is with SDM while the bandwidth is scaling with the number of array elements in TDM. The number of array connections required to implement SDM is huge and can be tremendously reduced with FDM and TDM. A comparison between the previously presented main array interfacing schemes based on our requirements is shown in Table 4.1. The numbers are based on single hair-sensor requirements with a bandwidth of B_s and array size of $(n \times m)$ hair sensors.

Table 4.1: Comparison between main array interfacing schemes as applied to our hair sensor arrays based on our requirements.

	SDM	TDM	FDM
Crosstalk	+	-	+/-
Scalability	--	-	+
Interfacing	Continuous	Intervals	Continuous
Simultaneous measurements	Real-time	Delayed	Real-time
Electronics complexity	Very complex	Complex	Less complex
Bandwidth per channel	B_s	$(n \times m) \times B_s$	B_s
Number of connections	$3(n \times m)$	$2n+m$	$2n+m$
SNR factor $\left({}^{\mathrm{SNR}_{\mathrm{single}}}\!/\!{}_{\mathrm{SNR}_{\mathrm{addressed}}} \right)$	1	$(n \times m)^{1/2}$	1 ([5])

---

[5] Taking into account perfect carrier signals and low common electrode resistance.

The following sections show the implementation of the FDM scheme in interfacing artificial hair-sensor arrays. The design and fabrication process of the hair sensor are modified, from the previous sensor design, allowing for the fabrication of single-chip arrays. The results are shown for arrays made of 5 × 4 hair elements but the extension to larger arrays is straightforward.

4.5. Experiments

4.5.1 Hair-sensor array fabrication

Previously we have shown the design and fabrication of high-density flow-sensitive hair sensor arrays [Krijnen et al., 2006] (see Figure 4.8a). Signals from a group of hair-sensors were combined to increase the SNR (i.e. increasing the common capacitance changes but averaging out noise from similar but independent hairs). However, in that (previous) sensor design the underlying silicon substrate forms the common electrode for the capacitors and integrates the signals of all hair-sensors. This prevents addressing hair-sensors independently and thereby hampers single-chip based arrays. Therefore, the design of the hair-sensor arrays has been adapted to implement FDM.

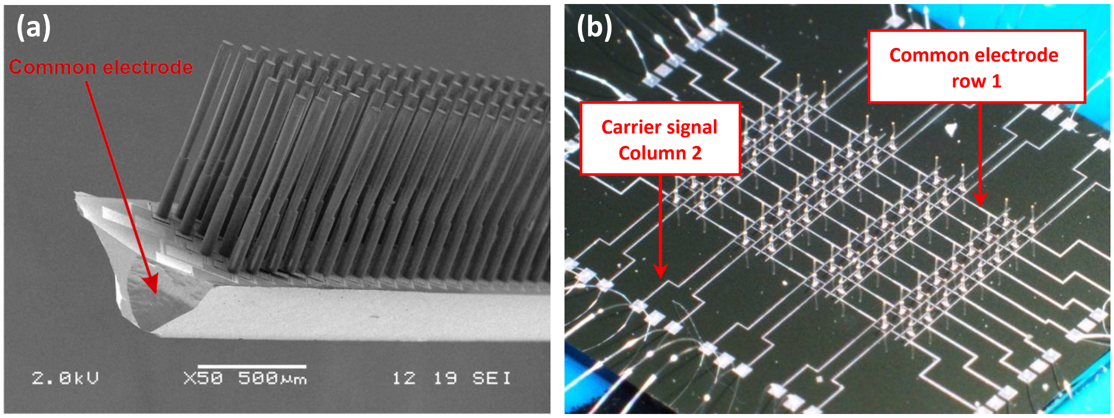

Figure 4.8: (a) An SEM image of a previous artificial hair flow-sensor array showing the grouping principle (many hairs arranged in parallel with the substrate as common electrode). (b) Image of a single-chip hair-sensor array dedicated to FDM and consisting of single-hair elements with pairs of sensors arranged perpendicular to each other.

Here we look into possibilities to make high-density single-chip hair-sensor arrays which can be interfaced using a capacitive measurement method comparable to what we have done before and which can be made in a compatible fabrication process. The fabrication process of the single-chip hair-sensor arrays (see Figure 4.8b) is identical to the process presented in chapter 3. Arrays of artificial hair flow-sensors were fabricated in rows and columns with single hair-sensors as basic array elements. The use of Silicon-on-Insulator (SOI) wafer technology allows us to isolate the sensing electrode of each hair element requiring primarily a redesign of the electrode system. This assists in interrogation of each individual hair-sensor by a differential capacitive measurement technique requiring only two anti-phase carrier signals. In the new hair-sensor design the carrier signal electrodes are defined in the silicon device layer (using deep trenches for insulation) while the common electrode for the output signal is implemented by an aluminium layer on the top silicon-nitride layer (including the sensor membranes). The common electrode of all single-hair elements for each row are connected together (i.e. facilitating FDM). Additionally, due to a reduction of parasitics and noise, this design improves the single-sensor detection limit to reach about 1 mm/s using a bandwidth of 3 kHz as shown in chapter 3.

4.5.2 Measurement setup

DDS system

Our hair sensor array consists of rows and columns with single hair elements at the intersections. Direct Digital Synthesis (DDS) systems are used to form a bank of oscillators to produce the required carrier signals. The current DDS system offers the possibility for eight channels to interface eight sensors. Each sensor channel can be connected in two different ways to the DDS channel system; either (i) directly to its own charge amplifier (i.e. the number of charge amplifier equals the number of sensor channels) or (ii) using FDM where all the sensors share a single charge amplifier. The output of the charge amplifier is fed back to the DDS system for synchronous demodulation. The demodulator outputs are synchronously sampled and fed into a CAN-bus to be interfaced to a computer through a 'CAN Gateway' interface. The output to the gateway is a data-stream of the output of all sensors with 1 kHz sampling frequency for each sensor channel. Groups of 4 samples are combined into one CAN-bus message and hence every 4 ms a sensor channel sends samples on the bus. For proper synchronous sampling, the period of the harmonic airflow signal should be much larger than the difference in sampling time between system channels. Figure 4.9 shows the interfacing and control system of the hair sensor arrays. More details about this system can be found in [Lammerink 2009].

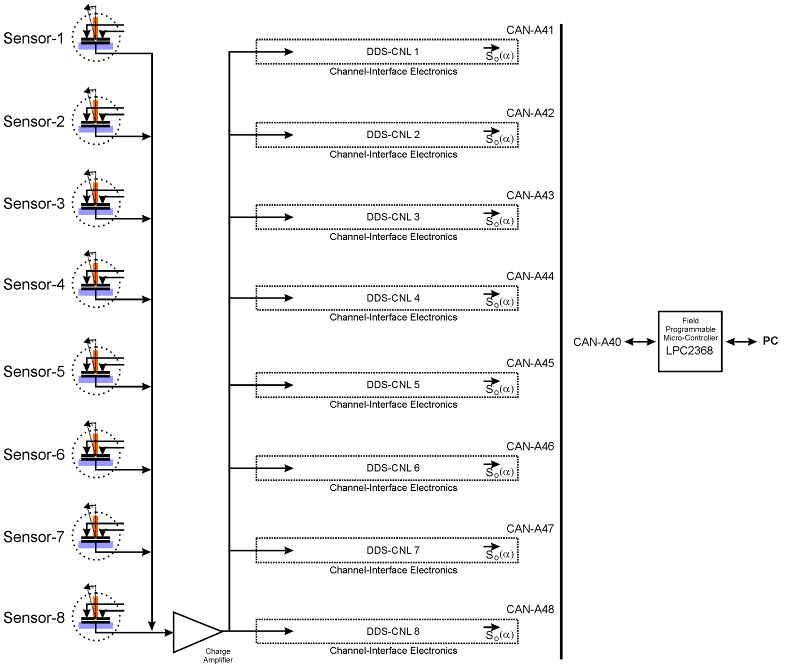

Figure 4.9: Block diagram representing the architecture of the DDS system [Lammerink 2009]

Figure 4.10 shows the experimental setup and the sensor array used to demonstrate the FDM scheme. An array of (5 × 4) artificial hair-sensors was addressed using FDM to simultaneously measure signals from individual hair-sensors. The 20 sensors were addressed using 4 times 2 carrier frequencies at the inputs of the columns and 5 row outputs to the charge amplifiers, giving a total of 13 interconnects rather than the 60 that would have been required for SDM. A bank of oscillators (made of DDS signal generators on dedicated printed circuit boards) was used to generate the carrier signals as applied to the array columns. Along the rows the AM signals were combined and connected off-chip to one charge amplifier per row. The array functioning was tested using a harmonic dipole field, since it is well described in literature [Lamb 1910]. A sphere with a radius of 5 cm was harmonically driven at 30 Hz (as stimulus) to examine the performance of the hair-sensor array in measuring flow fields and perform source localization.

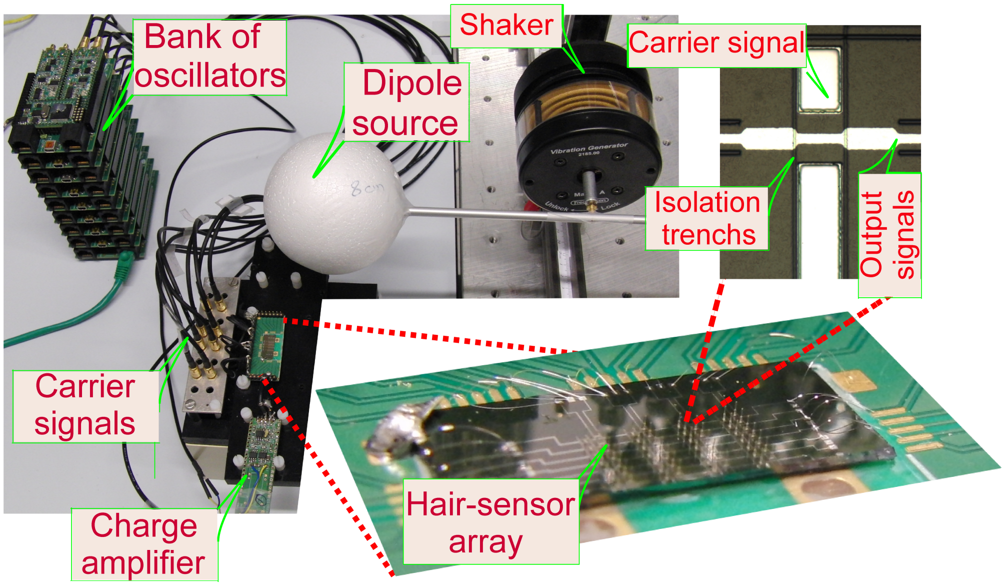

Figure 4.10: Photograph of the measurement setup and sensor arrays. Isolation trenches of the carrier electrodes are also shown.

4.6. Results

We were able to simultaneously measure airflows for each hair-sensor while using FDM. Due to the availability of the hardware channels, TDM (with relay system) was used to switch between the array rows in such that each row with 4 hair sensors were simultaneously measured using FDM. Figure 4.11 shows the frequency spectrum of the composite signal measured at the output of the charge amplifier representing the four AM carrier signals for two (arbitrarily) selected FDM channels (rows 1 & 5).

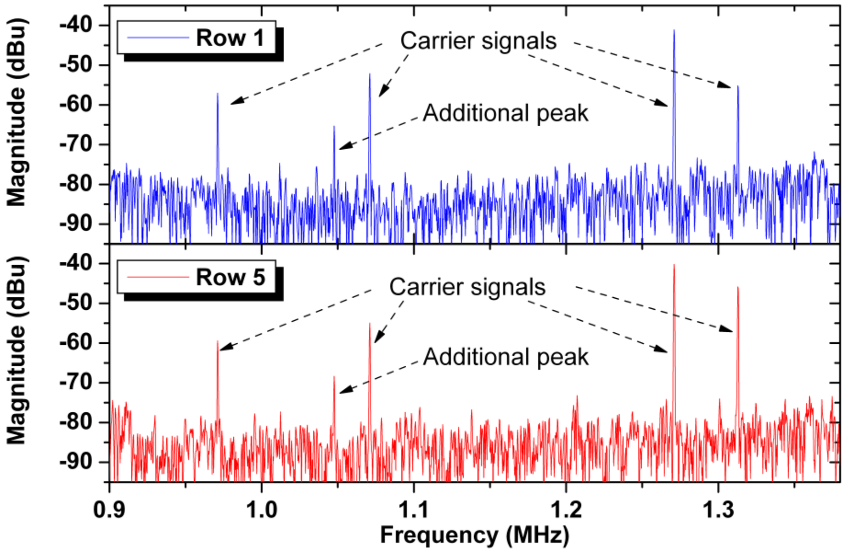

Figure 4.11: FFT spectrum of AM signals from two rows at the output of the charge amplifiers while employing FDM to an array of 5 × 4 hair-sensors.

First the performance of the FDM array interfacing scheme as applied to our hair sensor arrays was investigated using loudspeakers as airflow source. The synchronous demodulation process was performed using a 300 Hz low-pass filter. Outputs of the hair sensors, with and without FDM, were measured and compared. Figure 4.12 shows the frequency response of two hair sensors (two hair sensors in the same row were chosen)[6]. The results show virtually identical frequency response for each of the hair sensors irrespective of the use of FDM.

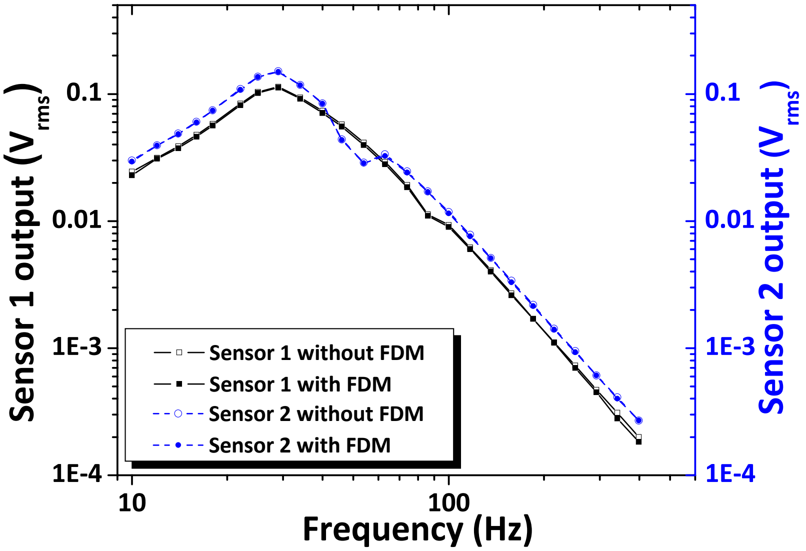

Figure 4.12: Frequency response of two hair sensors (located in the same row but in two different columns within a single-chip array) measured without and with FDM.

---

[6] Note: these graphs show ‘raw data’ which includes the loudspeaker characteristics (so the curves do not present the sensor transfer function).

Figure 4.13 illustrates the effects of FDM on voltage output of a hair sensor (measured at 80 Hz) when activating successively 1, 2 and 3 hair-sensor located in the same row. The results indicate that the performance of the addressed hair-sensor does not deteriorate significantly by the application of FDM.

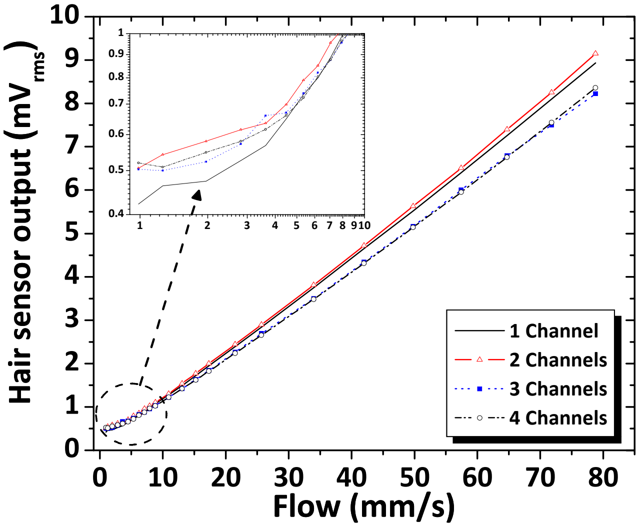

Figure 4.13: Effect of the application of FDM on the voltage output of a single hair sensor when an increasing number of channels is activated.

As demonstration for successful measurement of airflow fields using hair-sensor arrays, the dipole fields were measured by different hairs and for a systematically varied position of the vibrating sphere (virtual lateral-line). Afterwards the positions of the dipole source (relative to the array elements) were determined. Figure 4.14 represents the dipole fields detected by different hair-sensors located in one row by means of this virtual lateral-line [Dagamseh et al., 2010]. The shift in peak positions represents the column separation distance between sensors and precisely matches the physical design distance between the elements (2 mm).

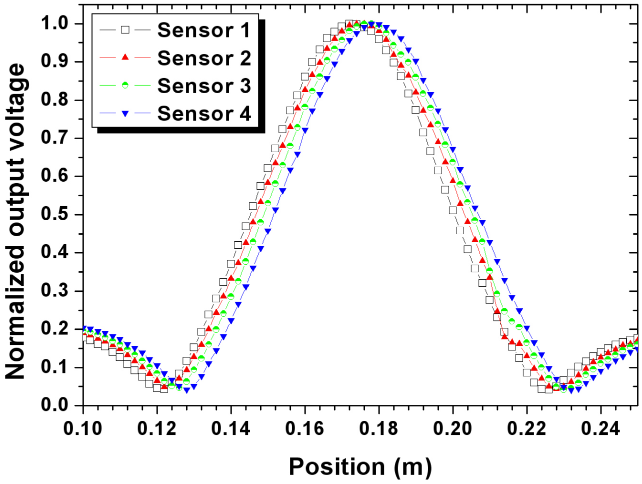

Figure 4.14: Flow field measurement vs dipole position simultaneously detected by 4 hairs in one row. The separation between peaks matches with the hair-sensor separation.

The source localization process, using either the signals as averaged over row 1 or averaged over row 5, as well as the signals averaged over both rows are shown in Figure 4.15. The distance between the source and the array is determined according to the methods described in [Dagamseh et al., 2010]. A clear linear relation between the real and estimated distances is observed.

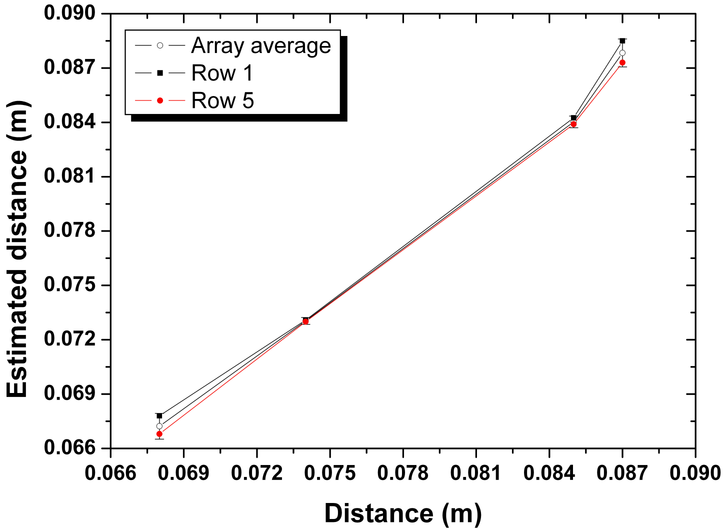

Figure 4.15: Dipole source localization using the hair-sensor array while applying FDM.

4.7. Discussion

In the new hair sensor design, some aspects in connection to the application of FDM for array interfacing have to be considered. Firstly, the combination of the series resistance and cable parasitics (from the carrier-signal source to the sensor capacitor) can pose limitations on the bandwidth and therefore the upper limit of the carrier frequencies (see chapter 3). Hence, the maximum frequency and minimum frequency spacing between adjacent channels (necessary to reduce crosstalk) limit the number of columns that can be multiplexed. To overcome this, the series resistance of carrier signal electrodes is reduced by depositing an additional aluminium layer on top. The resistance of the carrier electrodes is in the range of 1 kΩ thereby nearly matching the resistance of the common electrode (300-400 Ω).

Secondly, if the impedance of a connection to a summation point (the input of a charge amplifier) is not equal to zero the summed current signal will produce a voltage drop. Consequently, each hair sensor is not only probed by its own carrier frequency but also by the carriers of neighbouring hairs. This generates crosstalk in which each hair sensor modulates the amplitude of multiple carriers, i.e. cross-modulation. The crosstalk amplitude depends on the impedance value at the specific carrier frequencies. To limit this effect, the impedance of the common electrode is kept small using aluminium for signal carrying electrodes.

Thirdly, nonlinearities of the carrier-signal generators cause additional frequency components that may interfere with neighbouring carrier channels (see additional peak in Figure 4.11). If one of the carrier signals of neighbouring channels is carelessly selected to coincide at one of these additional peaks, crosstalk between FDM components occurs. As a result, the hair sensor's output would not only contain a modulated signal at its intended carrier frequency, but also frequency components at neighbouring channels, possibly modulated by neighbouring sensors (i.e. two carriers for a single hair sensor). Experimentally, the amplitude of some of the demodulated signals were found to decrease when the carrier-signal of one of the neighbouring channels was disconnected. To overcome this, the carrier frequencies were chosen appropriately to be free from additional frequency components from neighbouring channels.

The presented results show that array-wide we can measure the artificial hair-sensor rotations as caused by sphere-movements induced airflows. This confirms the successful application of the FDM addressing technique to our hair-sensor array. As a consequence we are able to reduce the number of interconnects considerably. In the demonstrated array the reduction was from 60 interconnects to 13 (4 times 2 carrier frequencies input along the columns and 5 rows output to the charge amplifiers). The measurements confirm that the application of FDM does not significantly affect the performance of an addressed hair-sensor neither its frequency response nor its linearity. The results presented in Figure 4.12 show very small deviations in frequency response of a hair sensor with and without FDM. On the other hand, when probing additional sensors in the same row reduction in the voltage response of a hair sensor is observed while it has almost no effect on noise level (see Figure 4.13). This can be attributed to the limitation of multiplier input amplitudes: as the number of addressed hair sensors is increased, the voltage level at the input of the multiplier increases and show saturation and other nonlinear effects. This poses limitations on the number of hairs that can be multiplexed in one channel. Proper selection of high-performance multipliers or demodulation in the digital domain can improve the FDM process in this respect.

The reconstructed virtual lateral-line responses proof that each hair element faithfully reflects the dipole field at its position while employing FDM. It demonstrates the hair-sensor array's ability to probe individual hair sensors independently and afterwards to accurately localize the positions of dipole sources, relative to either each hair element or to the entire array. Consequently, it is demonstrated that FDM makes it possible to perform simultaneous measurements with single-chip arrays consisting of multiple independent hair-sensors. These achievements, in combination with the use of high sensitive single-hair sensors arranged in single-chip arrays, enable us to accurately measure the projection of the flow field at the position of the array. Various processing tasks can be implemented taking advantage of these simultaneous measurements of signals from the entire array.

Importantly, FDM is not limited to addressing of capacitive sensor arrays, also (piezo-, thermo-, magneto-) resistive or inductively probed arrays can take advantage of it. In a resistive scheme, the variable resistors are probed with alternating voltages with distinct frequencies at the column side and the signals are summed at the row side. This makes FDM a universal array-interfacing scheme that allows reducing system complexity considerably.

4.8. Conclusions

In conclusion, this chapter detailed an important step of our work towards “flow-cameras” based on biomimetic hair flow-sensor arrays. By gathering signals from individual sensor elements, it is possible to obtain spatio-temporal images of airflows over hair-sensor arrays. Several schemes for interfacing individual array elements in array-settings have been discussed. It is found that the use of FDM is favourable for interfacing our capacitively interrogated hair-sensor arrays. Unlike TDM, FDM is free from propagation delays and synchronisation errors. Therefore, channel acquisition techniques and hardware for FDM are not as complex as for TDM. Further, FDM is rather scalable to larger array structures without reduction of the acquisition time and deterioration of the SNR of the individual sensors. SOI based fabrication technology in combination with FDM has opened-up the possibility for simultaneous interfacing of multiple sensors in single-chip arrays. This adds new dimensions to flow-imaging with potential applications in e.g. flow monitoring and robotics.

4.9. References

[Aw et al., 1996] Aw, C.H. & Wooley, B.A. (1996) "A 128 × 128-pixel standard-CMOS image sensor with electronic shutter", IEEE Journal of Solid-State Circuits, 31, pp. 1922-1930.

[Bruijn et al., 2004] Bruijn, M.P., Baars, N.H., Bergmann Tiest, W.M., Germeau, A., Hoevers, H.F.C., De Korte, P.A.J., Mels, W.A., Ridder, M.L., Krouwer, E., Van Baar, J.J. & Wiegerink, R.J. (2004) “Development of an array of transition edge sensors for applications in X-ray astronomy”, Nuc. Instr. Meth. Phys. Res., A520, pp. 443–445.

[Casas et al., 2010] Casas, J., Steinmann, T. & Krijnen, G. (2010) "Why do insects have such a high density of flow-sensing hairs? Insights from the hydromechanics of biomimetic MEMS sensors", Journal of the Royal Society Interface, 7, pp. 1487–1495.

[Chang 1970] Chang, R.W. (1970) “Orthogonal Frequency Division Multiplex data transmission system”, U.S. Patent, document number 3488445.

[Chervenak et al., 1999] Chervenak, J.A., Irwin, K.D., Grossman, E.N. Martinis, J.M., Reintsema, C.D. & Huber, M.E. (1999) “Superconducting multiplexer for arrays of transition edge sensors”, Appl. Phys. Letters, 74, pp. 4043–4045.

[Dagamseh et al., 2010] Dagamseh, A.M.K., Lammerink, T.S.J., Kolster, M.L., Bruinink, C.M., Wiegerink, R.J. & Krijnen, G.J.M. (2010) "Dipole-source localization using biomimetic flow-sensor arrays positioned as lateral-line system", Sensors and Actuators, A: Physical, 162, pp.355–360.

[Dandridge 1994] Dandridge, A. (1994) “The development of fiber-optic sensor systems”, In proc. 10th Optical Fibre Sensors Conference SPIE, 2360, Washington, pp. 154–161.

[de Korte et al., 2003] De Korte, P.A., Beyer, J., Deiker, S., Hilton, G.C., Irwin, K.D., Maclntosh, M., Nam, S.W., Reintsema, C.D., Vale, L.R. & Huber, M.E. (2003) “Time-division superconducting quantum interference device multiplexer for transition-edge sensors”, Rev. Sci. Instrum. 74, pp. 3807–3815.

[Doriese et al., 2007] Doriese, W.B., Ullom, J.N., Beall, J.A., Duncan, W.D., Ferreira, L., Hilton, G.C., Horansky, R.D., Irwin, K.D., Mates, J.A.B., Reintsema, C.D., Vale, L.R., Xu, Y., Zink, B.L., Rabin, M.W., Hoover, A.S., Rudy, C.R. & Vo, D.T. (2007) “14–pixel, multiplexed array of gamma-ray microcalorimeter with 47 eV energy resolution at 103 keV”, Appl. Phys. Lett., 90, pp. 193508.

[Gardner et al., 1992] Gardner, J. & Bartlett, P.N. (1992) “Sensors and Sensory Systems for an Electronic Nose”, Kluwer Academic Publishers, Dordrecht.

[Hauptmann et al., 2000] Hauptmann, P., Borngraeber, R., Schroeder, J. & Auge, J. (2000) “Artificial electronic tongue in comparison to the electronic nose - state of the art and trends”, In Proceedings of the 54th Annual IEEE International Frequency Control Symposium, U.S.A., pp. 22–29.

[Inaudi 2003] Inaudi, D. (2003) “State of the Art in Fiber Optic Sensing Technology and EU Structural Health Monitoring Projects”, In the 1st International Conference on Structural Health Monitoring and Intelligent Infrastructure, Tokyo, Japan.

[Kima et al., 2007] Kima, D. & Möller, R. (2007) "Biomimetic whiskers for shape recognition", Robotics and Autonomous Systems, 55, pp. 229–243.

[Kiviranta et al., 2002] Kiviranta, M., Seppä, H., van der Kuur, J. & de Korte, P. (2002) “SQUID-based read-out schemes for microcalorimeter arrays”, Proceedings of 9th International Workshop on Low Temperature Detectors (LTD-9), Madison Wisconsin, AIP Conference Proceedings, 605, pp.295–300.

[Ko et al., 2008] Ko, H.C., Stoykovich, M.P., Song, J., Malyarchuk, V., Choi, W.M., Yu, C.-J., Geddes III, J.B., Xiao, J., Wang, S., Huang, Y. & Rogers, J.A. (2008) "A hemispherical electronic eye camera based on compressible silicon optoelectronics", Nature, 454, pp. 748–753.

[Krijnen et al., 2006] Krijnen, G.J.M., Dijkstra, M., Van Baar, J.J., Shankar, S.S., Kuipers, W.J., De Boer, R.J.H., Altpeter, D., Lammerink, T.S.J. & Wiegerink, R. (2006) ”MEMS based hair flow-sensors as model systems for acoustic perception studies”, Nanotechnology, 17, pp. S84–S89.

[Krijnen et al., 2007] Krijnen, G., Lammerink, T., Wiegerink, R. & Casas, J. (2007) "Cricket inspired flow-sensor arrays", Proceedings of 6th IEEE Conference on SENSORS (IEEE SENSORS); Atlanta, USA, pp. 539–546.

[Lamb 1910] Lamb, H. (1910) “The dynamical theory of sound”, Edward Arnold, London.

[Lammerink 2009] Lammerink, T. (2009) “LM2043 Daisy based, modular CILIA-Instrumentation”, User’s manual, V1.2.

[Liu et al., 2008] Liu, Y. & Li, G. (2008) “F_TDM receiver for parallel acquisition of MRI”, Electronics Letters, 44, pp. 454–456

[McGarrity et al., 1995] McGarrity, C., Chu, B. & Jackson, D. (1995) “Multiplexing of Michelson interferometer sensors in a matrix array topology”, Applied Optics, 34, pp. 1262–1268.

[Nelson et al., 1980] Nelson, A.R. & McMahon, D.H. (1980) ”Passive Multiplexing System for Fiber Optic Sensors”, Appl. Optics, 19, pp. 2917–2920.

[Nigel 1999] Nigel, D.Y. (1999) ”Capacitive sensing array device”, U.S. Patent, document number 5952588 A.

[Reijniers et al., 2007] Reijniers, J. & Peremans, H. (2007) "Biomimetic sonar system performing spectrum-based localization", IEEE Transactions on Robotics, 23, pp. 1151–1159.

[Reintsema et al., 2008] Reintsema, C.D., Beall, J., Doriese, W., Duncan, W., Ferreira, L., Hilton, G.C., Irwin, K.D., Schmidt, D., Ullom, J., Vale, L. & Xu, Y. (2008) ”A TDMA hybrid SQUID multiplexer”, Journal of Low Temperature Physics, 151, pp. 927–933.

[Rogers 1980] Rogers, A. J. (1980) “Polarization-optical time domain reflectometry”, Electron. Lett., 16, pp. 489–490.

[Sartori et al., 1995] Sartori, A., Maloberti, F., Simoni, A. & Torelli, G. (1995) “A 2-D photosensor array with integrated charge amplifier”, Sensors and Actuators A: Physical, 46, pp. 247–250.

[Sergio et al., 2002] Sergio, M., Manaresi, N., Tartagni, M. & Canegallo, R. (2002) ”Method of reading a capacitive sensor and related integrated circuit”, U.S. patent, document number 7755683.

[Simoni et al., 1995] Simoni, A., Torelli, G., Maloberti, F., Sartori, A., Plevridis, S. & Birbas, A.N. (1995) "Single-chip optical sensor with analog memory for motion detection", IEEE Journal of Solid-State Circuits, 30, pp. 800–805.

[steinmann et al., 2006] Steinmann, T., Casas, J., Krijnen, G. & Dangles, O. (2006) "Airflow sensitive hairs: Boundary layers in oscillatory flows around arthropod appendages", Journal of Experimental Biology, 209, pp. 4398–4408

[Theuwissen 2003] Theuwissen, A. (2003), lecture notes, TUDelft.

[Wright et al., 1992] Wright, S.W. & Porter, J.R. (1992) “Parallel acquisition of MR images using time multiplexed coils”, Electron. Lett., 28, pp. 71–72

[Xu et al., 2006] Xu, Q., Wang, H., Xu, Z. & Li, G. (2006) “Frequency domain multiplexing for parallel acquisition of MR images”, Electron. Lett., 42, pp. 326–327

[Yaldiz et al., 2007] Yildiz, G., Duru, A.D. & Ademoglu, A. (2007) ”A Comparative Study of Localization Approaches to EEG Source Imaging”, In proceedings of IEEE/NIH Life Science Systems and Applications Workshop, LISA, Bethesda, pp. 156–159.

[Yoon et al., 2001] Yoon, J., Clark, J., Gildemeister, J., Lee, A., Myers, M., Richards, P. & Skidmore, J. (2001) “single superconducting quantum interference device multiplexer for arrays of low-temperature sensors”, Appl. Phys. Lett., 78, pp. 371–373.

[Zwijze 2000] Zwijze, A.F. (2000) “Micro-machined high capacity silicon load cells”. PhD thesis, University of Twente, Enschede-The Netherlands.

Chapter

5

ARTIFICIAL LATERAL-LINE

In nature, fish have the ability to localize prey, school, navigate, etc. using the lateral-line organ. Here we take advantage of our artificial hair flow-sensors arranged in a linear array shape (inspired by the lateral-line system in fish) to measure airflow patterns at the sensor positions. This is demonstrated by dipole-source localization in air using both the characteristics of the dipole velocity field and beamforming techniques. The results show the artificial lateral-line ability to image the position of the dipole source. The measurements along the lateral-line system are found to be in excellent agreement with theory and are successfully used for source-distance determination. This opens possibilities for flow-based near-field environment mapping which can be beneficial to e.g. biologists and robot guidance applications.

5.1 Array sensors

In nature, animals can detect events in their environment with varying aptness using different sources of sensory information as it is relevant for their survival. Crickets [Shimozawa et al., 2003], spiders [Albert et al., 2001], scorpions [Sturzl et al., 2000] and fish [Coombs 2001] all have flow sensory systems in the form of hair-sensor arrays that detect tiny fluid movements. These biological sensor arrays are highly sensitive, very acute (e.g. with respect to directivity) and often posses a fair amount of redundancy yielding a certain degree of robustness. In literature, specifically, the lateral-line system (LLS) has been the subject of extensive research in attempts to understand hydrodynamic imaging of the surroundings and source localization processes in fish [Blake et al., 2006]. The LLS is considered as array system where information can be draw not only from the temporal features of a flow field but also from its spatial characteristics.

Lately, sensor arrays have become important research topics across disciplines with respect to smart sensory system developments [Yildiz et al., 2007 & Atmoko et al., 2008]. Depending on the array task, the sensors can be arranged in e.g. planar or three-dimensional shapes. The array geometry and the sensors' positions (absolute or relative) are important design parameters and, in many applications such as antenna arrays, are prerequisite for further processing of the array signals. In modern communications and radar systems, antenna arrays are an essential part to extract weak signals from noisy backgrounds [Viberg et al., 1995]. Using the overall available spatio-temporal array data useful information related to the environment and objects in it may be extracted by integrating multi-sensors' readings in an appropriate manner while benefitting from array signal processing (ASP) techniques. Examples of such embedded parameters, detected by array sensors are direction-of-arrival (DoA) [Pirinen et al., 2004 & Haupy 2010], number of sources estimation [Atmoko et al., 2008 & Ishi et al., 2009] and acoustic source localization [Dowling et al., 1992].

The estimation of object parameters using an array of sensors has been reported extensively in literature. Being a highly interesting task, source localization has received great attention in ASP [Stark et al., 2002]. Tracking moving sources has many applications including health care [Yildiz et al., 2007], satellite communication [Brandes et al., 2007] and military purposes [Navrátil et al., 2010].

The methods for source localization that have been used intensively can be categorized into time delay estimation and beamforming [Atmoko et al., 2008]. The time delay method exploits the coherence between signals, as detected by various array elements, to extract information about the direction of the source. In beamforming a full directional scan is performed and the maximum signal-power indicates the source direction. The appropriate signal processing technique and associated complexity depend on the number of variables to be extracted, the number of array elements and array configurations, e.g. linear-line array, uniform square array, circular array etc.

In biomedical applications, several techniques take advantage of sensor arrays for source localization. The brain neurons' activities are recorded (Electro-Encephalo-Graphy (EEG)) using arrays of electrodes and the number, position and strength of the neural sources are estimated [Yildiz et al., 2007]. Various skull models [Radich et al., 1994], signal models and signal processing algorithms [Yildiz et al., 2007] are developed and tested to improve source position estimation.

In radar and satellite applications, sensor arrays are used in target estimation processes. The goal is to determine various target parameters; e.g. location, velocity and size. Various array shapes, signal models and tracking algorithms have been developed and implemented to minimize system complexity and/or reduce estimation errors [Brandes et al., 2007].

In robotic applications, arrays made of two microphones (mounted on a robot) have been used for direction of arrival estimations [Mochiki et al., 2008]. The ratio of power spectrum amplitudes for two microphones was employed as a feature vector, either with or without the use of the phase, and statistical pattern recognition was used to determine the direction of the source.

In sensor research the biomimetic approach may include materials, sensing principles, sensory systems, detection mechanisms, and computational algorithms inspired by biological models. Hearing in mammals and bats in particular, the LLS of fish, slit-sensilla based localization in scorpions and airflow detection by hair-sensor populated cercal arrays in crickets provide fascinating examples for engineers to imitate either in their hardware and/or information processing. Inspired by bats, the echolocation spectral analysis has been used to observe and localize features in realistic environments i.e. walls and obstacles [Reijniers et al., 2007]. Reflector localization is based on the comparison of measured echoes with echo templates from different angles and hence the shape and position of the surroundings are determined. The LLS in fish has been used as source of inspiration in the fabrication of a biomimetic, piezoresistive flow sensor arrays using the PDMA process [Fan et al., 2002]. The scorpion strategy is another example of source localization using sensor arrays. A biologically plausible prey localization scheme in scorpions has been presented and tested using a neuronal model [Stürzl et al., 2000]. In this model, the stimulus angle is determined using the received excitatory input from one tarsus and the inhibition from a triad opposite to it.

5.2 Lateral-line system

As relevant to their surviving, fish have evolved a sense organ (i.e. LLS) to detect water vibrations and disturbances transmitted through water. It allows fish to experience the surrounding objects without direct physical contact by means of detecting (near-field) water flow sources.

The LLS is a natural mechano-sensory system consisting of spatially distributed neuromasts sensitive to fluid-flow and arranged in a more or less linear array structure [Coombs 2001]. Each neuromast consists of several hair-cells embedded together inside a jelly-like structure called a cupula. The LLS may contain both Superficial Neuromast (SN) and Canal Neuromast (CN) [Dijkgraaf 1963]. The SN are located on the scales of the fish and are sensitive to fluid velocity while the CN are positioned inside canals beneath the skin and are sensitive to pressure gradients [Coombs 2001]. Each neuromast within the LLS only senses a local component of the flow field. Due to water movement the cupula, and with it the neuromast, deflect thereby generating action-potentials that travel the neuronal path-ways toward the brain. The combination of all flow signals is further processed to extract meaning from the detected flow fields rather than being just a collection of uncorrelated single point measurements, i.e. it allows for constructing flow images. These hydrodynamic images can be used to detect features and events in the environment, from the water flows and disturbances created by obstacles or probed by their self-generated flows. Figure 5.1 is a schematic representation of LLS in fish.

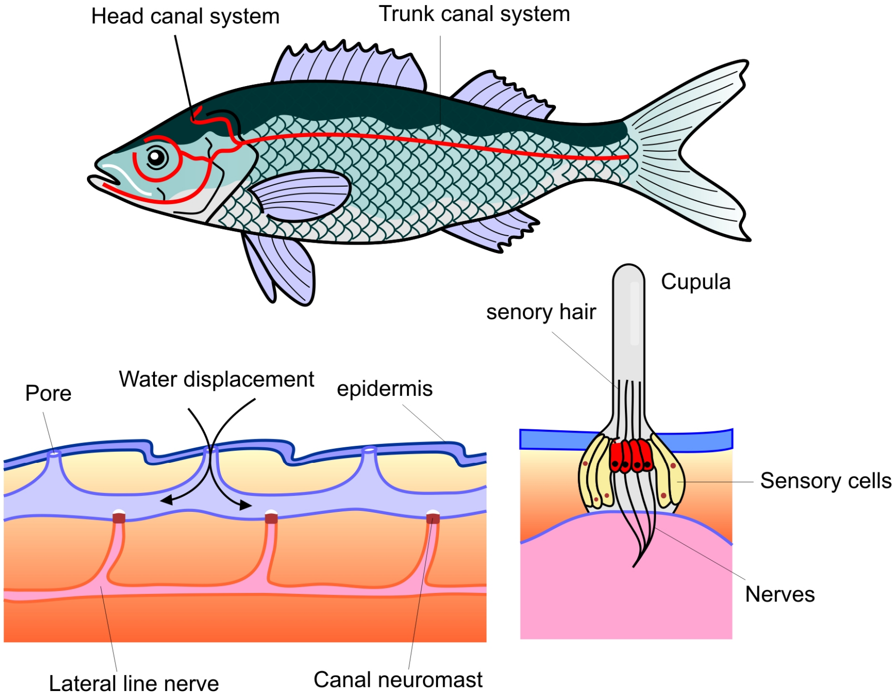

Figure 5.1: Schematic representing the LLS in fish [Izadi 2011].

5.3 Artificial lateral-line system

The biomimetic approach has gained ample attention driven by the desire to understand nature and make capable sensory systems matching the performance of their counterparts in nature [Ozaki et al., 2000 & Dijkstra et al., 2005]. The target is to translate the LLS into technology by investigating its operation principle, characteristic features, e.g. the details which need to be clarified from/about moving objects, and the methodology of processing these stimuli. When succeeding, this can lead to better equipped robots able to orient themselves and detect objects in noisy-dark environments either in water or in air.

Several attempts have been reported in literature to make artificial lateral-line system (ALLS) [Fan et al., 2002, MacIver et al. 2004 & Franosch et al. 2010]. Z. Fan et al. has made ALLS by fabricating hair flow-sensors using MEMS technology. J.-M.P. Franosch et al. have developed an ALLS prototype with a single hot-thermistor anemometric sensor positioned onto an under-water robotic system [Franosch et al.; 2010]. They experimentally showed its ability to avoid under-water objects by measuring the magnitude of flow velocity changes, which depends on the distance to an obstacle.

5.4 Dipole-field model

In literature, theoretical models were presented to investigate and describe the interactions between the lateral-line organ and the surrounding fluid by applying and solving the Navier-Stokes equation [Acheson 1990 & Goulet et al., 2008] according to:

$$\frac{\partial \vec{V}}{\partial t} + \left(\vec{V} \cdot \nabla\right)\vec{V} = -\frac{\nabla P}{\rho} + \nu \Delta \vec{V} + \vec{g} \tag{5.1}$$

where $\vec{V}$ is the fluid velocity, P the pressure, ρ the fluid density, $\vec{g}$ the acceleration of the fluid due to gravity and v the kinematic viscosity.

With the assumptions of incompressibility ($\nabla \cdot \vec{V} = 0$) and the no-slip boundary condition the fluid velocity vanishes at the surface of the body. With low viscosity fluids (like water or air), viscosity has only an effect in a small boundary layer. Outside the boundary layer the dissipative term in the Navier-Stokes equation vanishes ($\nu \Delta \vec{V} = 0$) and Euler's equation is applied as in eq. 5.2 (more details can be found in [Lamb 1932 & Acheson 1990]. These assumptions are valid here since we have sufficiently large Reynolds number (the dimensionless relation between inertial and viscous forces, e.g. for a sphere of 0.1 m diameter and a velocity of 0.2 m/s one finds an associated Reynold's number of about 1500>>1 which generates a boundary layer of about 1.2 mm thick) [Goulet et al., 2008].

$$\frac{\partial \vec{V}}{\partial t} + \left(\vec{V} \cdot \nabla\right)\vec{V} = -\frac{\nabla \vec{P}}{\rho} + \vec{g} \tag{5.2}$$

Together with the mass conservation equation ($\nabla \cdot \vec{V} = 0$) and the boundary condition $\vec{n} \cdot \vec{V} = 0$ (where $\vec{n}$ is the unit normal vector outward to the boundary) at the body surface, Euler's equation is sufficient to determine the motion for incompressible flows.

Since the characteristics of dipole sources are well-known from literature [Lamb 1932], a vibrating sphere generating a dipole velocity field can be conveniently used to analyze object-sensor array interactions. In an ideal fluid, a sphere vibrating parallel (//) with a linear array line, as indicated in Figure 5.2, generates a flow velocity with components in the *x* and *y* directions with amplitudes [Franosch et al., 2005 & Goulet 2010]:

$$V_{//}(x) = V_{x}\left(x\right) = s\,\omega a^{3}\,\frac{\left(2x^{2} - D^{2}\right)}{\left(x^{2} + D^{2}\right)^{5/2}} \tag{5.3}$$

$$V_{\perp}(x) = V_{y}\left(x\right) = s\,\omega a^{3}\,\frac{D\,x}{\left(x^{2} + D^{2}\right)^{5/2}} \tag{5.4}$$

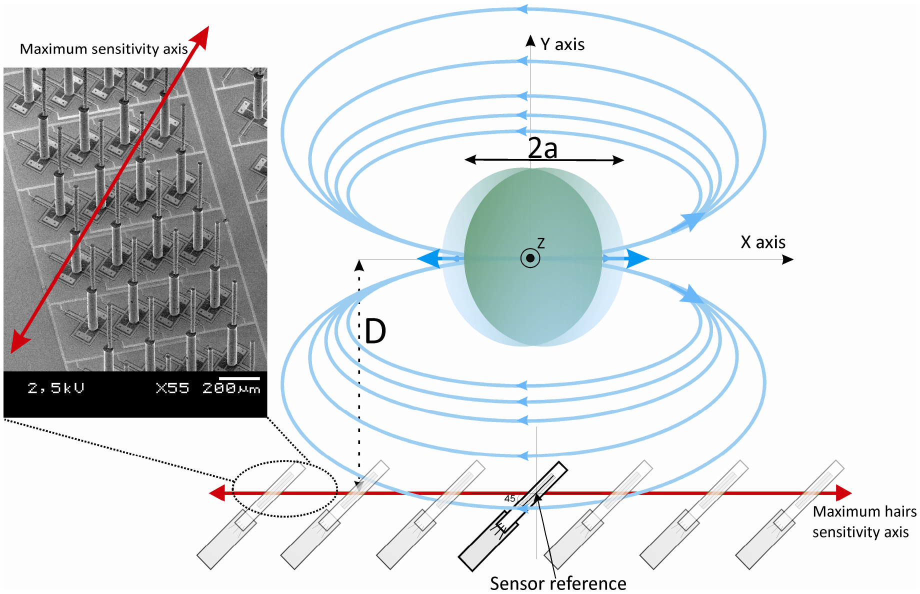

Figure 5.2: Sketch for the dipole velocity field and measurements setup. The maximum sensitivity axis of the hair sensor is aligned to be parallel with the *x*-axis.

where ω is the angular vibration frequency, a is the sphere radius, s is the sphere displacement amplitude and D is the distance between the centre of the sphere and sensor reference line (*x-axis*). Figure 5.3 shows the parallel and the perpendicular velocity components at the position of the LLS as typical receptive field plots.

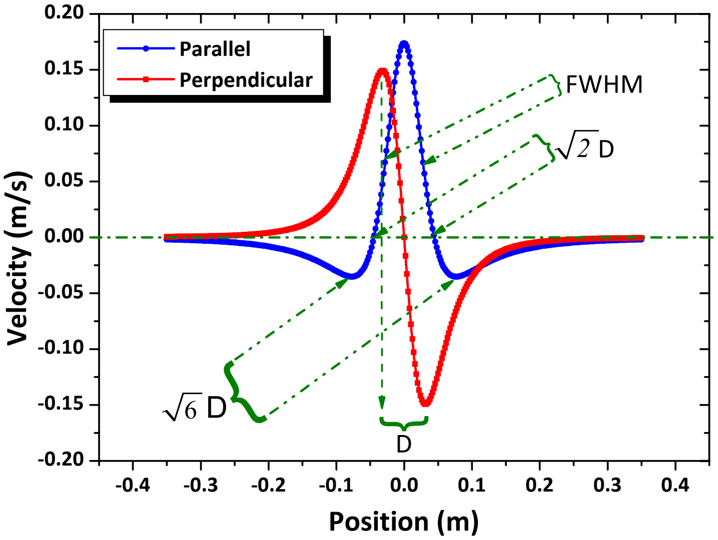

Figure 5.3: Simulated amplitudes of the velocity field of a dipole vibrating parallel with the *x*-axis as function of sensor position along the LLS (*x*-axis). The parallel component (along the *x*-direction, blue) and perpendicular component (along the *y*-direction, red line) are plotted. The LLS to dipole source distance (*D*) is encoded in the characteristic points of the dipole field (maxima-minima peak distance for the perpendicular component and distance between zero-crossing points for the parallel component).

The motivation here is to develop an ALLS which mimics the retrieval of sensory information as obtained by the lateral-line of fish and provides the same possibilities for source localization (despite the fact that the mechanism of source localization in fish may be different). The ability of our hair flow-sensors to measure the projection of the dipole flow field at positions along the ALLS is examined by the accuracy of localization of a vibrating dipole source. A vibrating sphere was used to represent the dipole source. Two techniques based on the characteristic points of the dipole field and ASP (represented by beamforming) are used to perform dipole source localization. In the following sections, we will discuss the implementation of these localization techniques in conjunction with our ALLS.

5.5 Dipole source localization

The function and operation of the LLS is not completely known but it is believed that with the LLS fish have the ability to sense their own movement, track positions of other animals within a distance proportional to their body-length (with low frequency range of 100 Hz or less), sexual communications and avoid collisions (e.g. in schooling). Biologists and bio-physicists try to understand the processes of source localization by the LSS through various hypotheses [Franosch et al., 2005]. One of these hypotheses is based on observing the flow field generated by a harmonic dipole source and by determination of the characteristic points of the flow field. E.g. the distance between a flow-sensor array and a dipole source is encoded in the distance between these characteristic points. To use this method to determine the source position it has to be positioned within the range of the LLS while maintaining sufficient signal-to-noise ratio (SNR).

From Figure 5.3 we see that the dipole velocity profile is characterized by three peaks separated by two 180^{o} phase shifts for the parallel component plot while the perpendicular component plot has two sequential peaks separated by a 180^{o} phase shift. The velocity components uniquely encode the distance to the source irrespective of the fluid properties, vibration frequency, amplitude, direction and dimensions of the moving object [Franosch et al., 2005]. Inspection of equation (5.3) and (5.4) shows that:

- The two x values for which $V_{x,//}(x) = 0$ are equal to $\pm D/\sqrt{2}$;
- The two x values at the Full-Width Half-Maximum (FWHM) of $V_{x,//}(x)$ are equal to $\pm D/\sqrt{7}$;
- $V_{x,//}(x)$ has three extrema: one maximum at $x = 0$ and two minima at $\pm D/\sqrt{2/3}$[1];
- $V_{x,\perp}(x)$ has two extrema, a maximum and a minimum at $\pm D/2$.

Hence the distance D can be determined in various ways: for $V_{x,//}$ the distance between the two zeros equals $\sqrt{2}\,D$, the distance of the FWHM equals $\sqrt{7/4}\,D$ and the distance between the two minima is $\sqrt{6}\,D$, while for $V_{x,\perp}$ the distance between the maxima and minima equals D. Depending on the SNR and orientation of the sensors relative to the source the most accurate method can be chosen. The separating space between the sensors should be small enough to faithfully determine position of the characteristic points, especially for short distances to the source. Therefore, to detect the source using the velocity pattern measured by the ALLS, the following condition has to be fulfilled:

---

[1] Private communication

$$2d < \frac{2D}{\sqrt{2}} < L \Rightarrow \sqrt{2}\,d < D < \frac{L}{\sqrt{2}} \tag{5.5}$$

where d is the spacing between the ALLS sensors and L is the LLS length.

5.5.1 Dipole field over sensor array

Previously, we have demonstrated (see chapter 2) that hair sensors consisting of 124 spatially distributed hairs (31 rows by 4 columns aligned in 45° with the x-axis) connected in parallel to increase capacitance changes. Therefore, the projection of the velocity field as detected by each single hair on the chip is slightly different and the average of overall projections represents the overall chip response. Therefore, the flow velocity field generated by a dipole source and projected on the hair-sensor chip is investigated and modelled.

An array of hair sensors is shaped linearly to construct an ALLS (see Figure 5.2). The flow velocity field is calculated (based on eq. 5.3 and eq. 5.4)[2] at the position of each single hair on the chip and the output is plotted as function of position along the ALLS. The source-distance is determined based on the characteristic points of the detected velocity fields as illustrated in Figure 5.3. The simulations show that averaging the detected fields by various elements within a single chip can be represented by the field located at its centre as illustrated in Figure 5.4a and Figure 5.4b. The estimated distance represents the distance separation between the dipole centre and centre of the sensor-array.

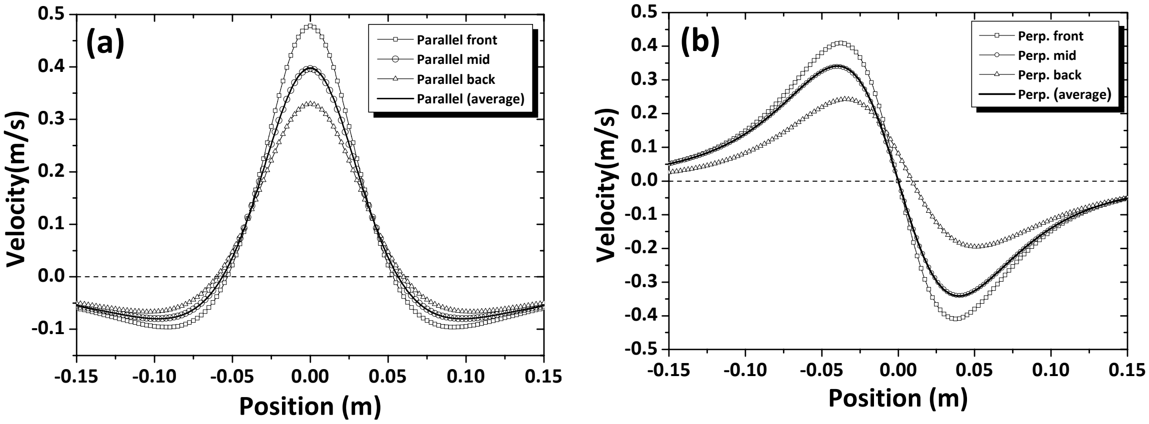

Figure 5.4: Amplitudes of the velocity fields ($V_x(x)$) at the front, mid and back of the sensor-array compared with the average of dipole field detected by 124 hairs on the same chip array using the same vibration conditions for the (a) parallel (b) perpendicular field components.

5.5.2 Experimental setup

In this section, an artificial-hair flow-sensor was used as the basic element of the ALLS. The fabrication process of the hair-sensor is described in chapter 2. A sphere was attached to a mini-shaker (PASCO Model SF-9324) via a stainless steel shaft to form the

---

[2] Note that in this approach any viscous coupling between the sensors is neglected.

dipole source. The flow sensor was fixed to a motorized single-axis stage and shifted in discrete steps to construct a virtual lateral-line with experimentally controlled distance *D* from the centre of the sphere. A lock-in amplifier was used for measuring the output voltage of the hair sensor and its phase relative to the dipole source actuation signal. The virtual lateral-line was subjected to a sinusoidal oscillating flow and aligned to localize the source in two dimensions. The maximum sensitivity axis of the flow sensor was first aligned parallel with the dipole vibration axis in order to measure the parallel velocity-field component. Subsequently it was aligned perpendicular to the dipole vibration axis to measure the perpendicular component. The measurement at each sensor position was carried out over an acquisition time of 3 seconds unless other values are mentioned. A theoretical model (described above) was used to calculate the velocity fields at the position of the sensor. The model was fitted to the experimental velocity field and the field parameters were extracted and used to localize the dipole source. The experimental setup, the definition of distance *D* and the reference coordinate points at the sensor and sphere positions are shown in Figure 5.2.

5.5.3 Results

The model predictions were confirmed by the experimental data. Typical dipole velocity-fields (the parallel and perpendicular components) at a distance of $D = 0.056$ m (theoretical fit and measurements) are shown in Figure 5.5. The measured phase for the parallel and perpendicular velocity components generated by a vibrating sphere is shown in Figure 5.6.

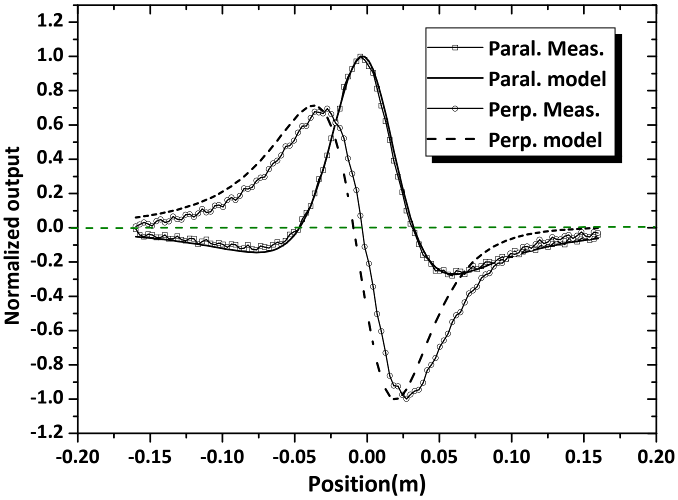

Figure 5.5: Amplitudes of the typical parallel and perpendicular components of the dipole velocity-field (measured and simulated) at a distance of D= 0.056 m. The simulations were fitted to the measurements by varying the angle between the source vibration axis and maximum sensitivity axis of the sensor.

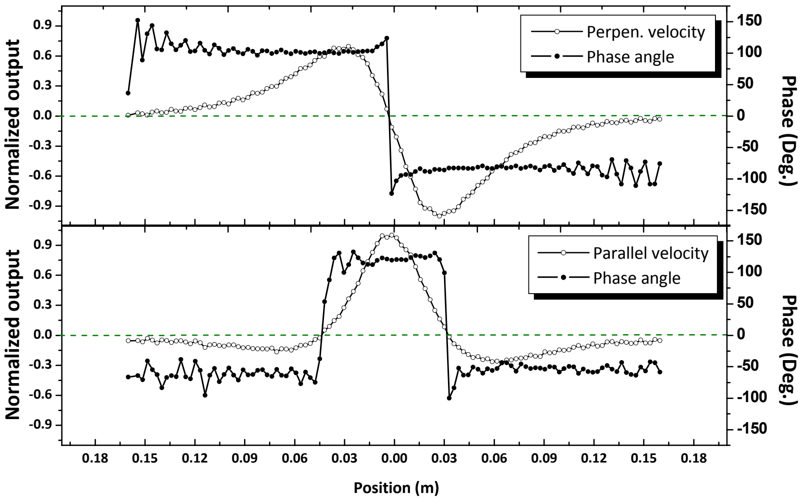

Figure 5.6: The measured phase of the parallel and perpendicular velocity component generated by a vibrating sphere. The phase measurements represent the relative phase between the sensor output and the actuation signal of the sphere.

We investigated the effect of different source parameters (i.e. source vibration frequency and sphere diameter) on the detected parallel components at constant *D*. The velocity amplitude displays a maximum at the position closest to the source and gradually decreases while decreasing the vibration frequency and/or sphere diameter, as shown in Figure 5.7. However, the positions of the characteristic points do not noticeably change. Additionally, the detected parallel profile has shown asymmetry (see section 5.5.4). Figure 5.7 shows the parallel velocity profiles at different vibration conditions.

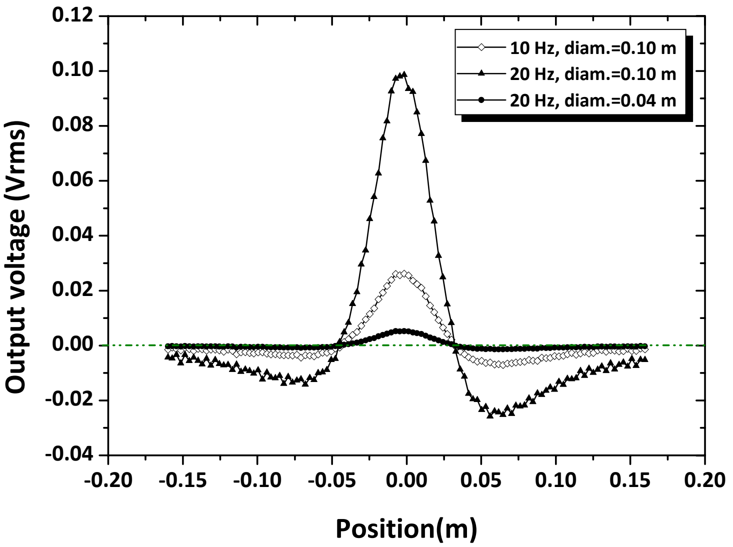

Figure 5.7: Effect of the source vibration frequency and sphere diameter on the detected parallel velocity components.

The influence of variations in *D* on the characteristic points is illustrated in Figure 5.8. The velocity amplitude decreases while increasing the distance to the source.

Additionally, the distance between the zero-crossing points varies while modifying the source to ALL distance. This confirms that *D* is the only parameter that affects the distance between the characteristic points allowing to determine the source-ALL distance using the velocity field as detected by the ALL system.

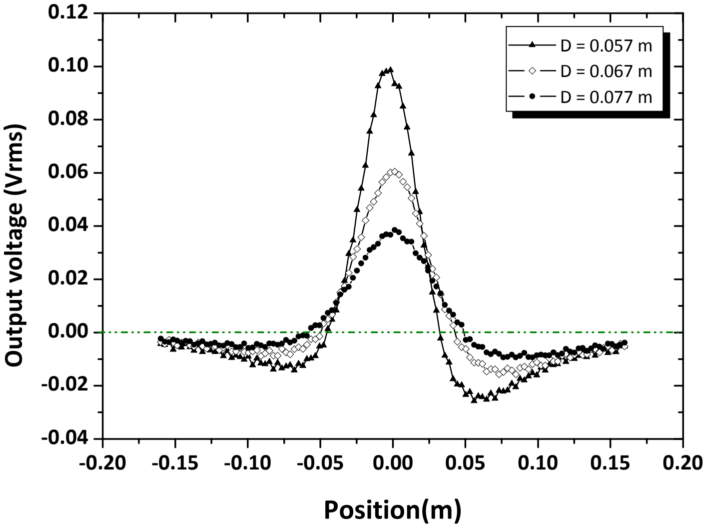

Figure 5.8: Amplitude of the parallel component of the velocity field while varying *D* and maintaining other source vibration conditions constant.

We plotted the estimated distance (D_{est}) as function of *D*. A linear relationship (shown in Figure 5.9) between *D* and D_{est} is obtained for varying vibration conditions. The procedure was done on the parallel component of the velocity field but is also applicable to the perpendicular component with D_{est} the distance between the peaks of the perpendicular velocity component.

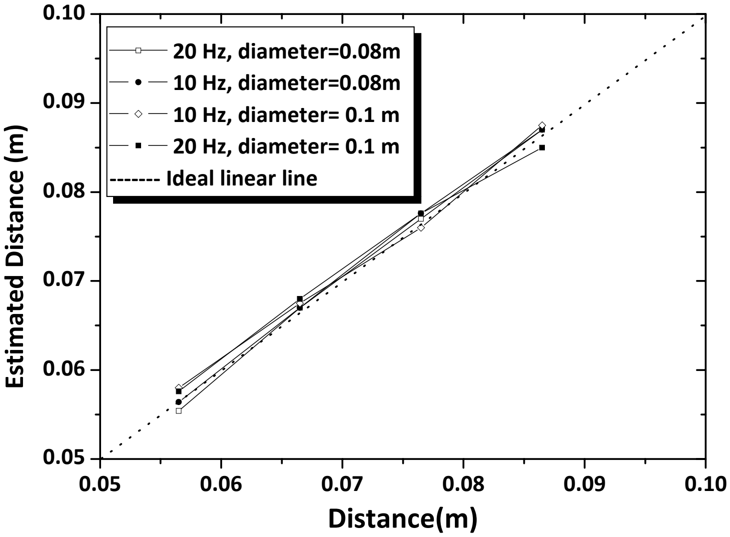

Figure 5.9: Ideal linear relation (dotted line) and measured relation between *D* and D_{est} for different vibration conditions showing the unique dependence between *D* and the characteristic points of the velocity fields.

The maximum detection range ($D_{\max}$) of the virtual lateral-line has been investigated. Using different operation bandwidths[3], the amount of noise was measured at the output of the hair flow-sensor and then used to determine $D_{\max}$ (i.e. by means of SNR). Two criteria have been used to determine $D_{\max}$ i.e. the x values at the FWHM and the x values at the minima. Accordingly, $D_{\max}$ is defined as the D value for which the output of the virtual lateral-line are just equal to the noise level (its SNR equals 1). Thereby, the x-coordinates of the FWHM or of the two minima determine D. The results show that up to D = 0.36 m we were able to detect the vibrating dipole source at a bandwidth of 10 Hz with 0.05 m sphere radius vibrating with an amplitude of 3 mm at 20 Hz. When increasing the operational bandwidth from 10 Hz to 1 kHz the detection range gradually decreases, due to the reduction in the SNR. The detection range as a function of bandwidth is useful in determining the thresholds of the lateral-line system (see table 5.1). Figure 5.10 shows the amplitude of the parallel velocity component measured at different source-sensor distances and the noise level at various bandwidths.

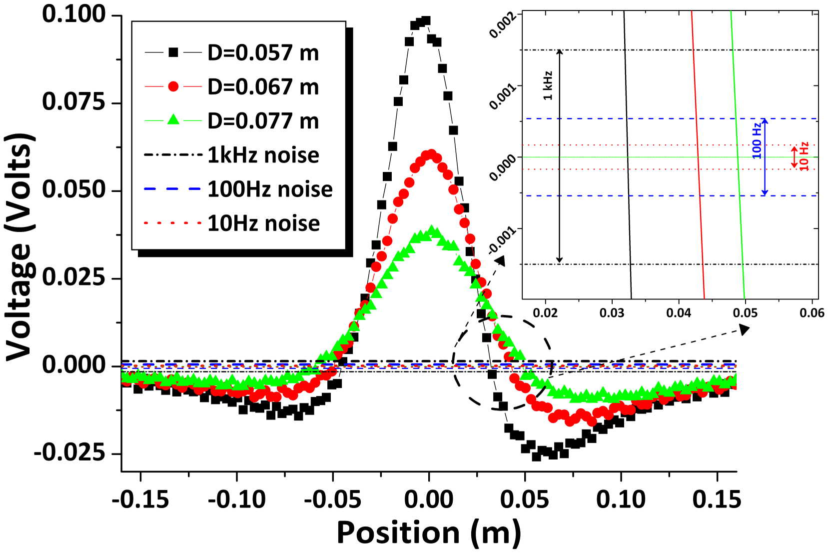

Figure 5.10: Response of hair sensor to the amplitude of the parallel velocity component at different source-ALL distance and with the noise level as measured at different bandwidth.

Table 5.1: Maximum detection range ($D_{\max}$) and normalized to the ALLS body-length (i.e. 0.32 m) determined using different methods at different bandwidths.

	D			*D* normalized to ALLS length		
Bandwidth	10 Hz	100 Hz	1 kHz	10 Hz	100 Hz	1 kHz
FWHM	0.36 m	0.26 m	0.17 m	1.12	0.81	0.53
Two minima	0.24 m	0.17 m	0.11 m	0.75	0.53	0.34

---

[3] The bandwidth represents 1/acquisition time e.g. an acquisition time of 1 ms represents 1 kHz bandwidth.

5.5.4 Discussion

We have shown the ability of our flow sensor to faithfully measure the velocity field generated by a dipole source. Using the flow sensor in a virtual lateral-line, it was possible to accurately detect the parallel as well as the perpendicular velocity components and therefore to determine the source-ALLS distance. We investigated the effect of different field parameters to determine the requirements for the distance estimation using both the modelled and experimental results. The results illustrate that the dipole-source position is encoded in the velocity field along the (virtual) lateral-line system. The sphere radius, vibration amplitude and frequency have no influence on the characteristic points of the velocity field and hence the source localization procedure is relatively robust. The distance from the source is the only parameter determining the characteristic points of the velocity field with a maximum detection range of 0.36 m measured using a bandwidth of 10 Hz.

The precision of the source localization is dependent on the determination of the characteristic points (i.e. peak magnitudes and zero crossings) and whether there is a sufficient SNR to result in reliable measurements. Additionally, we observed an asymmetry in the parallel and perpendicular component plots. This asymmetry can be due to the non-zero angle between the vibration axis of the sphere and the sensitivity axis of the hair sensor. The non-zero angle as well as the field disturbance cause partial addition of the perpendicular component to the parallel component at the sensor position. The origin of this tilting angle (ϑ) could be due to:

(i) non-perfect parallelism between the *x*-axis (i.e. reference axis of the ALLS) and the vibration axis of the sphere;

(ii) an angular shift of the directional sensitivity axis of the hair sensor (see Figure 2.11);

(iii) flow field disturbances resulting from the printed circuit board used for mounting and connecting the flow sensor to the charge amplifier.

The theoretical model was adapted to investigate the angle shift by the partial addition of the perpendicular component to the parallel one at the lateral-line position. The simulations were accurately fitting the flow velocity amplitudes to the measured ones (as shown in Figure 5.5 with fitting error of less than 3 %) for an equivalent tilting angle of 8 ^{o}.

5.6 Beamforming

In the previous sections, we have constructed a virtual ALLS (inspired by the LLS of fish) using a single hair flow-sensor, and used it to localize the position of a dipole source (vibrating sphere). The results show the ability of the hair sensors to faithfully determine the dipole field at the position of the ALLS and localize the position of a dipole source. The characteristic points of the dipole field were used in the source localization. However, this method has some limitations in the estimation of the source position when the flow source is not located alongside the ALLS. As the flow source is positioned beyond the length of the ALLS, the characteristics of the flow field do not appear within the ALLS length and the estimation becomes impossible. Thus, for successful localization the dipole source has always to be located within the length of the ALLS. Additionally, if the zero-crossing of the perpendicular flow-field component is used to determine the lateral source position, limited SNR causes large estimation errors. To overcome these limitations different ASP techniques and algorithms have been considered to estimate the position of the dipole source. The use of some of these (beamforming) techniques can provide high-resolution source localization and is highly appreciated when the source is positioned at the edges of (or even beyond) the ALLS. The following sections provide some theory, modelling and implementation specifics of a beamforming technique as applied to the ALLS.

5.6.1 System model

As part of ASP techniques, beamforming exploits the signal coming from one particular position as it impinges on all array sensors. This concept is used in various communication, voice and sonar applications [Krim et al., 1996]. The signal detected by each sensor is properly weighted, usually employing model-based predictions, and the ensemble signals are used to determine the position of the source.

Figure 5.11 shows a schematic drawing of the ALLS used in combination with a beamforming technique for source localization. In this model, the sensor array is formed by artificial hair sensors positioned in a linear array shape constituting an ALLS similar to the lateral-line in fish. The vibrating sphere represents the dipole source [Harris et al., 1962].

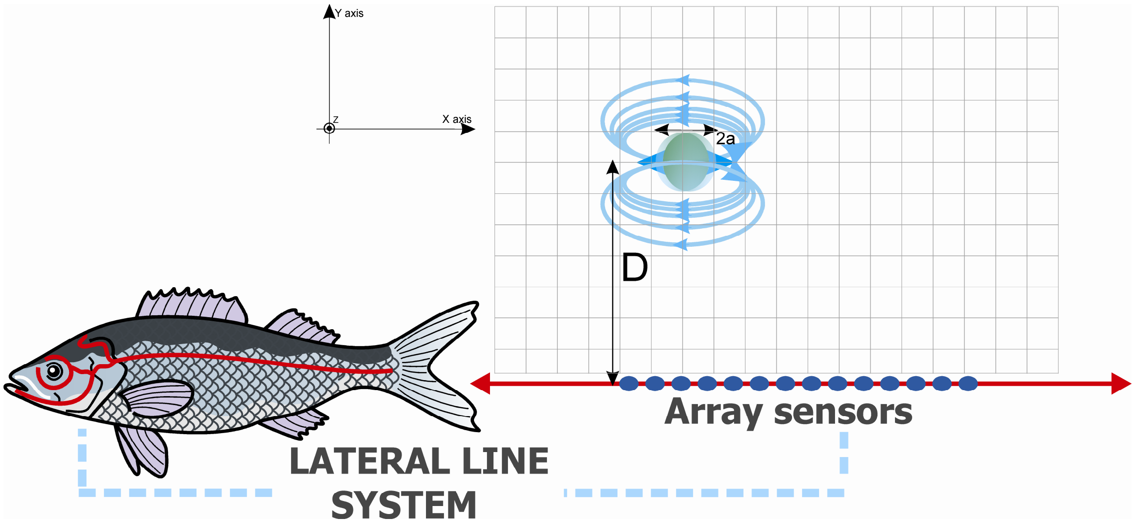

Figure 5.11: Schematic drawing of the ALLS and its source of inspiration used for source localization with a beamforming technique.

The current source-localization algorithm is based on calculation of a template for the anticipated array responses (eq. 5.3) when a dipole-source should be present at one of the many grid points within the area of interest (i.e. the dimension of the template matrix equals the number of grid points where each grid point is composed of a vector representing the array response). All other source parameters (e.g. direction, frequency and amplitude of vibration) were fed into the theoretical model (eq. 5.3) and the velocity amplitude represents its output. The goal is to generate a power image from the template matrix and the ALLS response vector, such that the position of maximum power corresponds with the most likely position of the source.

Once the dipole template is calculated for all possible source locations, the measured array response (**S**) is used to calculate an estimate of the sample covariance matrix ($\hat{\mathbf{R}}$) by calculating the outer product of **S** according to eq. 5.6.

$$\hat{\mathbf{R}} = \frac{1}{N}\sum_{k=1}^{N} \mathbf{S}(t_k)\cdot \mathbf{S}(t_k)^{\mathrm{T}} \tag{5.6}$$

where k represents the sample number at time instant t_k and $\mathbf{S}^{\mathrm{T}}$ is the transpose of **S**. With M the number of hair sensors in the ALLS and N the number of samples, ***S*** is a matrix of $M \times N$ elements in which:

$$\mathbf{S}(t_k)=\begin{pmatrix} S_1(t_k) & S_1(t_k-\Delta t) & \ldots & S_1(t_k-N\Delta t) \\ \vdots & & \ddots & \vdots \\ S_M(t_k) & S_M(t_k-\Delta t) & \cdots & S_M(t_k-N\Delta t) \end{pmatrix}$$

The advantage is that the correlation matrix can be considered as a spatial filter which annihilates signals from positions where the source is not physically positioned [Qureshi et al., 2007]. The estimation accuracy of the covariance matrix can be improved and made less sensitive to noise when it is performed and averaged over N samples. The covariance matrix has $M \times M$ elements in which each single element represents the sum of the cross-correlations between the sensor signals for different samples and with the autocorrelations at the diagonal of the matrix.

Once $\hat{\mathbf{R}}$ is computed, a beamforming technique based on Capon's algorithm [Capon 1969 & Stoica et al., 1995] is used. The concept of this algorithm is that for each position over the area of interest, a weighting vector ($\boldsymbol{\Psi}_{xy}$) is applied to the sensor data. The $\boldsymbol{\Psi}_{xy}$ is determined in such that the optimal solution to recover the source signal due to its position and decrease effect of noise and other positions will be [Lorenz et al., 2005]:

$$\Psi_{xy} = \frac{\mathbf{R}^{-1}\mathbf{A}_{xy}}{\mathbf{A}_{xy}^{\mathrm{H}}\mathbf{R}^{-1}\mathbf{A}_{xy}} \tag{5.7}$$

where $\mathbf{A}_{xy}$ denotes the theoretical array response (steering vector) to a dipole source positioned at coordinates x,y as calculated from the source model in eq. 5.3 and $\mathbf{A}^{\mathrm{H}}$ is the Hermitian transpose of **A**. The form of the ALLS response template at each grid point (x,y) is a matrix of $M \times 1$ elements in which:

$$\mathbf{A}_{xy} = \left(V_1(x,y), V_2(x,y)\ldots V_M(x,y)\right)^{\mathrm{T}}$$

where $V_M(x,y)$ represents the parallel velocity component of the dipole field (eq. 5.3) as an output of sensor number M due to the source at grid point position (x,y).

The associated output power (P_{xy}) at each grid point, where the source possibly could be, is calculated according to the following power weighting function:

$$P_{xy} = \frac{1}{\mathbf{A}_{xy}^{\mathrm{H}}\mathbf{R}^{-1}\mathbf{A}_{xy}} \tag{5.8}$$

The resulting power level at each grid point is used to visualize the area of interest i.e. power map. The (x,y) coordinates of the maximum power level represent the most-likely position of the dipole source.

5.6.2 Model performance

Modelling results at different conditions illustrate the application of the beamforming approach, based on Capon's algorithm, to the ALLS. The main target is determining a reliable estimate of the position of the source at varying positions and under different conditions. Figure 5.12 shows a successful localization of the dipole for two source positions within the area of interest. The results clearly show that, under favourable conditions, the hair array enables localization of the sphere position by beamforming, whether it is at the centre (Figure 5.12a) or at the edges (Figure 5.12b) of the ALLS. In contrast, using the methods described in section 5.5 [Dagamseh et al., 2010a] the source is only traceable as long as the characteristic points of the flow-field are positioned within the array boundaries.

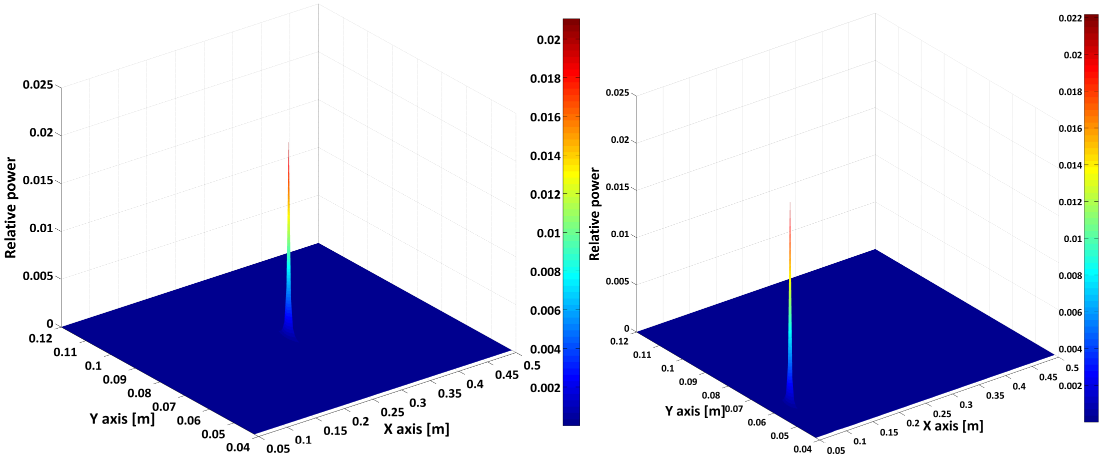

Figure 5.12: Dipole source localization while the dipole source is positioned at the array centre (left) (X_{pos}=0.275 m, Y_{pos}= 0.08 m) and at the array edge (right) (X_{pos}=0.08 m, Y_{pos}= 0.06 m). Eight sensors were assumed to be positioned (relative to the origin (0,0)) at 0.1 m to 0.45 m along the *x-axis* with 5 cm separation distance.

5.6.3 Experimental setup

We implemented and experimentally evaluated the performance of the ALLS (made of discrete artificial hair-sensors) using beamforming techniques. A vibrating sphere (with radius of 0.04 m oscillating with amplitude of 3 mm at 40 Hz) was attached to a mini-shaker (PASCO Model SF-9324) via a stainless steel shaft and used as harmonic dipole source. The sphere position was controlled by a motorized dual-axis stage. The *x-axis* is defined as the direction parallel to the array while the direction orthogonal to the array represents the *y-axis*. A linear array shape was constructed using 8 artificial hair flow-sensors imitating the LLS (much like an array line of superficial neuromast). The array length (body length) was 0.35 m with 5 cm separation distance between array elements (8 sensors are positioned at 0.1 m to 0.45 m relative to the (0,0) origin point). The maximum sensitivity axis for the hair sensors was aligned parallel to the dipole vibration axis to measure the parallel velocity-field component. The direct digital synthesis (DDS) system (see chapter 4) was used for generation of high-frequency (≈1 MHz) carrier signals in order to probe the hair sensors and to demodulate the generated AM signals from each of the array elements. The ALLS was subjected to a sinusoidal oscillating flow and aligned to localize the source in two dimensions. The measurements were carried out at a bandwidth of 300 Hz. A calibration process was conducted to exclude possible mismatches between individual array elements and, hence, the relative amplitudes are maintained. A theoretical model for the dipole source is used to estimate projections of the velocity pattern on the ALLS for each sphere position over the area of interest (needed to create the array response template **A**). The response of the ALLS was fed serially to the computer with 1 kHz rate data-streams for further processing using the MATLAB environment. The Fast Fourier Transform (FFT) amplitude of the sensor signal in windows of 256 samples is used to determine the signal amplitudes at the oscillation frequency of the sphere for each sensor channel. The beamforming technique (discussed above in section 5.6) is applied afterwards to the measurements and a power map is generated for the area of interest. The coordinates with maximum power level predict the sphere position. Figure 5.13 shows a photograph of the experimental setup for source localization using ALLS.

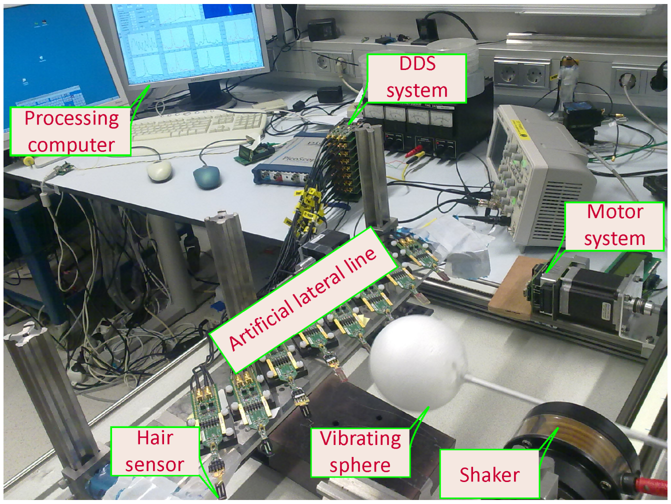

Figure 5.13: A photograph of the measurement setup dedicated to source localization with beamforming.

5.6.4 Results

Off-line measurements

Figure 5.14 shows a normalized representation of a dipole field measurement as detected by the ALLS compared with a normalized representation of the parallel component of the flow as given by the theoretical dipole field. The detected field matches satisfactory with theoretical predictions and is used to localize the dipole source.

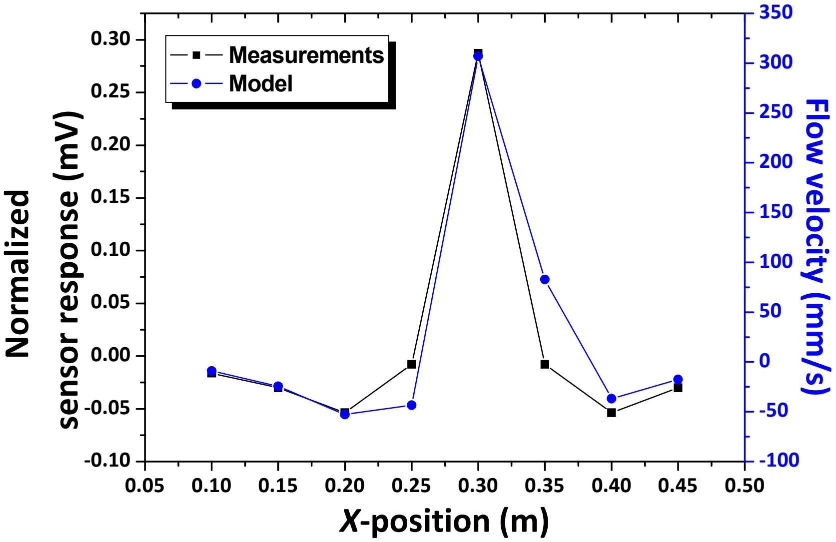

Figure 5.14: Dipole flow field measurements at position of hairs array (as detected by 8 hair-sensors at x= 0.3 m, D=0.068 m) versus theoretical model.

Afterwards the array responses were fed in an off-line fashion to the beamforming model discussed above. The results (Figure 5.15) show the possibility to faithfully determine the dipole field components at the position of the hair-sensor array, when arranged as ALL. The accuracy of the field detection is examined by the amount of error in the source localization. Figure 5.15 illustrates the prediction of the dipole source position (for the data presented in Figure 5.14) using the ALLS and the beamforming method.

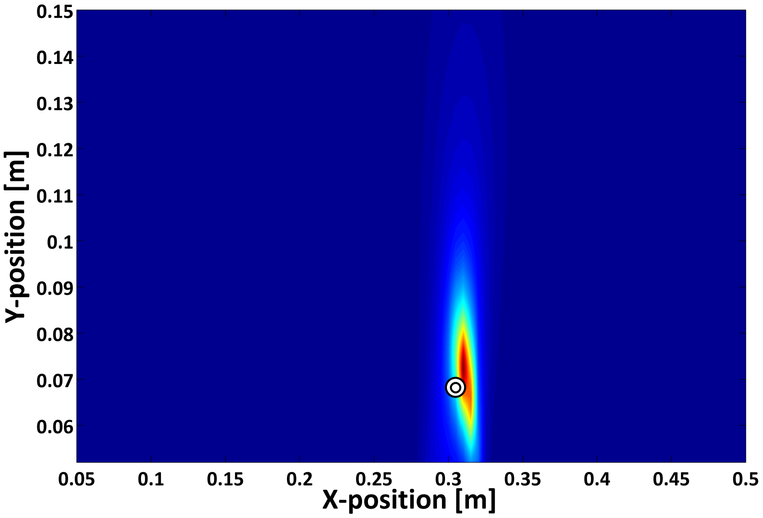

Figure 5.15: Dipole source localization using ALLS. Source positioned at x=0.3 m, D=0.068 m (indicated by the circle) and the estimated position is x_{est} = 0.31 m, D_{est}= 0.072 m. The red area indicates the area of increased likelihood of the source position.

Online measurements

Inspired by the lateral-line function in fish, we demonstrated dipole source localization using our hair sensors and Capon's method. A demonstrator was built using the same off-line experimental setup. Eight measurements from the hair sensors were collected and processed on-line with FFT snapshots of 256 samples each. The dipole source was placed at different (x,y) positions along and from the ALLS. Each D_{est} was determined using 3 measurements taken at the same D but at different X-positions along the ALLS (edges and centre). Afterwards, the average of D_{est} was calculated. Figure 5.16 shows a screen snapshot of the Graphical User Interface (GUI) of the demonstrator.

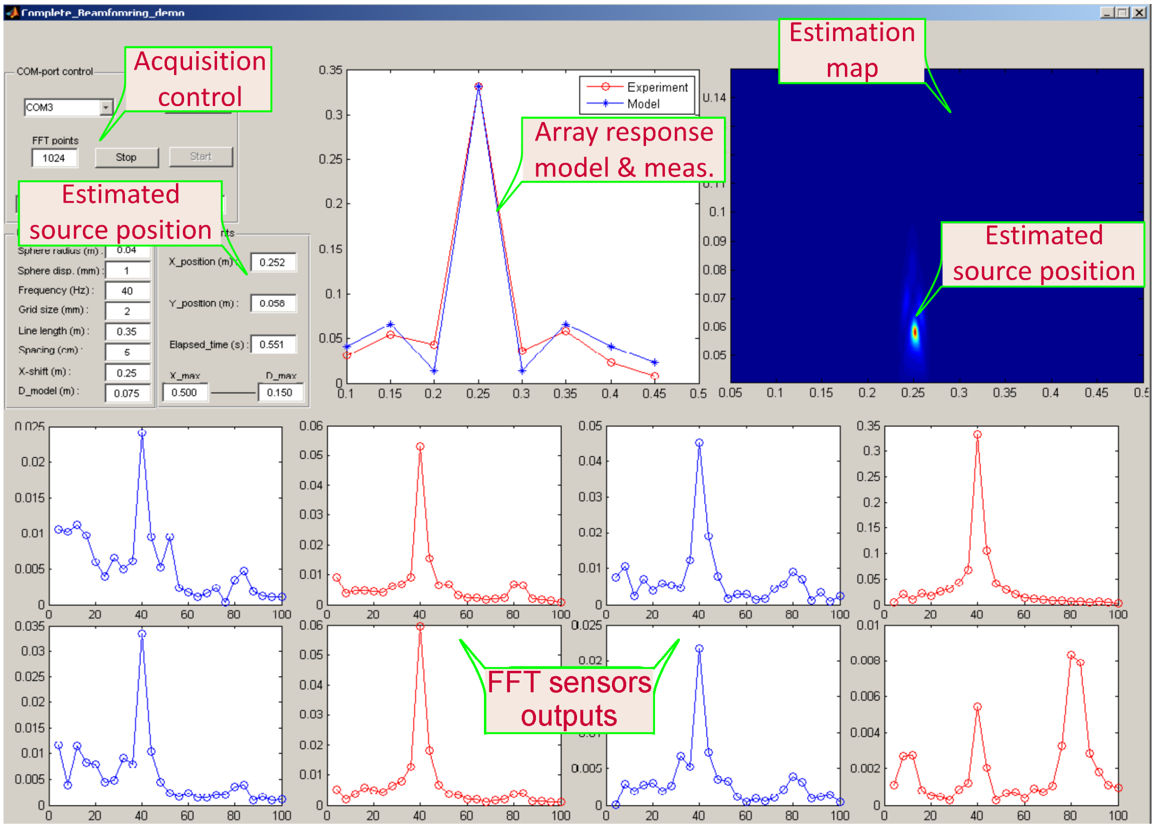

COM-port control: COM3
FFT points: 1024
Sphere radius (m) : 0.04
Sphere disp. (mm) : 1
Frequency (Hz) : 40
Grid size (mm) : 2
Line length (m) : 0.35
Spacing (cm) : 5
X-shift (m) : 0.25
D_model (m) : 0.075
X_position (m) : 0.252
Y_position (m) : 0.058
Elapsed_time (s) : 0.551
X_max: 0.500
D_max: 0.150

Figure 5.16: Screen snapshot representing the GUI of the dipole-source localization demonstrator.

The performance of the demonstrator in terms of position estimation accuracy is assessed by comparison with the real-physically measured distance values (D). The results show that the estimated distances between the sphere and ALLS match the set distance reasonably well. Figure 5.17 shows D_{est} versus D and Figure 5.18 shows the estimation for the x-position of the dipole source along the array with their linear fit lines.

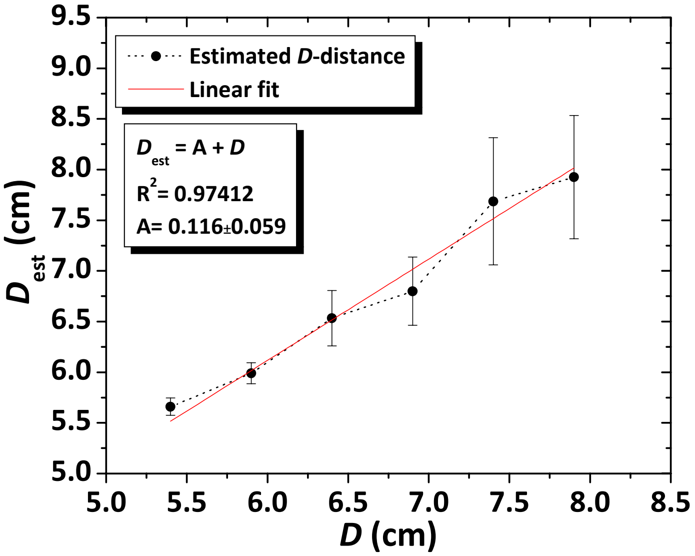

Figure 5.17: Dipole source localization determined using the beamforming technique (dots) and linear fit between *D* and D_{est} (solid line). Error bars represent standard error of the mean[4].

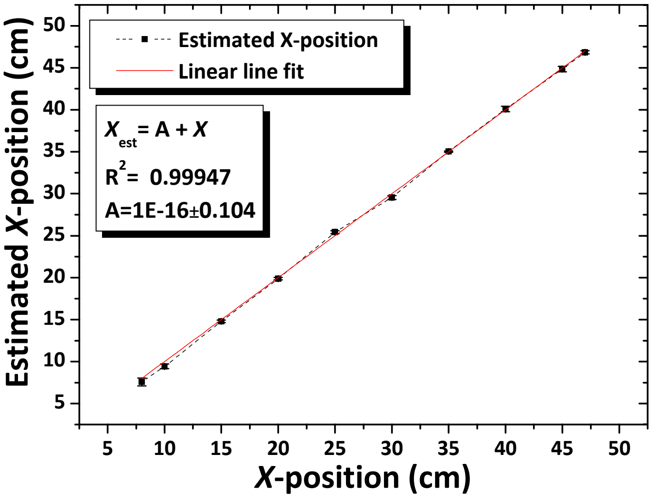

Figure 5.18: Near-linear relation between the actual and predicted *X*-position of the dipole source using beamforming techniques. Error bars represent standard error of the mean.

5.6.5 Discussion

The above results verify the usability of artificial hair-sensor arrays to localize dipole sources and can give insight in localization mechanisms in fish. However, D_{est} shows up to 0.17 cm shift from the set *D*. Estimation uncertainty can partially be attributed to the following factors, which add additional uncertainty to D_{est} and cause deviation from the theoretical model:

- Dissimilarities between individual ALLS elements, attributed to non-perfect matching even after sensors calibration is performed;

---

[4] Standard error of the mean represents the standard deviation of the samples used to determine the mean values.

- The sensor constitution (124 hairs over an area of 10 x 1 mm^2 connected in parallel to increase capacitance changes [Dagamseh et al., 2010b]) causes some blurring, effecting both the directivity and apparent position of the hair-sensor;
- Each D_{est} was determined using the average of 3 measurements taken at different X-positions along the ALLS (edges and centre). This causes uncertainty because the estimation error increases when moving the dipole source from the centre to the edges of the ALLS (Figure 5.19);
- Here, the beamforming technique is performed using 8 hair sensors with 5 cm separations in between. This limits the resolution of the measurements. We believe that increasing the number of sensors potentially improves the performance by providing higher resolution in the power images.

On the other hand, the x-coordinate estimation shows better performance compared to the estimation of the y-coordinate (D). When compared to D_{est}, X_{est} shows up to 0.1 cm shift from the set X. We ascribe this to the large SNR for the sensors neighbouring the x-projection of the main peak of the dipole field (see Figure 5.14). Thus, its contribution in the cost function (eq. 5.8) is large compared with other sensor outputs along the ALLS (see Figure 5.18).

The overall array performance at different x-y coordinates is shown in Figure 5.19 with its 3D representation in Figure 5.20. The array showed an ability to predict position of the dipole source within and outside the dimensions of the ALLS with estimation errors of less than 0.14 body-length at different distances of D. The estimation accuracy significantly improves to less than 0.02 body-length when the sphere is positioned within the length of the ALLS. This clearly confirms the advantage of using such array processing techniques over the characteristic points' technique to localize the dipole source (see section 5.5). This ALLS capability could shed some light on the source localization mechanisms in fish.

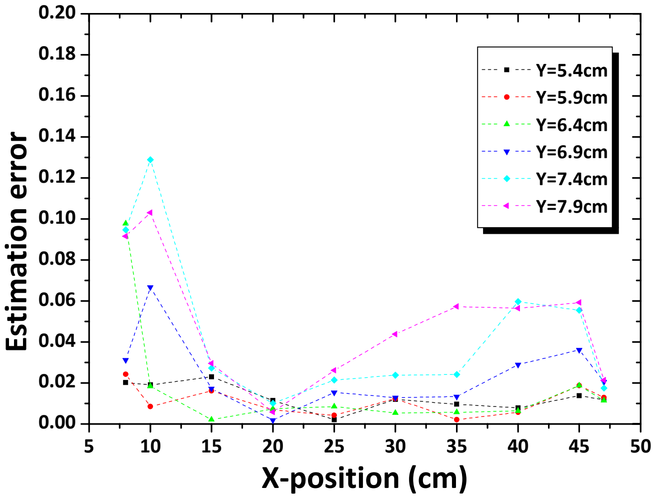

Figure 5.19: Source localization performance as function of source position relative to the ALLS. The absolute estimation error (Error= $[(D-D_{est})^2+(X-X_{est})^2]^{1/2}$) is normalized to the body-length of the ALLS i.e. 0.35 m.

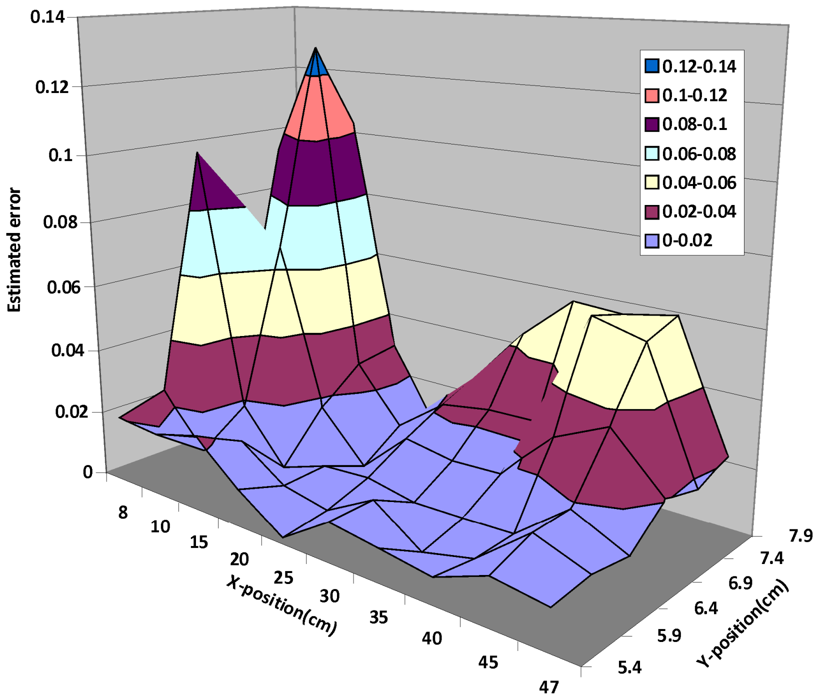

Figure 5.20: 3D representation for the source localization performance for the data presented in Figure 5.19.

5.7 Conclusions

We showed the capability of the hair flow-sensors to faithfully determine flow-velocity of dipole fields. A linear array made of either a virtual lateral-line system or eight artificial hair flow-sensors was used both to imitate the LLS in fish, exploiting the characteristic points of the flow-field, and beamforming techniques. Array signal processing in combination with an ALLS shows the possibility to localize positions of dipole sources very well even at the edges or outside of the ALL length while maintaining high robustness. Multi lateral-line structures can be oriented in different directions for 3D source localization. Additionally, simultaneous measurement of the parallel and perpendicular flow-velocity components opens possibilities to extract more information about the source and better localization especially for non-zero sensor-source angles. Once this is accomplished, pattern recognition techniques can be used to identify sources, phenomena and activities using spatial-temporal flow distributions.

5.8 Reference

[Acheson 1990] Acheson, D. (1990) “Elementary fluid dynamics”, Oxford university press, Oxford.

[Albert et al., 2001] Albert, J.T., Friedrich, O.C., Denchant, H.E. & Barth, F.G. (2001) “Arthropod touch reception: Spider hair sensilla as rapid touch detectors”, Journal of

Comparative Physiology-A Sensory, Neural, and Behavioral Physiology, 187, pp. 303–312.

[Atmoko et al., 2008] Atmoko, H., Tian, D.C., Tian, G.Y. & Fazenda, B. (2008) “Accurate sound source localization in a reverberant environment using multiple acoustic sensors”, Meas. Sci. Technol., 19, art. no. 024003.

[Blake et al., 2006] Blake, B.C. & van Netten, S.M. (2006) “Source location encoding in the fish lateral-line canal”, Journal of Experimental Biology, 209, pp. 1548–1559.

[Brandes et al., 2007] Brandes, T.S. & Benson, R.H. (2007) “Sound source imaging of low-flying airborne targets with an acoustic camera array”, Appl. Acous., 68, pp. 752–765.

[Capon 1969] Capon, J. (1969) ”High-resolution frequency-wavenumber spectrum analysis”, In proceedings of the IEEE, 57, pp. 1408–1418.

[Coombs 2001] Coombs, S. (2001) “Smart skins: information processing by lateral-line flow sensor”, Autonomous Robots, 11, pp. 255–261.

[Dagamseh et al., 2010a] Dagamseh, A.M.K., Lammerink, T.S.J., Kolster, M.L., Bruinink, C.M., Wiegerink, R.J. & Krijnen, G.J.M. (2010) ”Dipole-source localization using biomimetic flow-sensor arrays positioned as lateral-line system”, Sensors and actuators A: Physical, 162, pp. 355–360.

[Dagamseh et al., 2010b] Dagamseh, A.M.K., Bruinink, C.M., Droogendijk, H., Wiegerink, R.J., Lammerink, T.S.J. & Krijnen, G.J.M. (2010) “Engineering of Biomimetic Hair-Flow Sensor Arrays Dedicated to High-Resolution Flow Field”, In proc. of IEEE sensors, Hawaii, USA, pp. 2251–2254.

[Dijkgraaf 1963] Dijkgraaf, S. (1963) “The functioning and significance of the lateral-line organs”, Biological Reviewers, 38, pp. 51–105.

[Dijkstra et al., 2005] Dijkstra, M., Van Baar, J.J., Wiegerink, R.J., Lammerink, T.S.J., De Boer, J.H. & Krijnen, G.J.M. (2005) “Artificial sensory hairs based on the flow sensitive receptor hairs of crickets”, J. Microelectronics and Microengineering, 15, pp. S132–S138.

[Dowling et al., 1992] Dowling, E.M., Linebarger, D.A., Tong, Y. & Munoz, M. (1992) “An adaptive microphone array processing system”, Microprocessors and Microsystems, 16, pp. 507–516.

[Fan et al., 2002] Fan, Z., Chen, J., Zou, J., Bullen, D., Liu, C. & Delcomyn, F. (2002) “Design and fabrication of artificial lateral-line flow sensors”, Journal of Micromechanics and Microengineering, 12, pp. 655–661.

[Franosch et al., 2005] Franosch, J-M.P., Sichert, A.B., Suttner, M.D. & Van Hemmen, J.L. (2005) “Estimating position and velocity of a submerged moving object by the clawed frog Xenopus and by fish”, Biological Cybernetics, 93, pp. 231–238.

[Franosch et al., 2010] Franosch, J.-M.P., Sosnowski, S., Chami, N.K., Kühnlenz, K., Hirche, S. & Van Hemmen, J.L. (2010) "Biomimetic lateral-line system for underwater vehicles", In 9th IEEE Sensors Conference, Waikoloa, Hawaii, pp. 2212–2217.

[Goulet et al., 2008] Goulet, J., Engelmann, J., Chagnaud, B.P., Franosch, J.-M.P., Suttner, M.D. & Van Hemmen, J.L. (2008) "Object localization through the lateral-line system of fish: Theory and experiment", Journal of Comparative Physiology A: Neuroethology, Sensory, Neural, and Behavioral Physiology, 194, pp. 1–17.

[Goulet 2010] Goulet, J. (2010) "Information processing in the lateral-line system of fish", Ph.D. thesis, Technical university Munich, Germany.

[Harris et al., 1962] Harris,G. & Van Bergeijk, W. (1962) ”Evidence that the lateral-line organ responds to near-field displacements of sound source in water”, The journal of the acoustical society of America, 34, pp. 1831–1841.

[Haupy 2010] Haupy, R.L. (2010) “Antenna arrays: a computational approach”, John Wiley & Sons.

[Ishi et al., 2009] Ishi, C.T., Chatot, O., Ishiguro, H. & Hagita, N. (2009) "Evaluation of a MUSIC-based real-time sound localization of multiple sound sources in real noisy environments", IEEE/RSJ International Conference on Intelligent Robots and Systems, pp. 2027–2032.

[Izadi 2011] Izadi, N. (2011) “Bio-inspired MEMS Aquatic Flow Sensor Arrays“, Ph.D. thesis, University of Twente, Enschede-The Netherlands.

[Krim et al., 1996] Krim, H. & Viberg, M. (1996) ”Two decades of array signal processing research: the parametric approach”, IEEE signal processing magazine, 13, pp. 67–94.

[Lamb 1932] Lamb, H. (1932) “Hydrodynamics”, 6th ed., Cambridge University Press, Cambridge.

[Lorenz et al., 2005] Lorenz, R.G. & Boyd, S.P. (2005) "Robust minimum variance beamforming", IEEE Transactions on Signal Processing, 53, pp.1684–1696.

[Mochiki et al., 2008] Mochiki, N., Ogawa, T. & Kobayashi, T. (2008) “Ears of the robot: direction of arrival estimation based on pattern recognition using robot-mounted microphones”, IEICE Trans. Inf. & Syst., E91-D, pp. 1522–1530.

[Navrátil et al., 2010] Navrátil, M., Dostálek, P. & Křesálek, V. (2010) "Classification of audio sources using neural network applicable in security or military industry", In proceedings of International Carnahan Conference on Security Technology, pp. 369–374.

[Ozaki et al., 2000] Ozaki, Y., Ohyama, T., Yasuda, T. & Shimoyama, I. (2000) “An air flow sensor modeled on wind receptor airs of insects”, In proceedings of the 13th IEEE international conference on Micro Electro Mechanical Systems, Miyazaki, Japan, pp. 531–536.

[Pirinen et al., 2004] Pirinen, T. & Yli-Hietanen, J. (2004) “Time delay based failure-robust direction of arrival estimation”, In proceedings of the 3rd IEEE Sensors Array and Multichannel Signal Processing Workshop, pp. 618–622

[Qureshi et al., 2007] Qureshi, T.R. & Van Veen, B.D. (2007) "Effects of correlation matrix estimation on correlated source cancellation in beamformers", International Congress Series, 1300, pp. 261–264.

[Radich et al., 1994] Radich, B. & Buckley, K.M. (1994) "Map Estimation of EEG Dipole Source Locations for Head Models with Parameter Uncertainty", Statistical Signal and Array Processing, pp. 413–416.

[Reijniers et al., 2007] Reijniers, J. & Peremans, H. (2007) “Biomimetic sonar system performing spectrum-based localization”, IEEE Transactions on Robotics, 23, pp. 1151–1159.

[Shimozawa et al., 2003] Shimozawa, T., Murakami, J. & Kumagai, T. (2003) “Cricket wind receptors: thermal noise for the highest sensitivity known”, In Sensors and Sensing in Biology and Engineering (ed. : Barth, F.G., Humphrey, J.A.C. & Secomb, T.W.), Springer, Berlin, pp. 145–157.

[Stark et al., 2002] Stark H. & Woods, J.W. (2002) “Probability and random processes with application to signal processing”, Pearson education.

[Stoica et al., 1995] Stoica,P., Handel, P., & Soderstorm, T. (1995) “Study of capon method for array signal processing”, Circuits systems signal process, 14, pp. 749–770.

[Sturzl et al., 2000] Sturzl, W., Kempter, R. & van Hemmen, J.L. (2000) “Theory of arachnid prey localization”, Physical Review Letters, 84, pp. 5668–5671.

[Viberg et al., 1995] Viberg, M., Ottersten, B. & Nehorai, A. (1995) ”Performance analysis of direction finding with large arrays and finite data”, IEEE Transactions on Signal Processing, 43, pp. 469–477.

[Yildiz et al., 2007] Yildiz, G., Duru, A.D. & Ademoglu, A. (2007) “A comparative study of localization approaches to EEG source imaging”, In IEEE/NIH Life Science Systems and Applications Workshop, LISA; Bethesda, pp. 56–59.

Chapter

6

SPATIO-TEMPORAL FLOW PATTERN OBSERVATIONS

For many insects airflow patterns, as observed by means of their hair-sensors, carry highly valuable information exposing the sources of these flows. In this chapter we modelled and measured responses of our biomimetic hair sensors to airflow transients, imitating e.g. the natural spider-cricket attack sequence. The measurements show the hair-sensors' ability to determine the flow field with sufficient temporal and spatial resolution. The shape of the measured flow fields shows strong relation with the shape of a dipole field and is used to estimate the position of the source relative to the hair sensor. The results show good agreement between estimated distance and set distance. This opens possibilities for spatio-temporal flow pattern measurements, using high-density arrays of single-hair sensors. It forms the last step towards a proof of principle of a high-resolution 'flow camera'.

6.1. Introduction

In previous investigations on our hair-sensors the measurements were conducted with hair motion driven by sinusoidal airflows [Dagamseh et al., 2010]. This approach is very convenient to e.g. determine mechanical characteristics and response-functions of the hairs-sensors. However, such measurements do not exactly represent biological airflow stimuli (e.g. motion of spiders) nor is there much information contained in a continuous wave (CW) airflow, which, also in technical applications, is not exactly the intended modus operandi of the hair-sensor arrays. Obviously, without accurate transient response spatio-temporal information would be incomplete and array-measurements would miss-out important flow events. Aerodynamically transient airflows, while carrying much information for insects, pose severe problems for engineers in that they are awkward, if possible at all, to model and offer little possibilities to optimize SNR since the transients are short, wide bandwidth events not allowing narrow filtering.

In nature, there are numerous examples representing transient airflow stimuli such as spider motion [Dangles et al., 2006] and (passing) humming flies [Barth et al., 1995]. In frequency terms they consist of a band of frequencies with relative much low-frequency content superimposed on relative higher-frequency components up to a few 100 Hz, depending on the duration of the transient [Humphrey et al., 2008 & Kant et al., 2009]. During such relative short flow events, the boundary layer may not reach the steady state and hence the instantaneous boundary layer is different than predicted by steady state analysis [Obsorne 1996]. Additionally, in transient events the formation of the boundary layer depends on frequency content and amplitude of the airflow while for sinusoidal flow it depends on frequency only (as long as the Reynolds number is sufficiently low). Using transient airflows, producing spatio-temporal airflow patterns, for measurements is more representative for natural airflow sources. The successful extraction of the characteristics of these patterns will give us insight in their features and information contained in them, possibly revealing the cues that are essential in insect's behavioural patterns.

6.2. Case study: spider motion

It has been shown that in certain spider-cricket[1] predator – prey encounters, crickets are able to detect and escape (most of the time) from running spiders. The airflow patterns produced by spider motion are complex with small-scale high flow velocity content at the legs and more extended flow patterns due to the spider's body [Casas et al., 2008]. The cricket senses, perceives and responds to these airflow patterns efficiently. Spiders use at least two attacking strategies to catch crickets; either they apply an ambush strike or they hunt at high velocity. Figure 6.1 (a) illustrates the airflow field around a running spider as measured by particle image velocimetry (PIV) (from [Casas et al., 2008]).

The group of Casas in Tours has gone a long way in recreating situations relevant to the cricket-spider escape mechanism. They try to generate the airflow produced by spider

---

[1] The spider-cricket interaction studied in (Dangles et al., 2006 and Casas et al., 2008) were concerned with wolf spiders (Pardosa lugubris) and wood crickets (Nemobius sylvestris).

motion using a suddenly accelerated piston [Dangles et al., 2006]. Figure 6.1 (b) shows the airflow pattern generated by their moving cylindrical piston. A nice literature survey of the detection of transient flow fields as generated by approaching predators or moving prey is presented in [Kant et al., 2009].

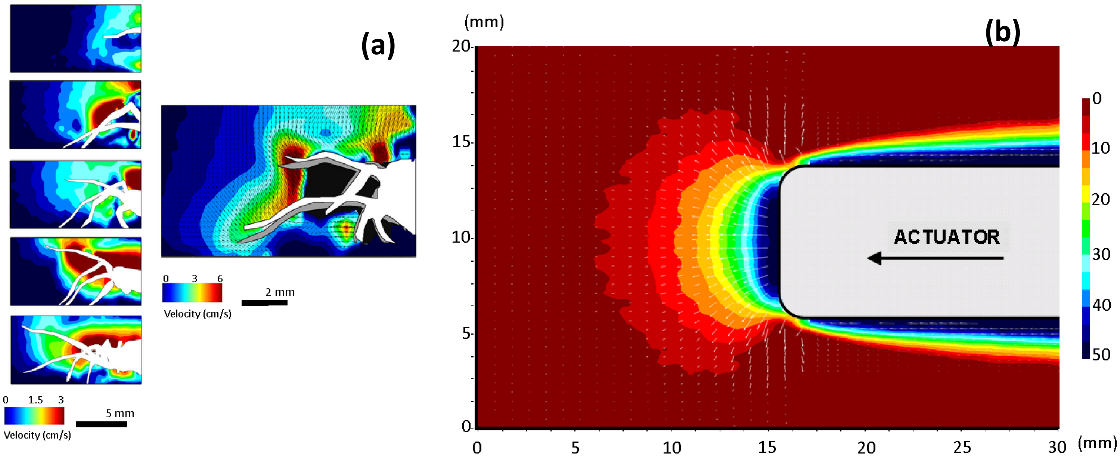

Figure 6.1: Close-up view of airflow velocity field around (a) running spider and (b) suddenly moved cylindrical piston imitating spider motion [Casas et al., 2008].

In this chapter, we investigate the possibility to measure spatio-temporal airflow fields generated by a pulsed-like airflow by means of our artificial hair-sensors and hair-sensor arrays. The artificial hair sensors are exposed to the flow of a moving piston[2] imitating spider motion. In this situation, the flow-field changes with both position and time. Figure 6.2 shows a block diagram representing the biomimetic counterpart of a cricket-spider attack interaction.

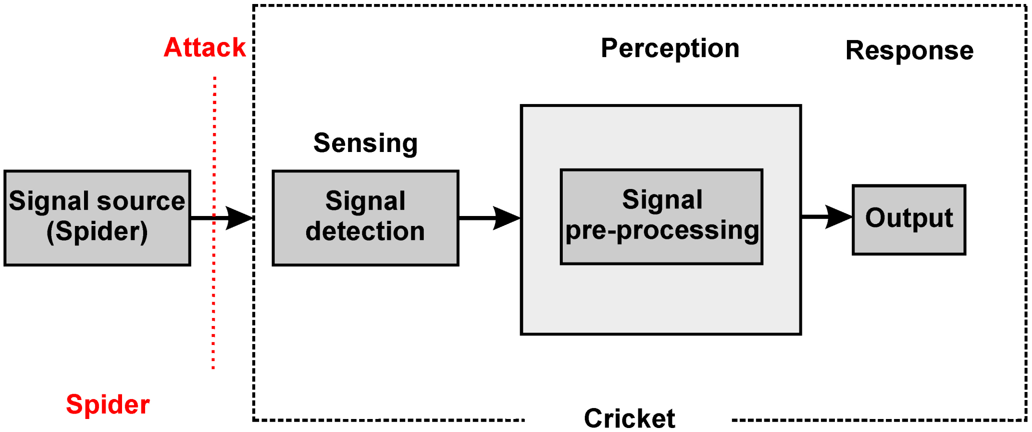

Figure 6.2: Block diagram represents the biomimetic principle of cricket-spider attacking process.

It consists of three main processes; (i) generation of an airflow field, (ii) airflow sensing and (iii) system response. The piston system is used to simulate the motion of the spider, which is sensed by the artificial hair-sensor array system. The artificial hair-

---

[2] The use of the piston of the group of Prof. Casas, and the help in using this setup by Thomas Steinmann are gratefully acknowledged.

sensors and sensor readout electronics, including signal amplification and demodulation, represent the sensing process. The perception part consists of determining the position of the flow-source from the array measurements. The response process is limited to a visualization of the "attack event"[3].

6.3. Modelling of transient hair response

In literature, several models have been used to describe transient airflow fields due to movements of a spider [Humphrey et al., 2008 & Kant et al., 2009]. Kant [Kant et al. 2009] represented the transient velocity field with an infinite number of sinusoidal velocities, varying in frequency and amplitude. In his model, the source starts from rest and moves in pulsed shape towards a virtual cricket in a short time and stops just in front of the hair-shaft. Casas [Casas et al., 2008] has measured the flow velocity fields ahead of a moving piston using PIV techniques. The results show that these flow fields can be well described by the flow field as produced by a moving sphere, essentially a dipole source [Casas et al., 2008 & Kant et al., 2009].

In our case, however, the situation differs in that the dipole source (represented by a sphere) is elevated (along the *z*-axis) from the substrate to its centre with a distance (*D*). The sphere moves in a pulsed-shape parallel with the maximum sensitivity axis of the hair sensor (i.e. the *x*-axis) and passes the hair-sensor shaft completely. This enables us to measure the developing flow field (at the position of the hair sensor) at different time instants and, hence, at different sphere positions. The substrate is considered infinity large compared to the hair sensor. Figure 6.3 shows a schematic representation of the sphere-hair-sensor geometry.

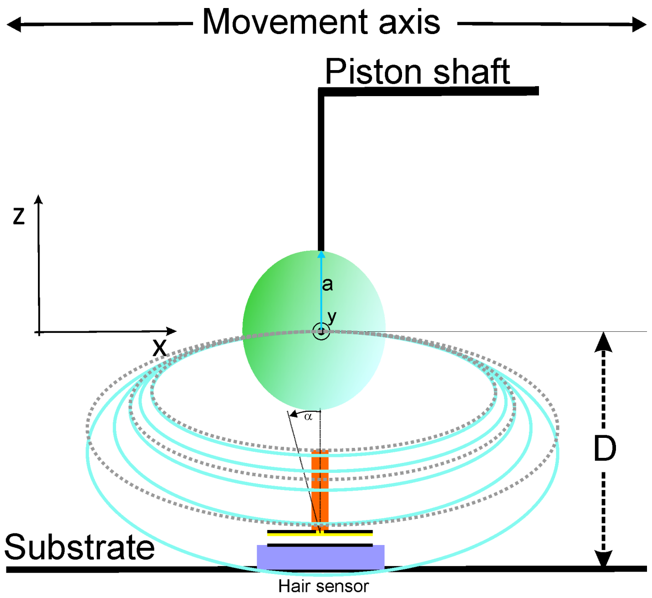

Figure 6.3: A schematic diagram representing the dipole-source–artificial hair-sensor geometry. Theoretical (solid) and squeezed (dashed) stream-lines are drawn for clarification (see text).

---

[3] Here, the purpose is not to build an artificial cricket system but to demonstrate the feasibility of a high-resolution 'flow camera' inspired by cricket-spider interactions.

A sphere with radius (a) and velocity ($\mathbf{V}$) generates a dipole field with velocity ($\mathbf{v}$) at position ($\mathbf{r}$) according to eq. 6.1 [Franosch et al., 2005].

$$\mathbf{v}(\mathbf{r},\mathbf{V})=\frac{a^3}{2|r|^5}\left(3(\mathbf{V}\bullet\mathbf{r})\mathbf{r}-|\mathbf{r}|^2\,\mathbf{V}\right) \tag{6.1}$$

The dipole field as measured by the hair-sensors is composed of two components; a component parallel to the direction of sphere movement and a component perpendicular to the direction of sphere movement (see chapter 5). For the chosen setup these components are both in the *x*-*z* plane. Due to the close proximity (*D*) of the substrate to the sphere, the perpendicular velocity component is arrested at the substrate. Hence, the airflow at the substrate is squeezed (substrate effect, see Figure 6.3).

In general, the hair sensor measures the projection of the dipole field on the axis of sensitivity (i.e. the *x*-axis in Figure 6.3) at the position of the hair. Therefore, from eq. 6.1 the signal produced by the sensor can be written as in eq. 6.2 while taking into account the directional sensitivity of the hair sensor.

$$\mathbf{v}(\mathbf{r},\mathbf{V})=\left[\frac{a^3}{2|r|^5}\left(3(\mathbf{V}\bullet\mathbf{r})\mathbf{r}-|\mathbf{r}|^2\,\mathbf{V}\right)\bullet\mathbf{S_h}\right] \tag{6.2}$$

$\mathbf{S}_h$ represents the direction of the sensitivity axis of the hair sensor where $|\mathbf{S}_h|=1$ represents the case when the movement axis of the sphere is aligned parallel with the maximum sensitivity axis (the *x*-axis).

To model the substrate effect, the “mirrored sphere” approach [Martiny et al., 2009] is applied where an identical sphere is introduced on the position of the sphere as mirrored in the air-substrate interface. Superposition this additional mirrored sphere forces the perpendicular flow-field component to be zero at the substrate-air interface and adds to the parallel velocity component of the airflow [Franosch et al., 2010].

Figure 6.4 shows a simulated example of the dipole field generated by two spheres where the substrate is located halfway between the sphere and its mirror. The overall flow field parallel to the substrate and the total fluid velocity ($\mathbf{v}_T$) at the position of each hair segment becomes:

$$\mathbf{v}_T(\mathbf{r},\mathbf{V})=\mathbf{v}_o(\mathbf{r}_{z1},\mathbf{V})+\mathbf{v}_m(\mathbf{r}_{z2},\mathbf{V}) \tag{6.3}$$

with

$$\mathbf{r}_{z1}=\mathbf{r}-\mathbf{r}_o$$
$$\mathbf{r}_{z2}=\mathbf{r}-\mathbf{r}_o+2D\hat{\mathbf{e}}_z$$

where $\mathbf{v}_o$, $\mathbf{v}_m$ are the velocity components of the original and mirrored sphere at position $\mathbf{r}$ from the substrate, $\mathbf{e}_z$ is the unit vector in *z* direction and $\mathbf{r}_{z1}$, $\mathbf{r}_{z2}$ are the effective separation distance of the original and mirrored sphere from each hair segment, respectively.

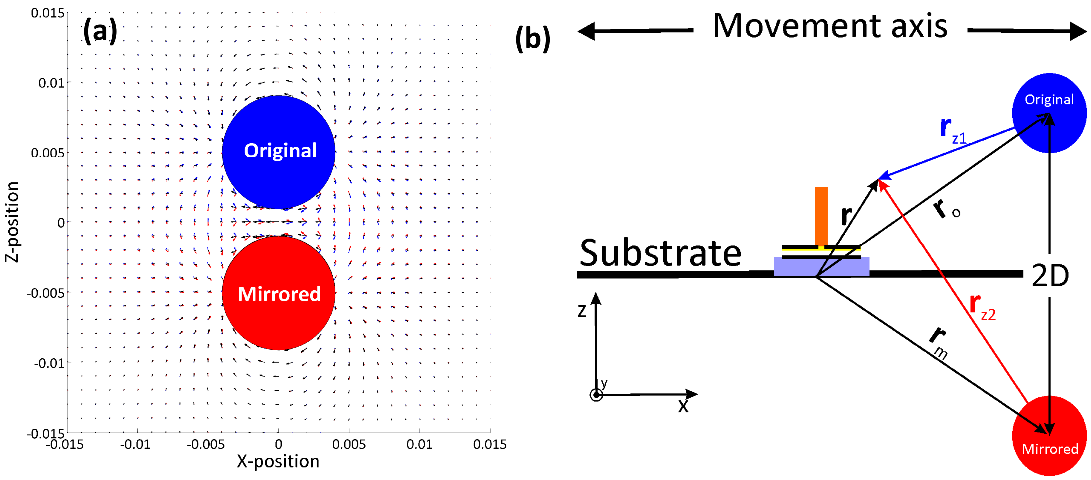

Figure 6.4: (a) Simulated flow velocity pattern of a dipole source generated by two spheres and (b) its schematic representation. The effect of the substrate is represented by introducing a mirrored sphere where the perpendicular velocity field components of both spheres cancel each other while the parallel field components are added at position of the hair sensor.

For oscillating airflow, in the vicinity of the substrate the airflow is attenuated in the boundary layer due to the no-slip condition. In transient flow, the situation is complex since the boundary layer is not at steady state conditions and becomes time dependent (see Figure 2.5 where the boundary layer is changed over time for an oscillatory airflow case). Additionally, the sphere is positioned in very near field conditions and *D* is at the same length-scale as the hair shaft (i.e. *D* varies from 5-11 mm while the hair-shaft is about 1 mm long). Under these conditions, the hair sensor cannot be represented by a point sensor. The drag torque becomes dependent on time (by varying the *x*-position of the sphere), *D* and the instantaneous boundary-layer thickness. But specifically the thickness of this instantaneous boundary-layer is difficult to estimate. Few efforts have been made to investigate the shape of the boundary layer due to transient stimuli [Humphrey et al., 2008]. However, no physical explanations correlated with theoretical models have been proposed.

In the current model we represent the transient effect as a composition of a series of flow velocities oscillating at distinct frequencies and amplitudes where the airflow velocity, for each frequency, can be represented by the model shown in chapter 2. Afterwards, for each *D* the airflow is adapted to a dipole shape that changes in its amplitude as function of *x*-position relative to the hair sensor (i.e. the *x*-axis). The position of the sphere can be converted into time by the prior-knowledge of the piston propagation speed (i.e. at different time instants the sphere will be located at different *x*-positions relative to the hair shaft and hence the velocity becomes time dependent). Afterwards, the frequency content of the velocity profile (due to the original and mirrored spheres) is calculated and multiplied with the boundary layer effect at each position along the hair shaft. This can be represented as:

$$\mathbf{U}_o(f,\mathbf{r}_{z1},z)=\mathrm{FFT}(\mathbf{v}_o(\mathbf{r}_{z1},\mathbf{V})).\mathrm{FFT}(\mathbf{v}_f(f,\mathrm{z})) \qquad (6.4a)$$

$$\mathbf{U}_m(f,\mathbf{r}_{z2},z)=\mathrm{FFT}(\mathbf{v}_m(\mathbf{r}_{z2},\mathbf{V})).\mathrm{FFT}(\mathbf{v}_f(f,\mathrm{z})) \qquad (6.4b)$$

where $\mathbf{U}_o$, $\mathbf{U}_m$ are the fluid velocities of the original and mirrored spheres, as function of the relative position of each hair segment to the spheres at the frequency f and $\mathbf{v}_f$ has been previously defined in chapter 2 which includes the effect of the boundary layer.

The fluid velocity and the drag torque ($T_{all}(f)$) are afterwards calculated for each hair segment at different airflow frequency contents due to the contribution of both; the original sphere and its mirrored version. The total drag torque is calculated by integrating the resulted forces along the hair shaft (in the z-axis) in which:

$$T_{all}(f) = \int_0^L \left(F_{o,Tot}(\mathbf{r}_{z1}, f) + F_{m,Tot}(\mathbf{r}_{z2}, f) \right) . \mathbf{r}_z \, \mathbf{dr}_z \tag{6.5}$$

where $F_{o,Tot}(r_{z1},f)$ and $F_{m,Tot}(r_{z2},f)$ represent the total drag forces per hair segment in direction parallel to the substrate (i.e. the x-axis) generated by the original and mirrored sphere at position D from the substrate.

The overall hair response is determined by multiplying T_{all} with the frequency response of the hair sensor and the inverse Fourier transform (FFT^{-1}) is then determined. The result is a sensor response as function of time that reflects the shape of the dipole flow field as a function of x-position. The x-position translates into time by the prior-knowledge of the piston propagation speed (i.e. at different time instants the sphere will be located at different x-positions relative to the hair shaft). Figure 6.5 shows simulated examples of hair response due to piston movement, as described above using the mirrored sphere approximation, at different D.

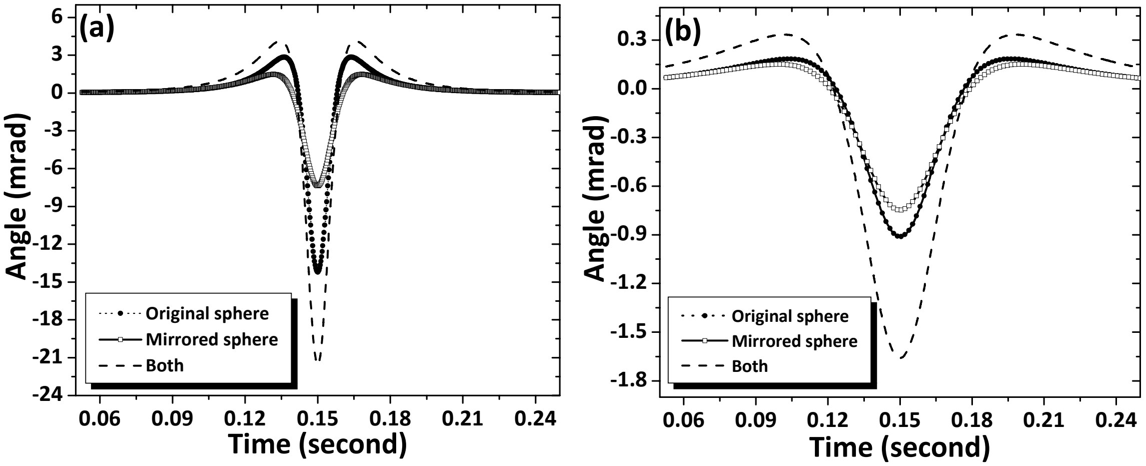

Figure 6.5: Simulated hair response to a transient airflow as represented by a dipole flow-field using spheres with 3 mm radius each. The response to a dipole field from the original sphere (solid circles), the mirrored sphere (open circles) and the sum of both (dashed line) are shown for (a) D = 5 mm and (b) D=15 mm.

6.4. Experimental

In the current measurement setup the maximum sensitivity axis of the hair flow-sensor is aligned parallel to the movement axis of the sphere. Thus, the output of the hair sensor will be sensitive to the parallel velocity component and not to the perpendicular component (i.e. the hair sensor responds to the airflow directed orthogonal to its rotation axis). Additionally, the symmetry in the design of the hair sensor in combination with the differential readout technique (see chapter 3) is assumed to cancel-out common signals at both sides of the membrane (i.e. in this case the perpendicular field component). Hence, we will focus on the parallel component of the dipole field in the *x*-*z* plane since it is the one that is driving the hair sensor (see eq. 5.3).

6.4.1 Measurements setup

In this section, we present the measured hair response due to a transient airflow generated by a moving piston, imitating spider motion. A sphere with 3 mm radius is attached to a piston system to represent the motion of a spider. The sphere is fixed at the head of the piston with an L-shaped shaft to exclude any effects of the piston shaft on the airflow (see Figure 6.3). The sphere is positioned at a distance (*D*) from the substrate with a minimum of *D* = 5 mm in order to prevent any impact on the hair-shaft. The artificial hair sensor is placed at the centre of the movement axis of the travelling sphere (parallel to the *x*-axis) and at such a distance from the start that the sphere passes the hair sensor completely within the piston's full stroke. This guarantees that the hair sensor is exposed to the (projection of) the entire dipole field and also that it will be minimally affected by the acceleration and deceleration of the piston at the start and end of its movement, respectively. The piston head (i.e. the sphere) moves parallel to the *x*-axis with a velocity of 0.38 m/s and 4.5 cm travelled distance from rest. The piston is controlled with hyper-terminal software and an RS232 port connection to approach the hair sensor with controlled velocity. A single-chip array[4] (see chapter 4) consisting of single hair sensors is used to detect airflow and the measurements are recorded using either a digital oscilloscope or via a MATLAB environment. The artificial hair-sensor is operated using a Direct Digital Synthesis (DDS) system to generate carrier signals and perform synchronous demodulation using a 300 Hz bandwidth (same procedure as presented in chapter 4). Figure 6.6 shows a photograph of the measurements setup.

---

[4] Using the single-chip array there is no viscous coupling effect or it is minor since the separation distance between two adjacent columns is 2 mm and between two adjacent rows is 650 µm. From previous studies [Jaganatharaja 2011], viscous coupling effect is more effective with separation distance of less than 200 µm.

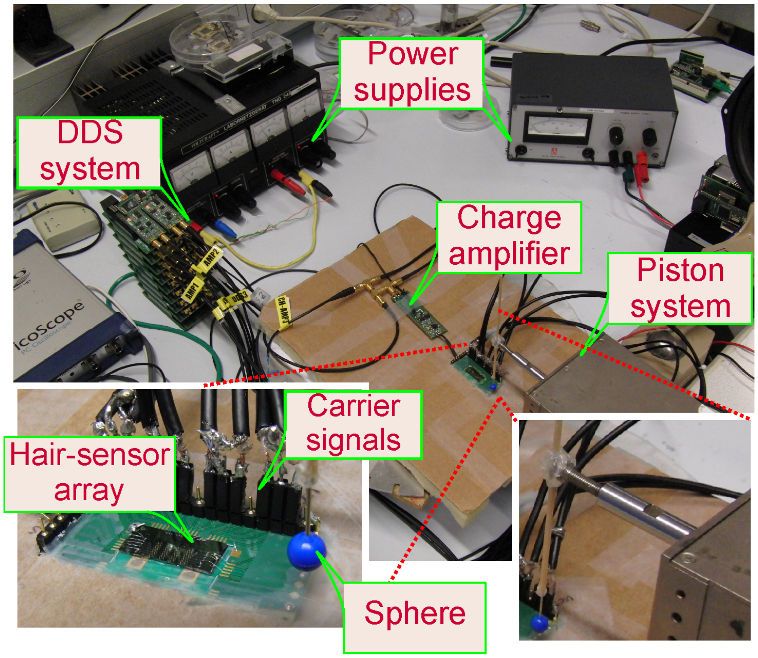

Figure 6.6: A photograph showing the setup of the transient response measurements with close-up view of the single-chip artificial hair-sensor array and piston shaft.

6.4.2 Results

Figure 6.7 shows an example of a hair-sensor response due to the sphere movement i.e. transient response. The measurement result shows that our hair sensor is able to capture the essential features of the transient airflow field generated by the moving sphere. Interestingly, the hair-sensor response shows strong similarity with the field shape generated by the dipole source (see Figure 6.7). The transient response has three peaks separated by two 180° phase shifts. The peak amplitude of the hair response as function of *D* is shown in Figure 6.8. According to dipole model, the velocity is proportional to D^{-3}. However, our measurements decay slower and show a maximum sensor output proportional to $D^{-2.45}$.

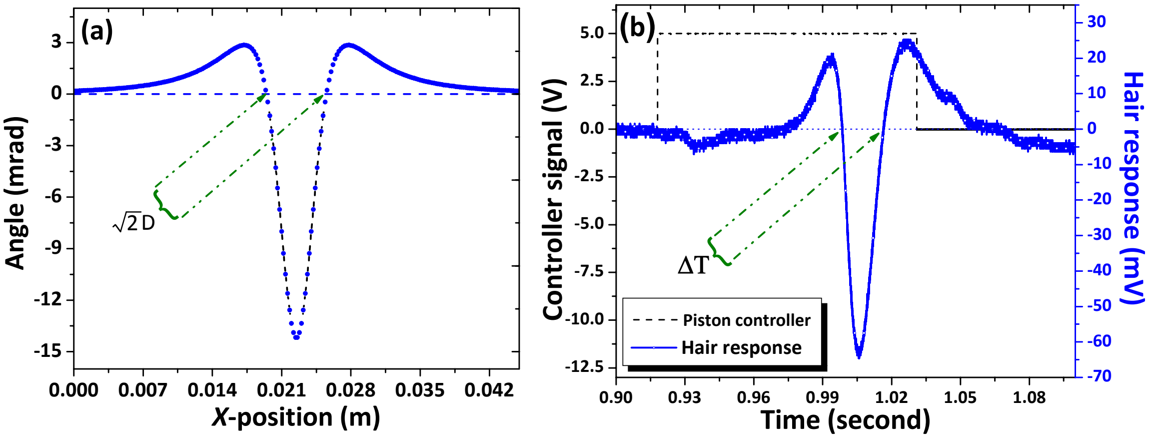

Figure 6.7: An example of (a) modelled hair-sensor response when exposed to a transient flow due to a passing sphere while showing the characteristic points and (b) measured hair sensor response (solid) under the same conditions. The dashed line in (b) indicates the control signal of the piston.

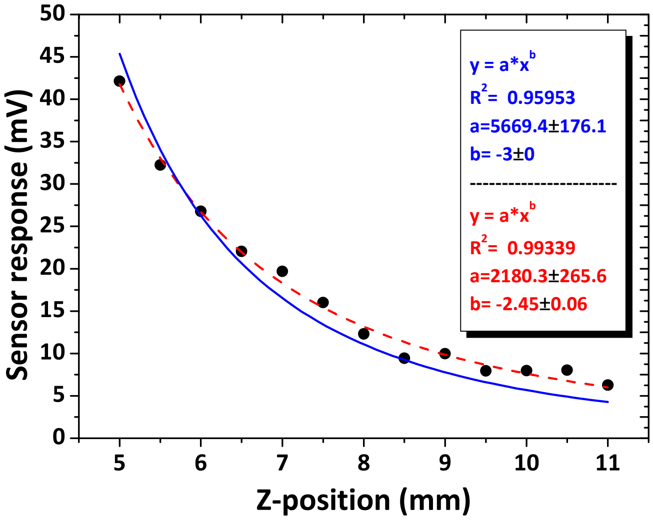

Figure 6.8: Peak amplitude of hair-sensor response measured as function of *D* (solid circles). Theoretical fits with dipole model (blue solid-line) in free space compared with the best fit (red dashed-line).

The output of the hair sensor represents the convolution of the airflow stimulus with the mechanical response of the artificial hair flow-sensor. In order to derive information about the flow-field a deconvolution process has to be performed to exclude the mechanical response of the hair sensor. The transient measurements involve changes in flow velocity in time which can be described by their Fourier equivalents. Hence, deconvolution can be achieved by Fourier transforming the measured signal and dividing the Fourier components by the response of the hair sensor in the frequency domain[5]:

$$T_{\mathrm{h}}(\omega)=\frac{u_s(\omega)}{H_s(\omega)} \tag{6.6}$$

where $T_{\mathrm{h}}(\omega)$ is the torque on the hair that we are interested in, $u_{\mathrm{s}}(\omega)$ is the sensor output and $H_{\mathrm{s}}(\omega)$ is the sensor's transfer function.

Hence, after performing the transient measurements, the output of the hair sensor is analyzed offline by applying the following steps:

- The measurements are filtered using a 1 kHz low-pass filter to reduce the effects of high-frequency noise (Figure 6.9 (a));
- The resulting signal is converted to the frequency domain using the Fast Fourier Transform (FFT) algorithm (Figure (6.9 (b));

---

[5] Convolution in the time domain converts to multiplication in the frequency domain.

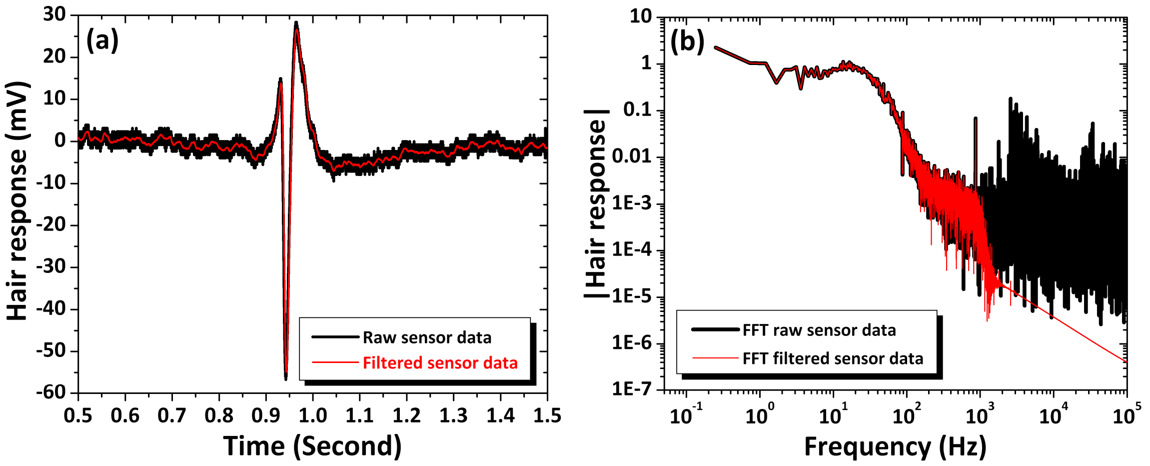

Figure 6.9: An example of (a) measured hair-sensor response due to a transient flow as function of time (i.e. raw and low-pass filtered sensor data) and (b) their FFT representations.

- The frequency response of the hair sensor is determined (using an oscillating airflow source with 3 kHz bandwidth) and a theoretical model is used to fit the measurements. The results shows a nearly critically damped system with a best fit at *Q*=0.59. Figure 6.10 represents the frequency response of the artificial hair flow-sensor with its theoretical fit;

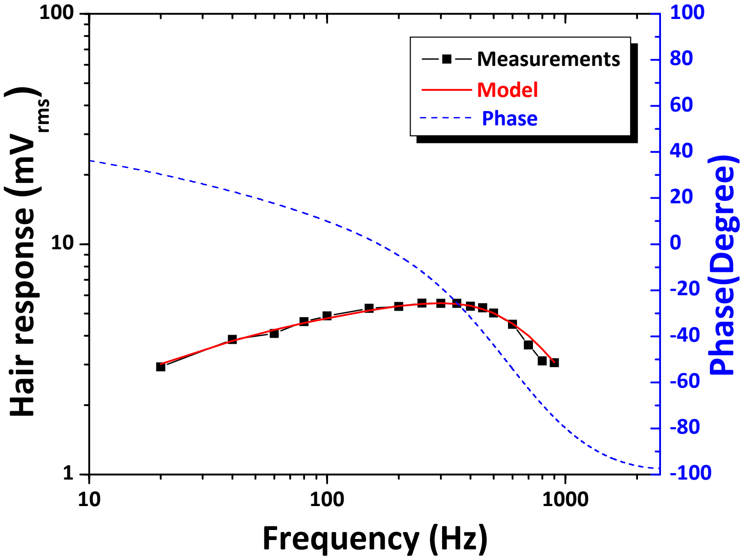

Figure 6.10: Frequency response of an artificial hair flow-sensor together with a model-based fit.

- Subsequently the frequency response is used to extract the torque due to the dipole field from the sensor output. The results are then converted back to the time domain (Figure 6.11);

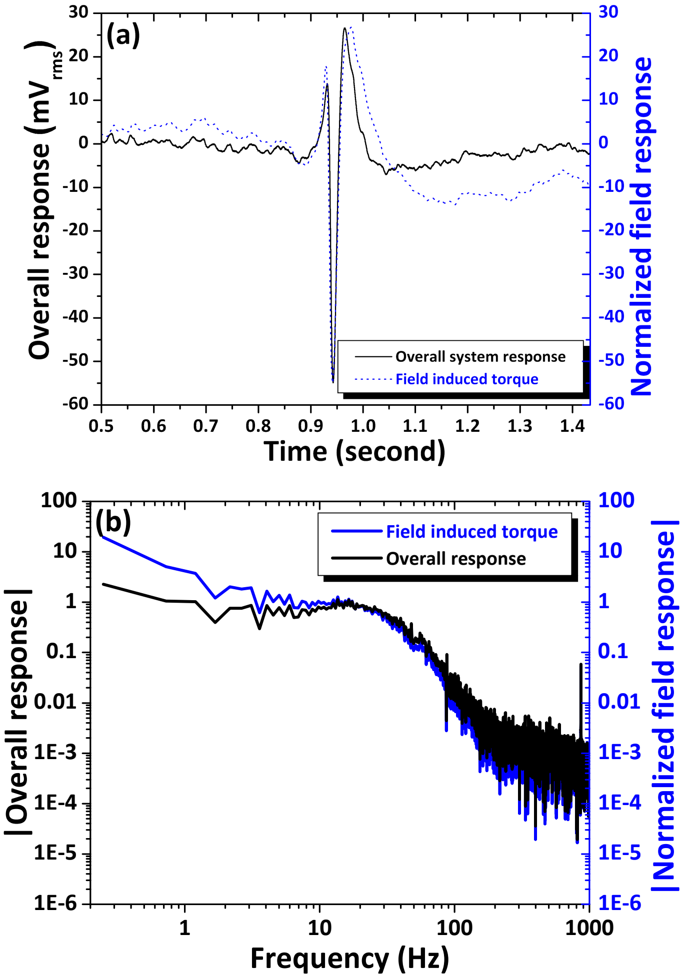

Figure 6.11: (a) The measured overall system response[6] due to a transient flow compared with the dipole field response after deconvoluting response of the hair sensor and (b) their FFT representations.

After correction for the hair-sensor response, the remaining signal represents the torque due to the dipole field. Since we know of no way to correct for the integrated drag-force on the length of the hair we consider the torque as a reasonable representation of the flow field at between 1/2 and 2/3 the hair length (i.e. about 600 – 700 µm above the substrate). Since the distance to the sphere is encoded in the characteristic points of the flow-field (comparable to what has been presented in chapter 5) the distance between the source and the hair-sensor can be derived from sensor output. In the transient response the time difference between the characteristic points can be translated into position using the piston speed (i.e. *x-position* = ΔT × *velocity*). The zero-crossing points are used to determine position of the dipole source. When this distance is estimated, it offers us the possibility to test the performance of the hair sensor and judge the accuracy with respect to the measurement of spatio-temporal airflow fields. Figure 6.12 shows D_{est} versus D using the transient hair response before and after convoluting response of the hair sensor.

---

[6] Overall system response represents the output of the hair sensor due to the stimulus where response of the hair sensor is part of the detected field.

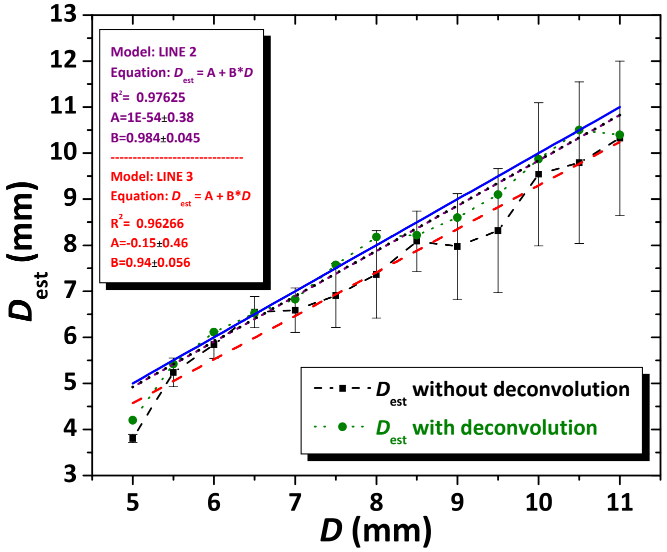

Figure 6.12: D_{est} versus D using transient hair-response measurements, before (solid-squares) and after (solid-circles) deconvolving the hair-sensor response. The best linear-line fit for both measurements are compared with ideal linear-line (blue). The D represents height of the sphere centre from the substrate. The error bars represent the uncertainty in determining the zero-crossing points of the measured dipole profile.

Previously (in chapter 4 and 5), we implemented arrays of hairs for the detection of airflow dipole fields. The added value is that arrays offer us spatial information, specifically if they are measured simultaneously. Here we integrated Frequency Division Multiplexing (FDM, discussed in chapter 4) to simultaneously measure the transient response of multiple hairs i.e. spatio-temporal airflow pattern measurements. Figure 6.13 (a) shows an image of a single-chip hair-sensor array indicating the separation distance between the two hairs (physical separation is 4 mm) and Figure 6.13 (b) shows the response of two single-hair sensors in one row, when both exposed to a transient airflow produced by a moving sphere.

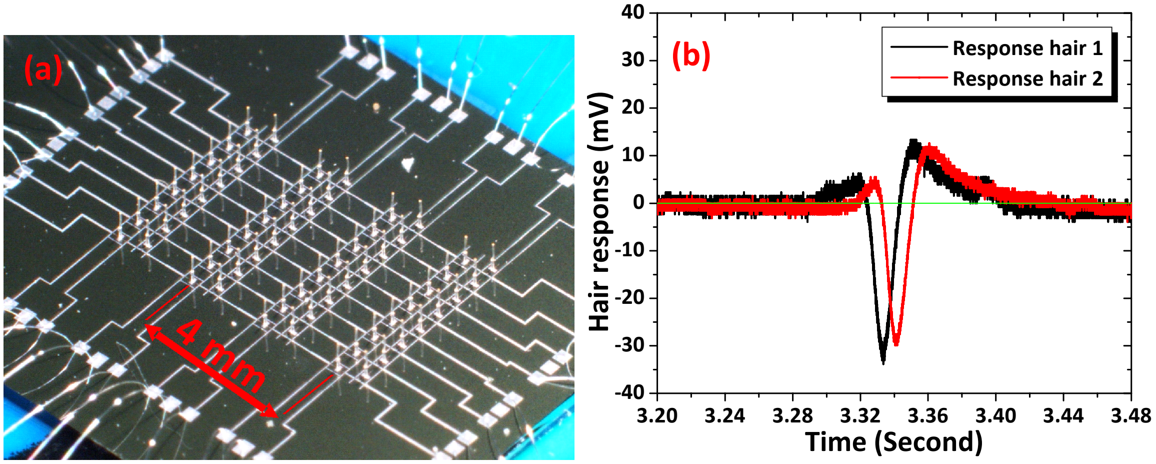

Figure 6.13: (a) An image example of a single-chip hair-sensor array showing the position of the hairs and (b) measured transient response of two hairs arranged in one row while using FDM for simultaneous readout.

The time delay between the responses of the two hairs offers us more information than just measuring response amplitudes. The time delay represents the time shift at the zero-crossing points of the detected signals. Additionally, the cross-correlation between the signals of both sensors is used to determine the time delay. The position of the peak in time represents the best approximation of the time delay between the two signals. Figure 6.14 shows an example of the cross-correlation for the output signals from two hair sensors using FDM in response to transient airflow. Figure 6.15 shows the estimated separation distance between two hairs as function of *D* for a given sphere velocity using the zero-crossing points compared with the time delay using cross-correlation.

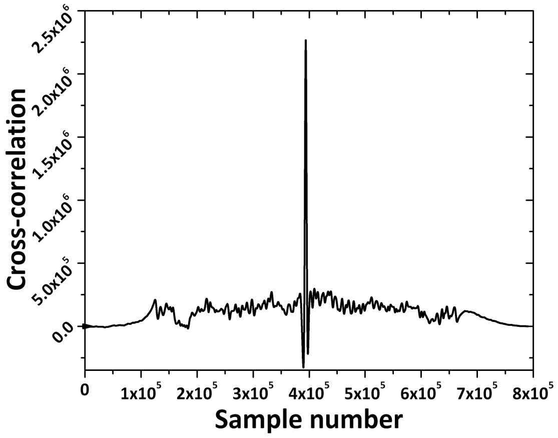

Figure 6.14: The cross-correlation of two hair-sensor signals, due to transient airflow, used to determine the time delay. The shift in the peak position represents the time delay between the two signals under test with known sampling frequency (F_s) (in this example F_s = 200 kHz).

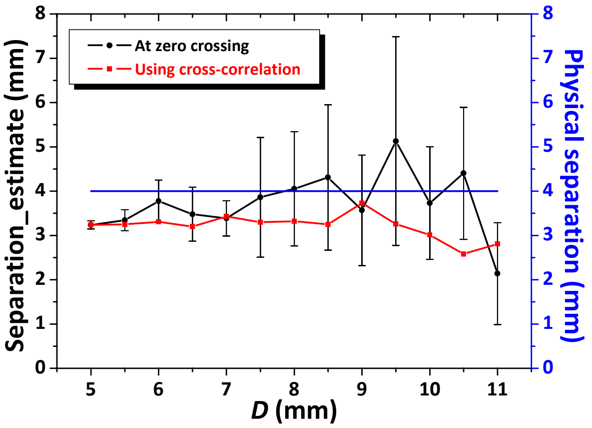

Figure 6.15: The estimation of the hair-separation distance as function of *D* for known sphere velocity using the delay at the zero-crossing points compared with the time delay determined using the cross-correlation method.

6.5. Discussion

Biologists believe that crickets are able to estimate speed, acceleration and direction of approaching spiders from their generated flow profiles using their hair-sensor arrays [CILIA 2008 & Kant et al., 2009]. The phase difference between hairs' movements [Mulder-Rosi et al., 2010], viscous coupling [Casas et al., 2010] in combination with hair characteristics provide crickets with this information. However, it is not yet understood how crickets achieve this and which source parameters can be extracted from the flow profile. Here we try to shed some light on a possible mechanism(s) that crickets use to detect approaching spider with the advantage of using the artificial hair flow-sensory array system.

The results show that the hair sensor is able to follow developments of the flow-field very well, both in time (using a single hair-sensor) and position (using an array of hair-sensors). J. Casas and R. Kant [Casas et al., 2008 & Kant et al., 2009] reported that the dipole field can be used to describe the flow field generated by a sudden moving piston. We also showed that the flow distribution due to a sphere passing-by can be well represented by a dipole flow field (see Figure 6.7). Note, however, that their studies were concerned only with the approach of a moving body, and not with its subsequent passing, and with the moving body being approximately at the same height as the observer (i.e. D=0).

Additionally, the measurements show that the maximum amplitude of the response of the hair sensor (largest peak in the hair's transient response) as function of D decays slower with distance ($D^{-2.45}$) than the theoretical dipole velocity field in free space (which decays with (D^{-3})). This can be due to the following reasons:

- The sphere movement causes a transient flow in which the boundary layer is not yet developed as it is in steady state conditions. This causes a thinner boundary layer and, hence, the driving forces are larger. L. Obsorne [Obsorne 1996] has reported the same for crickets' hairs in which the hair response due to noise stimulus is higher than the single tone response. She related this to the development of the boundary layer;
- The theoretical dipole model represents a flow field in free space and neglects boundary layers, also on the actual sphere producing the flow-field. Due to the substrate effect at small D the size of the sphere (radius of 3 mm) becomes large relative to D for each hair segment. This causes a difference in contribution between the original and mirrored sphere in the velocity profile (ΔU) along the hair-shaft. This effect increases from hair base to tip. As D increases, the contribution of the mirrored sphere approaches that of the original sphere (see Figure 6.5 b).

As verification, the separation distance D is estimated using the response of the artificial hair-sensor (without sensor-response deconvolution). The results show a clear linear relationship between D_{est} and the set D. However, the linear line fit shows up at a 0.45 mm ± 0.15 mm linear shift in D_{est}. This can be due to the relative short distance of the sphere to the hair-sensors comparable to the length of the hair-shaft. Since the contributions of the flow to the torque on the hair-shaft increases with the distance to the rotational axis, the overall response will be dominated by the flow-field at the end of the hair. Hence, the D as observed from the measurements will be smaller than the real value of D since, as we stated in the section of the measurements setup, D represents the distance between the centre of the sphere and the substrate. Depending on actual boundary layer thickness the determined distance will be the distance between centre of the sphere and the mid or higher point on the hair-shaft. As a result, correcting for this shift will improve the estimation accuracy (see Figure 6.12).

To exclude any further effects for the mechanics of the hair sensor, a deconvolution process has been performed (discussed in the section 6.4). The results show that the deconvolved sensor data nearly matches the raw sensor data with a slight widening in its characteristic points. Hence, we anticipate that the hair sensor is following the development of the flow profile rather well, a consequence of the nearly critical damped system with best frequency in the range of 250-300 Hz (see Figure 6.10) providing a bandwidth that amply covers the bandwidth of the transient flows. However, the slight widening in the characteristic points of the deconvolved sensor data contribute in determining D_{est}. The results using the deconvolved sensor data (Figure 6.12) indicate that the linear-line fit of D_{est} more closely matches the physical D while for the raw sensor data the D_{est} indicates the distance to the centre of the hair shaft. This highlights the effect of the mechanics and the hair-shaft of the sensor.

The detected flow signal has shown asymmetry (i.e. the left peak is slightly larger than the right peak). This can be related to a slight misalignment of the axis of movement of the sphere with respect to the maximum sensitivity axis of the hair sensor causing the partial addition of the perpendicular dipole field component to the parallel component. Additionally, since the used hair sensor performs as a slightly under-damped system with Q=0.59 (i.e. Q>0.5) a slight overshoot may contribute to this asymmetry. However, the deconvolution of the hair sensor response has not change this asymmetry significantly. Thus, we believe that the first option is the most plausible reason (see Figure 6.7 and Figure 6.13 (b)).

Using the transient response of two single-hairs integrated in one single-chip array, we determined the time-delay between the sphere passing the first and second hair sensor and, as verification, estimated the separation distance using the time shift between the characteristic points (since we know the sphere velocity). The separation distance estimated using the cross-correlation technique lies within the error margin of the delay estimated by the crossing points. The error and error – margins are seen to increase with increasing distance between the hair-sensors and the sphere. The estimation uncertainty can be related to the error in determining the time delay due to a decreasing SNR with increasing distance.

Using the signal profiles as detected by the entire array would allow us to determine an increasing number of source properties. By virtue of the piston velocity (about 38 cm/s) the delay represents the separation distance in between two hairs divided by the sphere velocity. Thus, the sphere velocity can be determined independently of the distance to the sphere. Moreover, when the velocity of the sphere and its distance are known (from the characteristic points) the magnitude of the signals actually is a measure for the (cube) of the sphere radius. As an example, using two sensors the sphere parameters size, velocity and distance can be determined.

As a first trial, we have been able to detect delays using the signals from four hairs in one row (with sphere propagation speed of 38 cm/s positioned at D= 5 mm with 2 mm separation distance in between each pair of hairs) while using FDM. The measurements show about 4 ms time delay between each two subsequent hairs-sensor responses. Figure 6.16 shows the normalized transient response of four single-hair sensors arranged in one row measured with FDM. This demonstrates the possibility to perform spatio-temporal flow pattern measurements using a single-chip hair sensor array with FDM and to, subsequently, use the features of these flow profiles to determine source parameters (i.e. size, speed and position).

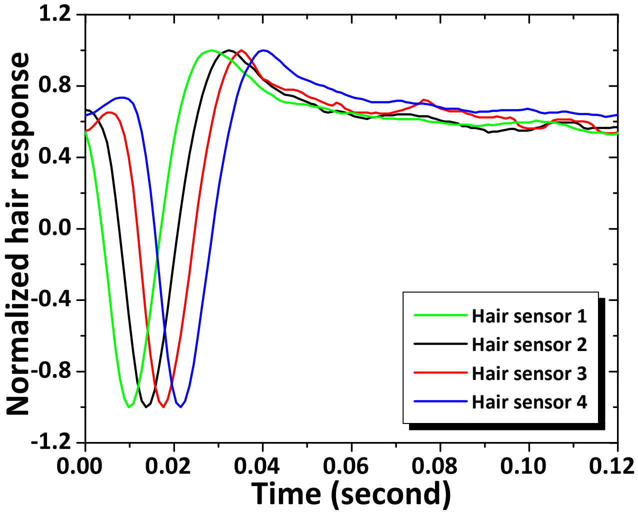

Figure 6.16: Normalized transient response of four single-hair sensors, arranged in one row, simultaneously measured using FDM.

6.6. Conclusions

In this chapter, the feasibility of artificial hair-sensor arrays to measure spatio-temporal flow patterns has been demonstrated, opening up the possibility to develop a high-resolution flow camera. As an example, we mimicked the cricket-spider escape mechanism using a moving sphere to generate spatio-temporal airflow patterns i.e. transient airflow. The response of single hair-sensors within an array was measured simultaneously using FDM array interfacing. As verification, it was shown that the source-hair separation distance and separations between two individual hairs can be estimated satisfactorily, though with room for improvement. It was not our goal to perform source localization but to demonstrate how far we can go with our hair-sensors, either as single sensor or in arrays to detect spatio-temporal airflow fields. The above results also can shed some light upon the mechanisms that are at work in crickets' flow sensing and how they might exploit spatio-temporal airflow patterns to estimate the occurrence and direction of moving objects in their close environment (both of which have been demonstrated in literature [Dangles et al., 2006] and [Theunissen et al., 1991]).

6.7. References

[Barth et al., 1995] Barth, F.G., Humphrey, J.A., Wastl, U., Halbritter, J. & Brittinger, W. (1995) "Dynamics of arthropod filiform hairs. III. Flow patterns related to air movement detection in a spider (Cupiennius salei KEYS.)", Philosophical Transactions of the Royal Society B: Biological Sciences, 347, pp. 397–412.

[Casas et al., 2008] Casas, J., Steinmann, T. & Dangles, O. (2008) "The aerodynamics signature of running spiders", PLoS One, 3, e2116.

[Casas et al., 2010] Casas, J., Steinmann, T. & Krijnen, G. (2010) "Why do insects have such a high density of flow-sensing hairs? Insights from the hydromechanics of biomimetic MEMS sensors", Journal of the Royal Society Interface, 7, pp. 1487–1495.

[CILIA 2008] Customized Intelligent Life-Inspired Arrays project (CILIA) (2008) "Multimodality and spider attack", Deliverable report: D3.1.8 http://www.cilia-bionics.org/publications.

[Dagamseh et al., 2010] Dagamseh, A.M.K., Bruinink, C.M., Droogendijk, H., Wiegerink, R.J., Lammerink, T.S.J. & Krijnen, G.J.M. (2010) "Engineering of biomimetic hair-flow sensor arrays dedicated to high-resolution flow field measurements", In: proceedings of IEEE Sensors, Art. no 5690705, pp.2251–2254.

[Dangles et al., 2006] Dangles, O., Ory, N., Steinmann, T., Christides, J. P. & Casas, J. (2006) “Spider’s attack versus cricket’s escape: velocity modes determine success”, Anim. Behav., 72, pp. 603–610.

[Franosch et al., 2005] Franosch, J.-M.P., Sichert, A.B., Suttner, M.D. & Van Hemmen, J.L. (2005) "Estimating position and velocity of a submerged moving object by the clawed frog Xenopus and by fish-A cybernetic approach", Biological Cybernetics, 93, pp. 231–238.

[Franosch et al., 2010] Franosch, J.-M.P., Sosnowski, S., Chami, N.K., Kühnlenz, K., Hirche, S. & Van Hemmen, J.L. (2010) "Biomimetic lateral-line system for underwater vehicles", Proceedings of IEEE Sensors, pp. 2212–2217.

[Humphrey et al., 2008] Humphrey, J.A.C & Barth, F.G. (2008) “Medium flow-sensing hairs: biomechanics and models”, In Advances in insect physiology. Insect mechanics and control, 34 (eds J. Casas & S. J. Simpson), pp. 1–80. Amsterdam, The Netherlands: Elsevier.

[Jaganatharaja 2011] Jaganatharaja, R. K. (2011) “Cricket Inspired Flow-Sensor Arrays”, Ph.D. thesis, University of Twente, Enschede - The Netherlands.

[Kant et al., 2009] Kant, R. & Humphrey, J. (2009) "Response of cricket and spider motion-sensing hairs to airflow pulsations", Journal of the Royal Society Interface, 6, pp. 1047–1064.

[Martiny et al., 2009] Martiny, N., Sosnowski, S., Kuhnlenz, K., Hirche, S., Nie, Y., Franosch, J.-M. P. & Van Hemmen, J. L. (2009) "Design of a lateral-line sensor for an autonomous underwater vehicle", In the 8th IFAC International Conference on Maneuvering and Control of Marine Craft (MCMC), Brazil, pp. 292–297.

[Mulder-Rosi et al., 2010] Mulder-Rosi, J., Cummins, G.I. & Miller, J.P. (2010) "The cricket cercal system implements delay-line processing", Journal of Neurophysiology, 103, pp. 1823–1832.

[Obsorne 1996] Obsorne, L.C. (1996) “Signal processing in a mechanosensory array: dynamics of cricket cercal hairs”, Ph.D. thesis, University of California, Berkeley, USA.

[Theunissen et al., 1991] Theunissen, F.E. & Miller, J.P. (1991) “Representation of sensory information in the cricket cercal sensory system. II. Information theoretic calculation of system accuracy and optimal tuning-curve widths of four primary interneurons”, Journal of Neurophysiology, 66, pp. 1690–1703.

Chapter

7

CONCLUSIONS & OUTLOOK

The concept of taking model systems from nature (to attain new materials, fabrication techniques, devices or even entire systems) has demonstrated to be a powerful route to improve upon more traditional engineering approaches for specific challenges. This chapter summarizes the work presented in this thesis to develop artificial hair-sensor array-systems targeting flow-based camera applications. This is followed by identified possibilities and trends for future developments meeting the requirements of our goals.

7.1 Conclusions

Crickets' hair-like flow-sensor arrays have been studied by biologists and considered by engineers with respect to the valuable information they provide to develop acute arrayed flow-sensing systems. The advantages of hair-like flow sensors are that they mediate simultaneous, local directional flow observations.

In this thesis, we presented the motivation and implementation of hair-like airflow sensor arrays in airflow-field measurements targeting flow pattern observations. Our bio-inspired artificial hair flow-sensor has shown the ability to measure tiny airflow amplitudes and to perform flow pattern measurements when arranged in arrays. Design guidelines and basic design rules were presented in which hair devices and systems were implemented. This has been attained by:

(i) Improving the performance, i.e. detection-limit and directionality, of the single-hair sensors by carefully considering the sensor interfacing;

Due to the parasitics inherent in capacitive sensing, optimal electrical interfacing is of major importance in attaining maximum performance. This is achieved by re-designing the electrode system and making the system relative immune to (symmetric) parasitics, allowing us to measure capacitance changes originating from single-hair sensors. The performance of the hair sensor was improved now at least by twelve-fold, down to airflow of 1 mm/s using 3 kHz bandwidth.

(ii) Fabricating high-resolution single-chip hair-sensor arrays with independent elements using a cleanroom fabrication process compatible with the fabrication process of the previous generation of hair sensors;

(iii) Interrogating arrays of hairs with a small number of interconnects while maintaining the performance of single hair-sensor using Frequency Division Multiplexing (FDM);

(iv) Performing spatio-temporal flow field measurements using either discrete or single-chip hair-sensor arrays.

As inspired by the lateral line system (LLS) in fish, arrays of artificial hair sensors were used to construct an artificial LLS (ALLS) as an example of a flow field observation system. These arrays have shown the ability to faithfully quantify the local dipole field and, using off-line calculations, to localize flow sources using the characteristic points of the flow field. Incorporating array signal processing (ASP) techniques (beamforming) improved the detection capability, even at the edges and outside the length of the ALLS.

Here, we have to clarify that the aim was not to compare various techniques or algorithms to improve the source localization process but rather to investigate the capabilities of our hair sensor-arrays in recording spatio-temporal flow field features. This can be beneficial in that it can provide information about characteristics of the flow field to the system which is performing the task of flow pattern recognition. Additionally, it forms the basic steps in understanding the meaning of flow fields as found in nature. This is what we have shown in chapter 6 by putting together the entire hair sensory system and used it to measure transient flow fields generated by a bio-inspired source (i.e. piston system which mimics the motion of an approaching spider). Such flow sources, matching to some degree biological relevant stimuli (e.g. direction, amplitude distribution, frequency contents and timing) may reveal some of the intricacies of biological interactions driving behavioural responses. As verification of the hair sensors' ability to perform flow field observations, separation distances between the flow source and the hair sensors or even between individual hairs were estimated by determining the characteristics of the measured flow field (e.g. dipole field).

7.2 Outlook

As stated repeatedly throughout this thesis, the hair sensory system of crickets is one of the most evolved and integrated flow sensory systems in nature. This motivated us to develop an artificial hair sensory system able to perform spatio-temporal flow field measurements, which is expected to be useful e.g. for surveillance, robotic and flow camera applications. Such an advanced bio-inspired system could be composed of high-density single-chip hair arrays arranged, potentially in 3D spatial distributions. These arrays can be mounted on conical-shaped substrates and will consist of high-sensitive single-hair elements and have high-levels of redundancy (i.e. robust systems in which the failure of a single element will not impair the entire array function).

Here, we discuss possible future work on flow-sensor arrays that may be done to realize performance and functionality of their counterpart in nature. This can be divided into three main activities (i) single-hair sensor performance, (ii) hair sensor arrays and (iii) flow field measurement and data-processing.

7.2.1 Single-hair sensor performance

Sensitivity

Performance of the single hair sensors can be evaluated against five main aspects; threshold velocity, sensitivity, bandwidth, directionality and sensor robustness. In chapter two, a figure of merit (FoM, i.e. sensitivity × bandwidth) was presented and used to drive hair-sensor optimization. Accordingly, our hair sensor will match the performance of cricket hairs with (i) an optimal mechanical design (including damping) and (ii) the availability of long thin, light, hair-like structures. This requires appropriate materials, especially for the hair-shafts and rotation springs. E.g. for the fabrication of hairs one would like to use low-density material which can be shaped in high aspect ratios. Likewise rotational springs with a large vertical-to-torsional stiffness ratio (VTR) require low Young's modulus materials that can be applied with little stress to ascertain small gaps between capacitor electrodes.

Long hair-shafts are essential to pick up sufficient viscous drag torque while thin hair-shafts are required to limit the moment of inertia (i.e. to retain appropriate sensor bandwidth, see chapter 2). Long SU-8 hairs with reduced moment of inertia were fabricated using a sequential lithography process with dissimilar top and bottom hair-sections. More natural hair shapes as well as improved torsion beams were investigated in [Jaganatharaja 2011] but have up to date been impractical to implement in the current fabrication process.

To reduce the moment of inertia further, hollow hairs can be made without considerably affecting the drag torque. This can be attained by design of the hair sensor by making an opening in the circumference of the hair-shaft. Consequently, during the lithography process, SU-8 contents of the interior will not be exposed to the UV light and hence during developing it will be partly removed. However, aspect ratio limitations pose difficulties and may endanger the fabrication yield.

Nonlinear effects, e.g. as exploited in parametric amplification and stochastic resonance, can be used to further improve the sensitivity of the hair sensors. In parametric amplification, electrostatically modulating the torsional stiffness in time (using AC bias voltages) may lead to a mechanical amplification of the rotational response of the hair sensor at the frequency of the pump [Droogendijk 2010]. Controlling the pump amplitude, frequency and phase results in improvements in the sensitivity, dynamic range of the hair sensor and provides a means of filtering the flow signal. Figure 7.1 shows the basic set-up used for parametric amplification as applied to artificial hair sensor.

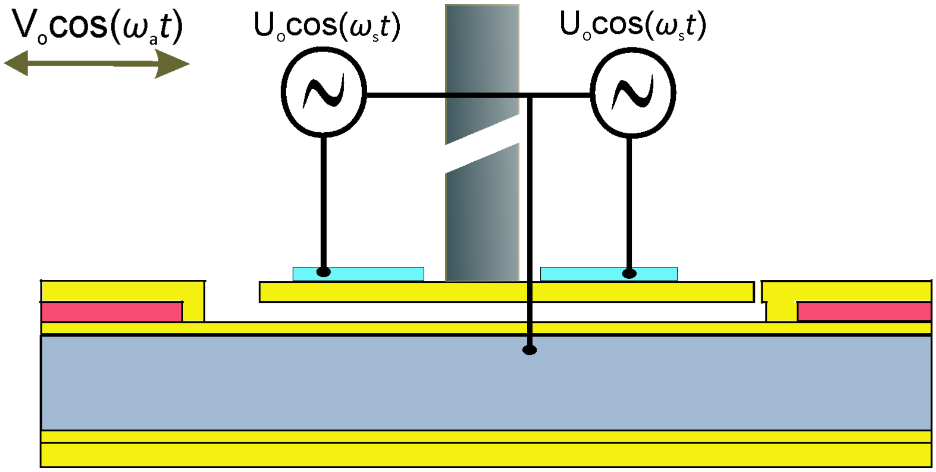

Figure 7.1: Parametric amplification set-up as applied to artificial hair flow-sensors by modulating their torsional stiffness.

Stochastic resonance is another non-linear effect to improve the detection-limit of artificial hair sensors and to increase the signal-to-noise ratio (SNR) by taking advantage of the noise itself [Droogendijk 2010]. In this technique, adding the proper amount of noise to a weak signal improves the SNR and lifts the output signal of the hair-sensor above the threshold.

Digital hair sensor

In crickets' hair sensor, deflection of the hair-shaft due to airflow is transmitted to the nervous system through compressive mechanical distortion [Gnatzy et al., 1980]. When this distortion exceeds a certain threshold, the sensory neuron generates a series of spikes [Shimozawa et al., 1984]. Depending on the stimulus, a variety of spike trains is generated [Murakami et al., 2005]. This system can be considered as a digital encoder since it converts the amplitude of airflow into discrete pulses i.e. ADC.

A fully biomimetic hair sensor would be more robust if it would be able to convert the analog flow signals into digital electrical signals. However, the idea is not to use electronics to perform ADC, since this would not benefit the robustness, but rather to use the sensor-structure itself. In principle digital flow sensors can be realized using floating gate transistors, if needed under pull-in conditions using additional electrostatic actuation.

Figure 7.2 illustrates the structure and basic principle of the proposed digital hair flow-sensor. A single digital hair sensor consists of three single-hair elements (see Figure 7.2a). Each single-hair has a certain airflow threshold (see Figure 7.3) which can be controlled by mechanical design (e.g. hair length, spring stiffness and moment of inertia or capacitor gap). Individual hair elements consist of two floating-gate transistors (M) operated in saturation mode (i.e. as switch, see Figure 7.2c). The drain and the source can be made by local highly-doped areas in a poly-silicon layer while the hair membrane provides the floating gate electrode. To constitute logic gates, electrostatic actuation (using the output of each transistor) can be used to counterbalance the airflow drag torque in the next single-hair thereby setting the next stage threshold.

In a single cycle of applied airflow, the membrane of the first single-hair (H1)[1] tilts in which one of its gate electrodes (say M_{11}) moves towards the substrate and the other gate electrode (say M_{12}) moves in opposite direction (see Figure 7.2b). Consequently, the gate capacitance (C_{gate}) of M_{11} increases and hence the drain current increases (i.e. switch is On) linked to a decrease in the threshold voltage (V_{th}) and vice versa in M_{12}. Increasing the airflow amplitude drives another single-hair (say M_{21} transistor in H2 is On). Its output (V_{o2}) is connected to the first hair (i.e. the gate of transistor M_{12} in H1) which is used to compensate the drag torque on the first analog hair sensor (H1) by means of electrostatic actuation to bring the hair back to the balance position (i.e. logic 0). The same principle is applied to the other hairs when they are exposed to airflow amplitudes exceeding its thresholds. Figure 7.3 shows the sequence of hair movements which leads to the subsequent logic-states.

Additionally, this principle (i.e. floating gate hair sensor) can be also exploited to operate the hair sensor in the analog mode in which the drain current is proportional to airflow amplitude. The drain current generated from the transistor operated in saturation mode is given by Eq. 7.1 [Sedra et el., 1987].

---

[1] H1, H2 and H3 represent the first, second and third single-hair sensors, respectively, all acting as a digital hair sensor. In each single-hair there are two transistors i.e. M1 & M2.

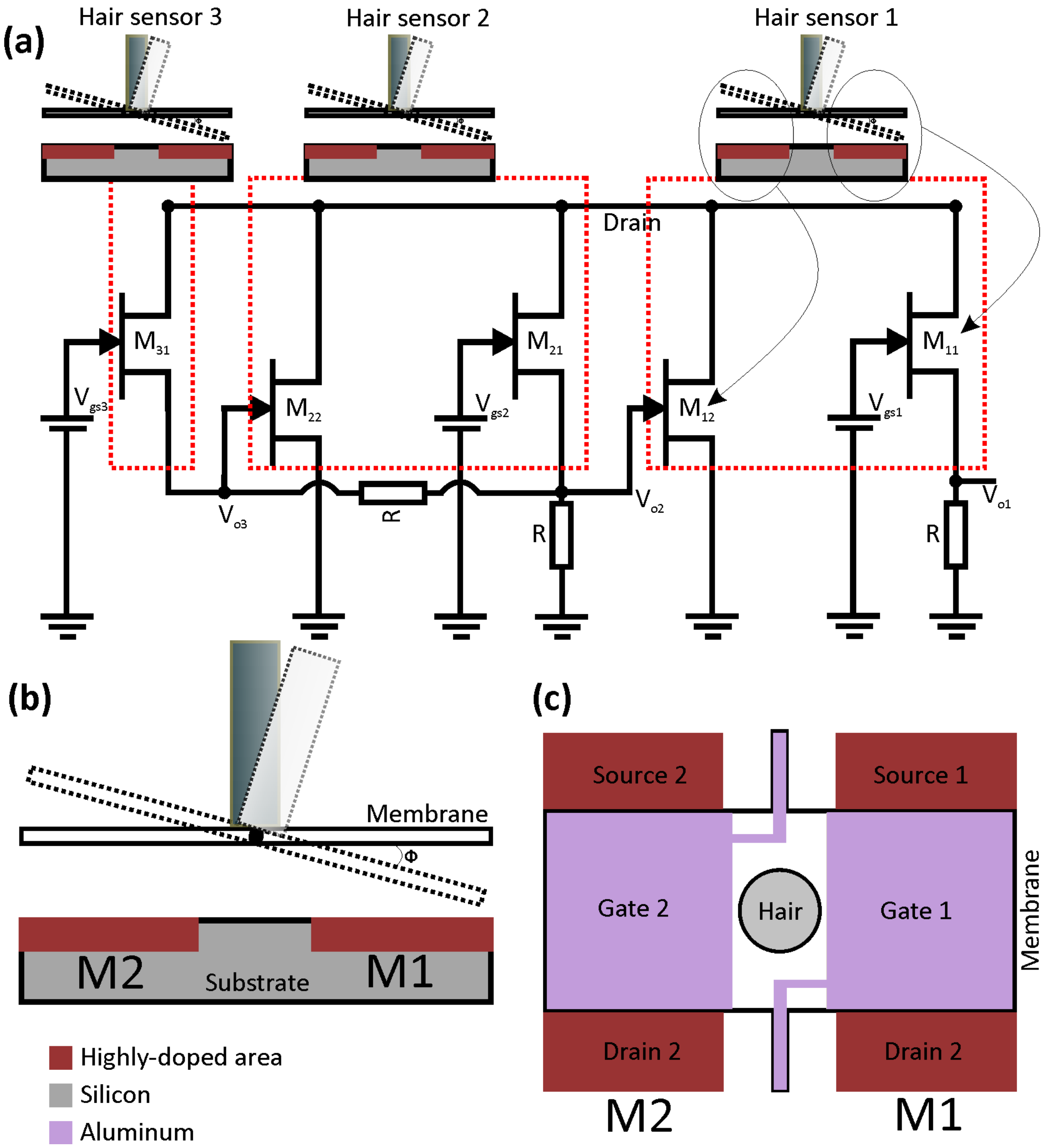

Figure 7.2: The proposed design of a digital hair flow-sensor[2] based on the floating gate transistor principle; (a) Equivalent circuit diagram with a (b) cross-sectional view and (c) top view for its basic element (i.e. single-hair). M1 represents the transistor which its output represents a logic state (0 or 1) based on hair threshold as well as amplitude of the airflow and M2 is the transistor where we apply the electrostatic actuation.

$$I_D = \frac{\mu_n C_{gate} W \left(V_{gs} - V_{th}\right)^2}{2L} \tag{7.1}$$

where W and L are the width and length of the gate, μ_n is the mobility of electrons in silicon and V_{gs} is the applied gate-source voltage.

---

[2] The output of the digital hair-sensor is a 3 bit number represented by the output of each individual single-hair element (i.e. H1, H2 and H3, see Figure 7.2a).

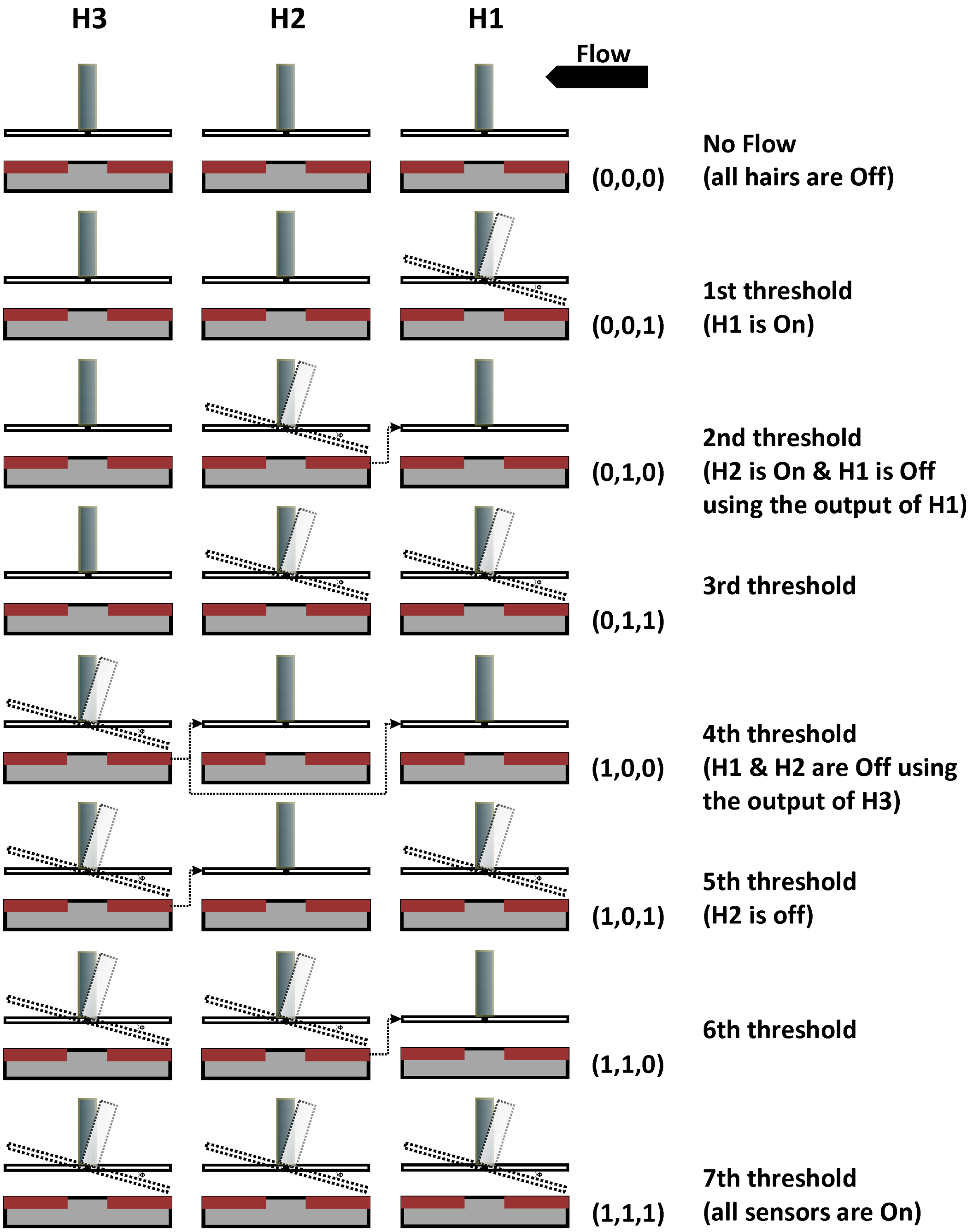

Figure 7.3: Schematic representing the individual logic-states of the digital hair-sensor at different airflow threshold amplitudes. In each single-hair (say H1) the output of the first transistor (M_{11}) is used as an output (i.e. either 0 or 1) and the gate of the second transistor (M_{12}) is used to compensate for the drag torque using the output of the neighbouring single-hair (say M_{21} in H2). The threshold airflow amplitudes (*Th*) of individual single-hairs are $Th_{H1}<Th_{H2}<Th_{H3}$.

Quadrature Amplitude Modulation

The transduction principle used in the hair sensor is based on differential capacitive readout. Accordingly, the magnitude of its output voltage is proportional to airflow. A potential other mechanism could be quadrature amplitude modulation (QAM), basically representing the airflow amplitude by phase. The idea is to make the carrier signals used to probe the hair sensor quadrature (i.e. 90° out-of-phase). Accordingly, the generated signals from both halves of sensor capacitors are orthogonal which can be later separated using coherent demodulation. The linear combination of a sine and a cosine of equal carrier frequency and amplitude gives a single sine with the same frequency but with a phase angle according to eq. 7.2. Figure 7.4 shows the basics of QAM principle.

$$m_1(t)\cos\left(\omega_c t\right)+m_2(t)\sin\left(\omega_c t\right)=C\cdot\sin\left(\omega_c t+\Phi\right) \tag{7.2}$$

where C represents the magnitude of the AM signal at the charge amplifier output, $m_1(t)$, $m_2(t)$ are the amplitudes of the AM signals as modulated by the two sensor capacitors and Φ is the phase shift which is proportional to the airflow $m(t)$.

Using this scheme, the phase between the carrier signal and the AM signal can be represented according to eq. 7.3.

$$\Phi(t)=\tan^{-1}\left(\frac{m_1(t)}{m_2(t)}\right) \tag{7.3}$$

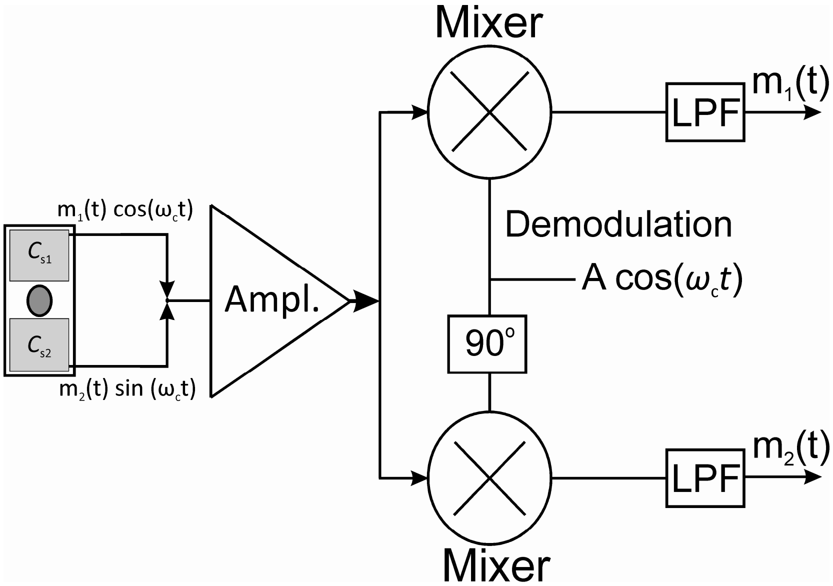

Figure 7.4: Basic principle of QAM as applied to artificial hair flow-sensor.

This approach is advantageous when it is used with the previous hair-sensor design[3]. During operation, the amplitudes of the carrier signals should be optimized to obtain the maximum sensor performance. This is impractical, specially with the large number of hairs, it causes each individual hair-sensor to operate sub-optimally. The output represents the summed output of all individual hairs. With the QAM approach, the output is proportional to the ratio between the airflow at both sides of the membrane. Thus, the resulted phase shift will be less sensitive to the carrier amplitudes or

---

[3] In previous hair-sensor, the hairs (i.e. 124 hairs) are connected in parallel on one substrate (see chapter 2).

imperfections and deviations between individual hair elements and, hence, more robustness hair sensor operating at/near its optimal is achieved. However, although the QAM principle is advantageous in representing the flow as function of phase, it implies a reduction in the amplitude of the AM signal (due to the loss of the differential property using both hair capacitors) and, hence, the SNR.

7.2.2 Hair sensor arrays

High-density arrays

While using arrays of hairs, implementing a variety of mechanical properties can be easily obtained. This allows for mechanical filtering (e.g. fractionation in frequency) where individual array elements are tuned by design (by variation of the length of the hair-shaft or rotational stiffness) to a specific frequency range of airflow. Exploiting the nature-like hairs [Jaganatharaja 2011] would allow us to make different hair lengths and hair diameters at once, even in single-chip hair-sensor array and using one lithography process. Potentially this approach would allow us the kind of functionality (i.e. frequency fractionation with separate read-out per frequency band) as the mammalian cochlea, albeit that the total frequency range and sensitivity would be much lower and the area consumed much larger. Nevertheless such an array would allow for passive mechanical filtering reducing the power otherwise required to do signal (post) processing in electronics.

In the current study, the SOI wafer technology has been used to make single-chip hair sensor arrays. This technology has some limitations in addition to wafer costs; sharp transition edges can occur across the isolation trench and can break the connection of the top electrode at crossing points (see Figure 3.16). SOI technology can be replaced by local doping of intrinsic silicon to create independent electrical connections. Poly-silicon layer can be deposited and afterwards n-doped to create the bottom electrode of the hair sensor capacitors. The resistance of the electrodes can be controlled by the doping levels and distribution. This will give advantages with respect to fabrication costs and provide alternatives to fabricate hair arrays with electrically independent elements with no sharp transition edges.

Flexible substrate

In crickets, the hairs are mounted on top of a conical shaped substrate. This shape is beneficial in reducing the boundary layer and, hence, improves the sensitivity of the sensors [Steinmann et al., 2006]. Currently our hair sensors are fabricated on top of a flat substrate. One possibility to obtain conical shaped substrate or at least to slightly bend the substrate is by fabricating hair sensors on top of flexible substrates. Such a substrate can be made of e.g. SU-8 material (or other cleanroom compatible flexible material) by reversing the fabrication process of the hair sensor and using a carrier wafer. This carrier wafer can be removed before the hair fabrication process is completed. Once the hair sensors are fabricated, a cylindrical shaped carrier can be used to mount them on top (i.e. mimicking crickets' cerci).

The fabrication process can be started with the deposition and patterning of stacked layers of SiRN, poly-silicon and then stoichiometric silicon nitride (reversing sequence of the traditional fabrication process of hairs, i.e. see chapter 2) on top of the carrier wafer. The carrier signal electrodes are afterwards formed by sputtering and patterning an aluminium layer. Spinning SU-8 is then performed to form the flexible substrate for the same thickness of the needed substrate. Subsequently the carrier substrate is removed and another aluminium layer is sputtered and patterned on top of the SiRN layer to shape the top electrode of the hair sensor capacitors. The traditional fabrication process of hair sensors (i.e. double lithography process of two SU-8 layers and sacrificial layer etching) is used to make the hair shaft and release the structure.

However, various challenges might appear; such as the best material for the flexible substrate and the bending extent allowed before the electrical connections or layers stack (which forms the hair sensor) will crack. Additionally, the layers stack in the hair-sensor is partly deposited at high temperatures which may result in stress-gradients and high stress-concentration areas, both hampering the proper functioning of the sensors.

7.2.3 Flow field measurements

3D airflow measurements

We have shown in this work that with linear arrays of hairs we are able to perform dipole field measurements at position of the array and then to localize dipole sources. In these measurements the only unknown parameter was position of the source (i.e. x, y coordinates) while the other source parameters were predefined (e.g. sphere radius, oscillation frequency and displacement amplitude). More advanced systems can be constructed, e.g. with multi lateral-lines oriented in different directions to perform dipole field measurements in 3D, resolving more unknown parameters (e.g. number of sources, separation distance in between, their orientations and sizes). Additionally, the simultaneous measurement of both the parallel and perpendicular flow-velocity components provides us with more information of the dipole field. Hence, potentially a 3D image for the flow profile may be constructed at the position of the array and an increased number of source(s) parameters may be extracted.

Spatio-temporal flow pattern

Airflow patterns may be investigated with a larger number of hair-sensors than shown in this thesis. This would allow us to recognize specific events and flow-signatures of moving objects by following the development of the flow profile in position and time. Whereas array signal processing (beamforming) may be appropriate to determine deterministic (model based) patterns, larger flexibility may be obtained by using artificial neural networks (ANN). ANN is the most popular and powerful pattern recognition technique presently used in different disciplines [Wasserman 1989 & Bishop 1995]. It is widely implemented in array processing to classify, determine and eventually recognize different patterns and hence to take an action based on prior knowledge of the input signals (i.e. signals template) or their statistical properties. The proper use of descriptive features as input vector to the network is essential for the accurate recognition and minimizing the processing time.

This can be applied, for example, to the source localization mechanism used in the ALLS or with different array shapes. Pattern recognition techniques can be used (with the help of ASP techniques) to determine source parameters, number of sources and their orientation using the spatio-temporal flow field measurements. A high-density hair-sensor array with clever interfacing (i.e. FDM, see Figure 7.5) such a system can be, for example, used for constructing live and high-resolution flow-field images to detect specific flow phenomena (see Figure 7.6). This could be beneficial for biologists to understand nature, for engineers to develop systems for guiding purposes in robotics applications even in total darkness, or for the visualization of flow patterns (i.e. a replacement for the high-speed camera, e.g. see Figure 7.6). Consequently, this further expands the biomimetic approach (which has been already used in the design of the artificial hair flow-sensor) to the data processing stage of the array signals towards more perceptive use of flow-fields.

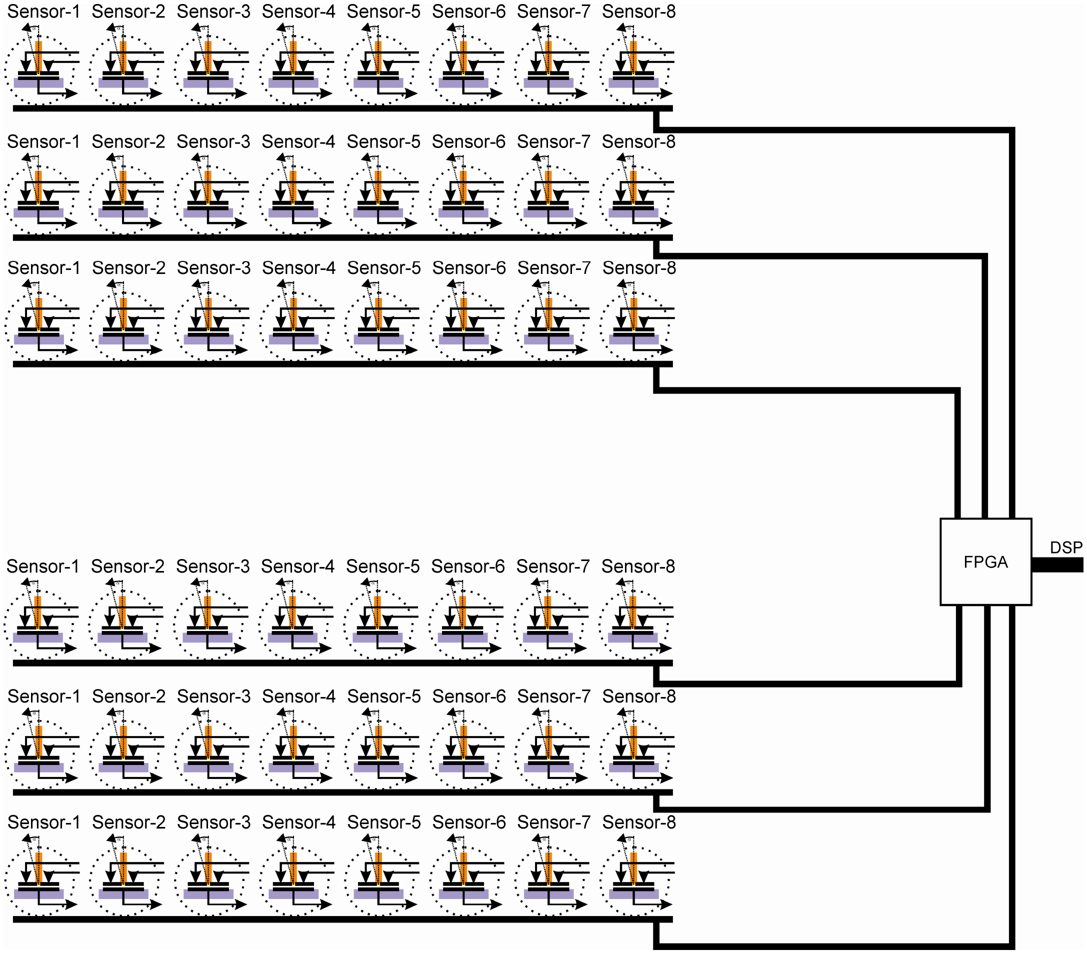

Figure 7.5: Schematic representing the basics of a 'flow camera'. High-density arrays of artificial hair-based flow-sensors with FDM array addressing can be used either in flow pattern recognition or in visualizing airflow. A high-speed central processing unit can be used to perform the online data analysis.

Figure 7.6: Cricket escaping from major impact warned by the spatio-temporal airflow signature produced by the approaching piston (Image taken from high-speed footage courtesy of Jerome Casas, IRBI, Université de Tours).

In conclusion, the work presented in this thesis has brought sensitive hair-sensors, arranged in single-chip arrays, read-out simultaneously in parallel and has proven the feasibility of bio-inspired flow-cameras. However, although flow-field data-collection by these arrays is an important step, the possibilities to extend on the work are large. More information (3D) and bio-inspired data-processing may open up an entire class of perceptive tasks that can be performed by these systems.

7.3 References

[Bishop 1995] Bishop, C.M. (1995) “Neural Networks for Pattern Recognition”, Oxford: Clarendon Press.

[Droogendijk et al., 2010] Droogendijk, H. & Krijnen, G.J.M. (2010) “Parametric Amplification and Stochastic Resonance in Bio-Inspired Hair Flow Sensors” In the Sense of Contact 12, Zeist, The Netherlands. FHI Federatie Van Technologiebranches.

[Gnatzy et al., 1980] Gnatzy, W. & Tautz, J. (1980) “Ultrastructure and mechanical properties of an insect mechanoreceptor: Stimulus transmitting structures and sensory apparatus of the cercal filiform hairs of gryllus”, Cell Tissue Res, 213, pp.441-463.

[Jaganatharaja 2011] Jaganatharaja, R.K. (2011) “Cricket inspired flow-sensor arrays”, Ph.D. thesis, University of Twente, The Netherlands.

[Murakami et al., 2005] Murakami, J., Kidachi, T., Haseyama, M. & Shimozawa, T. (2005) "Sample size dependence of estimation error of information carried by neuronal spike train", Systems and Computers in Japan, 36, pp. 84-95

[Sedra et el., 1987] Sedra, A.S., & Smith, K.S. (1987) “Microelectronic circuits”, 2nd edition (New York: Holt, Rinehart and Winston).

[Shimozawa et al., 1984] Shimozawa, T. & Kanou, M. (1984) “Varieties of filiform hairs:Range fractionation by sensory afferents and cercal interneurons of a cricket”, J Comp. Physiol. A, 155, pp.485-493.

[Steinmann et al., 2006] Steinmann, T., Casas, J., Krijnen, G. & Dangles, O. (2006) "Air-flow sensitive hairs: Boundary layers in oscillatory flows around arthropod appendages", Journal of Experimental Biology, 209, pp. 4398-4408.

[Wasserman 1989] Wasserman, P.D. (1989) “Neural Computing: Theory and Practice”, van Nostrand / Reinhold, New York.

Chapter

8

SUMMARY

Nature offers human being elegant solutions for various engineering problems. Mimicking principles and designs offered by nature enables humans to better understand related phenomena and may help to provide better-engineered systems. Hair-based flow sensing in crickets is an example of a biological system that has recently attracted great interest from engineers. With this system, crickets are able to detect approaching spiders utilizing the airflow generated by the spider motion. With arrays of these hair-based flow sensors (i.e. cerci) crickets can detect tiny airflows -using energies bordering thermal noise-, airflow direction and perceive meaningful information from it. This inspired engineers to develop an artificial system, a flow camera, as an alternative to more traditionally engineered systems.

A bio-inspired hair flow-sensor has been realized in our group exploiting Micro-Electro-Mechanical Systems (MEMS) fabrication techniques using surface micro-machining technology. It consists of a hair shaft made from SU-8 material standing on top of a suspended silicon-rich nitride membrane. A pair of electrodes, positioned on top of the membrane, forms two integrated capacitors with the substrate to measure airflows capacitively. Due to the airflow drag torque acting on the hair shaft, the membrane tilts which accordingly generates capacitance changes in the integrated capacitors at both halves of the membrane. These capacitance changes are detected differentially representing a measurement for the airflow at the position of the hair shaft. The advantage of using a hair-like sensor design is that it provides local measurements for the fluid velocity without considerably disturbing the flow by its presence.

Aiming at performing spatio-temporal pattern recognition of flow events, arrays of these hairs can be advantageous in extracting meaningful information from distributed measurements rather than just performing (averaged) local measurements at the single position of one hair-sensor. This is challenging since it requires a sensory system composed of high-density hair-sensor arrays with independent elements, all measured in parallel. Each individual element should be highly sensitive to minute amplitudes of airflow at sufficiently large bandwidth.

The work reported on in this thesis addresses the track to develop highly-sensitive sensor-array systems (made of artificial hair sensors) towards fulfilling the requirements for an air-flow camera. Such a system consists of artificial hair-based flow-sensors as basic units, arranged in array structures. The detection limit for each individual hair element is improved enabling us to measure the capacitance changes resulting from the rotation of a single-hair sensor. This opens up possibilities to make electrically identifiable hairs in a high-density single-chip array benefiting from SOI wafer technology. Hair-sensors were interrogated individually and simultaneously, without deteriorating the performance of the individual sensor, benefiting from Frequency Division Multiplexing (FDM) as interfacing technique. The ability of the hairs to perform useful flow field measurements was examined by means of dipole field observations. The hair-sensor array was shaped as an artificial lateral-line system, inspired by the lateral-line array system in fish, and used to measure the dipole field and to localize dipole sources. The localization process was either based on determination of the characteristics of the dipole field or by beamforming techniques. Summarizing all developments, a single-chip array of hair sensors was applied in observing the dipole field in time and space (i.e. spatio-temporal flow pattern) while using FDM. Determining the dipole field characteristics and thereby source parameters allows for the assessment of the capability of the artificial hair-sensor array in measuring flow fields.

Even with all of the advancements and developments in the design, fabrication and realization of the artificial hair sensor arrays, it is still challenging to achieve the performance of the natural hair sensory system of crickets. However, the current research could shed some light on the detection and processing of flow phenomena in nature. Additionally, it can be considered one-step further with the tendency of constructing live aerodynamic images. We believe that our target, the development of air-flow camera’s to be applied in spatio-temporal fluid monitoring, is achievable using MEMS hair-sensors hand-in-hand with insights from biology.

Chapter

9

SAMENVATTING

Een elegante oplossing voor een technisch probleem kan in vele gevallen in de natuur worden gevonden. Door principes en structuren uit de natuur na te bootsen is de mens vaak in staat bijbehorende fenomenen beter te begrijpen en de hieruit voortvloeiende kennis toe te passen. Een voorbeeld van een biologisch systeem dat veel aandacht heeft gekregen van ingenieurs is het luchtstromingsmeetsysteem waar krekels over beschikken. Middels gevoelige haartjes, genaamd cerci, zijn krekels in staat om een naderende spin te detecteren op basis van de gegenereerde luchtverplaatsing. Door hele series van haarstromingsensoren te gebruiken kan een krekel niet alleen zeer kleine luchtstromingen detecteren, maar ook informatie verkrijgen uit het gemeten stromingsprofiel. Dit alles vindt plaats bij energieën in de orde van de thermische mechanische ruis van de haarstromingssensoren. Al deze eigenschappen van dit sensorsysteem hebben ingenieurs geïnspireerd om een zogenaamde luchtstromings-camera te ontwikkelen voor het meten van spatio-temporele stroming, met het systeem van de krekel als uitgangspunt.

In onze vakgroep is een dergelijke haarstromingssensor ontwikkeld met behulp van Micro-Electrisch-Mechanisch-Systeem (MEMS)-technologie. De sensor bestaat uit een haarschacht gemaakt van SU-8, gepositioneerd op een beweegbaar membraan van silicium-rijk nitride. Op dit membraan en op het substraat van de sensor zijn electrodes gerealiseerd, waarmee het mogelijk is om de luchtstroming te meten door de capaciteit tussen de electrodes te meten. Ten gevolge van de luchtstroming en bijbehorende viskeuze krachten staat er een moment op de haarschacht. Hierdoor zal het membraan onder een hoek worden gebracht met een verandering van de capaciteitswaarde als resultaat. Door het verschil in waarde van beide condensatoren differentieel te meten is de positie van de haarschacht te herleiden. Een groot voordeel van het gebruik van een haargebaseerde stromingsensor is dat het mogelijk is lokale metingen te verrichten zonder het stromingsprofiel significant te verstoren.

Om spatio-temporele patroonherkenning in luchtstromingen te bewerkstelligen/ verwezelijken, kan een reeks aan sensoren een beduidend voordeel bieden ten opzichte van het meten met slechts een enkele haarsensor. Het meten met een reeks sensoren geeft een uitdaging, omdat dit een sensorsysteem vereist bestaande uit series van zeer gevoelige en wijdbandige haarsensoren met een hoge plaatsingsdichtheid. Bovendien opereert elke haarsensor parallel en onafhankelijk.

Dit onderzoek behandelt de ontwikkeling van deze reeks van zeer gevoelige haarstromingssensoren om uiteindelijk een stromingscamera te realiseren. Een dergelijk systeem bevat kunstmatige haarstromingssensoren als basiselementen, geplaatst in een bepaalde configuratie. De gevoeligheid van elke individuele sensor is verbeterd, zodanig dat de verandering in condensatorwaardes van slechts één haarschacht goed te meten zijn. Dit is mogelijk door gebruik te maken van Silicon-on-Insulator (SOI)-wafer technologie, met als perspectief series van elektrisch uitleesbare sensoren te realiseren met een hoge plaatsingsdichtheid. De uitlezing van elke individuele haarstromingssensor is uitgevoerd met behulp van Frequentie Divisie Multiplexing (FDM), zonder de prestaties van een andere willekeurige sensor te beïnvloeden. Om te toetsen of hiermee een luchtprofiel gemeten kan worden is de sensorrepons geobserveerd tijdens het aanbrengen van een dipool stromingsveld. Hiervoor is een reeks van haarsensoren als een kunstmatig laterale lijn gepositioneerd, geïnspireerd door de laterale lijn van de vis. Het aangebrachte dipoolveld is hierbij gemeten, evenals het lokaliseren van de bron van dit veld. Het lokaliseren van deze bron werd enerzijds gedaan door te kijken naar de karakteristieken van het dipoolveld, anderzijds door gebruik te maken van bundelvormingtechnieken.

Zelfs met alle ontwikkelingen en verbeteringen in ontwerp, fabricage en realisatie van reeksen haarstromingssensoren is het nog steeds een uitdaging om dezelfde prestaties te kunnen leveren als het sensorsysteem van de krekel. Echter, dit onderzoek geeft wel inzicht in het detecteren en verwerken van luchtstromingsfenomen in en door de natuur. Bovendien kan dit werk een bijdrage leveren om in de toekomst real-time luchtstromingsprofileen te meten en weer te geven. Door inzichten vanuit de biologie te combineren met onze haarstromingssensoren moet het mogelijk zijn om het uiteindelijke doel, een luchtstromingscamera, te realiseren.

Chapter

10

APPENDICES

10.1 Abbreviations

ADC: Analog-to-Digital Converter
ALLS: Artificial Lateral-Line System
AM: Amplitude Modulation
ANN: Artificial Neural Networks
ASP: Array Signal Processing
Bio-EARS: Bio-inspired Engineering of ARray Sensors
CN: Canal Neuromast
CCD: Charge Coupled Devices
CICADA: Cricket Inspired perCeption And Decision Automata
CILIA: Customized Intelligent Life-Inspired Arrays
CMOS: Complementary Metal-Oxide-Semiconductor
CW: continuous wave

DDS: Direct Digital Synthesis
DFDM: Double Frequency Division Multiplexing
DoA: Direction-of-Arrival
EEG: Electro-Encephalo-Graphy
EMI: Electromagnetic interference
FDM: Frequency Division Multiplexing
FFT: Fast Fourier Transform
FMCW: Frequency-Modulated Continuous Wave
FoM: Figure of Merit
FWHM: Full-Width Half-Maximum
GUI: Graphical User Interface
LDV: Laser Doppler Velocimetry
LED: Light Emitting Diode
LLS: Lateral-Line System
LPCVD: Low-Pressure Chemical Vapour Deposition
MEMS: Micro-Electro-Mechanical Systems
MRI: Magnetic Resonance Images
Op-amp: Operational amplifier
OTDR: Optical Time-Domain Reflectometer
PCB: Printed Circuit Board
PDMA: Plastic Deformation Magnetic Assembly
PIV: Particle Image Velocimetry
QAM: Quadrature Amplitude Modulation
RIE: Reactive-Ion Etching
SDM: Space Division Multiplexing
SLE: Sacrificial layer Etching
SN: Superficial Neuromast
SNR: Signal-to-Noise Ratio
SOI: Silicon-On-Insulator
SQUID: Superconducting QUantum Interference Device
TAG: Terminal Abdominal Ganglion
TDM: Time division multiplexing
TES: Transition Edge Sensor
VTR: vertical-to-torsional ratio

10.2 Process flow of hair sensor

10.2.1 Substrate selection

Step	Process	
1	Substrate selection – SOI (#subs016)	TST Supplier: 0kmetic Diameter: 100.0 mm ± 0.5 mm Device layer: 25 µm ± 0.5 µm 0xide layer: 1 µm ± 0.1 µm Thickness: 380 µm ± 0.5 µm Dopant: Boron

10.2.2 Patterning of the device layer – SOI

Step	Process	
2	Standard cleaning HNO_3 + 1% HF dip (#clean1003)	NL-CR-WB14 $HN0_3$ (99%) Selectiepur: MERCK $HN0_3$ (69%) VLSI: MERCK • Beaker 1: fumic $HN0_3$ (99%), 5 min • Beaker 2: fumic $HN0_3$ (99%), 5 min • Quick Dump Rinse > 10.5 MΩ • Beaker 3: boiling (95 °C) $HN0_3$ (69%), 10 min • Quick Dump Rinse > 10.5 MΩ • Beaker 4: HF (1%), 1 min • Quick Dump Rinse > 10.5 MΩ • Spin drying
3	Standard lithography Olin 907-17 (#lith1002) Dehydration bake	NL-CR Continue immediately with priming the step! NL-CR / WB 21-22 • Hotplate: 120 °C: 5 min
	Priming (HMDS) Coating (OLIN 907-7)	Spincoater • Spin program: 4 (4000 rpm, 30 sec) Primus Spinner • Spin program: 4 (4000 rpm, 30 sec, 1.7 µm) • Prebake (95 °C): 90 sec
	Alignment & Exposure (Olin 907-17)	Electronic Vision Group 620 Mask Aligner • Hg-lamp: 12 mW/cm^2 • Exposure time: 4 sec • Mask: TRENCH
	Development (Olin 907-17)	Developer: 0PD4262 • After exposure bake (120 °C): 60 sec • Time: 30 sec in beaker 1 • Time: 15–30 sec in beaker 2 • Quick Dump Rinse > 10.5 MΩ • Spin drying
	Postbake (Olin 907-17) Inspection by optical microscope	• Hotplate: 120 °C: 0 min NL-CR / Nikon Microscope Dedicated microscope for lithography inspection
	Comments	No postbake required for B-HARS

4	Plasma etching of Si B-HARS (#etch158)	NL-CR / Adixen AMS 100 SE Program: . . . • SF_6 flow: 250 sccm • C_4F_8 flow: 200 sccm • Time: 3/1 s • Priority: 2/1 • ICP: 1500 W • CCP (pulsed LF): 80 W • 0n/off: 10/90 (ms) • SH: 200 mm • APC: 100% • He: 10 mbar • Electrode: 10 °C • Etch-rate Si: ± 1–5 µm/min • Etch-rate PR: ± 25–50 nm/min Thickness: 25 µm Etch-time: 10 min # of dummies: 1
5	Standard cleaning after DRIE (#clean1008)	CR-NL Removal of 0lin PR and FluoroCarbon residue (metal free)
	Stripping of Olin PR by oxygen plasma (Tepla 300)	CR-NL / Tepla 300 Barrel Etcher (2.45 GHz) Ultra clean system only (no metals except Al) • See list with recipes in cleanroom • O_2 flow: 200 sccm (50%) • Power: up to 1000 W • Pressure: 1 mbar
	Stripping resist/cleaning in “Piranha” private use	NL-CR / WB 9 $H_2SO_4:H_2O_2$ (3:1) vol% • Add H_2O_2 slowly(!) to H_2SO_4; exothermic process! • Adjust the hotplate temperature to 85 °C, the temperature will increase to 130 °C • Cleaning temperature: 130 °C • Time 10–30 min • Quick Dump Rinse > 10.5 MΩ • Spin drying
	Standard cleaning HNO_3	• Beaker 1: fumic $HN0_3$ (99%), 5 min • Beaker 2: fumic $HN0_3$ (99%), 5 min • Quick Dump Rinse > 10.5 MΩ • Beaker 3: boiling (95 °C) $HN0_3$ (69%), 10 min • Quick Dump Rinse > 10.5 MΩ • Beaker 4: HF (1%), 1 min • Quick Dump Rinse > 10.5 MΩ • Spin drying

	Dry oxidation of Silicon at 800 °C	NL-CR / Furnace B3 Standby temperature: 800 °C • Program: DOX-800 • Temperature: 800 °C • Gas: O_2 • Flow: 2 L/min • Time: 30 min
	Etching in HF 1%	NL-CR / WB 15 • Beaker HF (1%) • Time: until hydrofobic surface • Quick Dump Rinse > 10.5 MΩ • Spin drying

10.2.3 LPCVD of Si3 N4 (200 nm)

Step	Process	
6	Standard cleaning HNO_3 + 1% HF dip (#clean1003)	NL-CR-WB14 $HN0_3$ (99%) Selectiepur: MERCK $HN0_3$ (69%) VLSI: MERCK • Beaker 1: fumic $HN0_3$ (99%), 5 min • Beaker 2: fumic $HN0_3$ (99%), 5 min • Quick Dump Rinse > 10.5 MΩ • Beaker 3: boiling (95 °C) $HN0_3$ (69%), 10 min • Quick Dump Rinse > 10.5 MΩ • Beaker 4: HF (1%), 1 min • Quick Dump Rinse > 10.5 MΩ • Spin drying
7	LPCVD Si_3N_4 Stoichiometric (#film101)	NL-CR / Tempress LPCVD F1 A flush purge of 2.5 hr is needed before deposition Tube: F1 • Program: Nitr01 • SiH_2Cl_2 flow: 22 sccm • NH_3 flow: 66 sccm • Temperature: 800 °C • Pressure: 200 mTorr • Stress: 1.09 ± 40 GPa • Deposition rate: 4–6 nm/min • N_f: 2.008 Thickness: 200 nm Deposition time:42 min # of dummies: 1
8	Optical inspection of LPCVD layers (#metro013)	NL-CR / Cold Light Source Particle inspection using Cold Light Source Layers: TEOS SiO_2, SiO_2, Si_3N_4, poly-Si Procedure: Check wafer for particles using streaking light

9	Ellipsometer measurement (#metro107)	NL-CR / Plasmos and Woollam Ellipsometer First Woollam: • Cauchy model • Fit on A, B and k • Read N_f and layer thickness t Then Plasmos: • Use N_f and t from Woollam • Raster 7x7 (-41,-41) – (41,41) • Wafer diameter 100 mm, edge 5.0 mm • 37 measurement points

10.2.4 LPCVD of poly-Si and annealing

Step	Process	
10	Micro balance measurement (#metro106)	NL-CR / Satorius Micro Balance
11	Standard cleaning HNO_3 + 1% HF dip (#clean1003)	NL-CR-WB14 $HN0_3$ (99%) Selectiepur: MERCK $HN0_3$ (69%) VLSI: MERCK • Beaker 1: fumic $HN0_3$ (99%), 5 min • Beaker 2: fumic $HN0_3$ (99%), 5 min • Quick Dump Rinse > 10.5 MΩ • Beaker 3: boiling (95 °C) $HN0_3$ (69%), 10 min • Quick Dump Rinse > 10.5 MΩ • Beaker 4: HF (1%), 1 min • Quick Dump Rinse > 10.5 MΩ • Spin drying
12	LPCVD Poly-Si – 590 °C (#film105)	NL-CR / Tempress LPCVD Tube: F2 Program: senspoly • SiH_4 flow: 50 sccm • Temperature: 590 °C • Pressure: 250 mTorr • Deposition rate: 3.7 nm/min • Stress: 30 MPa Put dummy in center of furnace Thickness: ≥1500 nm Deposition time: 7 hr # of dummies: 3
	Comments	Make sure trench is completely filled (inspection before and after), use margin of 10–20%

13	Annealing at 1050 °C with N_2 (#therm105)	NL-CR / Furnace B3 Standby temperature: 800 °C • Program: ANN1050C • Temperature: 1050 °C • Gas: N_2 • Flow: 1 L/min • Ramp: 10 °C /min Annealing time: 1 hr
	Comments	To prevent pinholes and cracks during high-temperature processing
14	Inspection by optical microscope (#metro101)	NL-CR / Nikon Microscope Dedicated microscope for lithography inspection
15	Micro balance Measurement (#metro106)	NL-CR / Satorius Micro Balance
	Comments	Calculate thickness (26.5 nm/mg for poly-Si)

10.2.5 Partial oxidation of polysilicon

Step	Process	
16	Standard cleaning HNO_3 (#clean1001)	NL-CR-WB14 $HN0_3$ (99%) Selectiepur: MERCK $HN0_3$ (69%) VLSI: MERCK • Beaker 1: fumic $HN0_3$ (99%), 5 min • Beaker 2: fumic $HN0_3$ (99%), 5 min • Quick Dump Rinse > 10.5 MΩ • Beaker 3: boiling (95 °C) $HN0_3$ (69%), 10 min • Quick Dump Rinse > 10.5 MΩ • Spin drying
17	Wet Oxidation at 1150 °C of Silicon (#film114)	NL-CR / Furnace B2 Standby temperature: 800 °C Check water level of bubbler • Program: WET1150B • Temperature: 1150 °C • Gas: H_2O + N_2 (Bubbler) Thickness: ≥400 nm Annealing time: ≥2 hr # of dummies: 1
	Comments	Check poly-Si thickness; total time > 4 hr

18	Ellipsometer measurement (#metro107)	NL-CR / Plasmos and Woollam Ellipsometer First Woollam: • Cauchy model • Fit on A, B and k • Read N_f and layer thickness t Then Plasmos: • Use N_f and t from Woollam • Raster 7x7 (-41,-41) – (41,41) • Wafer diameter 100 mm, edge 5.0 mm • 37 measurement points
19	Etching BHF (1:7) SiO_2 (#etch124)	NL-CR-WB15 Use dedicated beaker BHF (1:7) metal free • Quick Dump Rinse < 0.1 µS • Spin drying Etch-rate thermal $Si0_2$ = 60–80 nm/min Etch-rate PECVD $Si0_2$ = 125 nm/min Etch-rate TEOS $Si0_2$ = 180 nm/min Thickness: ≥900 nm Etch-time: ≥16 min # of dummies: 1
	Comments	Check hydrophobicity (forming of droplets)
20	Standard cleaning HNO_3 (#clean1001)	NL-CR-WB14 $HN0_3$ (99%) Selectiepur: MERCK $HN0_3$ (69%) VLSI: MERCK • Beaker 1: fumic $HN0_3$ (99%), 5 min • Beaker 2: fumic $HN0_3$ (99%), 5 min • Quick Dump Rinse > 10.5 MΩ • Beaker 3: boiling (95 °C) $HN0_3$ (69%), 10 min • Quick Dump Rinse > 10.5 MΩ • Spin drying
21	Wet Oxidation at 1150 °C of Silicon (#film114)	NL-CR / Furnace B2 Standby temperature: 800 °C Check water level of bubbler • Program: WET1150B • Temperature: 1150 °C • Gas: $H_2O + N_2$ (Bubbler) Thickness: 0–400 nm Annealing time: 0–2 hr # of dummies: 1
22	Ellipsometer measurement (#metro107)	NL-CR / Plasmos and Woollam Ellipsometer First Woollam: • Cauchy model • Fit on A, B and k • Read N_f and layer thickness t Then Plasmos: • Use N_f and t from Woollam • Raster 7x7 (-41,-41) – (41,41) • Wafer diameter 100 mm, edge 5.0 mm • 37 measurement points

23	Etching BHF (1:7) SiO_2 (#etch124)	NL-CR-WB15 Use dedicated beaker BHF (1:7) metal free • Quick Dump Rinse < 0.1 µS • Spin drying Etch-rate thermal $Si0_2$ = 60–80 nm/min Etch-rate PECVD $Si0_2$ = 125 nm/min Etch-rate TE0S $Si0_2$ = 180 nm/min Thickness: 0–400 nm Etch-time: 0–18 min # of dummies: 1
	Comments	Check hydrofobicity (forming of droplets)
24	Micro balance measurement (#metro106)	NL-CR / Satorius Micro Balance
	Comments	Till desired gap is achieved

10.2.6 Poly-Si patterning – Bumps

Step	Process	
25	Standard cleaning HNO_3 + 1% HF dip (#clean1003)	NL-CR-WB14 $HN0_3$ (99%) Selectiepur: MERCK $HN0_3$ (69%) VLSI: MERCK • Beaker 1: fumic $HN0_3$ (99%), 5 min • Beaker 2: fumic $HN0_3$ (99%), 5 min • Quick Dump Rinse > 10.5 MΩ • Beaker 3: boiling (95 °C) $HN0_3$ (69%), 10 min • Quick Dump Rinse > 10.5 MΩ • Beaker 4: HF (1%), 1 min • Quick Dump Rinse > 10.5 MΩ • Spin drying
26	Standard lithography Olin 907-17 (#lith1002)	NL-CR Continue immediately with priming the step!
	Dehydration bake Priming (HMDS)	NL-CR / WB 21-22 • Hotplate: 120 °C: 5 min
	Coating (OLIN 907-17)	Spincoater • Spin program: 4 (4000 rpm, 30 sec) Primus Spinner • Spin program: 4 (4000 rpm, 30 sec, 1.7 µm) • Prebake (95 °C): 90 sec
	Alignment & Exposure (Olin 907-17)	Electronic Vision Group 620 Mask Aligner • Hg-lamp: 12 mW/cm^2 • Exposure time: 4 sec • Mask: BUMPS

	Development (Olin 907-17)	Developer: 0PD4262 • After exposure bake (120 °C): 60 sec • Time: 30 sec in beaker 1 • Time: 15–30 sec in beaker 2 • Quick Dump Rinse > 10.5 MΩ • Spin drying
	Postbake (Olin 907-17)	• Hotplate: 120 °C: 30 min
	Inspection by optical microscope	NL-CR / Nikon Microscope Dedicated microscope for lithography inspection
	Comments	Use SACRI for alignment; postbake 30 min
27	Plasma etching (slow) of Si (Tetske) (#etch193)	NL-CR / Tetske Dirty chamber Styros electrode • Electrode temperature: 10 °C • CHF_3 flow: 25 sccm • O_2 flow: 5 sccm • Pressure: 10 mTorr • Power: 60 W • Etch-rate SiRN: ± 55 nm/min • Etch-rate SiO_2: ± 33 nm/min • Etch-rate 0lin-PR: ± 60 nm/min • Etch-rate Si: ± 15–25 nm/min Thickness: 100 nm Etch-time: 4 min, # of dummies: 1
28	Stripping of Olin PR by oxygen plasma (Tepla 300) (#lith142)	CR 125 A / Tepla 300 Barrel Etcher (2.45 GHz) Ultra clean system only (no metals except Al) • See list with recipes in cleanroom • O_2 flow: 200 sccm (50%) • Power: up to 1000 W • Pressure: 1 mbar
	Comments	Stripping of “inert skin” of PR caused by DRIE, RIE and ion implantation. Time 10 min.
29	Stripping of Olin PR – Standard (#lith116)	NL-CR-WB14 HNO_3 (99%) • Time: 20 min or 100% removal of PR • Quick Dump Rinse > 10.5 MΩ • Spin drying
30	Surface profile measurement (#metro105)	NL-CR / Veeco Dektak 8 Scan length: 80 mm for a 4-inch wafer Stylus force: 5 mg Duration: 60 sec Profile: Hills and valleys Deflection at 40 mm for stress calculation Scan 1: Middle of wafer, perpendicular to flat Scan 2: Middle of wafer, parallel to flat Measure: Along coded (convex!) side

10.2.7 Poly-Si patterning – Trenches

Step	Process	
31	Standard cleaning HNO_3 + 1% HF dip (#clean1003)	NL-CR-WB14 $HN0_3$ (99%) Selectiepur: MERCK $HN0_3$ (69%) VLSI: MERCK • Beaker 1: fumic $HN0_3$ (99%), 5 min • Beaker 2: fumic $HN0_3$ (99%), 5 min • Quick Dump Rinse > 10.5 MΩ • Beaker 3: boiling (95 °C) $HN0_3$ (69%), 10 min • Quick Dump Rinse > 10.5 MΩ • Beaker 4: HF (1%), 1 min • Quick Dump Rinse > 10.5 MΩ • Spin drying
32	Standard lithography Olin 907-17 (#lith1002)	NL-CR Continue immediately with priming the step!
	Dehydration bake Priming (HMDS) Coating (OLIN 907-17)	NL-CR / WB 21-22 • Hotplate: 120 °C: 5 min Spincoater • Spin program: 4 (4000 rpm, 30 sec) Primus Spinner • Spin program: 4 (4000 rpm, 30 sec, 1.7 µm) • Prebake (95 °C): 90 sec
	Alignment & Exposure (Olin 907-17)	Electronic Vision Group 620 Mask Aligner • Hg-lamp: 12 mW/cm^2 • Exposure time: 4 sec • Mask: SACRI
	Development (Olin 907-17) Postbake (Olin 907-17) Inspection by optical microscope	Developer: 0PD4262 • After exposure bake (120 °C): 60 sec • Time: 30 sec in beaker 1 • Time: 15–30 sec in beaker 2 • Quick Dump Rinse > 10.5 MΩ • Spin drying • Hotplate: 120 °C: 30 min NL-CR / Nikon Microscope Dedicated microscope for lithography inspection
	Comments	Postbake 30 min

33	Chamber cleaning by O_2 plasma (Tetske) (#etch198)	NL-CR / Tetske Dirty chamber Styros electrode • Electrode temperature: 10 °C • O_2 flow: 50 sccm • Pressure: 50 mTorr • Power: 100 W • V_{dc}: -600 V • Load/tune: 65/35 • Time: 10 min • Chamber is clean when plasma color is white
34	Plasma etching of polysilicon (Tetske) (#etch107)	NL-CR / Tetske Clean chamber Styros electrode • Electrode temperature: 10 °C • SF_6 flow: 30 sccm • CHF_3 flow: 7 sccm • O_2 flow: 11 sccm • Pressure: 100 mTorr • Power: 60 W • Etch-rate: ± 360 nm/min Thickness: 600–1000 nm Etch-time: 2.5–4.5 min # of dummies: 0
	Comments	End of etching is done on visual inspection
35	Stripping of Olin PR by oxygen plasma (Tepla 300) (#lith142)	CR 125 A / Tepla 300 Barrel Etcher (2.45 GHz) Ultra clean system only (no metals except Al) • See list with recipes in cleanroom • O_2 flow: 200 sccm (50%) • Power: up to 1000 W • Pressure: 1 mbar
	Comments	Stripping of “inert skin” of PR caused by DRIE, RIE and ion implantation. Time: 10 min.
36	Stripping of Olin PR – Standard (#lith116)	NL-CR-WB14 $HN0_3$ (99%) • Time: 20 min or 100% removal of PR • Quick Dump Rinse > 10.5 MΩ • Spin drying
37	Surface profile measurement (#metro105)	NL-CR / Veeco Dektak 8 Scan length: 80 mm for a 4-inch wafer Stylus force: 5 mg Duration: 60 sec Profile: Hills and valleys Deflection at 40 mm for stress calculation Scan 1: Middle of wafer, perpendicular to flat Scan 2: Middle of wafer, parallel to flat Measure: Along coded (convex!) side

10.2.8 LPCVD of SiRN (1000 nm, membranes and springs)

Step	Process	
38	Standard cleaning HNO_3 + 1% HF dip (#clean1003)	NL-CR-WB14 $HN0_3$ (99%) Selectiepur: MERCK $HN0_3$ (69%) VLSI: MERCK • Beaker 1: fumic $HN0_3$ (99%), 5 min • Beaker 2: fumic $HN0_3$ (99%), 5 min • Quick Dump Rinse > 10.5 MΩ • Beaker 3: boiling (95 ^{o}C) $HN0_3$ (69%), 10 min • Quick Dump Rinse > 10.5 MΩ • Beaker 4: HF (1%), 1 min • Quick Dump Rinse > 10.5 MΩ • Spin drying
39	LPCVD SiRN – Uniform stress (#film143)	NL-CR / Tempress LPCVD Program: SiRN02 (uniform stress) Tube: G3 • SiH_2Cl_2 flow: 150 sccm • NH_3 flow: 50 sccm • Temperature: 830/850/870 ^{o}C • Pressure: 200 mTorr • Deposition rate: ± 6.6 nm/min (G3) • N_f: ± 2.18 • Stress (range): 200–280 MPa (G3) Thickness: 1000 nm Deposition time: 2 hr 30 min # of dummies: 1

10.2.9 SiRN patterning (membranes, springs and bottom electrode contact)

Step	Process	
40	Standard cleaning HNO_3 + 1% HF dip (#clean1003)	NL-CR-WB14 $HN0_3$ (99%) Selectiepur: MERCK $HN0_3$ (69%) VLSI: MERCK • Beaker 1: fumic $HN0_3$ (99%), 5 min • Beaker 2: fumic $HN0_3$ (99%), 5 min • Quick Dump Rinse > 10.5 MΩ • Beaker 3: boiling (95 ^{o}C) $HN0_3$ (69%), 10 min • Quick Dump Rinse > 10.5 MΩ • Beaker 4: HF (1%), 1 min • Quick Dump Rinse > 10.5 MΩ • Spin drying

41	Standard lithography Olin 908-35 (#lith1003) Dehydration bake Priming (HMDS)	NL-CR Continue immediately with priming the step! NL-CR / WB 21-22 • Hotplate: 120 °C: 5 min
	Coating (OLIN 908-35)	Spincoater • Spin program: 4 (4000 rpm, 30 sec) Primus Spinner • Spin program: 4 (4000 rpm, 30 sec, 3.5 µm) • Prebake (95 °C): 120 sec
	Alignment & Exposure (Olin 908-35)	Electronic Vision Group 620 Mask Aligner • Hg-lamp: 12 mW/cm^2 • Exposure time: 9 sec • Mask: MEMBR
	Development (Olin 908-35) Postbake (Olin 908-35)	Developer: 0PD4262 • After exposure bake (120 °C): 60 sec • Time: 30 sec in beaker 1 • Time: 15–30 sec in beaker 2 • Quick Dump Rinse > 10.5 MΩ • Spin drying • Hotplate: 120 °C: 30 min
	Inspection by optical microscope	NL-CR / Nikon Microscope Dedicated microscope for lithography inspection • Power: 100 W • V_{dc}: -600 V • Load/tune: 65/35 • Time: 10 min • Chamber is clean when plasma color is white
	Comments	Change to Olin908-35 to etch the entire layer of SiRN (1µm); Postbake 30 min
42	Chamber cleaning by O_2 plasma (Tetske) (#etch198)	NL-CR / Tetske Dirty chamber Styros electrode • Electrode temperature: 10 °C • O_2 flow: 50 sccm • Pressure: 50 mTorr

43	Plasma etching of SiN (Tetske) (#etch193)	NL-CR / Tetske Dirty chamber Styros electrode • Electrode temperature: 10 °C • CHF_3 flow: 25 sccm • O_2 flow: 5 sccm • Pressure: 10 mTorr • Power: 60 W • V_{dc}: -500 . . . -540 V • Load/tune: 53/36 • Etch-rate SiRN: ± 60 nm/min • Etch-rate $Si0_2$: ± 30 nm/min • Etch-rate 0lin-PR: ± 50 nm/min Thickness: ≥1200 nm Etch-time: 20 min # of dummies: 0
	Comments	End of etching is done on visual inspection
44	Stripping of Olin PR by oxygen plasma (Tepla 300) (#lith142)	CR 125 A / Tepla 300 Barrel Etcher (2.45 GHz) Ultra clean system only (no metals except Al) • See list with recipes in cleanroom • O_2 flow: 200 sccm (50%) • Power: up to 1000 W • Pressure: 1 mbar
	Comments	Stripping of “inert skin” of PR caused by DRIE, RIE and ion implantation. Time: 10 min.
45	Stripping of Olin PR – Standard (#lith116)	NL-CR-WB14 $HN0_3$ (99%) • Time: 20 min or 100% removal of PR • Quick Dump Rinse > 10.5 MΩ • Spin drying
46	Surface profile measurement (#metro105)	NL-CR / Veeco Dektak 8 Scan length: 80 mm for a 4-inch wafer Stylus force: 5 mg Duration: 60 sec Profile: Hills and valleys Deflection at 40 mm for stress calculation Scan 1: Middle of wafer, perpendicular to flat Scan 2: Middle of wafer, parallel to flat Measure: Along coded (convex!) side

10.2.10 Sputtering of Al (200 nm)

Step	Process	
47	Standard cleaning HNO_3 + 1% HF dip (#clean1003)	NL-CR-WB14 $HN0_3$ (99%) Selectiepur: MERCK $HN0_3$ (69%) VLSI: MERCK • Beaker 1: fumic $HN0_3$ (99%), 5 min • Beaker 2: fumic $HN0_3$ (99%), 5 min • Quick Dump Rinse > 10.5 MΩ • Beaker 3: boiling (95 ^{o}C) $HN0_3$ (69%), 10 min • Quick Dump Rinse > 10.5 MΩ • Beaker 4: HF (1%), 1 min • Quick Dump Rinse > 10.5 MΩ • Spin drying
48	Sputtering of Al – Resist compatible (Oxford) (#film129)	NL-CR / 0xford PL 400 Program: 3000 nm Al pos 1 • Power: 700 W • Pressure: 10 mTorr • Deposition rate: 82 nm/min Thickness: 200 nm Deposition time: 2 min 30 sec # of dummies:

10.2.11 Patterning of Al – Membrane

Step	Process	
49	Cleaning HNO_3 private use (#clean104)	NL-CR / WB 9-10 $HN0_3$ (99%) Selectipur: MERCK • Beaker: $HN0_3$ (99%) • Time: > 10 min • Quick Dump Rinse > 10.5 MΩ • Spin drying
	Comments	No standard cleaning due to Al
50	Standard lithography Olin 907-17 (#lith1002)	NL-CR Continue immediately with priming the step!
	Dehydration bake Priming (HMDS) Coating (OLIN 907-17)	NL-CR / WB 21-22 • Hotplate: 120 ^{o}C: 5 min Spincoater • Spin program: 4 (4000 rpm, 30 sec) Primus Spinner • Spin program: 4 (4000 rpm, 30 sec, 1.7 µm) • Prebake (95 ^{o}C): 90 sec
	Alignment & Exposure (Olin 907-17)	Electronic Vision Group 620 Mask Aligner • Hg-lamp: 12 mW/cm^2 • Exposure time: 4 sec • Mask: ELECT

	Development (Olin 907-17)	Developer: 0PD4262 - After exposure bake (120 °C): 60 sec - Time: 30 sec in beaker 1 - Time: 15–30 sec in beaker 2 - Quick Dump Rinse > 10.5 MΩ - Spin drying
	Postbake (Olin 907-17) Inspection by optical microscope	- Hotplate: 120 °C: 1 hr NL-CR / Nikon Microscope Dedicated microscope for lithography inspection
	Comments	Postbake 1 hr → Prevent 0LIN to dissolve (partially) in 0PD4262
51	Etching of Al with OPD4262 (#Etch091)	NL-CR Etchant: 0PD4262 Etch-rate: 14 nm/min Use dummy first! Maximum etch-time about 6.5 min - Quick Dump Rinse > 10.5 MΩ - Spin drying Thickness: 100 nm Etch-time: 6 min # of dummies: 1
	Comments	User made 0PD4262
52	Stripping of polymers in HNO_3 multipurpose (#lith194)	NL-CR-WB6 $HN0_3$ (100%) - Beaker: $HN0_3$ (100%) > 10 min - Quick Dump Rinse > 10.5 MΩ - Spin drying

10.2.12 Backside patterning of SiRN

Step	Process	
53	Standard lithography Olin 908-35 (#lith1003)	NL-CR Continue immediately with priming the step!
	Dehydration bake Priming (HMDS) Coating (OLIN 908-35)	NL-CR / WB 21-22 - Hotplate: 120 °C: 5 min Spincoater - Spin program: 4 (4000 rpm, 30 sec) Primus Spinner - Spin program: 4 (4000 rpm, 30 sec, 3.5 µm) - Prebake (95 °C): 120 sec
	Alignment & Exposure (Olin 908-35)	Electronic Vision Group 620 Mask Aligner - Hg-lamp: 12 mW/cm^2 - Exposure time: 9 sec - Mask: TRENCH

	Development (Olin 908-35) Postbake (Olin 908-35)	Developer: 0PD4262 • After exposure bake (120 °C): 60 sec • Time: 30 sec in beaker 1 • Time: 15–30 sec in beaker 2 • Quick Dump Rinse > 10.5 MΩ • Spin drying • Hotplate: 120 °C: 30 min
	Inspection by optical microscope	NL-CR / Nikon Microscope Dedicated microscope for lithography inspection
	Comments	Change to Olin908-35 to etch the entire layer of SiRN (1µm); Postbake 30 min; Perform the steps “Priming” and “Coating” twice to protect the devices!
	Chamber cleaning by O_2 plasma (Tetske) (#etch198)	NL-CR / Tetske Dirty chamber Styros electrode • Electrode temperature: 10 °C • O_2 flow: 50 sccm
54	Plasma etching of SiN (Tetske) (#etch193)	NL-CR / Tetske Dirty chamber Styros electrode • Electrode temperature: 10 °C • CHF_3 flow: 25 sccm • O_2 flow: 5 sccm • Pressure: 10 mTorr • Power: 60 W • V_{dc}: -500 . . . -540 V • Load/tune: 53/36 • Etch-rate SiRN: ± 60 nm/min • Etch-rate $Si0_2$: ± 30 nm/min • Etch-rate 0lin-PR: ± 50 nm/min Thickness: ≥1200 nm Etch-time: 20 min # of dummies: 0
55	Comments	End of etching is done on visual inspection
	Stripping of Olin PR by oxygen plasma (Tepla 300) (#lith142)	CR 125 A / Tepla 300 Barrel Etcher (2.45 GHz) Ultra clean system only (no metals except Al) • See list with recipes in cleanroom • O_2 flow: 200 sccm (50%) • Power: up to 1000 W • Pressure: 1 mbar
56	Comments	Stripping of “inert skin” of PR caused by DRIE, RIE and ion implantation. Time 10 min.
57	Stripping of Olin PR – Standard (#lith116)	NL-CR-WB14 $HN0_3$ (99%) • Time: 20 min or 100% removal of PR • Quick Dump Rinse > 10.5 MΩ • Spin drying

58	Surface profile measurement (#metro105)	NL-CR / Veeco Dektak 8 Scan length: 80 mm for a 4-inch wafer Stylus force: 5 mg Duration: 60 sec Profile: Hills and valleys Deflection at 40 mm for stress calculation Scan 1: Middle of wafer, perpendicular to flat Scan 2: Middle of wafer, parallel to flat Measure: Along coded (convex!) side

10.2.13 SU-8 hairs

59	Standard lithography SU-8 100 (#lith1003) Dehydration bake	NL-CR NL-CR / WB 21-22 • Hotplate: 120 °C: 10 min
	Coating (SU-8 100) (Delta 20)	SüssMicroTec Spinner Delta 20 Experimental results: 8 – 1000 rpm – ± 380 µm
	Prebake (SU-8 100)	• Start @ 25 °C • 10 min @ 50 °C • 30 min @ 65 °C • 3 hr 30 min @ 95 °C • 5 °C /5 min down to 25 °C
	Alignment & Exposure (SU-8 100)	Electronic Vision Group 620 Mask Aligner • Exposure time: 160 sec • Proximity contact (≥20 µm) Use scotch tape on the mask and the proximity exposure mode (≥20 µm) to prevent sticking problems Mask: HAIR1
	After exposure bake (SU-8 100)	• Start @ 25 °C • 10 min @ 50 °C • 10 min @ 65 °C • 50 min @ 75 °C • 5 °C /5 min down to 25 °C
60	Standard lithography SU-8 100 (#lith1003) Coating (SU-8 100) (Delta 20)	NL-CR SüssMicroTec Spinner Delta 20 Experimental results: 8 – 1000 rpm – ± 380 µm
	Prebake (SU-8 100)	• Start @ 25 °C • 10 min @ 50 °C • 30 min @ 65 °C • 3 hr 30 min @ 95 °C • 5 °C /5 min down to 25 °C

	Alignment & Exposure (SU-8 100)	Electronic Vision Group 620 Mask Aligner • Exposure time: 160 sec • Proximity contact (≥20 µm) Use scotch tape on the mask and the proximity exposure mode (≥20 µm) to prevent sticking problems ; Mask: HAIR2
	After exposure bake (SU-8 100)	• Start @ 25 °C • 10 min @ 50 °C • 10 min @ 65 °C • 50 min @ 75 °C • 5 °C /5 min down to 25 °C
	Development (SU-8 100)	TC0 Spray Developer Developer: PGMEA (RER600, ARCH Chemicals) • Time: 25 cycles of 30 sec with spray gun • Time: 5 sec rinse with PGMEA bottle • Time: 5 sec rinse with IPA • Spin drying
	Hard bake (SU-8 100)	• Start @ 25 °C • 10 min @ 50 °C • 10 min @ 65 °C • 10 min @ 100 °C • 2 hr @ 120 °C • 5 °C /10 min down to 25 °C
	Comments	Use a metal tweezer during development
61	Inspection by optical microscope (#metro101)	NL-CR / Nikon Microscope Dedicated microscope for lithography inspection
	Comments	If necessary, use TEPLA 300E for removing residual SU-8 on the membrane

10.2.14 Sacrificial layer etching

Step	Process	
62	SLE of poly-Si by XeF_2 (#Etch1300) SLE of polysilicon by SF_6 (Oxford)	NL-CR NL-CR 0xford Plasmalab 100 ICP • Temperature: 20 °C • SF_6 flow: 50–120 sccm • CM pressure: 10 mTorr • ICP power: 600 W, CCP power: 7.5 W, He pressure: 10 mbar, V_{dc} : -40 . . . -55 V, Etch-time: 1 min
	XeF_2 SLE	NL-CR / XeF_2 apparatus • Pressure: 3 Torr, Cycle time: 30 sec, Etch-rate: ±4.9 µm/cycle, Etch-cycles: ± 8
63	Inspection by optical microscope (#metro101)	NL-CR / Nikon Microscope Dedicated microscope for lithography inspection
	Comments	Check release by color changes on membrane edges while blowing

Chapter

11

ACKNOWLEDGMENTS & VITA

In my time at the University of Twente, I have privilege to be in contact with many wonderful people, friends and talented colleagues. I take this opportunity to express my deep thanks to them for their help, support and cooperation. There are, however, a few people who I would like to thank in particular.

First, I would like to express my sincere gratitude to my supervisor Gijs not only for his expert guidance, kindness, friendship, and support but also for interesting me for MEMS, biology and micro-sensors' technology. His critical inputs and encouragement were vital to advance my academic skills and to the completion of this work. Indeed, he has been a distinguished teacher and deserves special thanks at this point.

I would like to thank my committee members and appreciate their willing to devote time to the reading of this thesis and judge this work. A special thank goes to all my colleagues at the Transducers Science and Technology (TST) group. I really appreciate the nice working environment and freedom I have had through the past four years. The rich mixture of cultures, languages and personal points of views as well as the steadily developed cleanroom and laboratory equipments have had a fruitful impact on my work. It has been an honour and fortunate to be a member of the TST group. In particular, special thank goes to Miko for providing us with such atmosphere. The work of the secretaries, Susy, Satie and Karen, in assisting and organizing all practical group issues (specially in the weekends) hand-in-hand with their kindness is highly acknowledged. I am also grateful to Theo and Remco for the fruitful discussions we had, their comments, suggestions and constructive criticisms. I thank Erwin, Kees and Meint; for the micromachining technical advices, possible problems and solutions they provided. Furthermore, I am also thankful to: Pino, Martin, Marcel K. and Thijs; for helping in introducing me and explaining various measurement setups. Henk; for providing me with computers, software packages and maintaining them. Vitaly; for the help in the physical explanations and mathematical derivations. It has been a great honour for me to work with such dedicated scientists. Ram, Chrix ☺ and Nima; for the nice teamwork, conversations and fun times we shared together. Narges, Harmen, Robert, Florian and Hadi; for the fruitful discussions and collaborations we had. Leon W.; for the nice company we had in Norway. Olti, Jeroen, Antoine and Maarten; I wish you all success in your Ph.D. Apart from work, there were numerous conversations, coffee breaks, lunches, conference evenings and TST outings. Certainly, it would have been less enjoyable without all of the TSTers.

I would like to thank the nice friends from various countries whom I was pleased to meet and know. Particularly, thanks go to my office mates Mubassira and Hammad for the nice discussions and conversations we had. Also I thanks Kazmi for his countless emails asking for coffee breaks and for being as a second author in one of his papers ☺. Many thanks go to brothers in UTMuslims group and to my dearest friends in Jordan for their friendship. Special thanks go to my parents in law (Dr. Qassem & Samar) for their love, kindness and support.

Furthermore, I would like to express my sincere thanks and appreciation to my parents (Mohammad & Heyam) for their patience, sacrifice and prayers. I thank them for what they have taught over the course of many years. I am and I will be forever grateful for their support and sacrifice. Great thanks go to my second mother and father (grand parents) for their supplications all of the time. I wished to see you both before passing away. '*EnshAllah*' their souls are rest in peace. I am also thankful for all of my beloved sisters and my brothers for their ultimate support and love.

Finally, I haven't got enough words to express my gratitude to my wife 'Sarah' for her love, close support and patience. Thanks for offering me a beautiful son 'Taym' who will be certainly proud of his 'young' mother. Just being both of you in my life will make it fully with love, success and happiness '*Ameen*'.

Ahmad Dagamseh

A.D

Enschede

2011

THE VITA OF AHMAD DAGAMSEH

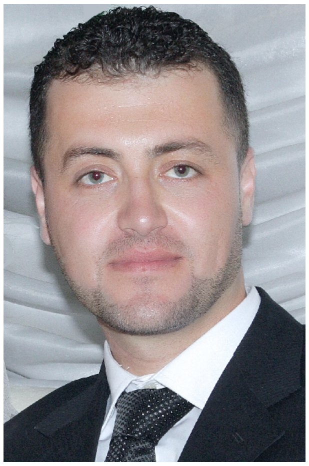

Ahmad was born on the 5th of December 1981 in Irbid, Jordan. He received the Bachelor degree in Electronics Engineering from Yarmouk University–Jordan in 2004 where he spent another year as a research assistant in the same department. Ahmad received Yarmouk Fellowship and TUDelft Top-Talent Fellowship in 2005 for the support of his graduate studies. He earned his master Degree in Microelectronics from Delft University of Technology–The Netherlands, with *cum laude*, in 2007. In the same year, Ahmad started as a Ph.D. student in the Transducers Science and Technology group at the University of Twente –The Netherlands, on the work presented in this thesis.